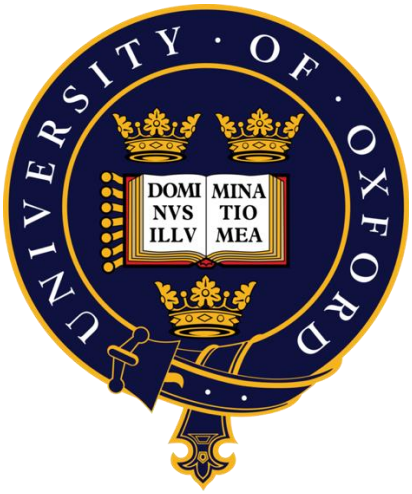

University of Oxford

A Nanoparticle Dynamics Model: Computational Analysis of Nanomedicine in the Circulatory System

Author:

Jeffrey Colin Howman

Supervisors:

Prof. Stephen J. Payne

Prof. Eleanor Stride

Department of Engineering Science

October 23rd, 2025

ABSTRACT: A Nanoparticle Dynamics Model: Computational Analysis of Nanomedicine in the Circulatory System

Info: Jeffrey Colin Howman, St. Cross College, DPhil Engineering Science, Michaelmas Term 2024

Background: The brain is one of the most complex organs in the human body and greatly varies from person to person. The delivery of drugs vital for fighting disease occurs largely within the microvasculature. This creates unique challenges when developing patient-specific medical therapies. Modern research has focused on nanoparticle drug delivery methods to treat diseases such as cancer. Generating a model that considers subject variability and nanoparticle characteristics to determine treatment efficacy thus has potential use in a clinical context.

Methods: A model was developed that utilises a Green's function method to simulate the transport of gold nanoparticles in human microvasculature. This open-source C++ code was adapted here to simulate gold nanoparticle delivery in the cerebral capillary bed using experimental and synthetic statistical networks. This code was used to simulate gold nanoparticles in both steady-state and time-dependent conditions.

Results: Simulations of flow within a series of experimental and synthetic networks provided a set of visual and statistical data describing the delivery of gold nanoparticles to cerebral tissue. Results show a high degree of variability within individual test networks but statistical similarity across all test networks. These results were compared to oxygen, which showed similar transport phenomena despite different solute characteristics.

Conclusions: This thesis emphasizes the importance of simulating the transport of gold nanoparticles within the microvasculature of the human brain. This will become especially significant when analysing nanoparticle treatment efficacy.

Table of Contents

NOMENCLATURE

A = corrective factor
A = cross-sectional area
C = concentration
C_D = shape factor
C_{HB}= concentration of haemoglobin-bound oxygen in a fully saturated blood cell
C_{Mb} = concentration of myoglobin
C_p^b = concentration of solute p in inflowing blood
C_p^e = extravascular concentration of oxygen
C_p^t = tissue concentration of oxygen
C_p^v = concentration of oxygen averaged over vessel cross sectional area
D = diffusion coefficient
D_p = diffusion coefficient of solute p
D_B = Brownian movement diffusion coefficient
D_{Mb} = diffusion coefficient of myoglobin
D_{endo} = endothelial layer diffusion coefficient
D_s = shear induced diffusion coefficient
D = domain of interest
E = second elliptical integral
F = external force
F = function
F = distribution of radial flux across a cylindrical surface
G = gain
G = Green's Function
G_0 = Green's Function unknown constant
G_{0p} = Green's Function constant, ambient concentration
$\bar{G}_p$ = integrated Green's Function of solute p
G_{pij}^{tt}, G_{pij}^{vt}, $\bar{G}_{pij}^{tt}$, $\bar{G}_{pij}^{vt}$, $\bar{G}_{pij}^{tv}$, $\bar{G}_{pij}^{vv}$ = diffusive interaction matrices
G = conductance
H = haematocrit
H_D = discharge haematocrit
J = transport flux
K = permeability tensor
K = intravascular resistance
K = first elliptical integral
K_M = Michaelis rate constant
K_s = Chen *et al*. updated Arrhenius Equation coefficient
K_e = derivative feedback gain
K_i = integral feedback gain
K_p = proportional feedback gain
L = vessel length
M = reaction term
N_b = number of boundary nodes
N_S = number of reacting solutes
N_t = number of tissue cuboidal regions

N_v = number of vessel segments
P = fluid pressure
P^* = myoglobin-facilitated partial pressure of oxygen
P_{bi}^0 = intravascular pressure of oxygen of segment *i* in the absence of diffusive oxygen exchange
P_p= coefficient dependent on permeability
$\boldsymbol{Q}$ = volumetric flow rate
$\boldsymbol{R}^3$ = spatial domain of interest
R_p = rate of production of solute p
S = source/sink term
R = vessel resistance
T = temperature
V = volume
V_m = molar volume
X_p = concentration of solute p
X_p^t = solute p concentration in the tissue
a = Arrhenius Equation constant
d = vessel diameter
d_{crit} = critical diameter threshold
d_{eff} = effective diameter
d_{off} = lower diameter threshold
e = subscript, denotes extracellular compartment
erf = error function
f = function
f^{-1}= inverse function
i = subscript, denotes element i in series or intracellular compartment
j = flux of oxygen at the capillary-tissue interface
j = subscript, denotes element j in series
k = kinetic rate constant
k = subscript, denotes element k in time series
k_B = Boltzmann constant
m = mass
p = subscript, denotes solute p
q_0 = distribution of source strength per unit length
q_l = oxygen efflux per unit length
q_p = vessel source strength of solute p
r = radius, distance from capillary centre line
r_H = hydrodynamic radius
r_b = red blood cell radius
r_c = capillary radius
r_D = sphere radius or near-sphere radius
r_{pore} = endothelial layer membrane pore radius
r_t = tissue radius
s = segment length
t = time
t_0 = starting time, typically 0

t^* = previous time point
t' = intermediate time
t = superscript, denotes tissue
$\boldsymbol{u}$ = fluid velocity
u_{Bmax} = maximum centreline velocity of blood
v = superscript, denotes vessel
x = distance, along x-axis
$\boldsymbol{x}^*$ = previous x location point
$\boldsymbol{x}'$ = intermediate x location point
y = distance, along y-axis
z = distance, along z-axis
β_{ij} = matrix of blood fractions in vessel segments i at times t_k from vessel segments j
α_{eff} = effective solubility coefficient
α_{ij} = matrix of time step fractions that the blood in segments i at times t_k spent in segments j
α_p = solubility of oxygen in plasma
α_{rbc} = solubility of oxygen in red blood cells
α_t = solubility coefficient
γ = bifurcation exponent
$\dot{\gamma}$ = strain rate
γ_{ij} = matrix of blood fractions in vessel segments i at times t_k from boundary nodes j
η = membrane shear viscosity
η_∞ = Quemada parameter
λ = Quemada parameter
τ = fluid shear stress
τ = time constant
τ_y = Quemada parameter
ρ = fluid density
μ = blood dynamic viscosity
θ = angle around vessel
δ_1 = one-dimensional delta function
δ_3 = three-dimensional delta function
ϕ_j = negative source strength of tissue region j
ψ_p = distribution of solute sources and sinks within the domain of interest
$\bar{\psi}_p$= spatially uniform solute source outside the domain of interest
ξ_{ij} = matrix of fractions of the outflowing blood that arrived from boundary nodes j
ω_{ij} = matrix of fractions of the outflowing blood that arrived from vessel segments j
ζ_{ij} = matrix of time step fractions that outflowing blood spend in segments j
φ = volume fraction

CHAPTER 1: INTRODUCTION

1.1 BACKGROUND

The brain is the most complex organ with many biological structures that vary from person to person. Due to its significance for life and normal functionality, malfunctions and adverse changes to the brain's structure are particularly severe. With the increase in human lifespan across the world, brain disorders and central nervous system (CNS) diseases are becoming more common and thus are of greater focus in medical research. It is estimated that 1.5 billion people worldwide suffer from central nervous system disorders (Wilson, 2019).

The prevalence of brain diseases has an increased burden on the medical industry and on the finances of those affected. In 2010, it was estimated that 179 million people in Europe were affected by some form of brain disease with resulting healthcare costs (both direct and indirect) totalling around 800 billion euros (DiLuca & Oleson, 2014). A breakdown of these costs is given below in Figure 1.1.

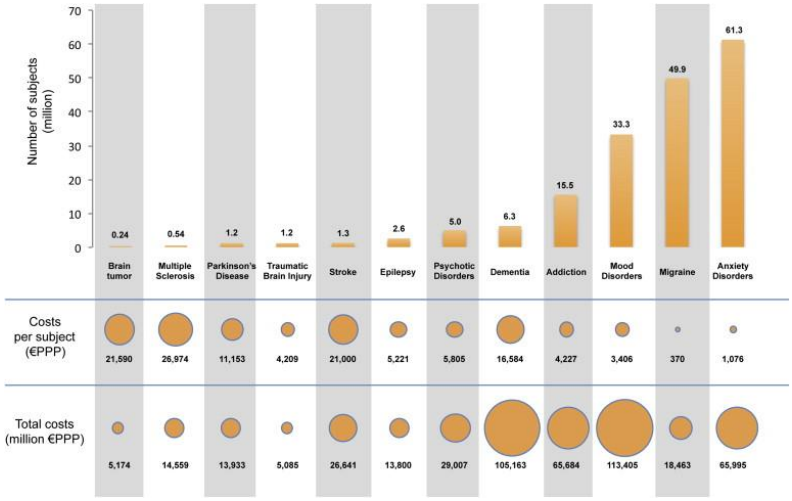

Figure 1.1: Diagram demonstrating the number of subjects for the most prevalent brain diseases and associated costs. Costs are broken down into cost per subject and total cost in the healthcare industry. Reproduced with permission from DiLuca and Oleson 2014.

A plethora of medicinal therapies have been proposed over the years. Some of these methods are invasive, including direct intracerebral injection of drugs into brain tissue, intraventricular administration through cerebrospinal fluid pathways, and surgical interventions. Example surgical interventions include temporary blood-brain barrier (BBB) disruption using osmotic agents, focused ultrasound-mediated barrier opening, and implantation of drug-eluting devices or convection-enhanced delivery systems. Others are non-invasive, focusing on modifying drugs through systemic routes (intravenous, oral, transdermal, or intranasal delivery) to enhance their acceptance by the human body and facilitate brain penetration. Figure 1.2 below presents several common drug targeting options in the brain.

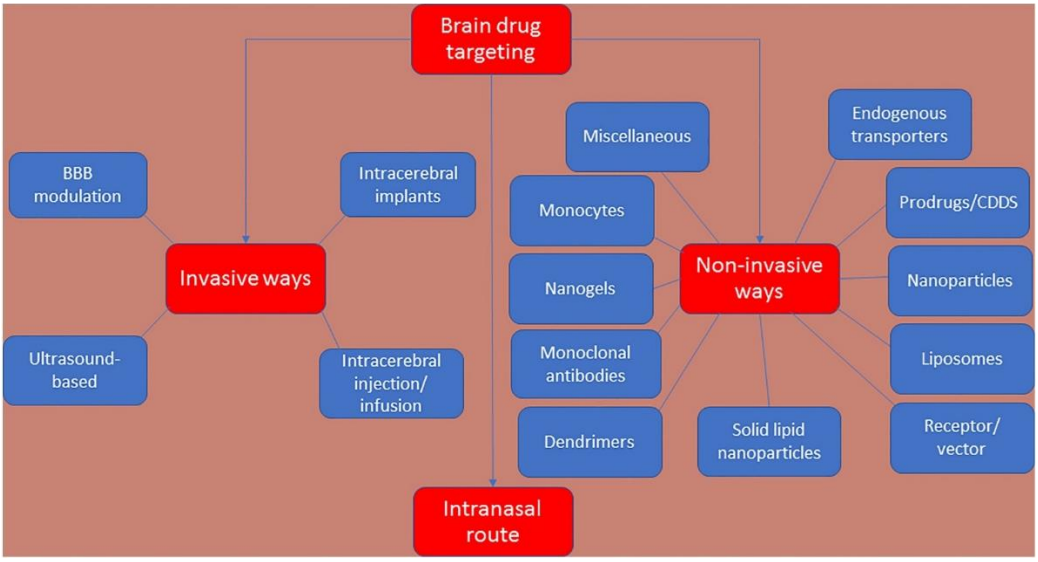

Figure 1.2: Figure presenting several of the methods for delivering medical therapies to the brain. Reproduced with permission from Wilson 2019.

All encounter a similar roadblock to effective treatments: the blood-brain barrier (BBB). The BBB is a monolayer lining of endothelial cells along the vascular walls that is permeable to only some compounds, acting as a physical obstacle to most composites. This selective lining can prevent harmful substances, such as microorganisms and neurotoxins, from entering the brain tissue and potentially harming sensitive neurons. The protective nature of the BBB also makes it difficult to treat the variety of brain disorders and CNS diseases previously listed: most clinical trials fail at crossing the BBB (Wilson, 2019). A figure demonstrating the structure of the BBB is shown below in Figure 1.3.

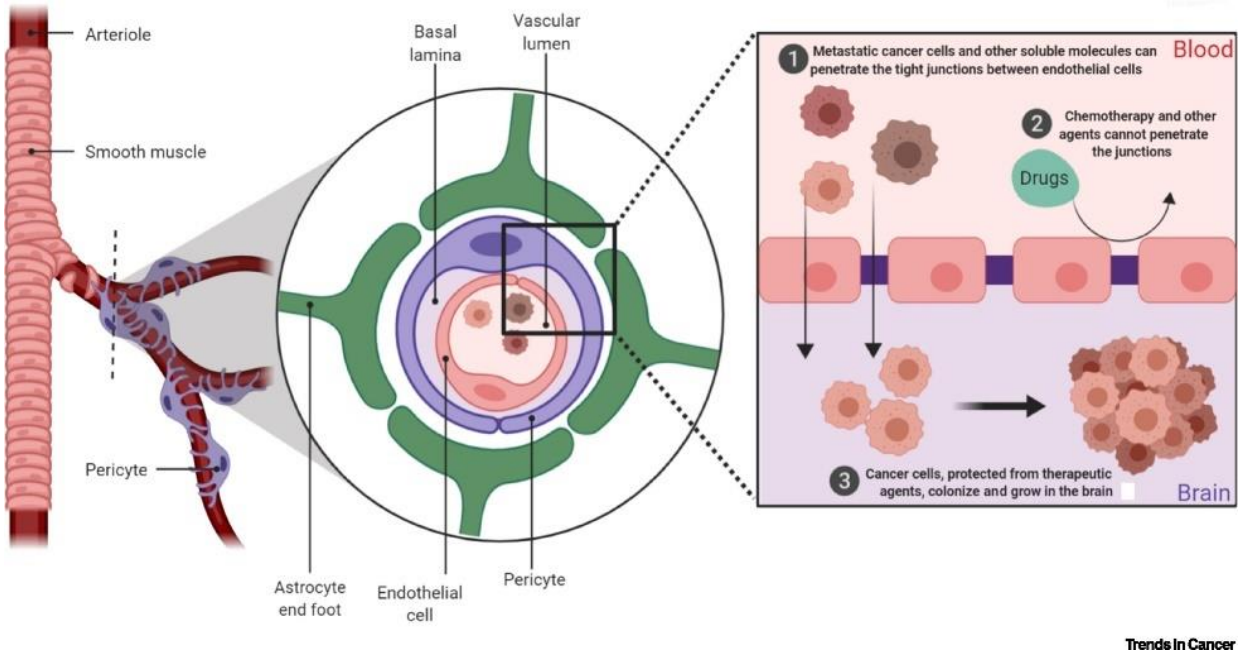

Figure 1.3: Diagram of the blood-brain barrier with examples of selectivity in what crosses the threshold (Fares, 2020).

1.2 CURRENT CHALLENGES

The reason that many clinical trials for drug deliveries fail is that the drugs are incompatible with the available BBB transport mechanisms (unable to be passively transported and lacking the functional group markers for active transport methods) and thus not allowed to enter the interstitium. To address this challenge, work has gone into developing molecular compounds that can transport the pharmaceutical drugs across this barrier; one such classification of compounds are nanoparticles, particles with diameters that fall between 1-100 nanometres.

Nanoparticle delivery systems enhance BBB transport through several mechanisms: altering surface functionalisation with targeting ligands to bind to specific receptors on brain endothelial cells for facilitated receptor-mediated transcytosis, modifying surface charge and hydrophobicity to exploit adsorptive-mediated transcytosis pathways, optimising nanoparticle size for improved passage through intercellular tight junctions, and finally enhancing passive diffusion across the BBB lipid bilayer through the use of lipophilic carriers. Examples of current nanoparticle therapeutics include the use of functionalised liposomal nanoparticles for the delivery of doxorubicin or erlotinib to treat brain tumours, chitosan nanoparticles for the delivery of Selegiline or Pramipexole for the treatment of Parkinson's disease, and PCGA (polylactic-co-glycolic acid) nanoparticles functionalized with chlorotoxin for the delivery of Lexiscan to assist with stroke therapies (Teleanu *et al*., 2018).

This area of medical research is still developing and financially expensive; the translation of nanomedicines into a clinical setting has financial and time limitations due to the dearth of theoretical and clinical models (Joseph *et al*., 2023). Additionally, every patient varies and may react to drugs differently which creates many challenges when developing subject specific pathologies (Goetz & Schork, 2018). Ideally the delivery of drugs through these novel compounds

to the brain could be optimised, reducing the need for costly experiments and potentially saving money for those undergoing treatment.

This challenge to nanoparticle therapy stems in part from the unknown nanoparticle dynamics and distribution in the blood flow of an entire organism. Current investigative methods offer little brain or BBB information or are highly idealized and under specific test conditions. The least invasive image-based techniques are often most cost prohibitive, requiring the use of specific medical equipment such as MRI machines and of tracers that may or may not impact the pharmacokinetics of the nanoparticles being studied. Additionally, depending on the specific method, the spatial resolution returned may be low and may not provide accurate results. Table 1.1 below presents a few examples of image-based techniques. In this table, spatial resolution defines the size of image voxels, temporal resolution defines the time it takes to capture a single image frame of the object being observed, and imaging duration refers to the amount of time taken to fully capture a subject's image profile.

Table 1.1: Representative imaging techniques and characteristics. Adapted from Fan *et al*., 2023; Hoover & Squier, 2013; and Lin & Alessio, 2009.

Imaging technique	**Spatial resolution**	**Temporal Resolution**	**Imaging Duration**
PET	0.1–1 mm	5s - 5 minutes	Seconds–minutes
SPECT	4–15 mm	15 minutes	Minutes
MRI	1–2 mm	20-50 ms	Minutes–hours
Two-photon imaging	250 nm	1 mircosecond/pixel	Seconds–minutes
	Mechanism	**Advantages**	**Disadvantages**
PET	Positron emitting radio isotope	High contrast; high tissue penetration depth	High cost
SPECT	Gamma emitting radio isotope	High tissue penetration depth; low cost	Poor spatial resolution
MRI	Excitation by a magnetic field	No radiation; high tissue penetration depth	High cost; long scanning time
Two-photon imaging	Fluorescence	High spatial resolution; no ionizing radiation	Poor penetration depth (<2 mm)
Abbreviations: PET, positron emission tomography; SPECT, single-photon emission computerized tomography; MRI, magnetic resonance imaging			

Other invasive methods are limited to rat models, as they involve measuring the concentration of nanoparticles or other drugs after extracting the brain and analysing using high-performance liquid chromatography (HPLC) (Fan *et al*., 2023). The prevalence of rat brain studies means that many blood flow models are dependent on rat brain vasculature data and are then applied to humans; this is only possible up to a certain scaling and is not an exact analogue for human cerebral vasculature systems (Payne *et al*., 2023). A comprehensive computational study of blood fluid dynamics and its effect on nanoparticle diffusion and distribution throughout the human brain would thus be valuable, providing increased predictive power for nanoparticle testing and circumventing potential hazards.

Beyond the brain, the model developed through this research has a variety of applications in the body. Standard drug delivery systems, while exhibiting properties different from those present in nanoparticle carriers, may still be accounted for using the simulation described. Updating parameters affected by change in molecular properties (weight, shape, degradation, and uptake rate) or in biological system (blood flow rate, vascular network, temperature, pressure, vessel characteristics, and tissue diffusivity) would not affect simulation function and would allow for similar optimisation of dosage, location, and cost. Current research has not fully produced optimisation of this level, so the results would help to improve the way drugs are administered.

1.3 RESEARCH OBJECTIVES AND NOVELTY

The purpose of this thesis is therefore to develop a series of mathematical models that performs two tasks: one, recreate the blood flow environment within a variety of vascular networks; and two, model nanoparticle transport within this environment. This research is specifically focused on developing predictive computational tools for optimising gold nanoparticle (AuNP) delivery to cerebral tissues, with the hypothesis that integrated multi-scale modelling approaches

can significantly improve therapeutic efficacy while reducing experimental costs and clinical trial failures.

The novel contributions of this work include: the development of new integrated computational models that combine cerebral arterial flow dynamics with microvascular nanoparticle transport mechanisms; the creation of subject-specific predictive tools that account for individual patient variability in vascular architecture and autoregulation responses; the establishment of a comprehensive multi-scale framework that bridges arterial-level haemodynamics with capillary-level drug delivery; and finally, the validation of these models against both theoretical predictions and experimental data to ensure clinical relevance.

The integrated computational models are based upon a variety of previous works. Cerebral arterial blood flow and autoregulation is handled in a method developed by Badiani (Badiani 2018). Raw patient data in the form of MRI scans are taken and converted to nodal data with blood flow calculated in a lumped flow compartment model analogous to an electrical circuit (Payne 2017). Autoregulation is handled with a Python PDE solver. For the microcirculation modelling a Green's function method is utilised to simulate blood flow and perfusion at the capillary level for a series of statistical synthetic networks (Secomb *et al*., 2004; Secomb *et al*., 2015; El-Bouri *et al*., 2015). This was completed under both steady-state and time-dependent conditions. Finally, both Green's function models were adapted to handle gold nanoparticles based upon pharmacokinetic data taken from both theoretical and experimental studies (Shamloo *et al.*, 2016; Zhou *et al*., 2018).

1.4 SCOPE OF THESIS

This thesis consists of a total of seven chapters with this introduction being the first. Chapter 2 contain a comprehensive literature review detailing research into the four cerebral haemodynamic fields that have relevance to the overarching topic: cerebral arterial structure,

microcirculation and perfusion, cerebral autoregulation, and nanoparticle pharmacokinetics. Within each topic both qualitative and quantitative theory will be presented with a focus on information pertinent to the models developed in this thesis. Chapters 3 through 5 focus on the three models developed for this thesis with subchapters detailing results and a discussion relevant to chapter topic.

Chapter 3 specifically delves into the cerebral arterial blood flow model and simulations. The architecture used in this chapter uses the work presented in Badiani 2018 as a guide for developing the cerebrovascular network and flow conditions therein (Badiani 2018). Chapter 4 presents a model that simulates solute delivery in synthetic capillary network under steady-state and time-dependent conditions. This is accomplished by utilising a Green's function method to analyse experimental and generated synthetic networks (El-Bouri *et al*., 2015; Secomb *et al*., 2004). Chapter 5 builds upon the model developed in Chapter 4 to simulate AuNP interactions within the cerebral microvasculature. Chapter 6 outlines potentials avenues for future studies built upon the results gathered in the preceding chapters.

AuNPs were chosen here for their cost effectiveness, easy parameter tuning, low toxicity, and high stability (Zhou *et al*., 2018). The architecture for this project is supplemented with parameters and pharmacokinetics drawn from Foehrenbacher *et al*., 2013 and Chen *et al*., 2022. Chapter six focuses on future work that may be performed with the models presented in chapters three through five. The topics presented therein were not able to be pursued within the constraints of a thesis but are of academic interest and could further develop the current understanding of nanoparticle pharmacokinetics.

CHAPTER 2: LITERATURE REVIEW

2.1 INTRODUCTION

This chapter provides a comprehensive literature review detailing research into the four cerebral haemodynamic fields that have relevance to the overarching topic: cerebral arterial structure, microcirculation and perfusion, nanoparticle pharmacokinetics, and cerebral autoregulation. The biology of the systems, qualitative theory, and quantitative theory will be presented. Various models will be considered and compared to select the models that will be used for simulation purposes.

This review covers existing knowledge to identify gaps that this thesis addresses through novel integrated modelling approaches. The key original contributions emerging from this analysis include the identification of limitations in current uncoupled modelling approaches that motivate the development of integrated multi-scale frameworks and the establishment of a comprehensive parameter space for gold nanoparticle transport that enables predictive modelling.

The large artery model, capillary model, and transport model reviewed here and further developed in this thesis are intentionally designed as uncoupled systems for specific methodological reasons. This approach allows for independent validation of each component against established experimental data, enables computational efficiency for parameter sensitivity studies, and facilitates modular application to different patient-specific scenarios. The large artery model provides boundary conditions for the capillary system, while the capillary model generates the vascular network topology for transport simulations. Future work will explore coupled approaches once individual model validation is complete, as discussed in Chapter 6.

2.2 HUMAN CEREBRAL LARGE ARTERIAL VESSEL NETWORK

2.2.1 Introduction

When blood enters the human brain, it does so through the carotid arteries and is split between several smaller, branching arteries. The flow then enters the capillary bed where most oxygen and nutrient dispersal occurs. Blood flow then leaves the capillary bed and leaves the brain through the veins. Blood flow rate and pressure is regulated though internal mechanisms throughout this entire structure for the safety of the individual. Understanding the general structure of the human cerebrovasculature is vital to determine drug delivery efficacy and will thus be discussed in the first half of this section. The second half will detail the mathematical equations and laws that govern the model and simulate the above four categories.

2.2.2 Biology

2.2.2.1 Cerebrovasculature

The human brain, while only a small portion of the body, requires the most blood flow out of any organ: approximately 14% (Kety and Schmidt, 1948). This is due to the hefty metabolic demand that neurons require, which is 20% of the entire body (Kety and Schmidt, 1948). This high energy demand stems from the continuous maintenance of ionic gradients across neuronal membranes, active neurotransmitter synthesis and recycling, and the energy-intensive processes of action potential propagation and synaptic transmission (Sethuraman, 2017). To deliver the necessary amount of oxygen and nutrients (primarily glucose), an optimised delivery method operating under the constraints of the mass transport equation is required. This delivery method is the cerebrovascular system.

Within the blood vessels of the cerebrovascular system, chemically bound oxygen molecules dissociate from haemoglobin while dissolved oxygen diffuses through the red blood cell membrane, blood plasma, the capillary wall, and interstitial fluid until it enters the neurons and glial cells. Other nutrients, such as glucose, within the blood travel along the same route but

are usually transported across membranes with the help of glucose transporters instead of freely diffusing. CO_2, a waste product of brain metabolism, rapidly diffuses out of the cerebral tissue and is cleared via the vascular system. The endothelial cells of the brain vessels are coupled by tight junctions and form the blood-brain barrier, selectively permitting the transport of other molecules (Schmid *et al*., 2019). The blood-brain barrier will be discussed in greater detail later in this chapter.

The main cerebral arterial vasculature structure consists of several large substructures: the internal carotid arteries, vertebral arteries (the left and right of which form the basilar artery), anterior cerebral arteries, middle cerebral arteries, and finally posterior circle arteries. These major arteries, in addition to the anterior and posterior communicating arteries, comprise the complete Circle of Willis (Flemming *et al*., 2015). The anterior cerebral arteries supply the frontal lobe and remainder of the forebrain; the middle cerebral arteries source the deep structures, such as the basal ganglia and thalamus; and finally the posterior cerebral arteries supply the posterior cortex, midbrain, and brainstem. These major arterial structures supply the necessary level of nutrients and oxygen to neurons in the frontal lobe. A visual representation of this anatomy is presented below in Figure 2.1.

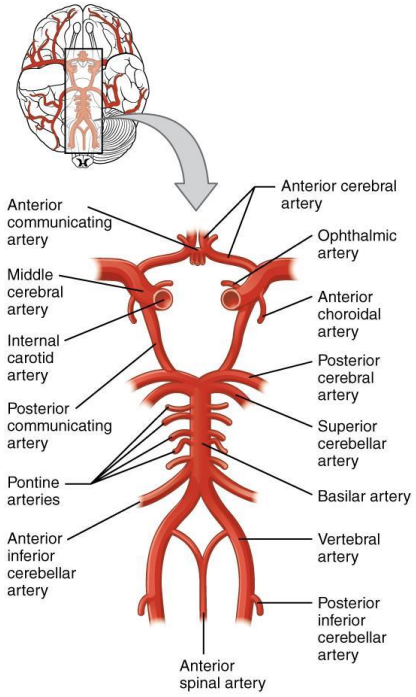

Figure 2.1: Schematic of large arterial vessels in the brain. Reproduced without changes from OpenStax College under license http://creativecommons.org/licenses/by/3.0/

The anterior, middle, and posterior artery pairs form a network of large vessels that is commonly thought of as a bifurcating tree of ever-decreasing diameter and length (Payne *et al*., 2023). The practical limit of this ever-decreasing diameter assumption occurs at the lower end of the arteriolar diameter range (approximately 10 micrometres), where vessel mechanics transition from elastic-dominated behaviour (found in large arteries) to resistance-dominated behaviour (found in capillaries).

Arterial blood enters sections of the brain via the leptomeningeal vessels and the penetrating/descending arterioles that delve deeper into the cortical tissue. The perivascular space that surrounds these vessels, the Virchow-Robin space, clears interstitial fluids as part of the glymphatic system. The penetrating arterioles within the Virchow-Robin space continue to bifurcate, decreasing in diameter and changing in wall composition (Cipolla, 2009). The

penetrating arterioles then structurally become parenchymal arterioles once they are almost fully surrounded by astrocytic end-feet. Parenchymal arterioles are the last artery structure before the capillary bed (Cipolla 2009). Veins work in reverse to the arteries, with postcapillary venules feeding into ascending venules and hence back into the venous pial circulation (Payne *et al*., 2023). Figure 2.2 below is a schematic showing the Virchow-Robin space to capillary bed with cross sections of vessels of the various arterial structure types.

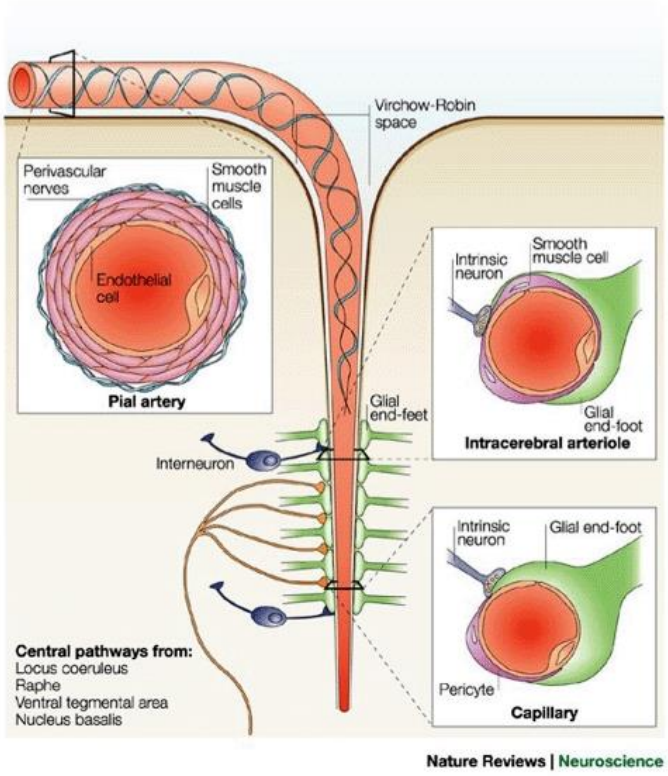

Figure 2.2: Schematic showing pial arteries on the brain surface. These arteries have perivascular nerves that give rise to penetrating arteries within the Virchow–Robin space. Reproduced with permission from Cipolla 2009.

While the above-mentioned structures are considered somewhat standard across the human population, this is not always the case. Human anatomy varies from person to person; just as some people are taller than others, some individuals have incomplete cerebrovascular structures. It was noted by Papantchev *et al*., 2013 in a study of 500 patients (250 from dissection and 250 from computed tomographic angiography) that 58% of those tested have some variation in the Circle of Willis (Papantchev *et al*., 2013). A Circle of Willis was said to be variant if an individual or several vessels were exhibiting aplasia or hypoplasia.

Specific variations include hypo/aplasia of the left posterior communicating artery (PComA) (35.6% of cases), hypo/aplasia of the anterior communicating artery (AComA) (2% of cases), hypo/aplasia of both the PComA and AComA (4.8% of cases), hypo/aplasia of the precommunicating segment of the left posterior cerebral artery (P1) or the right vertebral artery (VA) (9.2% of cases), hypo/aplasia of the precommunicating segment the right anterior cerebral artery (A1) (6% of cases), hypo/aplasia of both the rVA and AComA (0.2% of cases), and finally hypo/aplasia of both A1 and VA or both A1 and P1 (0.8% of cases) (Papantchev *et al*., 2013). Figure 2.3 below displays these segments in relation to the rest of the Circle of Willis. Even if the vasculature is complete, the way the vessels position and branch throughout the brain may also vary. This variability will have a large impact on model development and the generated results, especially if it is patient-specific.

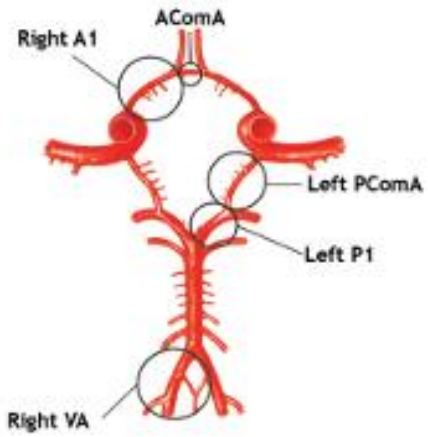

Figure 2.3: Diagram displaying Circle of Willis segments commonly most affected by aplasia or hypoplasia. A1: precommunicating segment of anterior cerebral artery; AComA: anterior communicating artery; PComA: posterior communicating artery; P1: precommunicating segment of posterior cerebral artery; VA: vertebral arteries. Modified with permission from Papantchev *et al*., 2013.

2.2.2.2 Cerebral Autoregulation

The cerebral vasculature, while efficient in delivery, is sensitive to changes within the system. In any given moment, the environmental conditions within the blood stream fluctuate. Straying too far from homeostasis may cause lasting problems and lead to disease or a lack of vital oxygen to brain cells. For this reason, the human body has developed a mechanism with which to maintain control. Poiseuille noted in his work that blood pressure and flow rate largely relied on vessel diameter, length, and blood haematocrit. Considering that vessel length and haematocrit are both fairly constant, the only variable left to change is diameter (Payne 2017). Figure 2.4 below illustrates how a change in vessel affects both cerebral blood flow and blood pressure.

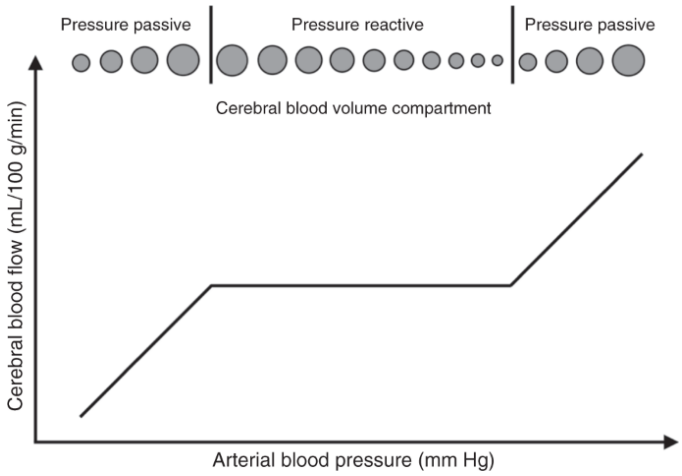

Figure 2.4: Graph of cerebral blood flow vs. arterial blood pressure when under the effects of cerebrovascular autoregulation. The top circles represent relative artery diameter. The body will attempt to maintain a constant blood flow rate over a pressure range and does so by decreasing vessel diameter as pressure increases. Should pressure drop too low or go too high blood flow rate and vessel diameter will also adjust accordingly to return to normal values. Taken from Rhee et. al 2018.

The assumption that only vessel diameter affects cerebrovascular autoregulation holds only in healthy individuals. A variety of vascular insufficiencies occur due to disease, trauma, or aging, all of which affect cerebral blood flow and autoregulation, in some cases through changes to the vessels within. Ageing specifically shows a decrease in autoregulatory ability, though it does not disappear (Payne, 2017). This may be in part due to the blood vessels increasing in length and tortuosity, though a variety of other confounding factors may be at play. Other forms of cerebral disease (brain trauma, stroke, dementia, etc.) will have unique effects on autoregulation; ageing, for example, shows greater variance in cerebral blood flow as autoregulation strength decreases (Payne, 2017). The type of trauma will directly impact autoregulation as well as other blood vessel

properties; only considering changes in vessel diameter serves as a baseline with which to compare against.

Autoregulation contains both a passive and an active component as the passive may lead to a positive feedback loop due to arterial compliance (Payne 2017). The active, or myogenic, response is usually able to counteract the passive response if needed. The myogenic response is in response to pressure: contraction for increased pressure or relaxation for decreased pressure. The larger vessels themselves contract using the vascular smooth muscle, while in the capillary bed small cells called pericytes perform this function (Attwell et. al 2016). There is still great debate regarding the extent of pericyte role in cerebral autoregulation (Payne 2017), but it is now accepted that pericytes play a significant role. It should be noted that this cerebral feedback system has a profound impact on what measured values of *in vivo* flow rates and pressures are compared to theoretical models and will be discussed in greater detail in further sections.

2.2.3 Mathematical Modelling

2.2.3.1 Cerebrovasculature Modelling

In terms of the physical equations behind said models, most simulations are derived mathematical structure from the Navier-Stokes equations and the mass transport equation. The incompressible form of Navier-Stokes is listed below as Equation 2.1, while the mass transport equation is shown in Equation 2.2. In these equations, ρ is the mass density (kg/m^3), $\boldsymbol{u}$ is the flow velocity (m/s), t is time (s), $\boldsymbol{P}$ is pressure (Pa), τ is the stress tensor (Pa), $\boldsymbol{F}$ is an external body force (such as gravity acting on the volume) (N/m^3), C is concentration (mol/m^3), M is the reaction term (mol/m^3/s), and D is the diffusion coefficient (m^2/s).

$$\rho\left(\frac{\partial \boldsymbol{u}}{\partial t} + \boldsymbol{u}\cdot\nabla\boldsymbol{u}\right) = -\nabla\boldsymbol{P} + \nabla\cdot\tau + \boldsymbol{F} \tag{2.1}$$

$$\frac{\partial C}{\partial t} = \nabla\cdot(D\nabla C) - \nabla\cdot(uC) + M \tag{2.2}$$

Under several assumptions Equation 2.1 may be simplified into Poiseuille's equation (shown below in Equation 2.3). Poiseuille's equation was derived explicitly for modelling flow through long, thin cylindrical pipes and is considered a staple in many modern steady-state simulations of cerebral blood flow. It assumes that the fluid flow is laminar in nature and describes an incompressible and Newtonian fluid.

$$R = \frac{128\mu L}{\pi d^4} \tag{2.3}$$

Here the vessel resistance R (Pa*s/m^3) is a function of vessel diameter d (m), vessel length L (m), and blood viscosity μ (Pa*s). It should be noted that blood viscosity is often considered constant, but this is not always the case; blood is a non-Newtonian fluid with a shear-thinning regime at low strain rates and a yield stress. Viscosity is thus strongly dependent on the strain rate at low values, most notably in the smaller blood vessels (Payne *et al*., 2023).

For the larger vessels, the viscosity is often taken as between 0.0035 and 0.0055 Pa*s, but this value may vary depending on the model used and other parameters (Nader *et al*., 2019). Viscosity typically decreases as the vessel diameter decreases in accordance with the Fåhræus-Lindqvuist effect, though it has been found that blood viscosity increases in vessels with diameter under 1 millimetre (Payne, 2018). Blood flow models for vessels with diameters less than 100 micrometres thus often utilise empirical relationships that determine the *in vivo* viscosity as a function of vessel diameter and tube haematocrit (Payne *et al*., 2023). Haematocrit also influences viscosity: while haematocrit is often assumed constant due to its relatively small effect on oxygen transport, it has been shown that haematocrit is spatially quite heterogeneous and can split at vessel bifurcations (Payne, 2024).

The application of the above equations for the modelling of the cerebral arteries typically falls into four different types of models: zero-dimensional (0D), one-dimensional (1D), two-

dimensional (2D), and finally three-dimensional (3D). Figure 2.5 below provides a brief description of the different archetypal models used in cerebral vasculature modelling.

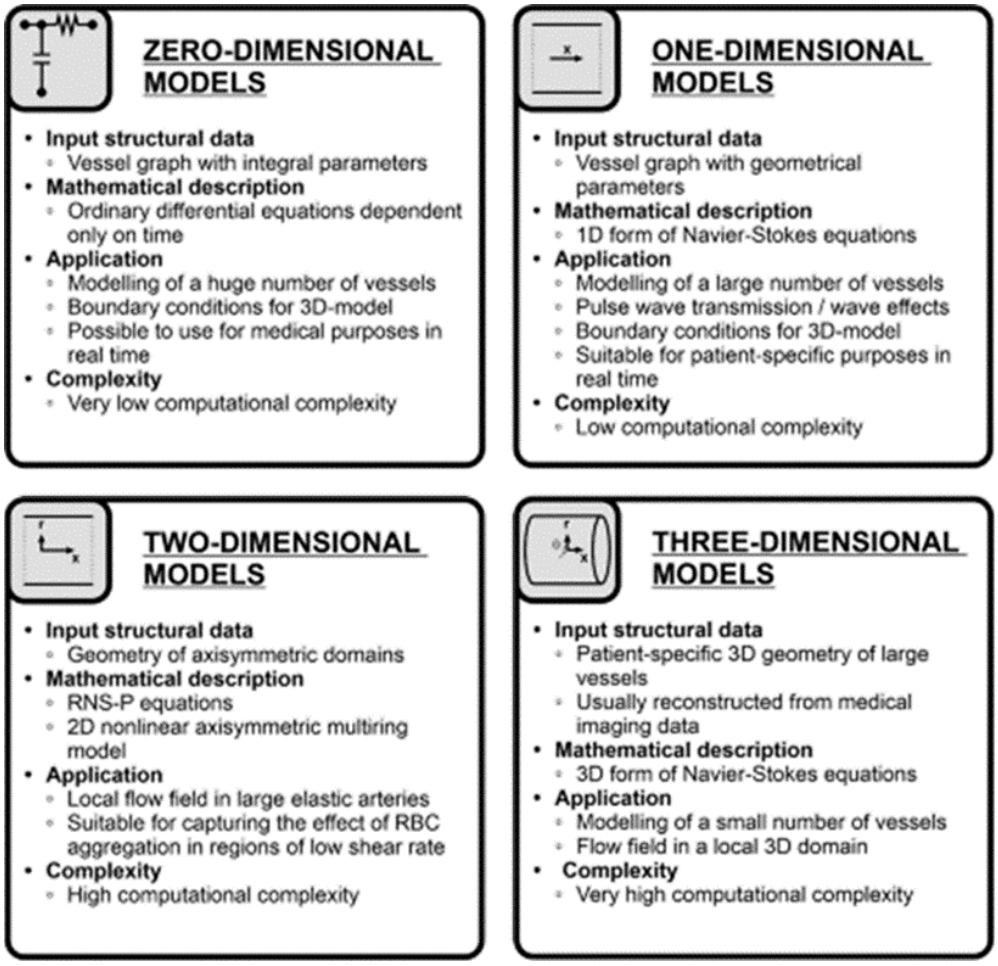

Figure 2.5: Graphic illustrating key points for each type of archetypal model used in the modelling of large cerebral arteries. Adapted from Kopylova *et al*., 2023.

Zero-dimensional models, also known as point models or spatially averaged models, are typically defined by ordinary differential equations that depend only on time. 0D models do not consider the spatial distribution of the parameters of interest, instead focusing on the impact of time dependence on variables such as volumetric blood flow, pressure, and volume. These models often use an electrical analogy that handles elasticity and hydrodynamic resistance within the

vessels: a popular model of this type is the Windkessel model. Zero-dimensional models are considered to be the simplest type of model due to the lack of spatial input and contain a large number of simplifications. This allows for significantly less computing power compared to the other models and flexibility in applications (Kopylova *et al*., 2023).

The second type of model, one-dimensional models, are similar to 0D models in their simplicity but are able to include the propagation and reflection of the pulse wave in the vascular system. 1D models are based upon averaging the long-wavelength Navier–Stokes equation by integrating over the cross-sectional area of the vessel (Sherwin *et al*., 2003). These models physiologically describe the effect of wave transmission in large arteries, such as the arteries of the Circle of Willis, due to the large wavelength of the arterial pulse compared to the artery diameter. 1D models balance accuracy and computational cost, while still being able to reproduce the features of the waveforms observed *in vivo*. These models are commonly used to simulate the Circle of Willis and other cerebral arteries (Kopylova *et al*., 2023).

Two-dimensional models use the two-dimensional Navier-Stokes equations to calculate the velocity change in radial and axial directions. This makes it possible to account for the effects of vascular wall elasticity on blood flow at any point in the vessel. 2D models are rarely used in the haemodynamic studies of blood flow and thus will not be considered discussed further with relation to this thesis (Kopylova *et al*., 2023).

Three-dimensional models are the most complex and computationally expensive of the previously described models. Implementing a 3D model requires that the boundary conditions, vessel geometry, surrounding tissue pressure, properties of the blood, properties of the vessel wall, and many other parameters are all correctly considered due to inherent structure limitations. The combination of these factors lead to a complicated mathematical model which may require

powerful computing resources. In addition, many of the parameters needed for 3D models may be patient-specific and not always viable for experimental measurement. Blood vessels are typically reconstructed from medical imaging or statistical data to accurately model their 3D geometry. Models of this class most accurately describe the blood flow in vessels with real geometry, but their scope is often limited to local areas (Kopylova *et al*., 2023).

One of the first models built to better understand brain arterial circulation was crafted by Zagzoule and Marc-Vergnes 1986, where the authors use continuity and momentum equations to determine blood flow using a 1D model. This model, however, makes several assumptions regarding the effect of changing viscosity and vessel resistance. A visual representation of their model is presented below in Figure 2.6.

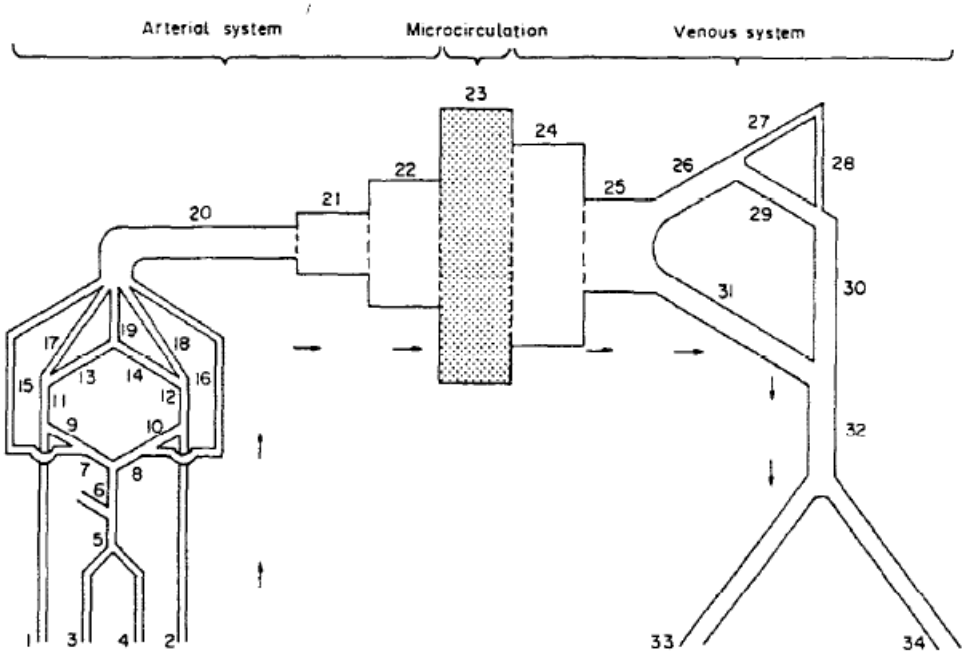

Figure 2.6: Schematic of complete cerebral circulation. Reproduced with permission from Zagzoule and Marc-Vergnes (1986).

Later, research from Hillen *et al*., 1986 and Viedma *et al*., 1997 would build on this initial model but focused more heavily on the Circle of Willis. Both models were 0D but incorporated vessel resistance to better elucidate cerebral blood flow. These studies would also form the basis for considering the arterial network as an electrical equivalent and a foundation for many future models. However, this research did not consider phenomenon seen in more recent studies, most notably cerebral autoregulation. Additionally, these early works have a more generalized focus and fail to capture the intricacies that arise from subject specific morphologies.

Other methods of creating branching arterial networks have been developed over the last two decades. The earliest and most popular is the Constrained Constructive Optimisation (CCO) algorithm (Kopylova *et al*., 2023). Developed by Schreiner in 1993 for coronary haemodynamics, the CCO algorithm gradually constructs an arterial tree with the intent of minimizing total intravascular volume and ensuring that perfusion within the region of interest is uniform. This optimises the structure and geometry of the arterial system. A bifurcation exponent was included to ensure physical agreement between parent vessel radii segments and daughter radii segments (Schreiner, 1993). Equation 2.4 below is the equation based upon the work of Murray used by Schreiner for calculating vessel radii.

$$r_0^{\gamma} = r_r^{\gamma} + r_l^{\gamma} \tag{2.4}$$

In this equation, r is the vessel radius (m) with subscripts 0, r, and l signifying parent, right daughter, and left daughter segment radii respectively and γ representing the bifurcation exponent. Schreiner used exponential values between 2.55 and 3, though later it was found that varying the exponent based upon branching order would lead to diameters that better agreed with experimental values (Meneses *et al*., 2017).

Several extensions were developed based upon the CCO approach, one of which is the Global Constructive Optimisation (GCO) algorithm. This method built upon the CCO approach by maintaining the original branching structure of the arterial system during optimisation. Another is the Staged Growth mechanism implemented by Karch *et al*., 2000 to model arterial structures between the epi- and endocardial layers of the human heart. With this method, the sequence of vessel growth regions within a given perfusion volume is determined by an additional time-dependent boundary condition that in turn generates new terminal regions (Karch *et al*., 2000). The downside of these CCO methods is that they do not accurately model tissue supplied by multiple arteries (Kopylova *et al*., 2023)

An alternative to the CCO methods is to use fractal models. Because the branching process is repeated at each step in the arterial network, they have the properties of self-similarity and have a fractal character; this allows for the creation of realistic vascular tree structures (Kopylova *et al*., 2020). This method is geometrically simpler than CCO but may still be utilised to study vascular networks and has been used in conjunction with experimental studies (Kopylova *et al*., 2023).

Combining anatomical and physiological imaging techniques with computer simulation technology generates more realistic results (Kopylova *et al*., 2023). One the first researchers to utilise raw patient data in their models was Charbel *et al*. in 2004, who developed patient-specific 1D computer models to understand blood flow patterns through vessel occlusions. This was done using magnetic resonance imaging (MRI) techniques to retrieve specific patient data.

Around the same time Cebral *et al*., 2003 and Kim *et al*., 2006 were performing similar research but with focus on making the simulation 3D. Due to the focus on the arterial network itself and recreating it within a computer program, these works did not extensively cover perfusion. Despite these shortcomings they would pioneer the use of magnetic resonance angiography (MRA)

in recreating detailed patient arterial networks. Three years later Alastruey *et al*., 2007 would further the work of Hillen et. al 1986 by applying accurate elasticity and vascular morphology components to the 1D Circle of Willis model.

While there have been several MRA studies since Alastruey *et al*., 2007 delving into cerebral macrovasculature reconstruction, not all may be utilised in this thesis due to their datasets remaining unavailable to the public (Payne *et al*., 2023). The dataset used in this thesis is taken from Wright *et al*., 2013. In their research, the Wright research group used 61 healthy test subjects and created an online database of patient-specific morphologies. This dataset is of important note for several reasons: one, the sample pool used in this report is one of the largest and statistically variant amongst all other research papers; two, it is one of the only databases to contain 3D data that are publicly available for usage; and three, it contains some of the most accurate data since it uses raw MRI imaging techniques to collect full cerebrovascular morphologies. The work did make some assumptions to ease the reconstructions, most notably excluding the Anterior Communicating Arteries to ensure a complete bifurcation network.

There are three other studies that utilise collections of publicly available reconstruction data that were considered but ultimately excluded from this thesis: Dunås *et al*., 2017, Bernier *et al*., 2018, and Mouches & Foukert 2019. All studies are confined to healthy subjects and are large enough that the results are statistically significant. The first study consisted of 167 subjects and had equal resolution to that of Wright *et al*., 2013: the downside is that the study focused on elderly (Dunås *et al*., 2017). While interesting for future work, this thesis focuses on idealized conditions, so this collection of data was not chosen.

The second study, Bernier *et al*., 2018 was similar to that of Wright in terms of subject quality and data resolution but consisted of only 42 healthy subjects to Wright's 61 (Bernier *et al*.,

2018). The final study, Mouches & Foukert 2019, boasted the largest collection of datasets: 603. This was achieved by combining several pre-existing collections from the UK Hammersmith Hospital, the UK Guy's Hospital, and the CASI Lab at the University of North Carolina. The downside of such a large and diverse collection is that the MRA resolutions and definition of what constitutes a healthy subject are not consistent (Mouches & Foukert 2019). While all the previously mentioned studies could be utilised for creating a cerebral macrovasculature model, the datasets from Wright *et al*., 2013 are best suited for the purpose of this thesis.

2.2.3.2 Cerebral Autoregulation Modelling

Many models ignore the complexity of the human brain: rather than a series of stiff, structured pipes, human cerebrovasculature can shift and regulate itself. This regulation, as discussed earlier, has great impact on cerebral blood flow and the delivery of nutrients to brain cells. One of the first forays into studying and understanding this phenomenon was a paper produced by Lassen *et al*., 1959. This paper labelled the phenomenon cerebral autoregulation. Later, Strandgaard *et al*., 1984 would suggest that the driving forces behind cerebral autoregulation were myogenic and metabolic in nature but gave no definitive proof.

While the exact mechanism behind the phenomenon is still not fully understood, the general mechanism is as follows: as perfusion pressure drops, cerebral blood flow slows. To counteract this, the small arteries and arterioles will dilate to decrease the vessel resistance. As vessel resistance declines, cerebral blood flow will rise to reach homeostasis again. Models of cerebral autoregulation typically fall into two categories: a lumped compartment/feedback circuit model or single vessel model (Payne 2018).

Lumped compartment and feedback circuit models are typically high-level in nature and constructed to use a relatively small number of parameters. As such, these models often rely on simplified feedback models and are not computationally expensive while still generating

information on the entire system. It should be noted that the validation of these mathematical models is mostly taken from animal models which may be a major limitation in their use (Payne 2018).

The second model type is the single vessel model. This model type focuses on individual vessels instead of the entire cerebrovascular system. In doing so, the model typically reduces to a dynamic relationship between blood pressure and vessel radius. This does not entirely simplify the single vessel model, as pressure and radius for a single vessel depend on several physical laws, biochemical relationships, and mechanical relationships. For ease, the single vessel model may be broken down into four major component models: mechanical, flow, myogenic, and vasodilating metabolites (Payne 2018).

The mechanical model, as the name suggests, focuses on the mechanical properties of the vessel wall and will return values for vessel wall radius and wall stress based upon pressure inside and outside the vessel as well as vascular smooth muscle (VSM) phosphorylation. The flow model takes the wall radius and a driving pressure to return flow rate, often calculated with the Poiseuille equation. The myogenic model and kinetic model take the wall stress and flow rate respectively to determine levels of intracellular levels of calcium and concentration of nitrous oxide. These two compounds act in combination to control the level of VSM phosphorylation that affects the mechanical model, thus closing the single vessel model loop (Payne 2018). Figure 2.7 below shows the interconnectedness of these model components within the single vessel model. The single vessel model provides greater information concerning autoregulation control, but as this thesis will focus on the entire cerebral artery system, a compartmental or feedback model is better suited for this work.

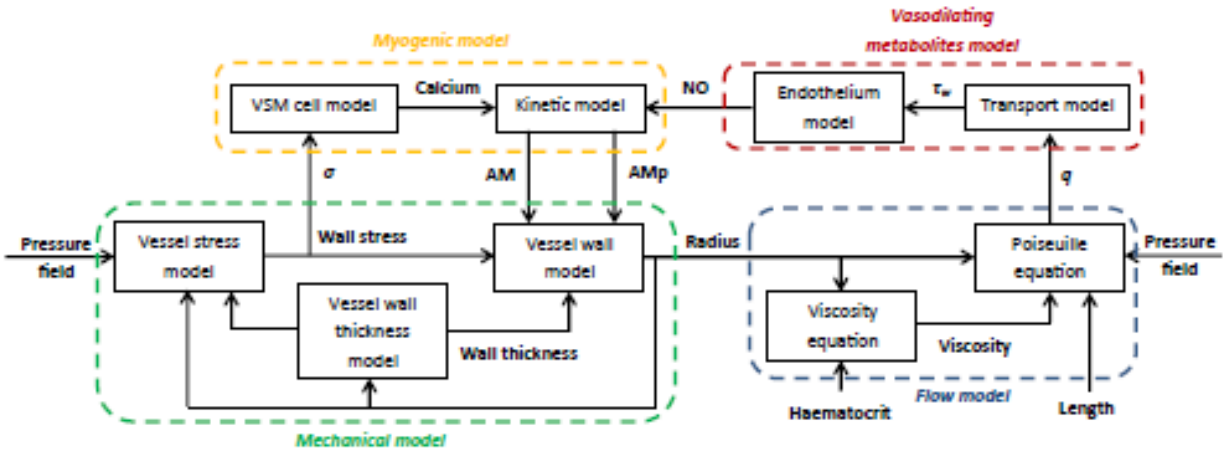

Figure 2.7: Schematic of relationship between the four major component models and other internal models of a single vessel model for cerebral autoregulation. Reproduced with permission from Payne, 2018.

One of the first researchers to investigate autoregulation, Ursino, developed a plethora of lumped parameter compartmental models from 1988 to 2010 focused on cerebral haemodynamics. Starting in 1988, the models focused on cerebral hydrodynamics based upon clinical data and would include cerebral blood flow and autoregulation models (Ursino, 1988; Ursino, 1991). The earliest study by Ursino in 1988 is often considered the foundation for nearly all subsequent compartmental models of cerebral autoregulation (Payne 2018). Ursino and Lodi would further improve on these models to include CO_2 reactivity and intracranial pressure for predictive applications (Ursino & Lodi, 1998; Ursino *et al*., 2000). A variation of this model developed in 2010 that simulates cerebral autoregulation in the cerebral arteries using flow compartments and a mechanical model is used in this this thesis. A representation of his model is shown below in Figure 2.8.

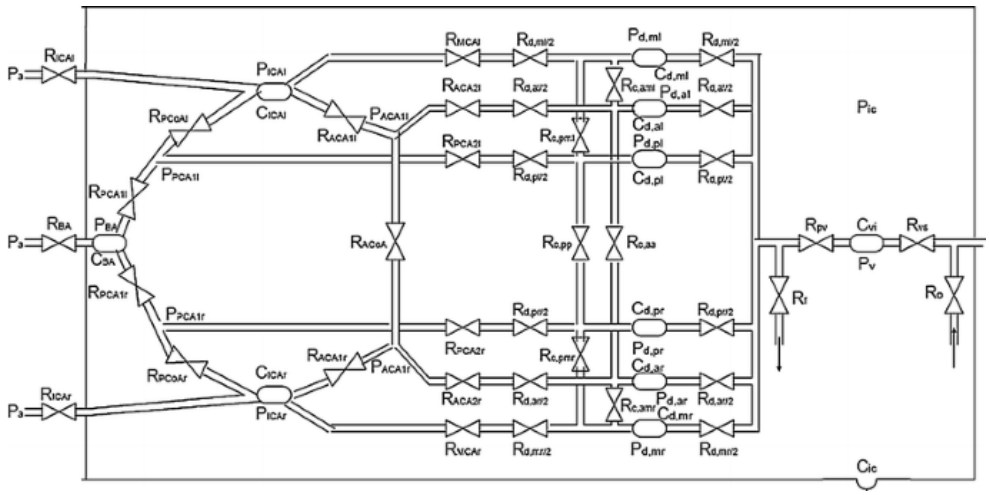

Figure 2.8: Mechanical analogue of Ursino *et al*., 2010 model. Each valve symbol represents a resistance to flow, while each tank symbol represents a major artery with associated compliance and pressure.

The control equations used by Ursino *et al*., 2010 are displayed below in Equations 2.5 and 2.6. In these equations, the *j* subscript refers to Anterior, Posterior, or Middle (with respect to arteries), the *s* subscript refers to left or right, the *aut* subscript represents autoregulation, $x_{aut,js}$ and $x_{CO_2,js}$ are two state variables for autoregulation and carbon dioxide reactivity (dimensionless), τ is a time constant (s), G is the gain (dimensionless), $\boldsymbol{P}$ is pressure (Pa), and A is a corrective factor (dimensionless).

$$\tau_{aut,js}\frac{dx_{aut,js}}{dt} = -x_{aut,js} + G_{aut,js}\left(\frac{\boldsymbol{u}_{js} - \boldsymbol{u}_{n,js}}{q_{n,js}}\right) \tag{2.5}$$

$$\tau_{CO_2,js}\frac{dx_{CO_2,js}}{dt} = -x_{CO_2,js} + G_{CO_2,js}A_{CO_2,js}log_{10}\left(\frac{\boldsymbol{P}_{aCO_2}}{\boldsymbol{P}_{aCO_2n,js}}\right) \tag{2.6}$$

McConnell *et al*., 2017 would use Ursino *et al*., 2010 and apply the work to arterial stenosis and occlusion; however, this thesis uses the McConnell autoregulation model solely to couple the large arterial networks presented by Wright *et al*., 2013. This was proposed in Badiani 2018, where

he used the works of Payne, El-Bouri, McConnell, and Wright to model stroke in patient-specific data and observe how it affects autoregulated flow to the remaining major arteries and perfusion in the capillaries. This thesis will utilise Badiani's algorithm for autoregulation within the major arteries based upon patient data, while the capillary network will be modelled separately. The human cerebral capillary network will be discussed in greater detail within Chapter 2.3.

2.2.4 Conclusions

In this section, background information regarding human cerebral anatomy and methods to model these complex structures were discussed. The approaches given by previous researchers will provide a strong basis for the work presented in this report. The details on how these methodologies were implemented are detailed in the next section.

2.3 HUMAN CEREBRAL CAPILLARY NETWORK

2.3.1 Introduction

The capillary network is critical for the delivery of oxygen and nutrients to the brain. With regards to many microvasculature models, the factors that regulate and affect blood flow parameters are often taken from the larger arterial network, though the actual transfer of solutes largely (though not entirely) occurs within the capillary bed. Understanding the capillary network, as well as the differences between it and the arterial network, is vital for any simulation occurring in the microvasculature. To this end, the first part of this section will deal with the general biology of the capillary bed, while the second will detail the history of mathematical models used to model this system.

2.3.2 Biology

The distribution of oxygen, nutrients, and drugs is strongly dependent on the capillary bed. As oxygen is perhaps the most essential compound found within the circulatory network, the

microvasculature is thought to be optimised around its delivery. The transport of oxygen is driven by passive diffusion that arises from concentration gradients between the blood and interstitial tissue (Hsu & Secomb 1989). Oxygen has a low solubility and can only diffuse up to 20 to 100 micrometres within tissue, depending on the tissue type. This necessitates closely spaced vessels to achieve sufficient oxygen delivery and prevent hypoxia. The nature of oxygen diffusion and microvasculature implies that tissue oxygen levels are strongly dependent on the spatial organization of the capillary microvessels (Secomb, 2004).

An important characteristic of the cerebral microvasculature is the blood-brain barrier, a highly selective semi-permeable membrane that exists between the capillary blood vessels and the tissue interstitium (Gawdi, 2023). The purpose of this structure is to control the influx of molecules, ions, and other compounds into the brain tissue to maintain brain homeostasis. Most of these molecules require active transport methods to cross the blood-brain barrier, with the exception of gases (such as carbon dioxide and oxygen) and specific lipophilic molecules. Through this high selectivity, the BBB maintains brain homeostasis and prevents damage from harmful substances (Gawdi, 2023).

The blood-brain barrier was discovered in 1885 by researcher Paul Ehrlich when he injected a water-soluble aniline dye into animal organs but found that the dye did not appear in the brain or the cerebrospinal fluid (Zhou *et al*., 2018). This phenomenon was later replicated in an experiment by Edwin Goldman (Ehrlich's student) utilising Trypan blue in dogs. It was Goldman that coined and popularized the term. The barrier itself would later be visualized in 1937 using electron microscopy.

The BBB is formed of five main structures: the capillary basement membrane, tight junctions, astrocyte end-feet, endothelial cells, and pericytes. The basement membrane is a sheet-

like type of extracellular matrix that acts as cell and tissue support for the other components. Tight junctions are highly selective barriers to the passive diffusion of proteins and polar solutes while allowing the transport of vital substances like oxygen, CO_2, and water. The endothelial cells form the capillary wall itself and are the locations at which the active transport of nutrients and waste occurs with tight junctions formed between the cells. Astrocyte end-feet and pericytes are supportive cells, with astrocyte end-feet inducing and maintaining the tight junction barrier and pericytes actively playing a role in the angiogenesis and differentiation of microvessels (Dotiwala *et al*., 2023). Pericytes have additionally been found to play a role in autoregulation (Milanovic *et al*., 2021). A figure demonstrating the composition of the blood-brain barrier is shown below in Figure 2.9.

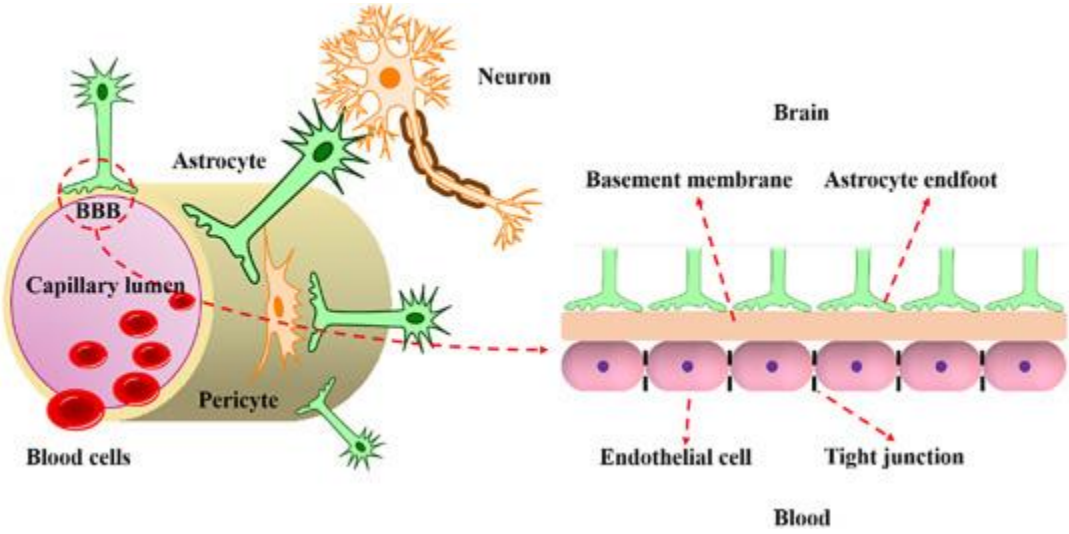

Figure 2.9: Structural illustration of the blood-brain barrier. Illustration taken with permission from Zhou *et al*., 2018.

The capillary system is a complex networked structure within the brain with a wide variety of characteristics. One of the first quantitative studies in humans into the statistical properties of the cerebral microvasculature and its characteristics was performed by Cassot *et al*. in 2006. This

study was based upon the collection of human brain tissues injected with India-ink collected by Duvernoy (Duvernoy, 1981). These sections were analysed using confocal laser microscopy and specifically focused on the temporal lobe. Once analysed in this way, advanced imaging techniques were used to reconstruct the vasculature and apply a radius and centre line to each. This allowed for a variety of data to be generated, such as vascular length, diameter, volume, and surface densities. These in turn could be used to generate reconstructed networks (Cassot, 2006). An example set of networks is presented below in Figure 2.10, with a table showing Cassot's statistical finding for the study presented in Table 2.1.

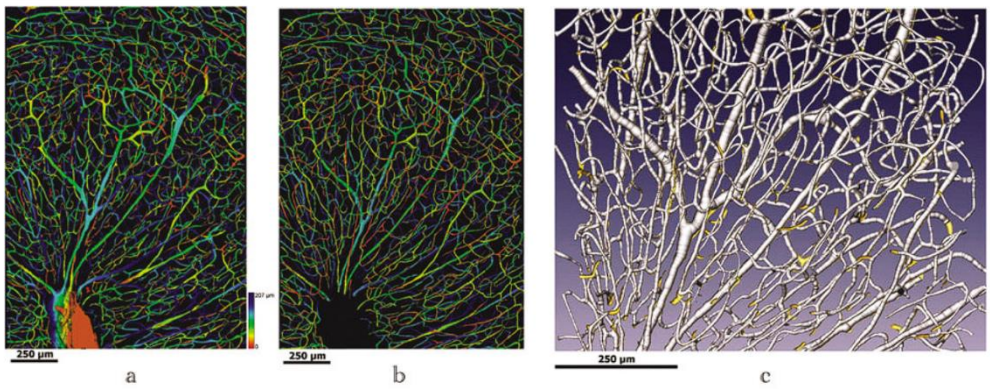

Figure 2.10: Reconstructed microvascular networks: (a) projection view of the network, (b) depth-coded visualization of the line set after segmentation, (c) 3D reconstruction (white cylinders) and original data (yellow cylinders). Figure reproduced with permission from Cassot *et al*., 2006.

Table 2.1: Vascular properties across reconstructed networks. Table reproduced with permission from Cassot (Cassot *et al*., 2006).

	M1	M2	M1 + M2
Number of bricks	27	34	61
Number of segments	14,099	15,250	29,349
by mm^3	8,817	7,219	7,826
Sampled points	503,025	588,447	1,091,472
by mm^3	314,587	273,696	291,059
Total length (mm)	798.32	946.01	1744.33
by mm^3	499.26	440	465
Segment mean length (μm)	56.6	62	59.4
Sampled points/elements	36	38	37
Mean point distance (μm)	1.6	1.6	1.6
Vascular volume (mm^3)	0.0392	0.0523	0.0915
(% of total volume)	2.45	2.43	2.44
Vascular surface (mm^2)	8.66	11.47	20.13
by mm^3	5.42	5.33	5.37

Cassot's statistical interpretations have proven to be valuable, as microcirculatory systems may be characterized with these data without having to specify the precise details of every vessel within the network. This is especially significant when considering that the human brain has around 8000 capillary vessels per cubic millimetre of tissue. This study is unique in that human high-resolution imaging data of the brain microcirculation are severely limited; Cassot's study is one of the most comprehensive studies and one of the few. Fortunately, there are several studies that present the statistical properties of animal brain microvasculature that may be compared against.

One such study was performed at around the same time as Cassot and focused on the brain of the macaque (Weber *et al*., 2008). The results of this study showed that macaque brain circulatory systems have many similar features to that of a human; notably, cortical blood vessels were shown to be centred around pial draining veins, each of which is supplied by between three and six penetrating arterioles (Payne *et al*., 2023).

Another popular choice for animal studies is the rat, which has been studied extensively with a variety of techniques (Payne *et al*., 2023). Common techniques implemented at around the same time as Cassot and Weber include two-photon microscopy with laser ablation and synchrotron radiation-based x-ray microscopy. Two-photon microscopy was used to image fluorescently labelled microvasculature, while the synchrotron radiation-based x-ray microscopy was implemented to obtain tomographic microvascular images (Tsai *et al*., 2009; Reichold *et al*., 2009). Both techniques developed highly detailed reconstructions of their subjects' microvasculature, accurately measuring vessel diameters at a much higher resolution compared to data from humans or primates (Payne *et al*., 2023).

More recently optical coherence tomography (OCT) was used to image rat brains. This was performed to validate previous estimates of red blood cell flux and velocity, and in the process, provided high resolution images of the microcirculation, though no statistical data or reconstruction of the system was presented (Marchand *et al*., 2020). Other techniques that have produced accurate reconstructions of rat brain vasculature include micro-optical sectioning tomography, selective plane illumination microscopy, and three photon microscopy (Xue *et al*., 2014; Ertürk *et al*., 2012; Horton *et al*., 2013). A review of studies focusing on the statistical properties of the brain was released by Schmid *et al*. in 2019 that includes many of the previously mentioned studies and includes data from humans, rats, macaques, and marmosets (Schmid *et al*., 2019).

Much of this section addressed numerical models and their evolution through the years. In practice, however, the models used for this study will often be empirical in nature. Referring to the history of empirical relationships is difficult, as each empirical relationship is closely linked

with the experiments performed, and thus are often very specific. The specific relationships used in this work will be presented where relevant.

2.3.3 Mathematical Tissue Modelling

2.3.3.1 Historic Models (Pre-2000)

There are many studies simulating transport in complex geometries, but most may be reduced to the following two formulations shown below in Equations 2.7 and 2.8 (Popel 1989). It should be noted that most models manipulate these equations, in addition to adding others, to fit the specific tissue under evaluation. In the following formulations, Equation 2.7 is a formulation of the transport equation and describes the transport of oxygen in three dimensions and in nonhomogeneous tissue, while Equation 2.8 is the solution to the integration of a mass balance equation for oxygen at the capillary-tissue interface. Within these equations, α_t is the solubility coefficient (kg/m^3), D is the diffusion coefficient (m^2/s), and $\boldsymbol{j}$ is the flux of oxygen at the capillary-tissue interface (kg/s/m^2). It is worth noting that the solubility coefficient for oxygen is constant in tissue but not in blood (Payne, 2017).

$$\frac{\partial \alpha_t \boldsymbol{P}_t}{\partial t} = \nabla D \nabla (\alpha_t \boldsymbol{P}_t) - M \tag{2.7}$$

$$\boldsymbol{j} = -D \frac{\partial \alpha_t \boldsymbol{P}_t}{\partial n} = k(\boldsymbol{P}_b - \boldsymbol{P}_t) \tag{2.8}$$

The equations above are extensions of one of the first models developed: the Krogh cylinder model. This classic model represents the microcirculation as an array of parallel, evenly spaced capillaries with each capillary providing oxygen through diffusion to a cylindrical region of tissue. This model was originally used to simulate the microvasculature within muscle tissue, as muscles have a more regular distribution of capillary vessels and display structure more parallel than that of brain tissue (Krogh, 1919). The relationship Krogh developed is presented below in Equation 2.9.

$$\boldsymbol{P}_0 - \boldsymbol{P}_r = \frac{M}{D\alpha_t}\left(\frac{1}{2}{r_t}^2 \ln\left(\frac{r}{r_c}\right) - \frac{r^2 - {r_c}^2}{4}\right) \quad (2.9)$$

In this equation, P_0 and P_r represent oxygen tensions, or pressure (Pa), in the capillary and the point *r* respectively, *r* represents the distance from the centre line of the capillary (m), r_c is the radius of the capillary (m), r_t is the radius of the tissue (m), and *M* represents the gas exchange (mol/m^3/s). This model functions on several assumptions: one, each capillary is the sole oxygen supply for a region of tissue; two, the capillary and the tissue region are both cylindrical; three, the pressure of oxygen at the vessel wall is equal to the pressure of oxygen in the blood; four, the drop of oxygen pressure along a capillary is constant; five, oxygen diffuses radially from the capillary; and finally, oxygen consumption within the tissue is constant (Krogh, 1919).

Most of these assumptions have been found to not be applicable in all scenarios, even within healthy individuals. Many of the models since developed address these assumptions, in some capacity, to more accurately model the capillary. A visual representation of the Krogh cylinder model is given below in Figure 2.11. The inner cylinder denotes the capillary, the outer cylinder represents the tissue cylinder, and the dark grey section denotes a potentially hypoxic tissue region.

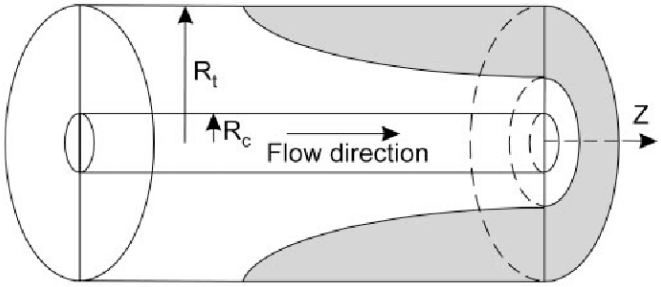

Figure 2.11: Diagram of Krogh Model Cylinder taken with permission from McGuire and Secomb, 2001.

While providing a basis for diffusion of oxygen into tissue at the microvasculature level, the Krogh model fails to accurately capture the more complex components of this phenomenon. For example, the Krogh model does not consider irregular diffusion, haematocrit, microvessel shape and geometry, transport of oxygen within the capillary, or multiple capillaries supplying the same tissue segment (Secomb, 2004). Additionally, the Krogh cylinder geometry may lead to hypoxic regions as artefacts of said geometry, often called “lethal corners”, a phenomenon not seen in more accurate geometries (Popel, 1989).

Considering oxygen transport within the capillary, Popel would outline an approach in his work reviewing all progress up until that point. At the time, Popel presented two approaches: one, treating the transport of oxygen, red blood cells, and plasma in explicit detail; and two, considering the above as new variables averaged over the cross section of the capillary. The latter approach was explored theoretically as the former would lead to a complex unsteady solution problem (Popel, 1989).

Previously, Knisely *et al*. developed an analytical solution for oxygen transport in a Krogh cylinder using finite difference methods. Their solution considered zero-order chemical kinetics of oxygen consumption, axial diffusion within the tissue, and axial and radial diffusion within the capillary. One of the focuses of this study was the impact of haematocrit on tissue oxygen pressure. Figure 2.12 below provides a depiction of their results and demonstrates the dependency of tissue oxygen concentration on oxygen-binding capacity. As seen in 2.12a, lowering the haematocrit value (denoted N, as normal oxygen capacity) causes a reduction in tissue oxygen pressure along the length of the capillary towards the venous end. These “lethal corners” with reduced oxygen pressure may lead to hypoxia and anoxia. Figure 2.12b shows an increase in the lethal corner area between two capillaries as haematocrit decreases.

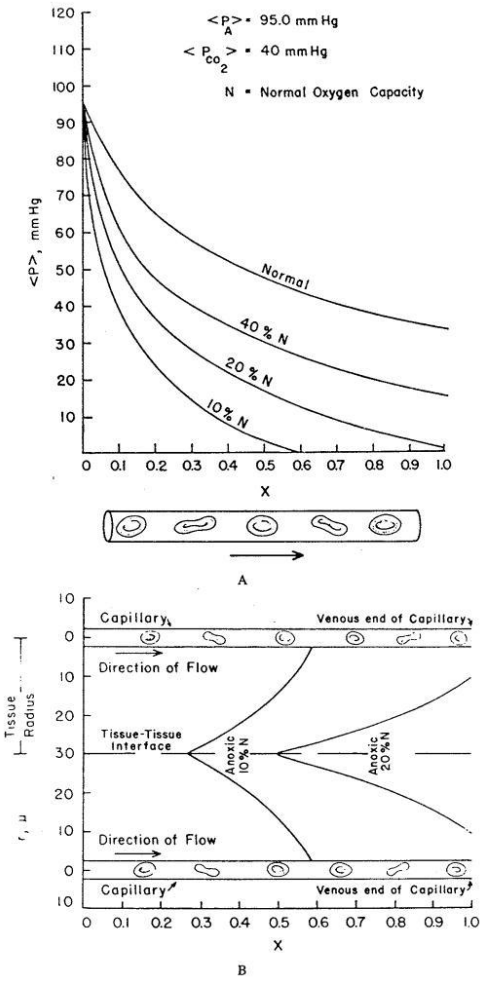

Figure 2.12: (a) Oxygen pressure profiles in a Krogh cylinder showing for variable haematocrit, and (b) diagram showing anoxic regions of tissue between two parallel concurrent capillaries from reduced haematocrit. It is shown that as haematocrit decreases, oxygen pressure also decreases along vessel length, which in turn increases the anoxic region within tissue. Reproduced with permission from Knisely *et al*., 1969.

The work performed by Knisely and his colleague Reneau utilised finite element methods and considered axial diffusion of oxygen, zero-order chemical kinetics of oxygen, anoxic regions, and unsteady diffusion; all of these characteristics had been previously neglected by Krogh and other researchers. While not able to account for complex geometries, their work provided a more complete and accurate solution for a Krogh cylinder.

Early iterations of more complex geometries were very similar to that of Krogh's, but instead of considering the tissue around the capillary as cylindrical, 3D geometries such as hexagonal and rectangular were used. This is due to the fact that cylinders are not space filling, however there was little difference between Krogh's and these models observed (Popel, 1989). The next iterations of complex geometries arose from the work of Grunewald and Sowa in 1977, who introduced microcirculatory units (MCU), which involved four capillaries with arteriolar inlets and venular outlets randomly placed along their lengths. These were placed into rectangular tissue regions, with different units created by the different arrangements of inlets and outlets. The set-up of this system allowed for it to be solved numerically with a finite difference method. An example of a microcirculatory unit is displayed below in Figure 2.13.

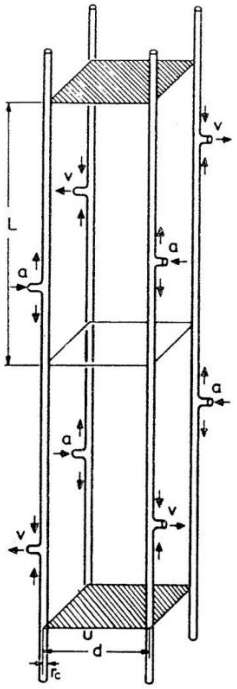

Figure 2.13: Microcirculatory Unit (MCU) developed by Grunewald & Sowa, 1977. In this figure, *L* is the length of a capillary and the half-length of a tissue fragment, *a* is arterial inflow, *v* is venous outflow, *d* is the shortest distance between two capillaries, and r_c is the capillary radius (Grunewald & Sowa, 1977).

While Grunewald and Sowa, as well as other researchers, would use this model and expand on it, said model still characterizes the capillaries as running parallel to each other. Such a geometry, while computationally simpler, does not accurately reflect actual microvasculature in any system except the skeletal (Popel, 1989). To that end, Metzger would propose a lattice-type MCU in which capillaries would form a cubic mesh with mixed concurrent and counter-current flow. An example of one of these systems in presented below in Figure 2.14. Flow was calculated for the capillaries using Kirchhoff's Laws (Popel, 1989).

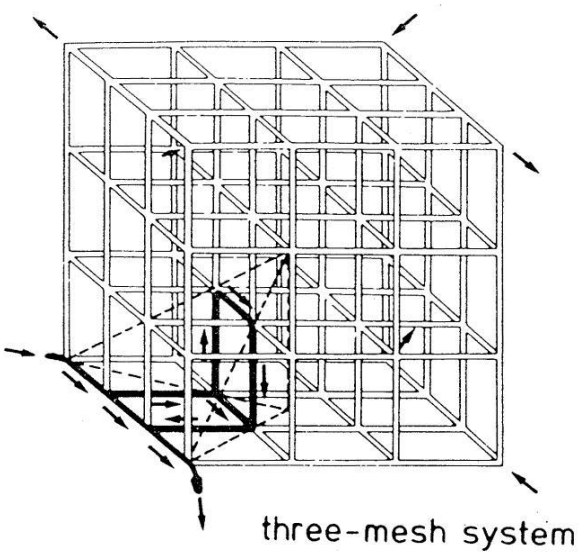

Figure 2.14: Three-dimensional cubic capillary mesh model with 3x3x3 capillaries (reproduced with permission, Metzger 1976).

Several of the models previously mentioned, such as Reneau's and Metzger's, have been applied to a variety of systems, including the brain. Building upon the work of Grunewald and Sowa, Kislyakov and Ivanov would adapt the four-capillary MCU to represent a spherical neuron and mass of glial cells. Ivanov would later develop a more realistic geometry model derived from anatomical studies with two capillaries around a spindle-shaped neuron, shown below in Figure 2.15. Such a model is a step forward from Krogh in terms of geometry, but results may differ based upon treatment of capillary transport.

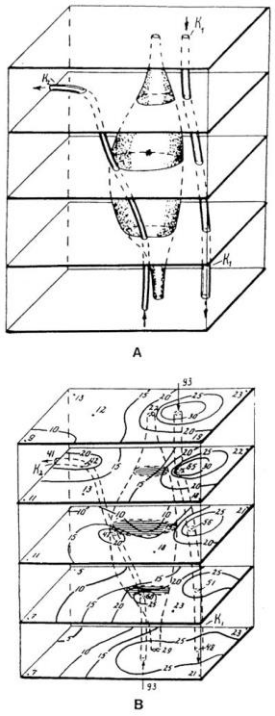

Figure 2.15: (a) A neuron surrounded by two capillaries, (b) distribution of oxygen partial pressure (PO2) in cross-sections. Lines in sections are isobars, with pressure in torr (Ivanov *et al*. 1979).

Bruley and his colleagues would be the first to attempt a different transport solution scheme. Instead of solving the model differential equations numerically with a finite difference or finite element discretisation method, they proposed a probabilistic scheme utilising the Monte Carlo method (Williford *et al*., 1980). Such a method has the advantage compared to discretisation methods for simulation stability and accuracy, especially when it comes to complex geometries. The disadvantage of such methods is the computational expense, which may lead to long simulation run times.

Many of the works previously mentioned focused on the geometry of the microvasculature and the surrounding tissue, but Zagzoule and his colleague Marc-Vergnes would create mathematical models based upon continuity and momentum equations to better understand

cerebral blood flow (Zagzoule & Marc-Vergnes, 1986). This study contained a few limitations: for one, it did not consider variable viscosity or vessel resistance, instead focusing on combining multiple scales under one model and the application of autoregulation to the system. Additionally, the model presented was restricted to one dimension, ignoring complex geometries and any transport of oxygen and solutes across the blood-brain barrier.

2.3.3.2 Recent Models (Post-2000)

In general, many recent studies of the capillary haemodynamics may be categorized as either single-cell methods or continuum flow models (CFMs) (Kopylova *et al*., 2023). Single-cell methods follow the movement of individual blood cells which are considered an incompressible viscous liquid within an elastic membrane. While accurate, this method is computationally expensive as such simulations analyse a large number of particles. This method is thus usually reserved for the modelling of blood flow within a single vessel or in bifurcations (Bryngelson *et al*., 2019). CFMs instead analyse an entire capillary network, representing the region of interest as a homogeneous medium with the appropriate characteristics (Gkontra *et al*., 2019). These models allow for the analysis of local transport and are modifiable to allow for hybrid approaches that also consider the haemodynamics of the arteriolar system in addition to the capillary bed (Shipley *et al*., 2020).

The most common example of CFMs are the compartment models. These models are often used as they simplify the governing set of haemodynamic equations to a smaller set of linear differential equations, allowing for simulations at low computational cost (Acosta *et al*., 2015). Barret and Suresh utilised this type of model to explore the effect of permeability on functional recruitment of capillaries when delivering oxygen during local neuron activation. The oxygen delivery model they presented was mathematically simple, consisting of only four compartments;

complexity was added through additional mechanisms such as arterial oxygen leak. These additional mechanisms were implemented as extra functions within the model. The ability to add supplementary dependencies is another strength of the compartment models. Figure 2.16 below shows a diagram of their compartmental model with arteries, tissue, capillaries, and veins compartments.

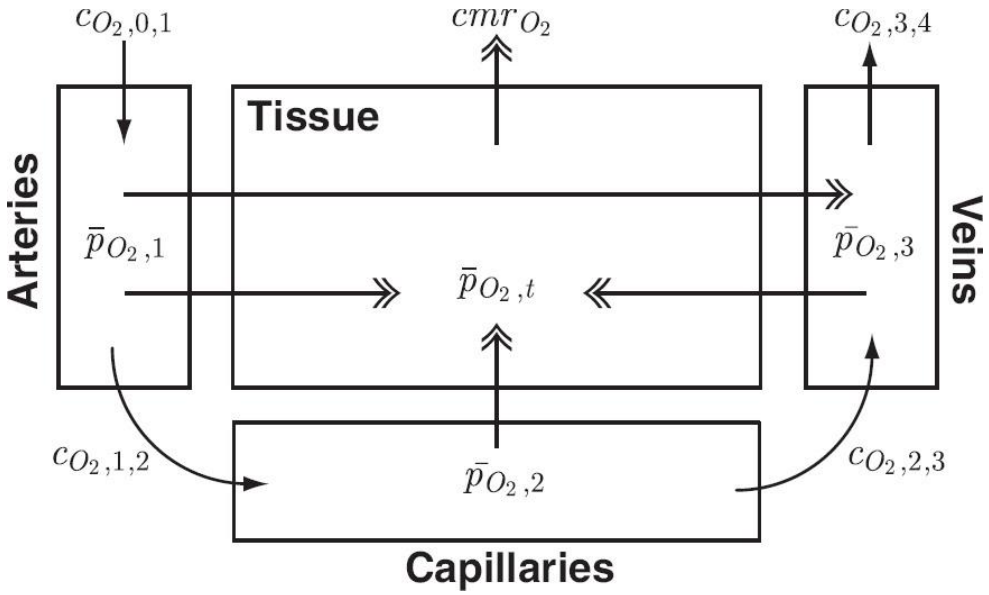

Figure 2.16: Example schematic diagram of the oxygen transport model showing O_2 concentrations (CO_2), mean oxygen partial pressures (PO_2), and cerebral metabolic rate of oxygen consumption ($CMRO_2$). Subscripts 1, 2, 3 and *t* refer to arterial, capillary, venous, and tissue compartments, while subscripts 0 and 4 refer to notional larger arterial and venous compartments, respectively. Movement of O_2 by convection (i.e., via blood flow) is shown with single arrowheads, while movement via diffusion is shown with double arrowheads. Reproduced with permission from Barret & Suresh 2013.

These models, often referred to as lumped parameter models, share similarities to electrical circuits system models, with resistance and compliance as important parameters within the system of equations. Lumped parameter models are typically used when simulating the mechanical properties of the vessel walls. Acosta *et al*., 2015 used this lumped parameter model to simulate hypertensive and hypotensive scenarios within the capillary bed. This derivation is carried out from the basic principles of mechanics which consider the influence of blood volume/pressure on the resistance and compliance and the nonlinear interdependence between these two properties (Acosta *et al*., 2015). Both compartment and lumped parameter models ignore the geometry of the vessel system and are essentially mathematical abstractions.

Finite element methods also fall under CFMs and are commonly used in the modern research of capillary bed haemodynamics, building upon many of the studies presented previously. These methods can solve complex biological models at the cost of computational speed. One such example is Chen *et al*., 2007, which considered NO (nitric oxide) and O_2 transport in a capillary-perfused tissue cuboid containing an arteriole and a venule. The analysed geometry was simple, with the arteriole and venule considered as two parallel straight tubes, but consisted of five regions: the arteriolar core, arteriolar RBC-poor layer, venular core, venular RBC-poor layer and capillary-perfused tissue. The model included mass transport of the two gases and additionally incorporated the Fåhraeus effect and a modified O_2 and NO-coupled consumption by tissue cells using a modified Michaelis–Menten kinetics. Figure 2.17 displays the geometry of the model used by Chen *et al*., 2007.

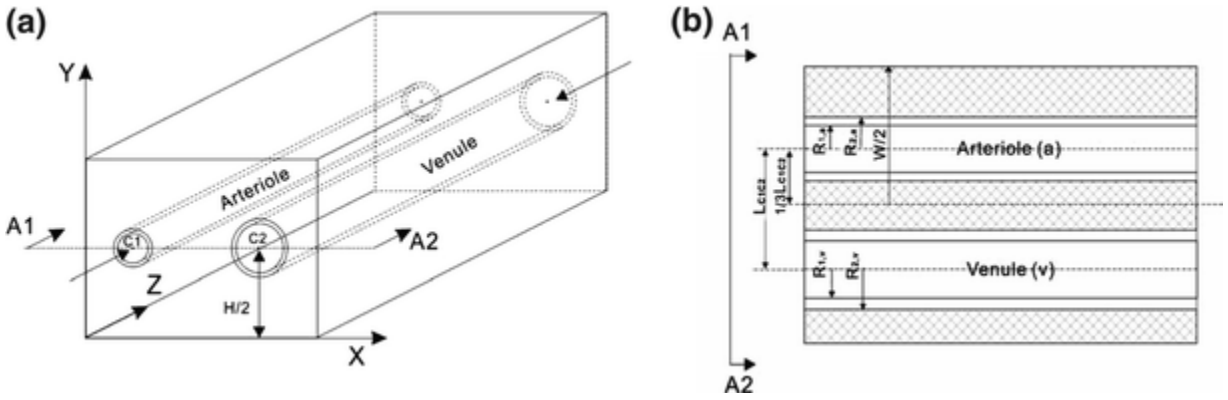

Figure 2.17: Geometry of a capillary tissue model. (a) View of the capillary-perfused tissue cuboid in which an arteriole–venule pair is embedded, with a (b) cross-sectional view of the cuboidal geometry. Reproduced with permission from Chen *et al*., 2007.

Many modern models utilise Voronoi diagrams (often in conjunction with the previous methods) to simulate capillary bed haemodynamics. A Voronoi diagram is a partition of a plane or volume (if 3D) into regions close to each of a given set of objects. In the simplest case, these objects are just finitely many points in the plane. For each point there is a corresponding region, called a Voronoi cell, consisting of all points of the plane closer to that seed than to any other. For capillary modelling, it is common for the Voronoi diagram edges to represent the capillary vessels and the internal area or volume to represent tissue space. Figure 2.18 below demonstrates example 2D and 3D Voronoi diagrams used in capillary bed modelling.

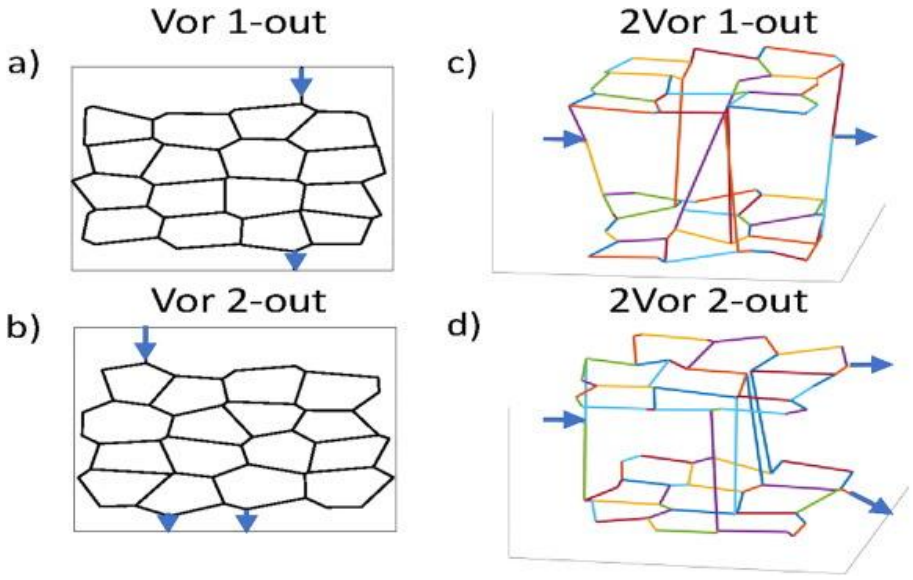

Figure 2.18: a-b) 2D Voronoi diagrams of capillary systems with a) one inlet node and one outlet node vs b) one inlet node and two outlet nodes. Subfigures c-d) demonstrate how stacking two 2D diagrams creates a 3D volume, again with c) one inlet node and one outlet node vs d) one inlet node and two outlet nodes. Reproduced with permission from Terman *et al*., 2021.

Safaeian and colleagues would combine complex geometry and computational modelling in 2011 to create a CFM, building upon previous works by Hudetz, Cassot, Lauwers, Pries, and Secomb (Safaeian, 2011). In this study, Safaeian crafted a randomised two-dimensional Voronoi tessellation as a generic model of the intricate capillary network; then, linear and non-linear methods were applied to calculate haemodynamic parameters such as pressure, flow, haematocrit, and viscosity. As Zagzoule did previously, Safaeian would choose to ignore oxygen and solute diffusion, instead focusing on the flow itself.

Linninger *et al*. would directly build upon the works of Zagzoule and Safaeian to develop a mathematical model for cerebral microcirculation in the secondary cortex of a human brain (Linninger, 2013). This multiscale model accounted for all arterial, capillary, and venous blood

vessels as well as the tissue space within a generated 3x3x3 mm^3 subsection of tissue. The study draws upon a variety of works both biological and numerical and serves as a seminal source for many modern works due to its comprehensive nature. For the capillary bed specifically, Voronoi tessellations were computer generated, while the arterial and venous systems were reconstructed using 3D images. Figure 2.19 below is a computer-generated reconstruction of the vascular network developed by Linninger. This reconstruction displays the complexity of the *in silico*, and by extension *in vivo*, networks.

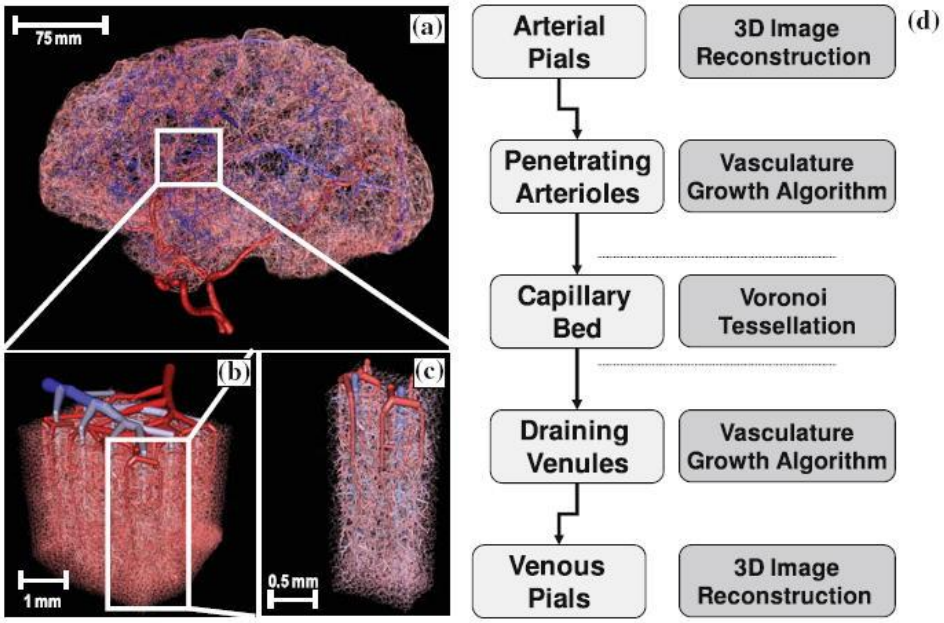

Figure 2.19: Overall multi-scale hierarchy of the human cerebral circulation. (a) Sagittal view of the full brain vasculature model generated *in silico* by combing image data with constrained constructive optimisation. (b) Magnified section of the secondary cortex in the right temporal lobe. (c) Isolated view of the territories of two draining pial veins supplied by six penetrating arterioles. (d) The construction principles for the computer aided construction and analysis of cerebral blood flow networks (reproduced and shortened with permission from Linninger *et al*., 2013).

Peyrounette and colleagues would focus on the coupling aspect of the multiple scales present in the human cerebral vasculature. Under more specific examination is blood pressure, though concentration and temperature are mentioned as experiencing a similar challenge computationally (Peyrounette *et al*., 2018). This study utilises 3D lattice structures similar to those previously used for simplified representation of the capillary networks. While the focus of this report is solely on the microvasculature and mass transport therein, future work would make use of this study.

Smith *et al*. built upon the capillary mesh model of Metzger and Peyrounette to characterize and compare the cerebral capillary network in both mice and humans using 2D Voronoi diagrams. The focus of their study was to develop a proper comparison between the networks of the two species with focus on structure and function (Smith *et al*., 2019). This work built on Metzger's study by utilising imaged anatomical data of mice and human cerebral cortices to generate flow and transport data before segmenting and producing 2D synthetic capillary networks. These 2D networks were then extended into 3D before being used in further simulations (Smith *et al*., 2019). Terman *et al*., 2021 would also use 3D Voronoi diagrams to determine how perturbations of network properties impact tissue oxygen levels. While simple in terms of modelling, this simplicity may be a detriment as the structures produced by Voronoi diagrams may be geometrically dissimilar to that of real capillary beds.

One method for numerical solving involves a Green's function method. First developed in the 1820s by mathematician George Green, Secomb would be the first to use this in relation to steady-state oxygen delivery in 1989. The computation of this method is more rigorous than earlier models by avoiding an unacceptably substantial number of unknown parameters that finite difference or finite element methods may supply. Additionally, the model assumes consumption

in the tissue to be uniform. This initial study would be expounded upon over the following years to account for the transport of solutes other than oxygen and time-dependency in the system. An outline of the mathematical formulations, both steady-state and time-dependent, is provided in Chapter 4.1 and serves as the framework for this project.

The Green's function method is often compared to finite element and finite volume methods. Finite element analysis (FEA) offers a few key benefits. Primarily, FEA can manage complex geometries with high accuracy by dividing the domain into smaller elements, making it suitable for intricate designs. Additionally, FEA can readily incorporate various material properties and nonlinear system of equations, allowing for comprehensive analysis of complex structures. Finally, by discretising the domain, FEA can provide detailed distributions across the entire structure under analysis.

While the Green's function method does not have these same benefits, it does excel at computational speed. This is true provided the system under analysis is simple and has well-defined boundary conditions. The system in this thesis is a capillary network, a system that fulfills these requirements. The Green's function method was chosen here for its computational efficiency (Secomb 2015). The Green's function method, when applied to cerebral blood flow, requires several assumptions. Example assumptions include considering the vessel curvature and length to be larger than the radius of the vessel segment and solute metabolism and diffusivity is uniform. These assumptions are necessary to linearise certain governing equations so that a Green's function method may be applied. Most assumptions may only be applied to healthy individuals or specific solutes; the validity of the assumptions used in this thesis that allow for the use of a Green's function method are discussed in greater detail in Chapter 4.

2.3.4 Conclusions

In this section, background information regarding the human cerebral microvasculature and methods to model these complex structures were discussed. The methods and techniques given by previous researchers will provide the necessary basis for the work presented in this report. The details on how these methodologies were implemented, as well as results from simulations, are detailed further below in Chapter 4.

2.4 NANOPARTICLES AND PHARMACOKINETICS

2.4.1 Introduction

Nanoparticle pharmacokinetics represent a complex interplay of physicochemical properties, biological barriers, and physiological processes within the body. As such, unravelling the intricacies of nanoparticle behaviour *in vivo* requires a multidisciplinary approach that integrates principles from nanotechnology, pharmacology, physiology, and biophysics. The first part of this section will deal with the properties of nanoparticles and their associated pharmacokinetics, while the second part will detail the development of mathematical models used to describe their mechanics within the vasculature system.

2.4.2 Biology

Every nutrient and drug within the body travels using the cardiovascular system. To protect the brain, one of the most important and complex organs in the human body, the cerebrovascular blood vessels are comparatively thicker compared to those throughout the rest of the body. This stems from the increased cellular lining of the vessels with specialized cells that have the capability to actively exclude harmful chemicals. While this is certainly beneficial to the human brain, it does pose a challenge for introducing therapeutic drugs. Drugs that are used in treating brain-related diseases are often unrecognized or considered foreign by the cellular lining and thus unable to enter the interstitium.

A portion of current research into optimising drug delivery to the brain involves nanoparticles. Nanoparticles are a broad class of compounds that form more complex structures on the nanometre scale. These constructs may be specifically engineered to house drugs and maintain a form that can permeate the blood-brain barrier, allowing entry into the cerebral tissue. Utilising the nano-scale stems directly from this principle: the particles are small enough to move throughout the body mostly unhindered but large enough to contain drug molecules. When the nanoparticle enters a neuron or other brain cell, it either degrades or is opened by enzymes to release the drug. Figure 2.20 below displays some of the more common nanoparticle types.

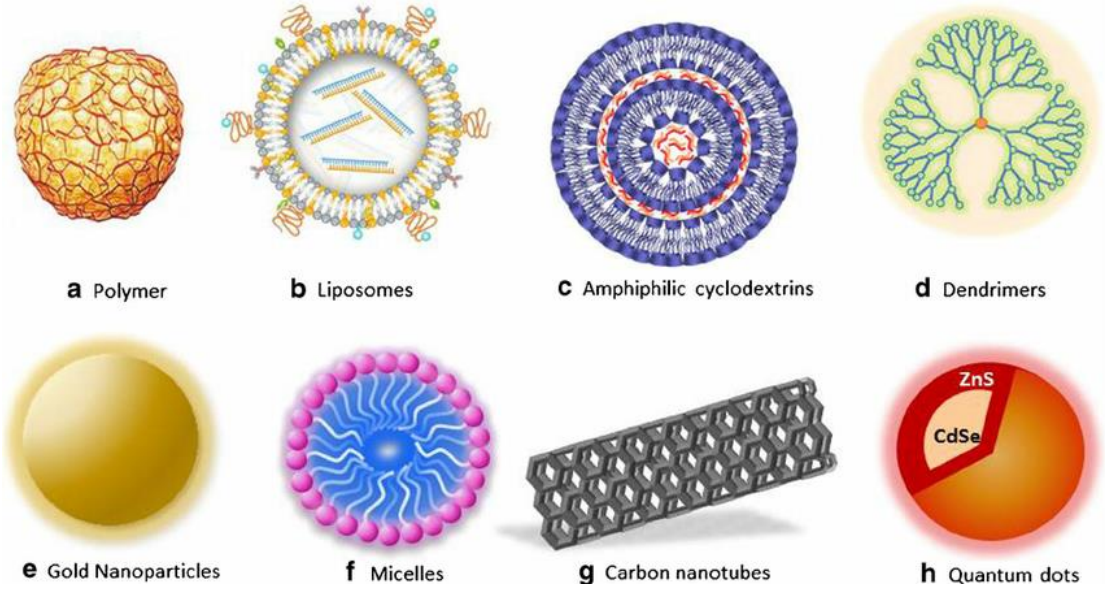

Figure 2.20: Eight most common types of nanoparticles used in therapeutic delivery. Reproduced with permission from McCarthy *et al*., 2014

The design of nanoparticles is therefore very complex: the particle must be chemically stable enough to withstand body conditions until it reaches its destination, be able to release the drug at the appropriate time, must not be toxic or release toxic byproducts, be mass producible, be able to traverse the blood-brain barrier, and finally have a sufficiently long clearance time (on the

scale of hours or days). Understanding how nanoparticles behave in the blood is of great importance, as it will directly affect therapeutic optimisation.

Mathematical modelling would allow for estimation of required geometry, dimensions, and composition of the nanoparticles to be administered, improving the accuracy and efficiency of drug application. This in turn saves time and reduces cost: there would be a reduced need for experimental studies to develop and optimise nanoparticle therapies (Siepmann & Siepmann, 2012). From a scientific perspective, mathematical modelling could provide deeper insight into nanoparticle behaviour and drug release when compared to experimental data (Siepmann & Siepmann, 2008). Modelling nanoparticle haemodynamics is therefore important for developing a clinical optimisation tool for determining nanoparticle and drug dosage.

An important consideration for nanoparticles in general is that some compositions may actually be toxic to the human body. One such example of this is the once-popular quantum dots that have been used and studied less due to this health risk (Hardman, 2005). Some methods of transporting drugs to the brain are also dangerous; disruption of the tight junctions between endothelial cells through osmotic pressure changes, microbubbles, and ultrasound may cause lasting damage (Zhou *et al*., 2018).

Mechanisms for crossing the blood-brain barrier are typically divided into active and passive modes (Zhou *et al*., 2018). Passive transport routes are defined as those that do not require energy to move substances across the cell membrane, while active transport routes do require energy. The energy for active transport is supplied through the hydrolysis of adenosine triphosphate (ATP). Active transport routes are expressed in three categories: receptor-mediated endocytosis, adsorption-mediated endocytosis, and carrier-mediated transport. The type of transport is integral when determining medicinal therapies, as certain drugs and nanoparticles lend

themselves to one route specifically. A diagram showing the relationships between the mechanisms of transport and example nanoparticles in each category is shown below in Figure 2.21.

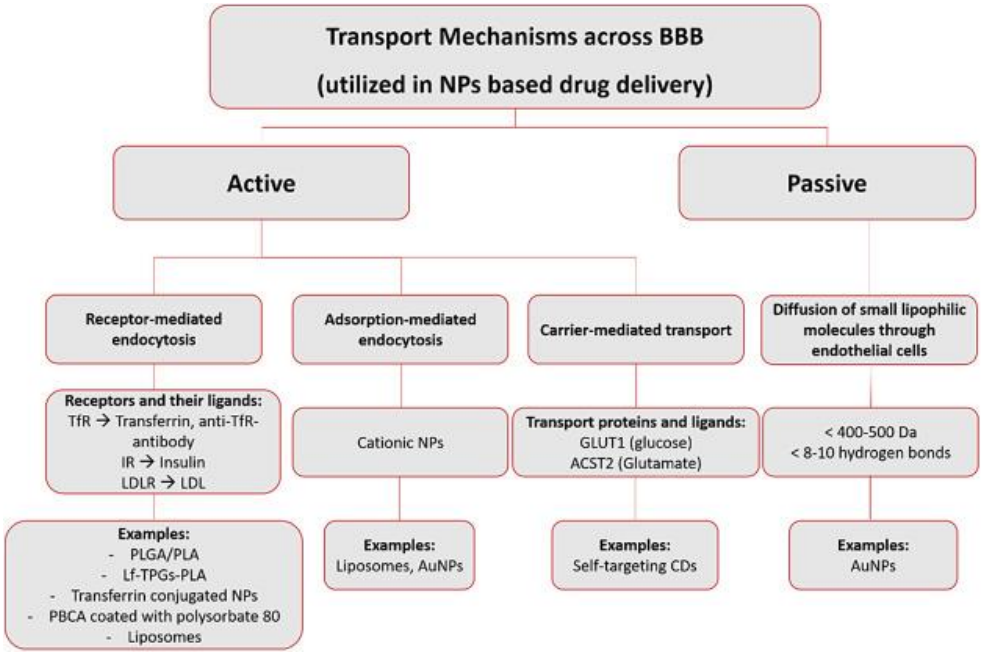

Figure 2.21: Flow chart of the blood-brain barrier transport processes of a variety of nanoparticles. Taken with permission from Zhou *et al*., 2018.

Much of modern nanoparticle research focuses on the studied compound's effect on the body. Many studies that do investigate the dynamics tend to either be experimental in nature or specialize in a specific nanoparticle type with data that are often not relevant to the study presented here. This is a challenge when pursuing applications in this field, as the particle interactions prevent the creation of an all-inclusive general model. To that end, the work presented in this thesis will focus on a specific nanoparticle type: the gold nanoparticle (often abbreviated AuNP for brevity). AuNPs were chosen for this thesis due to their customizability, safety profile, and ability

to cross the blood-brain barrier, leading to their prominence in drug delivery studies and medicinal therapies.

An early comprehensive biological study into gold nanoparticles and their effectiveness in crossing the blood-brain barrier was performed by Sela *et al*. in 2015. In this study, a variety of AuNPs with different functional groups were developed and injected into rats. AuNP concentrations were measured in three major regions of the brain (hippocampus, hypothalamus, and frontal cortex) and other major organs (kidneys, liver, and spleen). Additionally, the effect of ion channel blockers (K+ and Na+ or Ca 2+) on AuNPs transport was also tested. It was found that AuNPs could indeed cross the blood-brain barrier and did so in a uniform fashion, suggesting a lack of regional preference (Sela *et al*., 2015). It was also found that coating the AuNPs in a hydrophobic material, or the presence of ion channel blockers, would result in a reduction in AuNP concentration within the brain.

Of nanoparticle types available, AuNPs have been chosen due to their wide use as drug carriers in disease treatment and experiments (Zhou *et al*., 2018). This stems from the specific chemistry that allows for easy tuning of nanoparticle diameter, surface modifications (with a wide variety of customizations available), stability, and biocompatibility. This biocompatibility prevents any toxic reactions from occurring between the human body and the AuNPs, while other nanoparticle types may sometimes carry that risk (most notably quantum dots) (Zhou *et al*., 2018).

In terms of the surface modifications, a popular choice is to coat AuNPs with polyethylene glycol, often abbreviated as PEG. The process of this surface modification is often called PEGylation. PEGylating AuNPs promotes retention and BBB crossing efficiency, as the AuNPs no longer aggregate, opsonize, or undergo phagocytosis, thereby prolonging circulation time within the blood stream (Reznickova *et al*., 2019). These effects are often attributed to PEGylation

preventing the formation of a protein corona around the nanoparticles. This in turn prevents the immune system from recognizing these compounds and allowing them to circulate with "stealth" (Pelaz *et al*., 2015). These properties, combined with FDA approval, make PEGylation one of the most common modifications to nanoparticle surfaces (Liu *et al*., 2015). Other ligands have also commonly been used, such as insulin, transferrin, and polyethylene glycol. Coating AuNPs with these molecules can facilitate BBB crossing through receptor-mediated endocytosis (Chen *et al*., 2022).

2.4.3 Mathematical Modelling

The simulation of pharmacokinetics falls into two realms: statistical and mechanistic. Statistical simulations may be traced back to the early 1990's, where research performed by Jackson *et al*., 1991 used FORTRAN and Monte Carlo models to create virtual populations. A virtual population is a weighted distribution of virtual patients meant to reflect the baseline characteristics of a clinical group of actual patients, with the virtual patients themselves being collections of physiological parameters that simulate an actual biological system (Allen *et al*., 2016). These virtual populations were then used to predict genetic polymorphisms in human metabolism using *in vivo* indices and *in vitro* data. Towards the later 1990's pharmaceutical companies, such as Pharsight, would create in-house simulators meant to reduce operational costs by reducing physical testing. These programs were used to predict the outcomes of clinical trials based upon *in vivo* and *in vitro* data.

While useful for forecasting the effects of a medical compound on an entire population, such models do not offer much insight into the mechanics of drug dispersal within the human body or the impact of variation between subjects. It should, however, be noted that often times mechanistic models are built around specific nanoparticles and/or diseases, thus making a generalized model for all options increasingly difficult (Moss and Siccardi, 2014). In general, these

physiologically based pharmacokinetic (PBPK) models follow similar steps: absorption, distribution, cellular uptake/drug metabolization, and finally excess drug excretion (Bachler *et al*., 2013). A figure demonstrating two of the PBPK models used in this study that demonstrates the basic principles is shown below in Figure 2.22.

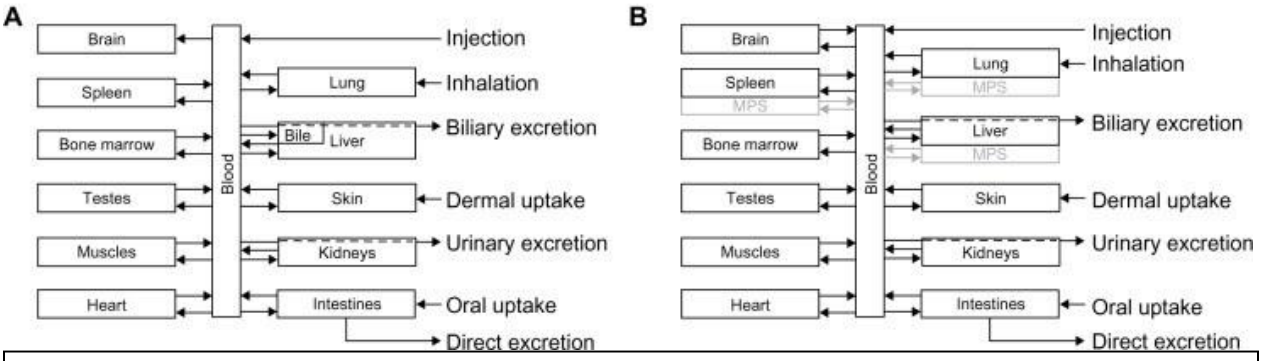

Abbreviations: MPS, mononuclear phagocyte system; PBPK, physiologically based pharmacokinetic.

Figure 2.22: Diagram of two separate PBPK model structures for (A) ionic and (B) nanoparticulate silver. Absorption occurs at uptake, inhalation, or injection one-way arrows that enter either the blood compartment or an organ compartment. Distribution occurs through the blood compartment and between blood and organ compartments. Cellular uptake/metabolism occurs within the various organ compartments. Excretion occurs at one-way arrows that exit organ compartments and the system. The system is then solved as a series of mass balance equations. Taken with permission from Bachler *et al*., 2013.

The kinetics used to describe these processes are complicated and vary greatly depending on nanoparticle type. Equation 2.10 below represents a method for modelling the movement of particle mass between compartments such as blood to cell or blood to tissue (Bachler *et al*., 2013). Compartmental model equations such as this are derived from the mass balance equation as shown in Equation 2.2; as compartmental models are zero dimensional by nature, any terms with spatial

components are simplified to contain only terms with the dependent variable of concentration and independent variable of time. Terms related to diffusion, source, or reaction are then contained within rate constants.

$$\frac{dm_1}{dt} = k_{21}m_2 - k_{12}m_1 \tag{2.10}$$

Here, m_1 is the mass of nanoparticles in compartment 1 (kg), m_2 the mass in compartment 2 (kg), t is time (s), and k_{21} and k_{12} the kinetic rate constants for particle movement from compartments 2 to 1 and 1 to 2 respectively (1/s). This model may be extended out to n compartments and solved in matrix form (provided that the mass flow equations are simple like that above). A matrix representation is displayed below in Equation 2.11.

$$\begin{bmatrix} k_{11} & k_{12} & \cdots & k_{1(n-1)} & k_{1n} \\ k_{21} & k_{22} & \cdots & k_{2(n-1)} & k_{2n} \\ \vdots & \vdots & \ddots & \vdots & \vdots \\ k_{(n-1)1} & k_{(n-1)2} & \cdots & k_{(n-1)(n-1)} & k_{(n-1)n} \\ k_{n1} & k_{n2} & \cdots & k_{n(n-1)} & k_{nn} \end{bmatrix} \begin{bmatrix} m_1 \\ m_2 \\ \vdots \\ m_{n-1} \\ m_n \end{bmatrix} = \begin{bmatrix} \frac{dm_1}{dt} \\ \frac{dm_2}{dt} \\ \vdots \\ \frac{dm_{n-1}}{dt} \\ \frac{dm_n}{dt} \end{bmatrix} \tag{2.11}$$

It should be noted that the diagonal of the rate constant matrix usually refers to the generation or consumption of chemical mass within that compartment. Once the compound is inside the cell, the nanoparticle shell will degrade and release the drug. The value of k is usually determined experimentally and is calculated using a chemical rate equation. Equation 2.12 below is taken from Seoud *et al*., 2016 and represents the integrated chemical rate equation of the nth order.

$$\frac{1}{[\mathrm{A}]^{n-1}} = \frac{1}{[\mathrm{A}]_0^{n-1}} + (n-1)kt \tag{2.12}$$

In this equation [A] is the concentration of chemical species A (in this case the nanoparticle) (mol/m^3), t is time (s), n is the order of the reaction, and k represents the chemical rate constant used to describe the consumption of species A (1/s). For degradation reactions, n is typically 1, which means the rate of degradation is directly proportional to the compound that is degrading. This equality may be integrated to determine how the amount of A changes with time. Equation 2.12 is only meant to represent a potential rate law to simulate nanoparticle degradation. In reality, depending on nanoparticle type, the actual law used could be pseudo-first order, fractional order, or something else entirely different and more complex.

Similarly, the metabolism of the drug and nanoparticle shell is complicated and will vary greatly between nanoparticle types; for example, gold nanoparticle shells may be broken down in the lysosome into smaller gold nanocrystals that are eventually removed from the body, but this is not necessarily true for other nanoparticle types (Balfourier *et al*., 2019). Typically, drug and cellular waste is processed using enzymes. Oxidative enzymes of the peroxidase family (such as lactoperoxidase) have been found to be effective at nanoparticle degradation (Kotchey *et al*., 2013). Michaelis-Menten kinetics is one of the best-known equations for modelling enzyme-molecule interactions. The simplest form is shown below in Equation 2.13.

$$v = \frac{d[P]}{dt} = \frac{v_{max}[S]}{K_M + [S]} \tag{2.13}$$

Here, v represents the reaction rate (mol/m^3/s), v_{max} is the maximum reaction rate that may be achieved (mol/m^3/s), [S] is the concentration of substrate (mol/m^3), [P] is the concentration of product (mol/m^3), t is time (s), and K_M is the Michaelis rate constant (mol/m^3). The Michaelis-Menten kinetics shown here is one of the simpler representations; other models include the ternary-complex mechanisms, the Haldane equation, cooperative model, and inhibition model.

A variety of approaches have been taken to determine gold nanoparticle characteristics such as mass and molecular diameter, as these directly influence the dynamics of diffusion and transport. Shamloo and colleagues in 2016 investigated AuNPs at the molecular scale, developing a molecular dynamics model to characterize the AuNP diffusion coefficient when crossing the blood-brain barrier (Shamloo *et al*., 2016). The model itself utilises a Steered Molecular Dynamics approach to calculate the diffusion coefficient as well as other molecular characteristics.

The nanoparticle used for testing was 2 nanometres in diameter and coated with 18 thiol molecules, each connected to a molecule of insulin. The simulated nanoparticle was considered to be a rigid body to simplify the non-bonded atomic interactions. The epithelial cell membrane was simplified to a phospholipid bilayer with only insulin receptors. One section of membrane is 100 by 100 Ångströms with one insulin receptor, scaling up to 200 by 200 Ångströms. This is shown below in Figure 2.23.

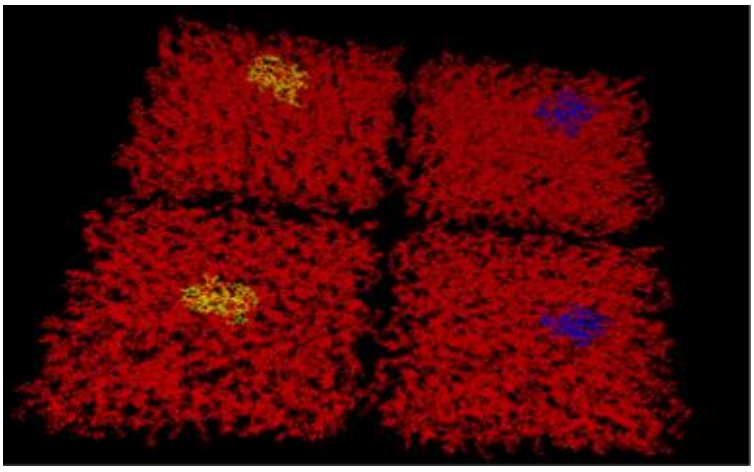

Figure 2.23: Top view of a 200 by 200 Angstrom phospholipid bilayer with insulin receptors. Taken with permission from Shamloo *et al*., 2016.

The mathematical model for diffusivity utilised by Shamloo is a variant of the Stokes-Einstein-Sutherland equation, itself derived from Fick's Law, the Arrhenius equation, Nernst-Einstein equation, and the Langevin equations. The resulting model is shown below in Equation 2.14. It should be noted that many current studies consider the Stokes-Einstein equation (or a variant) when calculating the diffusion of gold nanoparticles (Schleyer *et al*., 2024). Some work has investigated other effects, such as sedimentation, but such experiments were not conducted fully under biological conditions (Cho *et al*., 2011). For now, passive diffusion models remain the standard for gold nanoparticles as opposed to fractional diffusion models.

$$D = \frac{k_B T}{\eta r_D a} \tag{2.14}$$

Here, η is the membrane shear viscosity (Pa*s), r_D is the sphere or near sphere radius (m), k_B is the Boltzmann constant (J/K), T is temperature (K), and finally a is a constant depending on boundary conditions. The estimations of a range from 10^{-13} m^2/s for proteins diffusing through membrane to 10^{-12} for lipids.

In 2022, Chen and colleagues developed a physiologically based pharmacokinetic model using AuNPs conjugated with polyethylene glycol (Chen *et al*., 2022). Up to this point, many models had focused on tumours, and/or leaky vasculature in general, for application in cancer therapies; this study chose to consider healthy cerebral vasculature. The work presented here developed the model for the entire rat body, with compartments for major organs such as the brain, lungs, and kidneys, but also included separate sub-models which described transport within each organ individually. A diagram of the general PBPK model used by Chen *et al*., 2022 is shown below in Figure 2.24.

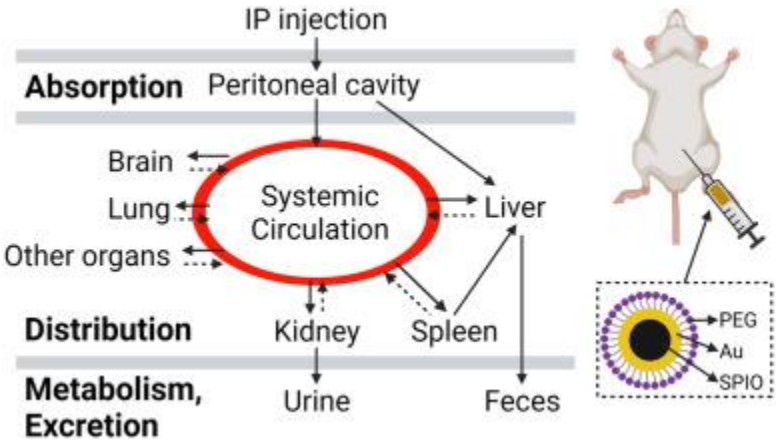

Figure 2.24: Physiologically based pharmacokinetic model used by Chen *et al*., 2022 for gold coated superparamagnetic iron oxide nanoparticles that had been PEGylated (SPIO-Au-PEG NPs, a pictorial representation is shown in the bottom right of the figure) intraperitoneally (IP) injected into rat subjects. This figure displays confirmed (black lines) and hypothetical (dashed lines) nanoparticle pathways in a typical adsorption, distribution, metabolism, and excretion model. Taken with permission from Chen *et al*., 2022.

In this study, brain permeability is estimated using advection-diffusion equations; for the purpose of the experiment, AuNPs were considered to have entered the brain through the Circle of Willis. Like Shamloo *et al*., 2016, Chen and colleagues calculated the diffusion coefficient through a simplification of the Arrhenius equation but considered variation in hydrodynamic radius. The updated equation based upon Brownian movement is given below in Equation 2.15. Again, η is the membrane shear viscosity (Pa*s), k_B is the Boltzmann constant (J/K), and T is temperature (K), while r_H is the hydrodynamic radius (m).

$$D_B = \frac{k_B T}{6\pi\eta r_H} \tag{2.15}$$

The diffusion coefficient in blood is given by the combination of Equation 2.15 above with the shear-induced diffusion coefficient given below in Equations 2.16 and 2.17.

$$D_s = K_s(r_b)^2\dot{\gamma} \tag{2.16}$$

$$\dot{\gamma} = 4\frac{u_{Bmax}}{d} \tag{2.17}$$

$$D_{endo} = D_B\left(1-\frac{r}{r_{pore}}\right)^2\left(1-2.1044\left(\frac{r}{r_{pore}}\right)+2.089\left(\frac{r}{r_{pore}}\right)^3-0.948\left(\frac{r}{r_{pore}}\right)^5\right) \tag{2.18}$$

Here, $K_s \approx 5 \times 10^{-2}$ (a dimensionless coefficient based upon red blood cell concentration), r_b is the red blood cell radius (m), and $\dot{\gamma}$ is the local value of the fluid shear rate given by Equation 2.17. Additionally, u_{Bmax} is the maximum centreline velocity of blood (m/s) and *d* the diameter (m). The diffusion coefficient for crossing the endothelial layer of the vessel wall (D_{endo}) is given above in Equation 2.18, where r is the exact radius of the nanoparticle (m) and r_{pore} is the average radius of pores in the membrane, typically 10 nanometres or 10^{-8} metres (Chen *et al*., 2022). The diffusion coefficient within the tissue is simply taken as $0.56D_B$, giving a complete set of diffusion coefficients for the organ system.

With Equations 2.14 through 2.18, a range of nanoparticle diffusion coefficients may be calculated based upon standard radius sizes such as the ones given by Zhou *et al*., 2018. A table for these values expressed as diameters is given below in Table 2.2. It should be noted that most of the diameters listed are exact diameters – considering AuNPs are often PEGylated or otherwise surface-modified, the exact diameter may not accurately describe the kinetics of the molecule, and thus, the hydrodynamic diameter will be more accurate.

The hydrodynamic diameter is the diameter of a perfect solid sphere that would exhibit the same hydrodynamic friction as the molecule of interest. For example, in Chen *et al*., 2022 the diameter of the AuNPs used were 8.8 nm, but the hydrodynamic diameter was found to be 38.3 nm – a 435.23% increase (Chen *et al*., 2022). Coupled with the fact that some sources do not

specify whether the size used is the actual diameter or hydrodynamic diameter, a range based upon the values in Table 2.2 will be used to calculate diffusivity for testing.

Table 2.2: Collection of metallic colloidal nanoparticle diameters and targets, ordered by type then study date. Adapted from Zhou *et al*., 2018.

Delivery NPs	Size (diameter)	Target	Reference
TAT-modified and unmodified PEGylated AuNPs	5 nm	Intracranial glioma in mice	Cheng et al. 2014
Transferrin-linked AuNPs	80 nm (hydrodynamic)	Mice brain parenchyma	Clark and Davis 2015
Barbiturate molecule coated AuNPs	20-110 nm	Brain endothelial cells	Shilo et al. 2014
AuNPs	2.5 nm	Rat brain	Sela et al. 2015
WGA-HRP conjugated to AuNPs	4 nm	Rat diaphragm	Zhang et al. 2016
AgNPs	25, 40, and 80 nm	rBMEC	Trickler et al. 2010
AgNPs	7 ± 2 nm	Coculture of rBMEC, pericytes, and astrocytes	Xu et al. 2015
AgNPs	8 nm	Coculture of endothelial and astrocyte-like cells	Chen et al. 2016

Abbreviations: TAT, transactivator of transcription; PEG, polyethylene glycol; WGA-HRP, wheat germ agglutinin horse radish peroxidase; rBMEC – rat brain microvascular endothelial cells

Regarding testing and validation of the models, Chen *et al*., 2022 contains the best data available for model development but does not provide specific experiments or theoretical data to compare against within a human brain. This is common: many modern research studies focus on rats and on general structures of the brain (i.e. concentration of AuNPs with lobes, white matter vs. grey matter, etc.). Ideal experimental data for validation would include time-resolved nanoparticle concentrations in plasma and brain tissue, nanoparticle size distributions before and

after BBB crossing, and regional distribution patterns within brain tissue. Other alternatives for validation are thus required.

One option is an extension of what is performed later: an evaluation against another compound. Oxygen is presented in this thesis for computational model validation due to the large amount of experimental data available but is not a 1-to-1 substitution. Other compounds should be considered if an exact analogue. Example analogues include other nanoparticles specifically or other molecules (glucose, drugs, etc.). Otherwise, validation will have to be against petri dish experiments or will be delayed until more data are available, at which point a comparison may occur and model improvements may be made in response.

It should be further noted that the above equations apply specifically to crossing the blood-brain barrier. The movement of nanoparticles, gold or otherwise, through the brain extracellular space requires additional considerations. Even in the extracellular space, compounds move through diffusion (active or otherwise), but now they are affected by the volume fraction and tortuosity (measurement of hindrance to molecular diffusion by cellular obstructions) as well as cellular uptake, clearance, bulk flow, and the extracellular matrix. Fick's Law and its derivations may still be used, provided these effects are considered (Nicholson *et al*., 2000).

2.4.4 Conclusions

In this section, background information regarding nanoparticles and their associated pharmacokinetics was discussed. The approaches given by previous researchers will provide a strong foundation for the work presented in this thesis. The details on how these methodologies were implemented, as well as results from simulations, are detailed in Chapter 5.

2.5 CONCLUSIONS

The work presented in this chapter details the background literature and motivations for this study. Major artery modelling will be developed from methodology published by Badiani, Payne, and Wright. From the variety of capillary studies available, a Green's function method established by Secomb will be used for simulating the microvasculature dynamics. Finally, gold nanoparticles were chosen as the compound of choice for nanoparticle modelling. The next chapters will focus on developing and applying the robust methodology discussed in this chapter.

CHAPTER 3: MODELLING OF HUMAN CEREBRAL ARTERIAL NETWORK

3.1 INTRODUCTION

This chapter focuses on the modelling of the human cerebral arterial network. The methods and assumptions used for the large vessel simulations draw largely on work from Badiani, Payne, and Wright. The original contributions presented in this chapter include: the development of patient-specific viscosity models incorporating the Fåhræus-Lindqvist effect for large cerebral arteries, the implementation of a novel coupling methodology between large artery flow calculations and autoregulatory mechanisms, and the validation of flow predictions against multiple independent datasets. This work generates new knowledge regarding inter-patient variability in cerebral haemodynamics and provides details about the relationship between vessel geometry and autoregulatory effectiveness. The results of the current version of the model will then be presented and examined with reference to previous works for comparison. Additionally, a look at the effect of missing major artery structure is examined. Finally, the results will be analysed, with the assumptions re-evaluated and discussion on how this work will be implemented into the overall project architecture.

3.2 METHODS

3.2.1 General Overview

Modelling begins at the edge of cerebral vasculature: it is estimated that out of the total cardiac output only approximately 15% of oxygen & nutrient rich blood enters the Circle of Willis (Williams & Leggett, 1989). As this blood is dispersed throughout the efferent arteries, parameters such as flow rate and pressure are calculated using an electrical equivalence model. The flow is then adjusted through autoregulatory effects before entering the capillary bed. After blood perfuses in and throughout the microvasculature, it eventually exits to the venous system and drains towards

the heart. The current overall model is a concert of three sub-models: simulation of flow through the large arteries, adjustment for autoregulation, and perfusion in the capillary beds. A diagram representing this process is shown below in Figure 3.1.

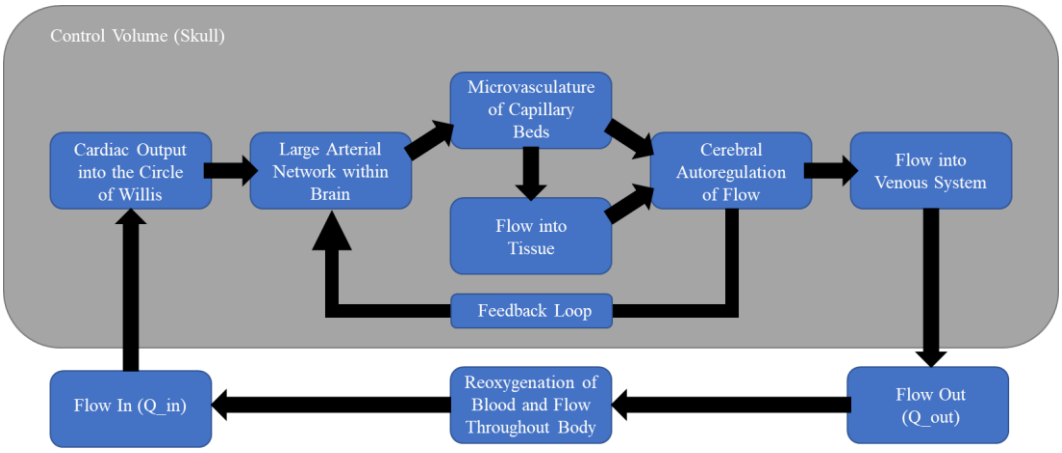

Figure 3.1: Simple schematic representing the major modules of the cerebral vasculature modelling.

3.2.2 Modelling the Large Arterial Network

3.2.2.1 Major Assumptions Used in Flow Network Development

To create a simplified simulation of the human cerebrovascular system, several assumptions must be made. The first is less of an assumption and more the nature of the datasets: all subjects taken from Wright *et al.*'s 2013 study are healthy individuals. Subjects were screened for pre-existing cerebrovascular diseases and disorders before participation in the research study. It is therefore a reasonable assumption that the inlet (aortal, or P_A) and outlet (capillary, or P_C) pressure of the system would be the adult averages of 100 and 45 mmHg respectively, as stated by Payne 2017.

Secondly, all subject datasets from Wright removed the Anterior Communicating Arteries (ACoA). The ACoA structure is variable from person-to-person. Removing the ACoA maintains

a binary tree structure in all reconstructions for easier comparison within and across population samples. The implications of this removal include a potential underestimation of collateral flow capacity and altered pressure distribution within the Circle of Willis; however, this standardization enables robust inter-patient comparisons and reduces computational complexity. In future diagrams in this report the ACoA will not be labelled to represent this premise.

The third assumption is that healthy subjects all have fully developed laminar blood flow. This assumption is quite standard considering the relatively low Reynolds numbers of blood in the arteries. Specifically, the Reynolds number in large cerebral arteries typically ranges from 200 to 531, well below the critical value for transition to turbulent flow (Cebral *et al*., 2009). This ensures that the Hagen-Poiseuille equation remains valid throughout the network, as flow maintains its parabolic velocity profile across vessel cross-sections.

Fourthly, it may be assumed that the arteries may be modelled as non-leaky pipes of linear diameter change. This means that there is no leaking of blood into brain tissue and that flow remains within the network. Additionally, since diameter data from Wright *et al*., 2013 are taken at the bifurcations, the aperture diameter is taken as the average of the end points for a section of artery. This linear interpolation scheme provides a computationally efficient approximation while capturing the gradual tapering observed in cerebral vessels. The assumption of impermeability is justified for healthy vessel walls where the endothelial barrier remains intact, though it would require modification for pathological conditions involving blood-brain barrier disruption.

The fifth assumption is that the arterial system operates under steady-state conditions. While there is a cyclical rate at which blood leaves the heart (due to its peristaltic nature), the effects of blood perfusion and nanoparticle distribution happen over a large enough time scale that cerebrovascular behaviour may be described as quasi-steady state rather than transient.

Additionally, the vascular walls typically expand and contract with the systolic and diastolic blood pressures, though this compliance may be averaged out over the cardiac cycle with a long enough time span.

The final assumptions are that the healthy haematocrit in humans is at a constant level of 40% or .4 (as is assumed in Payne 2017) and that venous structures and dynamics have no bearing on the current model or on future research within the scope of this project. The validity of the assumptions presented here will be later discussed in Chapter 3.4.

3.2.2.2 Creating Arterial Network and Modelling Basic Flow

Data for this project come from 61 test subjects under a study performed by Wright *et al*., 2013. The arterial network reconstruction was performed by Wright *et al.* using high-resolution time-of-flight magnetic resonance angiography (TOF-MRA) with subsequent manual segmentation and centreline extraction. The reconstruction process involved image preprocessing, vessel segmentation using region-growing algorithms, and manual verification of connectivity. The resulting network topology was validated against anatomical atlases and clinical knowledge. These network topologies are published online and publicly available as open-source material.

Arterial information is stored in nodal fashion: measurements are taken along an artery, and each data point is assigned a nodal number. Each node contains three sets of information. The first information set is a $n \times 3$ matrix of node coordinate location in the Cartesian system, where n is the number of nodes for a specific subject and each column represent $\vec{x}$, $\vec{y}$, and $\vec{z}$, data respectively.

The second set represents “colour”, or the type, of data: each node is placed into a major cerebrovascular structure. The structures and their corresponding number identifiers are the Circle of Willis (CoW) with value 0, Posterior Cerebral Artery (PCA) with values 1 and 4, Middle

Cerebral Artery (MCA) with values 2 and 5, and finally Anterior Cerebral Artery (ACA) with values 3 and 6. Some structures have two numbers to represent left and right sides of the brain respectively. This anatomical labelling scheme serves two purposes: one, it facilitates regional analysis of haemodynamic parameters, and two, enables the validation of computed flow distributions against known physiological patterns.

The third set of data is a $n \times 1$ vector representing the connections between nodes; each row corresponds to node i while the value listed matches that of node j connected to node i. From the connectivity vector an $n \times n$ connectivity matrix $\mathbf{C}$ is constructed, where an entry of 1 represents a connection between nodes i and j while a 0 represents no connection. The matrix is sparse and symmetric with a diagonal of zeros as a node is not connected to itself. The connectivity matrix is used throughout the simulation as a logical operator to remove extraneous solutions, as only non-zero entries are stored. The final dataset is an $n \times 1$ vector representing the aperture diameter at a given node.

The discretisation strategy employed here utilises a node-based approach, where each measurement point represents a discrete location along the vessel centreline. This approach captures the branching topology of the cerebrovascular network and provides computational efficiency for the electrical circuit analogy. The spatial resolution between nodes averages 2-3 mm, which is sufficient to capture the major geometric features while maintaining computational efficiency.

From the provided x, y, and z coordinate data a $n \times n$ matrix $\mathbf{L}$ for length (units in metres) may be created. This was done using the 3D Euclidean length formula provided below in Equation 3.1. The algorithm iterates through all connected node pairs identified in the connectivity matrix $\mathbf{C}$, computing the straight-line distance between each pair. For disconnected nodes, the

corresponding entry in L remains zero. It is assumed that the arterial connection between two nodes is the shortest path available and does not have any large, tortuous turns. This assumption is valid for young, healthy subjects but does not necessarily hold true for older individuals and will be discussed later in Section 3.4.

$$L_{i,j} = \sqrt{\left(x_i - x_j\right)^2 + \left(y_i - y_j\right)^2 + \left(z_i - z_j\right)^2} \tag{3.1}$$

From the assumption listed in Section 3.2.2.1 stating that the aperture change between nodes is linear, another $n \times n$ matrix **d** may be generated to store a more accurate diameter (units in metres) between nodes i and j. This was approximated using the basic average formula presented in Equation 3.2. This averaging scheme implicitly assumes that the vessel tapers linearly between measurement points, which is physiologically reasonable for healthy vessels over short segments.

$$\boldsymbol{d}_{i,j} = \frac{d_i + d_j}{2} \tag{3.2}$$

Additionally, the type of node may be determined by summing across rows of matrix **C**. This summation yields the nodal degree (number of connections), which directly indicates the node's functional role in the network. The three types are: starting, intermediary, and terminal. A starting node is where blood enters the cerebrovascular network, a terminal node is where blood exits said network to enter the capillary bed, and an intermediary node is any other node along the artery. Filtering by nodes by lowest z coordinate (representing height within the brain) and a connectivity of 1 determines inlet nodes. Other nodes with 1 connection are terminal nodes. Intermediate nodes, having connectivity equal to or greater than 2, represent either simple continuation points along a vessel or bifurcation points where flow divides

Under the assumption of fully developed laminar flow, Poiseuille's Equation (shown previously in Equation 2.3 but reproduced in an expanded form below in Equation 3.3) may be

used to determine the volumetric flow rate $\mathbf{Q}$ (m^3/s) of a vessel as a function of the pressure differential ΔP (Pa) across it. This equation also uses the vessel length and average vessel diameter (previously calculated above) and blood viscosity μ.

$$\frac{\Delta \mathrm{P}}{\mathbf{Q}} = \frac{128\mu \mathrm{L}}{\pi \mathrm{d}^4} = \frac{1}{\mathrm{G}} = \mathrm{R} \tag{3.3}$$

The vessel resistance R and its inverse the conductance G are also be calculated from Poiseuille's Equation. The resistance formulation establishes a direct analogy with Ohm's law in electrical circuits (V = IR), where pressure difference corresponds to voltage, flow rate to current, and hydraulic resistance to electrical resistance. This analogy justifies the use of Kirchhoff's laws for network analysis. As previously mentioned, blood viscosity μ varies with vessel diameter and subject haematocrit: μ is taken here as 3.5 mPa∗s or $3.5*10^{-6}$ Pa*s (Payne 2017).

3.2.2.3 Establishing Subject Specific In Vivo Blood Viscosity

To add robustness and realism to the model, equations outlined in Pries *et al*., 1992 and in Pries and Secomb 2005 are used to acquire subject specific blood viscosities. These empirical relationships capture the complex rheological behaviour of blood, which exhibits non-Newtonian characteristics due to the presence of deformable red blood cells in plasma. The experimental data used in Pries and Secomb 2005 was taken from male Wistar rats (Pries and Secomb 2005). At a haematocrit of 0.4 and equivalent shear rate, rat whole blood viscosity is typically higher than that of a human (6.288 mPa*s for rats versus 5.996 mPa*s for humans at 94 s^{-1} shear rate) (Windberger *et al*, 2003). The general trend observed in this study is that as blood shear rate increases, the difference between the two viscosities decreases. As previously mentioned in Chapter 2, the *in vivo* blood viscosity μ_{vivo} (mPa·s**)** depends on vessel diameter and haematocrit. It is assumed here that the haematocrit level is constant, an assumption that will be explored and discussed later.

The viscosity calculation proceeds through multiple stages, beginning with the in vitro apparent viscosity, and subsequently applying corrections for in vivo conditions. This multi-step approach is necessary because blood behaves differently in large tubes (as used in viscometry experiments) compared to small vessels where red blood cell interactions with vessel walls become significant. An empirical relation was taken from Pries *et al*., 1992 that builds off the Fåhræus-Lindqvuist effect to determine μ_{vivo}. This relationship is shown below in Equation 3.4.

$$\mu_{\mathbf{vitro}} = \mu_{plasma}\left(1 + \frac{(\eta_{\mathbf{H}} - 1)((1-H)^{\mathbf{C_D}} - 1)}{(1-0.45)^{\mathbf{C_D}} - 1}\right) \tag{3.4}$$

Here the effective viscosity $\mu_{\mathbf{vitro}}$ (mPa$*$s) is dependent on plasma viscosity μ_{plasma}, relative apparent *in vitro* viscosity $\boldsymbol{\eta_H}$ (mPa*s), haematocrit *H* (dimensionless), and vessel shape factor $\mathbf{C_D}$ (dimensionless). The value of μ_{plasma} is taken here to be 1.05 mPa·s and the value of H is taken as the average adult value of 0.45. The apparent viscosity $\boldsymbol{\eta_H}$ and shape factor $\boldsymbol{C_D}$ both rely on the diameter of the vessel and are taken from Pries and Secomb 2005. The two equations describing their respective relationships are found below in Equations 3.5 and 3.6.

$$\eta_{\mathbf{H}} = 220e^{-1.3\mathbf{d}} + 3.2 - 2.44e^{-0.06\mathbf{d}^{0.645}} \tag{3.5}$$

$$\mathbf{C_D} = 0.8e^{-0.075\mathbf{d}}\left(\frac{1}{1+10^{-11}\mathrm{d}^{12}} + 1\right) + \frac{1}{1+10^{-11}\mathrm{d}^{12}} \tag{3.6}$$

While providing a strong basis with which to calculate the *in vivo* viscosity, the *in vitro* counterpart does not fully encapsulate all effects upon viscosity. Biphasic equations were developed to account for the large increase in *in vivo* viscosity as vessel diameter decreases based upon apparent diameter. These equations are presented below.

$$\mathbf{W_{as}} = \begin{cases} 0 & \mathrm{d} \le d_{off} \quad (3.7a) \\ W_{max}\dfrac{\mathrm{d} - d_{off}}{\mathrm{d} + d_{50} - 2 * d_{off}} & d_{off} < \mathrm{d} \quad (3.7b) \end{cases}$$

$$\mathbf{W_{peak}} = \begin{cases} 0 & \mathrm{d} \leq d_{off} \quad (3.8a) \\ E_{amp} \dfrac{\mathrm{d} - d_{off}}{d_{crit} - d_{off}} & d_{off} \leq \mathrm{d} \leq d_{crit} \quad (3.8b) \\ E_{amp} \mathrm{e}^{-E_{width}(\mathbf{d} - d_{off})} & d_{crit} \leq \mathrm{d} \quad (3.8c) \end{cases}$$

In these equations, d_{off} and d_{crit} represent a lower and critical threshold with values of 2.4 micrometres and 10.5 micrometres respectively. The rest of the parameters are again provided by Pries and Secomb 2005 and are as follows: W_{max} with a value of 2.6 micrometres, d_{50} with a value of 100 micrometres, E_{amp} with a value of 1.1 (dimensionless), E_{width} with a value of 0.03 (dimensionless), and E_{peak} with a value of 0.6 (dimensionless). Using $\mathbf{W_{as}}$ and $\mathbf{W_{peak}}$, an effective diameter may be found using Equations 3.9 and 3.10 below. In Equation 3.9 E_{Hct} is taken to be 1.18 (dimensionless).

$$\mathbf{W_{eff}} = \mathbf{W_{as}} + \mathbf{W_{peak}} * (1 + H * E_{Hct}) \quad (3.9)$$

$$\mathrm{d_{eff}} = \mathrm{d} - 2 * \mathbf{W_{eff}} \quad (3.10)$$

Using the effective vessel diameter $\boldsymbol{d_{eff}}$ and the *in vitro* viscosity, a more accurate *in vivo* viscosity may be found using Equation 3.11.

$$\mu_{\mathbf{vivo}} = \mu_{\mathbf{vitro}} * \left(\frac{\mathrm{d}}{\mathrm{d_{eff}}}\right)^4 \quad (3.11)$$

3.2.2.4 Determining Blood Flow Through Each Vessel

Equation 3.12 (shown below) may be derived from Equation 3.3, where flow rate **Q** (m^3/s) is dependent on the pressure differential and vessel conductance G ($m^3/s/Pa$)**.** This linear relationship between flow and pressure difference is the cornerstone of the electrical circuit analogy, enabling the application of network analysis techniques developed for electrical circuits.

$$\mathbf{Q} = \mathrm{G}\Delta\mathrm{P} \quad (3.12)$$

To solve for the pressure distribution throughout the network, we must satisfy both the conductance relationships (Equation 3.12 at each vessel segment) and conservation of mass at each

node (Kirchhoff's current law analogue). The conservation principle states that the sum of flows entering any node must equal the sum of flows leaving that node, except at boundary nodes where net inflow or outflow occurs. With the pressure at distal ends of arterial branches known, Equation 3.13 may be rewritten to the form below:

$$\sum_{i=1}^{n} G_{i,j}\left(P_i - P_j\right) = c_i \tag{3.13}$$

As stated above, $G_{i,j}$ is a value within matrix **G** and is the conductance between nodes *i* and *j* and is zero if no connection exists. Vector **c** is a logical vector describing the state of blood flow (m^3/s) at node *i*. Every entry should be 0 except at terminal nodes due to the conservation of mass principle. With **G**, **c**, and distal pressures known, a system of linear equations may be created to solve for the pressure at every node. The form of this equation system is displayed below in Equation 3.14. Matrix **G** is a square matrix whose size depends on the number of vessels in each patient's arterial network. This number ranged from 2006 to 4327 vessels, with an average of 3178 vessels.

$$\begin{bmatrix} G_{1,1} & G_{1,2} & G_{1,3} & \cdots & G_{1,n} \\ G_{2,1} & G_{2,2} & G_{2,3} & \cdots & G_{2,n} \\ \vdots & \vdots & \vdots & \ddots & \vdots \\ G_{(n-1),1} & G_{(n-1),2} & G_{(n-1),3} & \cdots & G_{(n-1),n} \\ G_{n,1} & G_{n,2} & G_{n,3} & \cdots & G_{n,n} \end{bmatrix} \begin{bmatrix} P_1 \\ P_2 \\ \vdots \\ P_{(n-1)} \\ P_n \end{bmatrix} = \begin{bmatrix} P_A \\ 0 \\ \vdots \\ 0 \\ P_C \end{bmatrix} \tag{3.14}$$

This linear system of equations may be solved for the pressure at each node using standard numerical linear algebra solvers provided by Python's SciPy library. These pressures may be reevaluated in Poiseuille's Equation to get **Q** at each node. It should be noted that matrix **Q** will contain both positive and negative values for a single node. A negative value is used for flow leaving a node while positive pertains to the flow entering a node. Summing across the matrix

rows should return a value of 0 due to conservation of mass. Boundary nodes are the exception, which will have a net input or output. This is represented below in Equation 3.15.

$$\mathbf{Q} = \frac{\pi d^4 \Delta P}{128 \mu_{vivo} L} \tag{3.15}$$

3.2.2.5 Incorporating Autoregulatory Effects

While this model operates under the assumption of steady-state flow, it is important to note that cerebral autoregulation occurs and has an impact on moving blood volumes. Each subject will have an autoregulatory system of varying strength thus including these effects will lead to a more accurate model. Using a venous pressure of 5 mmHg (Alastruey *et al*., 2007) and the total resistance between the distal ends of the arterial network (R_p) (mmHg*s/mL), the effective pressure and flow rate of each efferent artery may be calculated using Equation 3.16.

$$P_{\mathbf{end}} = P_v + R_p \mathbf{Q} \tag{3.16}$$

The total resistance may be calculated by looking at the baseline resistance within the small arteries ($\overline{R_{sa}}$) and that of the veins (R_v). The baseline values for these two variables are taken as 5.03 mmHg·s/mL and 1.88 mmHg·s/mL respectively (Payne 2006). The equation used to calculate R_p is given below in Equation 3.17. It is important to note that these values are for a single artery/vein combination and are scaled by the total number of arteries to reflect individual vessel behaviour rather than whole-brain values (Badiani 2018).

$$\overline{R_{sa}} + R_v = R_p \tag{3.17}$$

Payne 2006 suggests employing the electrical equivalence model presented in Equation 3.18, where P_{ic} is taken as 10 mmHg from McConnell et. al 2017, P_1 is the arteriolar compartment pressure (mmHg), $\mathbf{C_a}$ is the arterial compliance (mL/mmHg), and V_{sa} is the blood volume within the small arteries (mL).

$$\frac{dV_{\mathbf{sa}}}{dt} = \frac{d\left(\mathbf{C_a}(P_{\mathbf{1}} - P_{ic})\right)}{dt} \tag{3.18}$$

This differential equation describes the time-varying relationship between blood volume, compliance, and pressure in the small arteries. Under steady-state conditions ($\frac{dV_{\mathbf{sa}}}{dt}$), the time derivative vanishes, simplifying the expression to Equation 3.19, where $\overline{V_{sa}}$ is 12 mL. There are two important distinctions to note: one, the bar over variables (such as $\overline{V_{sa}}$ in this instance) does not represent the average but rather the baseline value (the value taken under baseline system conditions, not subject to any perturbations); and two, that $\overline{V_{sa}}$ must be scaled by the number of arteries as it is for the entire system as opposed to individual vessels.

$$V_{\mathbf{sa}} - \overline{V_{sa}} = \mathbf{C_a}((P_{\mathbf{1}} - P_{ic}) - (\overline{P_1} - P_{ic})) \tag{3.19}$$

Arterial compliance is not constant across arteries and must be modelled as well to account for these changes. Payne 2006 presents the asymmetrical sigmoidal curve in Equation 3.20 to calculate the arterial compliance, where ΔC_a^+ and ΔC_a^- are upper and lower bounds on the compliance (mL/mmHg). The values for the limits are 2.87 mL/mmHg and 0.16 mL/mmHg. G_q, in keeping with electrical equivalence, symbolizes the gain of the flow feedback mechanism and has a value of 3 mL/mmHg. This gain parameter quantifies the sensitivity of the compliance response to relative flow changes, with a higher gain indicating stronger autoregulatory feedback. The flow q (mL/s) through an individual artery has a baseline value $\bar{q}$ equivalent to the total net flow through the network. ΔC_a^+, ΔC_a^-, G_q, and $\bar{q}$ must also be divided by the total number of arteries in the system to account for scaling.

$$C_{\mathbf{a}} = \overline{C_a} + 0.5 \begin{cases} \Delta C_a^+ \tanh\left(-\frac{2 * G_q}{\Delta C_a^+}\left(\frac{\mathbf{q} - \bar{q}}{\bar{q}}\right)\right) & \mathbf{q} < \bar{q} \\ \Delta C_a^- \tanh\left(-\frac{2 * G_q}{\Delta C_a^-}\left(\frac{\mathbf{q} - \bar{q}}{\bar{q}}\right)\right) & \mathbf{q} > \bar{q} \end{cases} \tag{3.20}$$

To generate a governing equation that gives the autoregulated blood flow **q**, a relationship between vessel resistance and vessel volume is required. It is known that vessel resistance is proportional to the inverse of radius to the power of four (Poiseuille's Law) and volume is proportional to the radius squared (for a given length, cylindrical volume formula) (Payne, 2006). This combination of formulas allows for the relationship given by McConnell *et al*., 2017 (shown in Equation 3.21) below to be used. In conjunction with the above equations, a single equation (shown in Equation 3.22) may be algebraically derived to determine the autoregulated flow rate **q**. The SciPy fsolve function (a verified built-in nonlinear solver) was applied in Python to derive the numerical solution to Equation 3.22 from the given parameters.

$$\frac{\mathbf{V_{sa}}}{\overline{V_{sa}}} = \sqrt{\frac{\overline{R_{sa}}}{\mathbf{R_{sa}}}} \tag{3.21}$$

$$\left(\frac{P_{in} - P_v - \mathbf{q}R_v}{\mathbf{q}}\right)(\mathbf{C_a}(P_{in} - 2P_{ic} + P_v + \mathbf{q}R_v) - \overline{C_a}(2\overline{P_{in}} - 2P_{ic} - \mathbf{q}\overline{R_{sa}}) + 2\overline{V_{sa}})^2 - 4\overline{R_{sa}V_{sa}}^2 = 0 \tag{3.22}$$

In this equation $\overline{C_a}$ equals 0.21 mL/mmHg, while P_{in} is the distal pressure of each artery (mmHg). As mentioned above, values for $\overline{R_{sa}}$, R_v, ΔC_a^+, ΔC_a^-, G_q, $\overline{C_a}$, and $\overline{V_{sa}}$ are taken from Payne 2006 and are representative of the entire brain's blood supply. These parameters are therefore scaled by the number of arteries *n* to reflect the haemodynamic contribution in an individual artery; $\overline{R_{sa}}$ and R_v are multiplied by *n*, while the remaining parameters are divided by *n*. The value of n may be the total number of arteries or the number of major arteries as scaling by region. For example, if an analysis were considering the flow rates in the right anterior cerebral artery (RACA), the scaled version of $\overline{C_a}$ would be 0.21/6 mL/mmHg = 0.035 mL/mmHg and the scaled version of R_v would be 1.88*6 mmHg·s/mL = 11.28 mmHg·s/mL.

While the true values for these parameters will vary from vessel to vessel, using the scaled values will provide an approximate result closer to the expected value than an unadjusted total

would. This scaling assumption is a simplification that treats all terminal arteries as having equivalent autoregulatory capacity. Different vascular territories exhibit varying autoregulatory strengths; however, the uniform scaling provides a reasonable first-order approximation for modelling purposes when lacking subject-specific data for these parameters.

In summary, the complete computational model operates through the following mechanistic steps: first, data are input into the model by loading patient-specific network topology (node coordinates x y and z, connectivity, and diameters) from the Wright et al. 2013 dataset. Next, vessel lengths (Equation 3.1) and average diameters (Equation 3.2) are computed for all connected node pairs. Third, for each vessel segment the subject-specific blood viscosity is calculated using diameter-dependent relationships (Equations 3.4–3.11), accounting for the Fåhræus-Lindqvist effect and the cell-free layer. Then, the conductance matrix G is constructed and populated using Poiseuille's equation (Equation 3.3) with computed viscosities, lengths, and diameters. Fifth, the linear system (Equation 3.14) is solved with baseline boundary conditions to obtain initial pressure distribution and flow rates. Next, autoregulatory effects are applied to network solution with autoregulatory equations (3.16–3.22). Finally, pressure, flow rate, and resistance values for each vessel segment are exported to Microsoft Excel for analysis. This analysis is presented in Sections 3.3 and 3.4 below.

3.3 RESULTS

3.3.1 Introduction

Simulated arterial data were produced using the models developed above. Patient data, taken from Wright *et al*., 2013, were used in Python code to produce arterial blood flow values for pressure and flow rate. The resulting data were then taken and compared against other literature sources.

3.3.2 Healthy Subject Simulations

Detailed volumetric flow rates and blood pressures were produced from the non-autoregulation simulations of all patients. From these data statistical analysis was performed to better capture the variability of cerebral haemodynamics between each patient. Figure 3.2 below shows the average and total volumetric flowrates entering the major arteries. This is a representative boxplot with statistical data across all 61 patients, with box height representing the range between the 25th and 75th percentile values, whiskers representing 2.5 times the standard deviation, single points representing outliers, and X marks representing the mean. It may be seen from the data that the average vessel flow rate across all patients and major arteries is approximately 16.0 millilitres per second, while the average total is 96.2 millilitres per second.

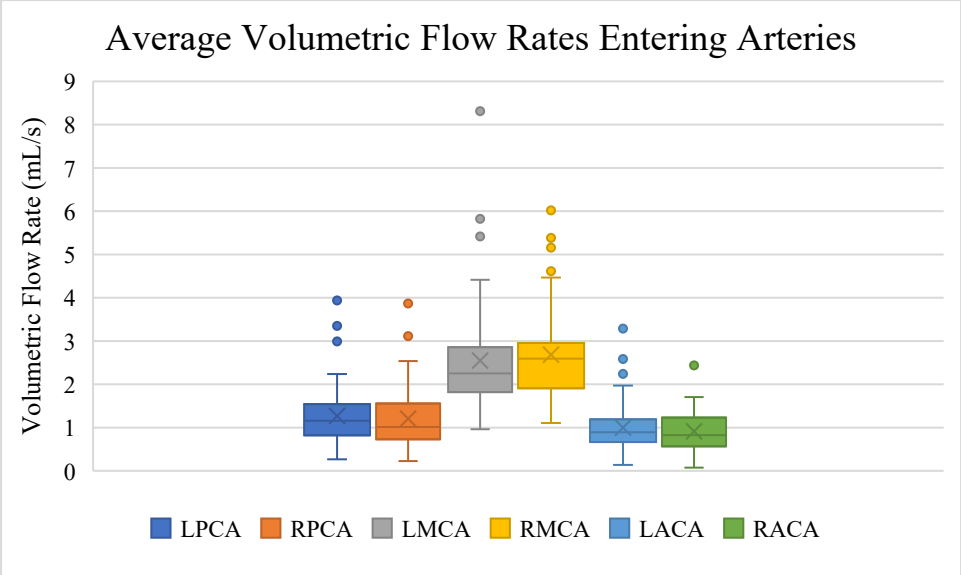

Figure 3.2: Box plot of average vessel flow rates leaving the Circle of Willis and entering the respective major arteries: the Left posterior cerebral artery (LPCA), the right posterior cerebral artery (RPCA), the left middle cerebral artery (LMCA), the right middle cerebral artery (RMCA), the left anterior cerebral artery (LACA), and finally the right anterior cerebral artery (RACA).

In Figure 3.3 below, much like the volumetric flow rates, the average inlet arterial pressures are displayed in box plots. Pressure is an important driving factor for the perfusion of blood into the cerebral tissue; thus, it is important to analyse these values. It should be noted that patient 17 was excluded from the data plots as an outlier due to arterial flow values a tenth of the average in the LACA and RACA, and that the pressure values displayed are given in gauge pressure not absolute.

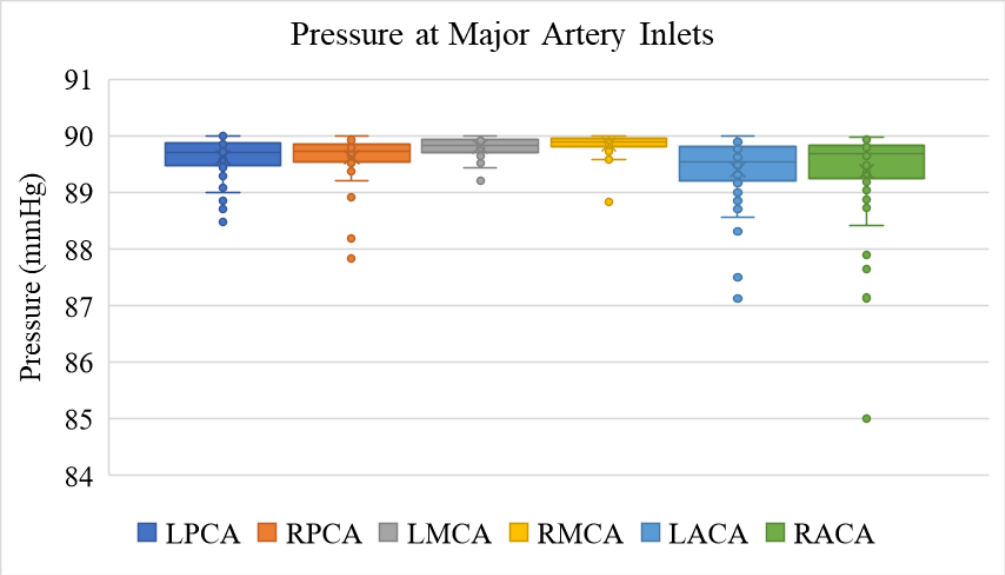

Figure 3.3: Box and whisker plot of average pressures at the inlets to the major arteries.

Next, average arterial resistances may be derived from patient volumetric flow rates and arterial pressure differences (calculated from arterial pressure minus capillary bed pressure). While less useful in calculating perfusion of blood into brain tissue, the arterial resistance serves as a marker for patient health and determining the validity of the presented model. Figure 3.4 below shows the average arterial resistances across the six major arteries as well as the average total arterial resistances for the 61 patients. As with the pressure inlet figures, patient 17 was removed as an outlier for the sake of presenting these data.

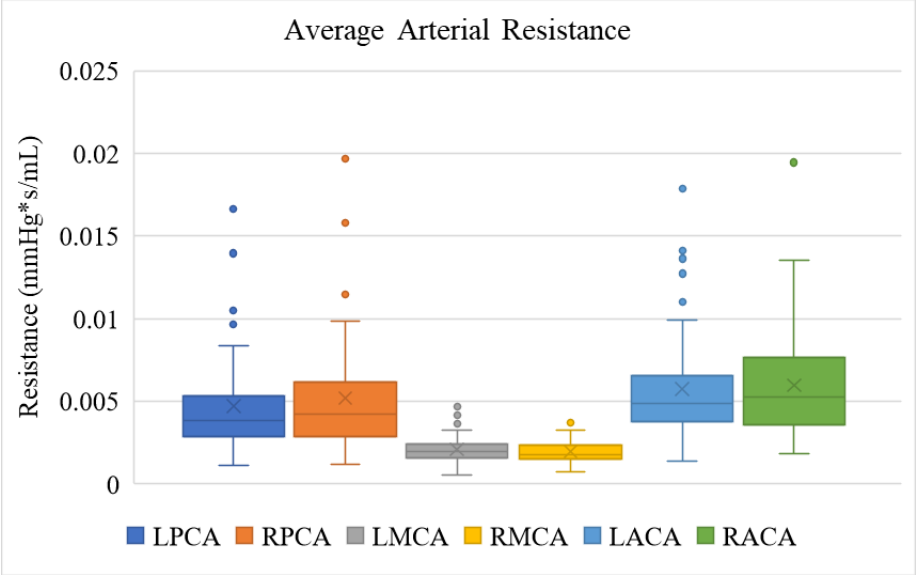

Figure 3.4: Box and whisker plot of average arterial resistances at the inlets to the major arteries.

Finally, the autoregulation model discussed in Section 3.2.2.5 was applied to the generated patient volumetric flow rates. These data are shown below in Figure 3.5. As with the previous figures, patient 17 was removed as an outlier for the sake of presenting these data.

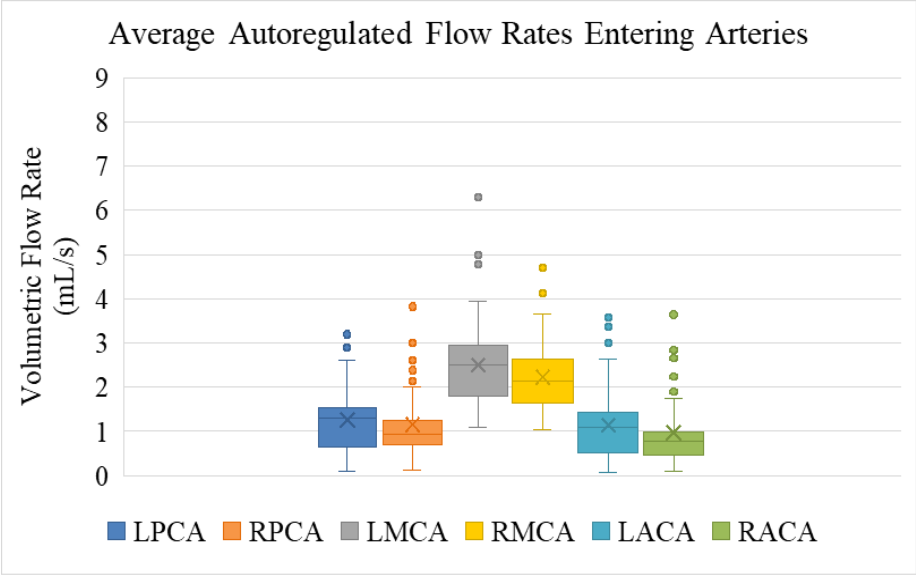

Figure 3.5: Box plot of average autoregulated vessel flow rates leaving the Circle of Willis and entering the respective major arteries

It is important to compare the data produced here against those generated in previous reports. This document considers the statistics generated by Badiani (2018), McConnell *et al*., 2017, and other mathematical and clinical data from a variety of literature resources to determine the validity of generated results. This comparison is shown below in Table 3.1, with standard deviations presented in Table 3.2. Sources with a star (*) next to them had combined the flow rate for each major artery pair. For these tables it was assumed that dividing the given value by 2 would give mean flow and standard deviation (STD) values for each artery.

Table 3.1: Table comparing arterial flow rate (mL/s) between literature sources and simulated data

	LMCA	RMCA	LACA	RACA	LPCA	RPCA	Type
Generated Flow Rate	2.55	2.68	1.00	0.91	1.27	1.21	Modelled
Generated Autoregulated Flow Rate	2.50	2.23	1.15	0.97	1.26	1.15	Modelled
Badiani 2018	4.10	4.05	1.80	1.75	1.50	1.49	Modelled
McConnell et al., 2017	2.06	2.06	1.42	1.42	1.09	1.09	Modelled
Zhu et al., 2015*	3.26	3.26	1.34	1.34	1.73	1.73	Modelled
Enzmann et al., 1994	1.80	2.12	1.52	1.47	0.88	0.85	Experimental
Ooji et al., 2013 (0.8mm resolution)*	3.10	3.10	1.50	1.50	1.00	1.00	Experimental
Ooji et al., 2013 (0.5mm resolution)*	2.40	2.40	1.50	1.50	1.00	1.00	Experimental
Zhao et al., 2007	2.50	2.42	1.42	1.33	1.10	1.05	Experimental
Moore et al., 2006	2.78	2.78	1.39	1.39	2.08	2.08	Modelled
Cieslicki et al., 2005 (Physical Model)	2.44	2.41	1.54	1.56	1.88	1.88	Experimental
Cieslicki et al., 2005 (Nonlinear Model)	2.41	2.42	1.55	1.53	1.79	1.79	Modelled
Cieslicki et al., 2005 (Linear Model)	2.56	2.56	1.68	1.68	1.97	1.97	Modelled

Table 3.2: Standard Deviation (mL/s) of flow rates in the six major arteries from generated data and literature sources.

	LMCA	RMCA	LACA	RACA	LPCA	RPCA	Type
Standard Deviation (mL/s)	1.24	1.07	0.56	0.43	0.71	0.70	Modelled
Standard Deviation/Mean	0.49	0.40	0.56	0.48	0.56	0.58	Modelled
Autoregulated Standard Deviation	0.95	0.82	0.44	0.39	0.35	0.40	Modelled
Autoregulated Standard Deviation/Mean	0.38	0.37	0.39	0.40	0.28	0.34	Modelled
Autoregulated Flow Standard Deviation (mL/s) (from Badiani 2018)	1.56	1.61	0.49	0.50	0.39	0.31	Modelled
Ooji et al., 2013 (0.8mm resolution)*	0.80	0.80	0.40	0.40	0.30	0.30	Experimental
Ooji et al., 2013 (0.5mm resolution)*	0.40	0.40	0.40	0.40	0.30	0.30	Experimental
Zhao et al., 2007	0.52	0.45	0.43	0.47	0.23	0.23	Experimental
Enzmann et al., 1994	0.12	0.12	0.17	0.18	0.07	0.07	Experimental
Cieslicki et al., 2005 (Physical Model)	0.05	0.05	0.03	0.03	0.04	0.04	Experimental

Of the six major arteries, the LMCA contained the largest variation in both non-autoregulated and autoregulated flow, the RACA had the least variation in non-autoregulated flow, and the LPCA had the least variation in autoregulated flow. Generally, the average autoregulated flow rate for each major artery was lower than the non-autoregulated flow except for the LACA and RACA. Standard deviations were lower for autoregulated flow than for non-autoregulated flow. Physically this variation is expected as every individual person is anatomically different, not just within the cerebral cortex and its vasculature but across the entire body.

Compared to other works listed in Table 3.2, the major artery flow rate STDs were higher than literature counterparts: the percent change between the values generated by this model and the literature average varied from 31.3% for the RACA to 234.0% for the RPCA for non-autoregulated flow. For autoregulated flow these values were 17.75% and 90.55% respectively.

The data from Cieslicki *et al*., 2005 was extremely precise, which exacerbated this difference. When excluding the Cieslicki *et al*., 2005 from the comparison, these values were reduced to 11.1% for the RACA and 64.04% for the RPCA. For autoregulated flow these values were 3.7% and 90.55% respectively. It should be noted that all the literature sources above were performed on single networks/patients: averages and standard deviations are within one subject, whereas the averages and standard deviations produced by this work are for a large sample size of subjects.

3.3.3 Major Artery Removal Simulations

All simulations thus far have been performed for utilising healthy subject datasets with whole arterial trees and a complete Circle of Willis. In an unhealthy or diseased individual this is not always the case: segments may be imperfect, missing, or blocked (as is the case for diseases such as stroke). This was investigated in the models developed above by removing major arteries and examining the results of autoregulated flow entering the remaining arteries. The diameter of the major artery being removed was reduced by 90% while keeping the other major artery diameters constant to simulate arterial blockage. The results of these simulations are shown below in Figures 3.6 through 3.11 as well as Table 3.3, where the figures display distribution of flows in each of altered system and the table compares average flow rates and standard deviations across all altered systems. In general, the unaltered system (all major arteries present) had higher flow rates but lower standard deviations compared to systems with missing major arteries.

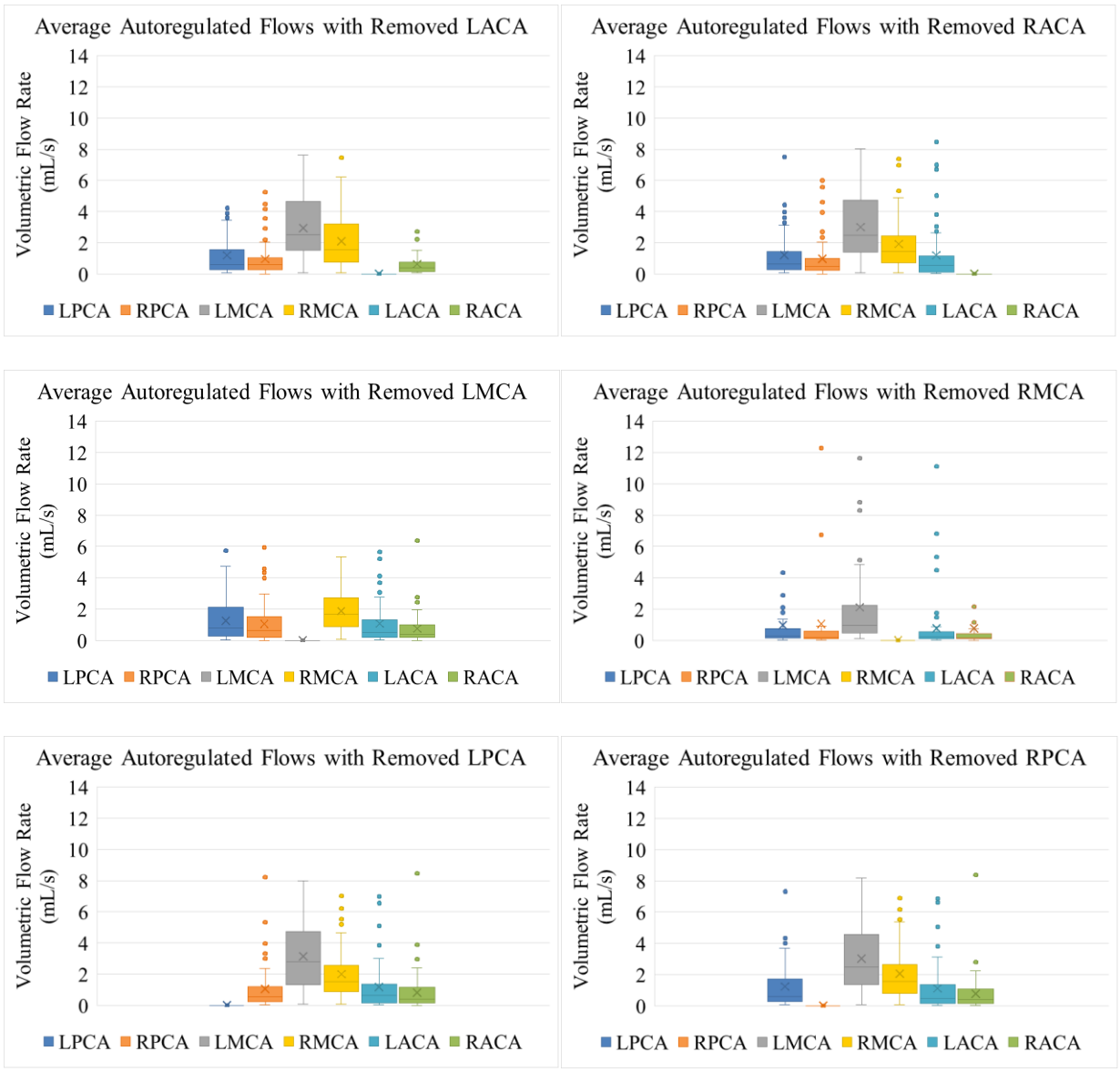

Figures 3.6-3.11: Box plots of average autoregulated vessel flow rates leaving the Circle of Willis and entering the respective major arteries when certain major arteries are removed.

Table 3.3: Average autoregulated flow rates and Standard Deviations in healthy arterial system versus systems with major arteries removed.

	LMCA	RMCA	LACA	RACA	LPCA	RPCA
No Removal Average (mL/s)	2.498	2.23241	1.14538	0.97025	1.26307	1.15207
No Removal Standard Deviation	0.94897	0.82157	0.44234	0.38896	0.35293	0.3973
Removed LACA Average (mL/s)	2.93951	2.09947	0.00637	0.6418	1.19057	0.96323
Removed LACA Standard Deviation	1.98893	1.77713	0.01026	0.34932	0.62173	0.57242
Removed LMCA Average (mL/s)	0.00523	1.88087	1.08164	0.74757	1.2635	1.05127
Removed LMCA Standard Deviation	0.01494	1.29971	0.65249	0.48701	0.64856	0.6044
Removed LPCA Average (mL/s)	3.15296	1.99974	1.17086	0.82647	0.00645	1.06621
Removed LPCA Standard Deviation	2.27855	1.67897	0.77664	0.63135	0.01025	0.73813
Removed RACA Average (mL/s)	2.9965	1.92871	1.20529	0.00626	1.21292	0.97565
Removed RACA Standard Deviation	2.19447	1.69662	0.87521	0.01027	0.723	0.64825
Removed RMCA Average (mL/s)	2.11743	0.00841	0.78628	0.78398	0.9738	1.05424
Removed RMCA Standard Deviation	3.22709	0.02738	0.89734	1.78188	1.52822	1.86861
Removed RPCA Average (mL/s)	3.01959	2.05723	1.12047	0.77199	1.24711	0.00629
Removed RPCA Standard Deviation	2.25656	1.80578	0.76338	0.5967	0.71616	0.01027

3.3.4 Conclusion

Simulations were executed across all 61 subjects to present a working model of cerebral vasculature. The results above show that the current version of this model qualifies as a baseline for future comparison studies based upon the following criteria: mean autoregulated flow rates fall within 35% of literature values across all major vessels, pressure distributions remain within physiological ranges, and computed resistances align with expected cerebrovascular resistance values. The model would have been disqualified if any of the gathered data significantly deviated from literature values or exceeded physiological limits. These results will be discussed in greater detail as well as the validity of the underlying assumptions in the following section.

3.4 DISCUSSION

In the previous sections a cerebral blood flow model was derived from patient-specific large arterial networks and investigated the application of cerebral autoregulation into the overarching simulation. Due to the complex nature of such a problem, several assumptions were made to reduce the intricacy of the mathematical formulations involved and to reduce computational expense. In this section, these assumptions and other aspects regarding validity of the model will be discussed.

3.4.1 Modelling Assumptions

Several assumptions were included in the formulation of this model, one such assumption being that haematocrit level is constant. The viscosity formulation developed by Pries et. al where $\mu = \mu(H, \boldsymbol{D})$ is dependent on both haematocrit and vessel diameter, but with this assumption viscosity becomes dependent only on one variable. According to both Payne 2017 and Pries *et al*., 1989, haematocrit for an average healthy human body is on average between 0.4 to 0.45 but may vary in large vessels from 0.35 to 0.5 (Payne, 2017; Reinhart *et al*., 2017). The haematocrit value tends to drop by 5% within smaller vessels as part of the Fåhræus effect (Reinhart *et al*., 2017). In the future, this effect could be included in the model using an equation that has variable haematocrit.

Another major assumption discussed only partially is the fact that the morphology files used to generate the networks and simulations are entirely bifurcating. To that end, all ACoAs were removed from the data to represent vessel flow patterns more accurately, though it should be noted that a portion of the variation within the Circle of Willis is derived from the ACoA. Future work will involve developing models based upon data that are not derived from an entirely bifurcating network.

Several of the other assumptions derive from the fact that all subjects used were young and healthy. Age plays a significant role in the health of the cerebral vasculature system, affecting both morphology and flow mechanics (though the two are closely related). The large conduit arteries become elongated and tortuous as age increases, while the radius of the arterial vessel increases as both lumen size and vessel wall thickness increase. The elasticity of arterial walls is also affected, as molecular compounds such as calcium, lipids, and nucleic acids accumulate in the endothelial cells. These morphological changes all affect cerebral blood flow: typically, as age increases cerebral blood flow (CBF) decreases (Nagata *et al*., 2016).

Even young subjects that are unhealthy may have altered morphology and circulation. Stroke was simulated by removing segments of the Circle of Willis, but other vessel characteristics change with disease. As with older subjects, vessels may be tortuous and inelastic or CBF may be dangerously low, but there may be other complications as well. To name a couple, the vessel walls may be more elastic than the average person or the subject may have increased blood pressure or CBF. Any future results on unhealthy patients will be skewed by preexisting conditions. Focusing on healthy subjects gives a baseline with which to compare future results.

The assumptions derived from a subject being healthy follow in the same vein: arterial inlet pressure, capillary bed pressure, and vessel elasticity will all vary between patients. These parameters are challenging to measure without being intrusive to the patient or disrupting other variables being measured. Implementing these changes is less of a challenge, as only several constants require modification.

Finally, the current model assumes steady-state behaviour as opposed to transient behaviour. This is due to the time scale under observation; under the longer time scales used in this simulation, the behaviour caused by cyclic heart pumping may be averaged over multiple

cycles to give beat-to-beat average values for variables such as pressure and volumetric flow rate. The longer time scale is required to accurately predict nanoparticle distribution and metabolism, so pulsatility is neglected. Should specific nanoparticle types have more rapid cellular uptake this assumption will need to be revisited.

3.4.2 Model Verification for Healthy Subjects

The results from healthy subject model simulation are displayed in Section 3.3 and Figures 3.2 through 3.11. They are evaluated against literature sources with a focus on volumetric flow rates for direct comparison. It may be observed in Figure 3.1 that the average flowrates generated by this model tend to fall between comparative sources. The percent change for the mean autoregulated flow and the mean literature value varied from 1.34% for the LMCA and 34.09% for the RACA. The flows values for non-autoregulated and autoregulated flow generated from this model differed only slightly: an average difference of 0.49%, with the largest difference in the two types of flows being in the RMCA.

Care must be taken when interpreting this agreement, as the comparison involves both experimental measurements and computational predictions, each with inherent limitations. The apparent agreement may reflect similar modelling assumptions rather than true validation, and the use of single parameter sets across diverse patient populations requires careful interpretation of the results' clinical significance. Regardless, the current strong agreement with other data both clinical and numerical supports the validity of the blood flow model developed here.

While the mean flow rates of the major arteries agree closely with other literature values, the standard deviations tend to differ by a larger degree. Both Badiani's and this work were based upon the same dataset and mostly agreed apart from the LMCA and the RMCA. This difference between the two models could be resolved due to the Badiani’s values being an estimation (his

values presented in Table 3.2 were estimated from graphs and not explicitly quoted in his study), or that his method of algorithm implementation differed in some unspecified way (different nonlinear solver, different coding language, unstated parameters, etc.). This discrepancy is highlighted when compared to other literature works: at its largest, the percent change between the autoregulated STD of the RPCA and the average STD found in literature was 90.56% (or 64.5%, if one extremely precise source is ignored).

The difference between the simulated results of this thesis and of Badiani to that of the literature sources may be ascribed to the nature of the studies. All the literature sources with available standard deviations were experimental studies that focused on one subject: this means that the standard deviations presented are with regards to multiple physical measurements taken on the subject. It is reasonable that the difference between measurements would be small when utilising precise measuring instruments it (further substantiated by the preciseness found in Cieslicki *et al*., 2005). Conversely, the standard deviations calculated from the simulated flow values are with regards to multiple subject networks (61). The standard deviations here, then, describe the variability between subjects and not multiple measurements on one network. Comparing these works serves to emphasize the extent by which network variability between subjects affects the flow rate as opposed to directly comparing for validation. True comparison would require access to the network data used in the experimental studies.

Otherwise, the drop in STD (or drop in variance) makes sense: autoregulation is a negative feedback system put in place to reduce the spread of flow values as the system attempts to achieve homeostasis. Ideally, there would be little to no variation; lower average flow rate STD signifies more consistent oxygen and nutrient delivery, the purpose of autoregulation. This is supported in Badiani 2018, where he recorded that IQR (interquartile range, in this case measuring the

variability across all 61 patients) was reduced by 21.74% from the non-autoregulated flow to the autoregulated. Similarly, the average flow rate STD decreased by 28.64% when autoregulation was applied.

3.4.3 Removal of Major Arteries

The results presented in Section 3.3.3 examine arterial networks with major vessel blockages and reveal physiologically significant phenomena and insights into how imperfect arterial networks affect cerebral blood flow. Major artery removal was simulated by reducing the diameter of one of the arteries by 90% while keeping the other arteries constant. A major artery diameter reduction of 100% would cause the model to produce nonphysical values for all the arteries. This process was repeated for each of the 6 major arteries.

It was observed that the unaltered network maintained a higher total autoregulated flow rate of 9.26 mL/s with lower variability (as evidenced by reduced standard deviations) compared to the flows found in remaining arteries within the incomplete networks. The largest reductions in total flow occurred with the removal of the MCAs, where the total flow was reduced by 3.53 mL/s for RMCA removal and 3.23 mL/s for the LMCA. Removal of the RACA, LACA, RPCA, and LPCA produced reductions of 0.93 mL/s, 1.42 mL/s, 1.04 mL/s, and 0.94 mL/s respectively. The variability of the flow in remaining arteries increased by a significant margin; the exact percent change from the unaltered network ranged from 53.36% for the LMCA to 281.9% for the RMCA.

Notably, the persistence of flow through remaining major arteries, despite significant compromise of individual vessels, demonstrates the robustness of the network: presumably, other major arteries handle the flow that would have been directed through the removed artery. The exception to this is the removal of one of the MCAs, both cases presenting much lower total flow reductions compared to the unaltered networks. Physically, a large percentage of cerebral blood flow is contained in the MCAs compared to the other major arteries; the reduction of such a load

bearing artery will have a much larger impact on total major artery blood flow than that of a smaller major artery.

When a major artery is compromised, the variability in the remaining arteries increased, with the removal of the RMCA displaying the most drastic change. The observed increase in flow variability across remaining vessels suggests that the autoregulatory response, while effective in maintaining some degree of cerebral blood flow levels, operates with reduced efficiency in its attempt to overcompensate for the reduction in total blood flow. The reduction and high variability of flow to the remaining major arteries of an incomplete network have important clinical implications: even one major artery failing due to stroke (for example) may cause hypoperfusion throughout the entire arterial network.

The major artery removal simulations demonstrate that while the Circle of Willis provides effective compensation for major vessel removal, this compensation occurs at the physical cost of reduced total flow and increased variability within said flow. The model developed in this chapter provides a controlled experimental framework understanding the effects of autoregulation in cerebrovascular networks, while also emphasizing the limitations of the autoregulation response.

3.4.4 Conclusion

The patient-specific model developed here is a strong basis for exploring nanoparticle pharmacokinetics within the cerebrovascular system. The work thus far is unique in its combination of modelling methods with real world subject morphology files to simulate cerebral blood flow behaviour. These results demonstrate that the model successfully captures physiological flow distributions across major cerebral arteries and that patient-specific geometric variations produce realistic inter-subject variability and physical values. The significance lies not merely in reproducing known flow values, but in providing a validated framework with which to

investigate pathological conditions, drug delivery scenarios, and individualised treatment planning. The advantage over using measured data as a baseline is that the model allows for controlled perturbation studies and predictive scenario analysis that would be impossible or unethical in clinical settings. Additionally, the model was applied to several different subjects and is not tailored to one specific network, as many of the other current literature studies have done.

3.5 CONCLUSION

This chapter presented original work that includes the development of patient-specific viscosity models, novel autoregulatory coupling approaches for real world 3D arterial networks, and comprehensive validation against multiple literature sources, generating new insights into the relationship between vascular geometry and flow regulation. The current working model successfully generate data describing autoregulated cerebrovascular blood flow, such as volumetric flow rate and pressure. After discussing the assumptions used within this report and considering the validity with regards to the simulation, it was determined that the results are physically consistent and serve as a strong basis for further research into the pharmacokinetic behaviour of nanoparticles within the cerebrovasculature system.

CHAPTER 4: MODELLING OF CEREBRAL MICRO-CIRCULATION

4.1 INTRODUCTION

The purpose of the research presented in this chapter is three-fold: develop a model that simulates solute delivery in a synthetic capillary network under steady-state and time-dependent conditions, validate said model using anatomical data from previous research focusing on oxygen as the main solute, and observe the effects of input variables (such as inlet pressure and tissue consumption rate) on tissue solute levels. This is accomplished by utilising a Green's function method to analyse experimental and generated synthetic networks (El-Bouri *et al*., 2015; Secomb *et al*., 2015). The assumptions and models used will thus be discussed in full detail within the next few sections.

The first section of this chapter will describe the methodology behind the model crafted in this thesis, which largely draws upon previous research performed by Secomb *et al*. Results from this study are then presented and discussed with emphasis on how a variety of variables impact tissue solute levels. The results of this research will be presented and examined with regards to nanoparticle drug delivery in the following chapter, Chapter 5.

4.2 METHODS

4.2.1 General Overview

The model presented in this chapter draws on the work of Dr. Timothy Secomb and utilises his open-source C++ code available on GitHub (https://github.com/secomb). Initially, this code was validated using a 1-D Krogh cylinder model and previous capillary network datasets supplied by Secomb on his website, after which this code is used to evaluate statistical synthetic networks generated by El-Bouri (El-Bouri *et al*., 2015). The code itself utilises a Green's function method to iterate and return values for tissue and vessel solute levels. Oxygen is primarily used as the solute of choice in this chapter to validate the computational methods of the model; differences in

physical transport regimes and other parameters will limit comparisons between the two solutes. Application to nanoparticles and AuNP methodology modification is discussed in Chapter 5.

The code was developed to be self-contained, with four major input files determining the model parameters: these files described the solute mass balance in the tissue, the vessel network and spatial discretisation, a directory of solute parameters (such as diffusion coefficients), and finally the time range and time discretisation (time-dependent model file that also includes inlet solute information over time). The output data for oxygen levels are visualized using MATLAB and Excel. An illustration representing this process is displayed below in Figure 4.1.

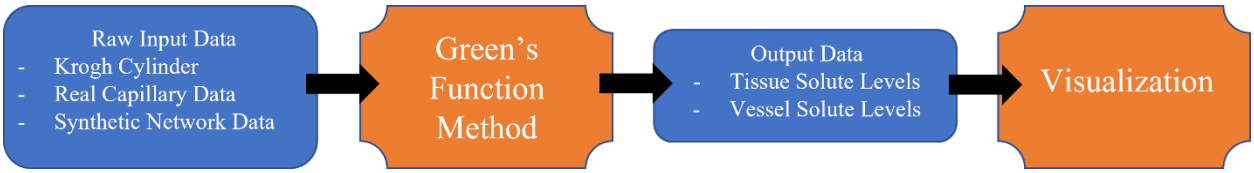

Figure 4.1: Schematic representing the major modules of the microvasculature modelling.

4.2.2 Green's Function Model – Time-Dependent

4.2.2.1 Motivations for Studying Time Dependency

Time-dependent analysis of cerebral microcirculation is critical for two interconnected reasons spanning clinical, physiological, and therapeutic domains. First, many cerebrovascular injuries and diseases operate on timescales where steady-state assumptions fail. For example, during ischemic stroke the occlusion of vessels create hypoxic regions within minutes (Xue *et al*., 2021). Steady-state models cannot fully capture the transient behaviour of these dynamics; however, steady-state models are developed to compare the time-dependent models against.

Second, the therapeutic delivery of nanoparticles exhibits intrinsically time-dependent pharmacokinetics. Unlike oxygen which typically transports with constant supply to cerebral tissue, AuNPs are not present in the blood but instead injected as part of a therapy. Time-resolved simulations are essential to most accurately model AuNP transport phenomena.

The development of both steady-state and time-dependent models constituted much of the work in this thesis. As such, many of the scenarios affected by time constraints could not be studied within the given scope of limitations. The time-dependent models developed in this chapter for oxygen and refined for AuNPs in Chapter 5 provide a validation case and strong groundwork for future studies into the scenarios where transient phenomena dominate.

4.2.2.2 Assumptions

Modelling the behaviour of particle diffusion from capillaries into surrounding cerebral tissue represents a computationally intensive challenge, necessitating several assumptions to reduce the complexity while delivering a rigorous simulation. The framework established by Secomb *et al.*, 2004 and 2015 provides foundational assumptions that are adopted throughout this work. The assumptions supplied here are specific to oxygen; though nanoparticles are not considered wholly in the chapter, the assumptions that change with regards to nanoparticle delivery are discussed in the more relevant Chapter 5.

First, the length and curvature of each vessel segment is much larger (minimum factor of 10) than the radius of the segment. This constraint will allow for several simplifications in the many equations describing diffusion and the Green's method for solving the system of equations. The morphological data provided by Cassot *et al*., 2006 supports this, demonstrating on average that the length of each capillary vessel is 13.47 times as large as the capillary radius (Cassot *et al*., 2006).

The second assumption stipulates that other than vessel endpoints or connections, the distance from each segment to other segments and vessel boundaries should be large compared to vessel radius. This, combined with the previous assumption, dictates that the oxygen field resulting from neighbour segments is constant across the circumference of a given segment.

Third, variations in oxygen flux and the partial pressure of oxygen in blood, as well as the effects of myoglobin facilitated diffusion, are ignored. These phenomena contribute second-order effects that are negligible relative to primary diffusive transport in the parameter regime examined here.

Fourth, the diffusivity and metabolic rate of oxygen consumption are considered uniform excluding the interior of the blood vessels, with the vessel walls being considered part of the tissue. Any localized variations in metabolic rate are neglected in favour of utilising the mean metabolic rate. Additionally, the metabolic rate of oxygen is assumed to be independent of its partial pressure, a valid approximation provided the tissue is not anoxic. This linearisation is essential for applying the Green's function solution methodology.

Finally, a linear relationship between oxygen concentration and the partial pressure of oxygen in the tissue is assumed, with the additional stipulation that the solubility is fixed. This is perhaps the biggest assumption, as in conjunction with the previous two assumptions it ensures that the diffusion equation within the tissue is linear, and the Green's function may be applied.

4.2.2.3 Governing Equations

To establish the algorithmic framework, several fundamental equations are defined as the foundation for this chapter. As time-dependent equations represent more generalized and complex cases, the algorithm will be developed with regards to time dependency; steady-state solutions emerge as limiting cases and will be derived subsequently in Section 4.2.3. The concentration of solute p is kept generalized to accommodate oxygen (Chapter 4) and gold nanoparticles (Chapter 5), with solute-specific modifications noted where relevant.

The tissue space governing equations of the time-dependent problem are derived from Fick's law of diffusion and conservation of mass and yield Equation 4.1, where D_p is the uniform diffusivity (cm^2/s) of solute p. Should multiple solutes be present, then p exists within the range

of 1 to N_S maximum reacting solutes. C_p^t represents the tissue concentration of solute (cm^3 solute/cm^3), ∇^2 is the Laplacian operator, *t* is time (s), and R_p represents the rate of production of the solute in question (cm^3 solute/cm^3/s). By convention the value of R_p is negative to denote consumption (as for oxygen, described by Michaelis-Menten kinetics) and positive for solute production.

$$\frac{\partial C_p^t}{\partial t} - D_p \nabla^2 C_p^t = R_p\left(C_1^t, C_2^t \ldots, C_{N_S}^t\right) \tag{4.1}$$

The vessel governing equation is defined by Equation 4.2 below. Here, $C_p^v(s,t)$ represents cross-sectionally averaged vessel (intravascular) solute concentration (cm^3 solute/cm^3) with *s* representing the axial distance along the vessel segment under analysis (cm). Throughout the rest of this subsection, superscripts *v, t*, and *e* denote values within the vessel, tissue, and in tissue adjacent to a vessel (extravascular). *Q* within Equation 4.2 is the volumetric flow rate (cm^3/s) within the vessel *v* (which is potentially time-dependent), *A* is the cross-sectional area (cm^2), and $q_p(s,t)$ is the rate of diffusion per unit length of solute from the vessel to the tissue (cm^3 solute/cm/s).

$$A\frac{\partial C_p^v}{\partial t} + Q\frac{\partial C_p^v}{\partial s} = -q_p \tag{4.2}$$

It should be noted that the extravascular concentration of solute $C_p^e(s,t)$ (circumferentially averaged tissue concentration C_p^t evaluated at the vessel wall) may differ from that of the intravascular concentration. This is usually due to gradients in the vessel wall caused by finite permeability to the solute, lack of significant solute gradients in the blood preventing radial diffusion from occurring, or different solubility/binding characteristics of the solute in blood versus tissue. Oxygen exemplifies this behaviour: as a soluble gas, concentration disparities arise from solubility differences between plasma and tissue.

To unify the treatment of such multiphase systems, generalized concentration variable X_p is introduced incorporate these effects and represent the solute concentrations across different media and physical states (i.e. aqueous vs soluble gas). For the example of oxygen, its concentration in tissue C_p^t (cm^3 solute/cm^3) may be expressed as Equation 4.3, where X_p^t is the value of X_p within the tissue (mmHg) and a_p^t is the solubility (cm^3 solute/cm^3/mmHg).

$$C_p^t = a_p^t X_p^t \tag{4.3}$$

4.2.2.4 Boundary Conditions

The selection of boundary conditions critically influences both solution accuracy and computational efficiency in a Green's function methodology. Secomb *et al*., 2004 and Secomb *et al*., 2015 consider three boundary conditions: pointwise no-flux, net no-flux, and the infinite domain solution. In the no-flux formulations, the total flux is set equal to 0 for each point inside the domain or for each of the domain faces (6 for a cube) respectively. The infinite domain formulation places the tissue region in an infinite domain and sets the total net flux of solute out of the tissue region to zero. For both the time-dependent and stead-state implementations in this work, an infinite domain solution was selected.

The decision to use the infinite domain solution was motivated by four key considerations. First, pointwise and net no-flux boundary conditions often produce local solute fluxes at arbitrary tissue locations when applied to irregular, realistic vascular geometries. The networks examined in this thesis are both geometrically complex and periodic; flux artefacts may occur at tissue domain corners, reducing accuracy in generated results. Second, the infinite domain Green's function is the simplest of the three cases, reducing the computation necessary to reach a solution. Third, the infinite domain solution does not require a specific boundary condition on the vascular network region, an advantageous feature when the optimal domain extent remains uncertain. Finally, the tissue domain under examination is not restricted to a cuboidal geometry. This

flexibility accommodates future extensions to patient-specific geometries or complex tissue architectures.

Throughout this section, $\boldsymbol{D}$ defines the region of interest containing the network of vessels and associated tissue, while $\boldsymbol{R}^3$ represents the infinite domain itself. $\boldsymbol{D}$ is treated as a subset of the infinite domain $\boldsymbol{R}^3$. Figures 4.2(a) and 4.2(b) below illustrate the similarities and differences in the pointwise no-flux and infinite domain boundary conditions of the system.

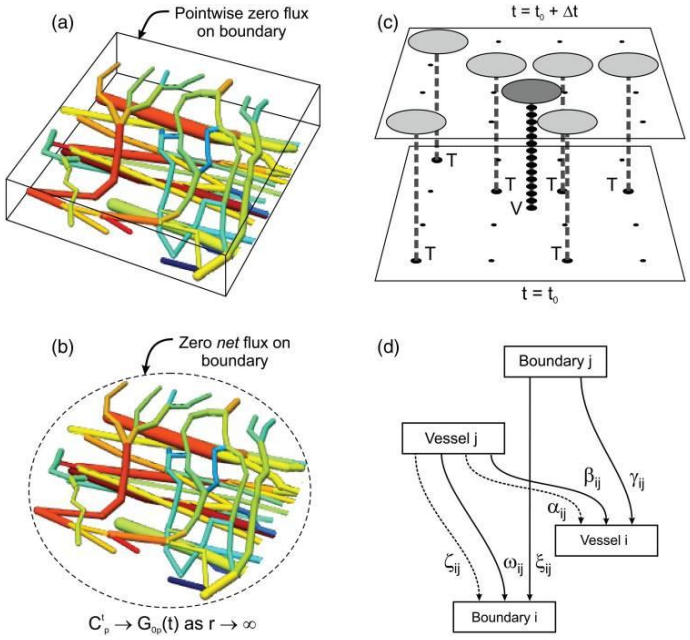

Figure 4.2: (a) Pointwise no-flux approach, zero solute flux across boundary of cuboid box, (b) Infinite-domain approach, zero net exchange of solute across boundary, (c) Illustration of the time-dependent Green's function approach, for a 2-D spatial domain. The lower plane represents a known distribution of solute level in the domain at time $t=t_0$, with the upper plane representing one time step later. Large dots are tissue source points T, with vessel source point V, (d) Matrices describing the convective redistribution of intravascular volume over one time step (reproduced with permission and shortened from Secomb *et al*., 2015).

4.2.2.5 Time-Dependent Numerical Formulation

The zero net flux boundary condition implies that the rate of change of total solute in tissue domain $\boldsymbol{D}$ has a rate of change equal to the total number of sources within that region. Combination of this implication and the governing equations (Equations 4.1-4.2) leads to Equations 4.4 and 4.5, which together constitute the problem to be solved.

$$\frac{\partial C_p^t}{\partial t} - D_p \nabla^2 C_p^t = \psi_p(\boldsymbol{x}, t) \quad for \ \boldsymbol{x} \in \boldsymbol{R}^3 \tag{4.4}$$

$$\int_{\boldsymbol{D}}^{0} \left(\frac{\partial C_p^t}{\partial t} - \psi_p(\boldsymbol{x}, t) \right) dV = 0 \tag{4.5}$$

Within this equation pair, V is the domain volume (cm^3) while $\psi_p(\boldsymbol{x}, t)$ (cm^3 solute/cm^3/s) represents the distribution of solute sources and sinks, including reactions within the tissue and exchange with vessels. Outside of the domain of interest, $\psi_p(\boldsymbol{x}, t)$ is equal to $\bar{\psi}_p(t)$ (cm^3 solute/cm^3/s), a spatially uniform source. The relationship between $\bar{\psi}_p(t)$ and the ambient solute concentration $G_{0p}(t)$ (cm^3 solute/cm^3) is given by Equation 4.6 below.

$$\frac{dG_{0p}}{dt} = \bar{\psi}_p(t) \tag{4.6}$$

For the time-dependent formulation, the unsteady Green's function characterizes the concentration at spatial point $\boldsymbol{x}$ and time point t resulting from an instantaneous source at spatial point $\boldsymbol{x}^*$ and time point t^*. It takes the form $G_p(\boldsymbol{x} - \boldsymbol{x}^*, t - t^*)$ and is the solution to Equation 4.7 below. In this expression, δ represents the Dirac delta function.

$$\frac{\partial G_p}{\partial t} - D_p \nabla^2 G_p = \delta_3(\boldsymbol{x} - \boldsymbol{x}^*)\delta(t - t^*) \tag{4.7}$$

Equation 4.8 is then employed o express the concentration of solute p as a spatiotemporal integral, with C_{0p} being the initial uniform concentration (cm^3 solute/cm^3). The field at time t (s) due to the point source t^* as defined by Equation 4.8 may alternatively be calculated by taking an evaluation at some intermediate time point t', where t' is greater than t^* and less than t, then taking

a second evaluation while treating the resultant field as a source at *t*'. G_p satisfies the composition property given below in Equation 4.9, verifiable by direct integration. It is from this property that a solution that advances with time is developed via convolution with the Green's function over interval Δt. Convolution with the Green's function over Δt will allow for concentration values to be calculated for any arbitrary time input.

$$C_p(\boldsymbol{x}, t) = \int_0^t \int_{\boldsymbol{R}^3}^0 G_p(\boldsymbol{x} - \boldsymbol{x}^*, t - t^*)\psi_p(\boldsymbol{x}^*, t^*)d\boldsymbol{x}^* dt^* + C_{0p} \tag{4.8}$$

$$G_p(\boldsymbol{x} - \boldsymbol{x}^*, t - t^*) = \int_{\boldsymbol{R}^3}^0 G_p(\boldsymbol{x} - \boldsymbol{x}', t - t')G_p(\boldsymbol{x}' - \boldsymbol{x}^*, t' - t^*)d\boldsymbol{x}' \tag{4.9}$$

Confining the integration in Equation 4.8 to the finite domain allows for reformulation into Equation 4.10 below. By assumption, Equation 4.11 holds for any $\boldsymbol{x}^*$ outside of the region of interest. The second integral within Equation 4.10 is spatially independent and therefore reduces to the temporal integral of $\bar{\psi}_p(t)$. The reduction is written as Equation 4.12, with Equations 4.6 and 4.13 applying.

$$C_p(\boldsymbol{x}, t) = \int_0^t \int_{\boldsymbol{R}^3}^0 G_p(\boldsymbol{x} - \boldsymbol{x}^*, t - t^*)[\psi_p(\boldsymbol{x}^*, t^*) - \bar{\psi}_p(t^*)]d\boldsymbol{x}^* dt^* + \int_0^t \int_{\boldsymbol{R}^3}^0 G_p(\boldsymbol{x} - \boldsymbol{x}^*, t - t^*)\psi_p(t^*)d\boldsymbol{x}^* dt^* + C_{0p} \tag{4.10}$$

$$\psi_p(\boldsymbol{x}^*, t^*) - \bar{\psi}_p(t^*) = 0 \tag{4.11}$$

$$C_p(\boldsymbol{x}, t) = \int_0^t \int_D^0 G_p(\boldsymbol{x} - \boldsymbol{x}^*, t - t^*)[\psi_p(\boldsymbol{x}^*, t^*) - \bar{\psi}_p(t^*)]d\boldsymbol{x}^* dt^* + G_{0p}(t) \tag{4.12}$$

$$G_{0p}(0) = C_{0p} \tag{4.13}$$

From Equation 4.12 and the properties of G_p, as the magnitude of $\boldsymbol{x}$ approaches infinity the concentration of solute at point $\boldsymbol{x}$ and time *t* approaches $G_{0p}(t)$. This confirms that $G_{0p}(t)$ is the ambient concentration previously described.

Having established a Green's function formulation that relates $G_{0p}(t)$, time, space, and solute concentration the spatial and temporal discretisation may proceed. In the temporal

discretisation scheme, the time interval from 0 to t is partitioned into n equal segments of length Δt. Each subsegment spans $[t_{k-1}, t_k]$, where $k = 1,\ldots,n$. The initial value of t, t_0, is set equal to 0 s. The solute source and sink distribution function, $\psi_p(\boldsymbol{x}, t)$, is approximated by a time-independent function $\psi_{pk}(\boldsymbol{x})$ on the subsegment $[t_{k-1}, t_k]$, with $\bar{\psi}_{pk}$ defined analogously.

This subinterval discretisation serves two purposes: one, it linearises the otherwise nonlinear dynamics within each time step, enabling efficient solution via the biconjugate gradient stabilised method; and two, it permits adaptive time-stepping where Δt may vary mid-simulation in response to solution dynamics. As an example, smaller time steps may be employed during rapid transients (e.g., immediately following a perturbation), while larger steps suffice during time periods that approach steady-state. Theoretically, adaptively changing Δt mid-simulation should maintain accuracy while reducing computational time; it was instead found that Δt changes at time point t produce perturbations in resulting solute concentrations before reaching convergence again. This phenomenon was first observed in Chapter 4 and is discussed further in Chapter 5.

Equation 4.14 below describes the contribution of a constant unit point source at $\boldsymbol{x}^*$ during the time interval $[t_{k-1}, t_k]$ to the overall field at time t. The integral of Equation 4.14 is evaluated in terms of the error function *erf* as Equation 4.15 below, with $r_x = |\boldsymbol{x} - \boldsymbol{x}^*|$.

$$\bar{G}_{pk}(\boldsymbol{x} - \boldsymbol{x}^*, t) = \int_{t_{k-1}}^{t_k} G_p(\boldsymbol{x} - \boldsymbol{x}^*, t - t^*)dt^* \tag{4.14}$$

$$\bar{G}_{pi}(\boldsymbol{x} - \boldsymbol{x}^*, t) = \left(4\pi D_p r_x\right)^{-1} \left\{ \operatorname{erf}\left[\frac{r_x}{\left(4D_p(t-t_k)\right)^{\frac{1}{2}}}\right] - \operatorname{erf}\left[\frac{r_x}{\left(4D_p(t-t_{k-1})\right)^{\frac{1}{2}}}\right] \right\} \tag{4.15}$$

At a time t_k the field may be calculated by convoluting the field at the preceding time t_{k-1} with the Green's function for that interval and including the concentration resulting from the source distribution during the time interval. This is represented below in Equations 4.16 and 4.17. Equation 4.16 is derived from the right-hand side of Equation 4.12 by expressing it as a summation

of integrals over the spans of 0 to t_{k-1} and t_{k-1} to t_k. The integrals over [0, t_{k-1}] and [t_{k-1}, t_k] are evaluated using Equations 4.9 and 4.14 respectively. Equation 4.17 is derived from the relationship between Equations 4.6 and 4.13.

$$C_p(\boldsymbol{x}, t_k) - G_{0pk} = \int_D^0 G_p(\boldsymbol{x} - \boldsymbol{x}^*, \Delta t)\left[C_p(\boldsymbol{x}^*, t_{k-1}) - G_{0pk-1}\right]d\boldsymbol{x}^* + \int_D^0 G_p(\boldsymbol{x} - \boldsymbol{x}^*, \Delta t)\left[\psi_{pk}(\boldsymbol{x}^*) - \bar{\psi}_{pk}\right]d\boldsymbol{x}^* \quad (4.16)$$

$$\bar{\psi}_{pk} = \frac{G_{0pk} - G_{0pk-1}}{\Delta t} \quad (4.17)$$

The first integral in Equation 4.16 is approximated by its integral over the domain of interest $\boldsymbol{D}$ and not the entire infinite-domain as in Equation 4.9 because the field $C_p(\boldsymbol{x}, t_k) - G_{0pk}$ equals zero outside of $\boldsymbol{D}$. This reduces the computational cost, as only the previous time point field is necessary for current time point calculations. The integrals in Equation 4.16 therefore may be processed in parallel.

Once the time range is appropriately discretised, the spatial domain is then also discretised. First, the network of vessels is divided into N_v short cylindrical segments. Then, the tissue region (including the vessels) is similarly divided into N_t cuboidal regions of volume V_t (cm^3). Six diffusive interaction matrices (G_{pij}^{tt}, G_{pij}^{vt}, $\bar{G}_{pij}^{tt}$, $\bar{G}_{pij}^{vt}$, $\bar{G}_{pij}^{tv}$, and $\bar{G}_{pij}^{vv}$) are then created from the specific spatiotemporal discretisations. Should either the spatial or the temporal discretisation change, the diffusive interaction matrices must be recomputed.

The first two matrices G_{pij}^{tt} (N_t x N_t) and G_{pij}^{vt} (N_v x N_t) give the average concentration (cm^3 solute/cm^3) at time t_k (s) in the tissue region *i* and on the surface of segment *i* respectively. The two matrices G_{pij}^{tt} and G_{pij}^{vt} are the result of a unit concentration of solute (cm^3 solute/cm^3) distributed over tissue region *j* at time t_{k-1} (s). The matrices $\bar{G}_{pij}^{tt}$ (N_t x N_t) and $\bar{G}_{pij}^{vt}$ (N_v x N_t) give the average concentration of solute *p* (cm^3 solute/cm^3) at time t_k (s) in tissue region *i* and on

the surface of segment *i*, respectively. These matrices result from a unit source distributed over tissue region *j* during the preceding interval Δt. The final two matrices $\bar{G}_{pij}^{tv}$ (N_t x N_v) and $\bar{G}_{pij}^{vv}$ (N_v x N_v) give the average concentration (cm^3 solute/cm^3) at time t_k (s) in the tissue region *i* and on the surface of segment *i* respectively. These final matrices result from a unit source distributed over the interior of segment *j* during the preceding interval Δt.

The six diffusive interaction matrices are calculated for each solute *p* and stored for use at each time step. Each tissue source is distributed uniformly over a sphere of radius r_t (cm), with volume equal to V_t. This allows for closed form integral calculations of the diffusive matrices.

The first diffusive matrix G_{pij}^{tt} is calculated using Equations 4.18 through 4.23 below, with Equations 4.19 through 4.21 representing three cases depending on the value of r_{ij}, the distance between midpoints of tissue regions i and j. Equation 4.18 is the solution to Equation 4.7 when $t > t^*$ and equals 0 at infinity taken from Carslaw & Jaeger, 1959.

Equations 4.19 through 4.21 (and seen similarly for other diffusive matrix) represent the interactions between two distributed sources at three different distances: 0 (a point source sourcing itself), closely spaced ($x_0 < 10$), and far apart ($x_0 \geq 10$). The interaction between two far apart distributed sources can generally be approximated by the interaction between two separate point sources, but the interaction between two closely spaced sources must be calculated by averaging over one of the source volumes to improve the approximation and to remove the singular behaviour as r_x approaches 0. Distributed sources are considered to be far apart when the value of r_{ij} is an order of magnitude (ten times) large than r_t (Secomb *et al*., 2015).

When $x_0 = 0$ (Equation 4.19), Equation 4.18 is averaged with respect to both $\boldsymbol{x}$ and $\boldsymbol{x}^*$over the interior of sphere of radius r_t. When $x_0 < 10$ (Equation 4.20), Equation 4.18 is averaged with respect to $\boldsymbol{x}$ over the interior of the sphere centred on tissue region i with $\boldsymbol{x}^*$at the centre of tissue

region j. For $x_0 \geq 10$, Equation 4.18 uses r_{ij} instead of r_x. The diffusive matrix G_{pij}^{vt} is simply the average tissue concentration on the surface of segment i at time step k resulting from a unit concentration of solute distributed over tissue region j at the preceding time step.

$$G_p(\boldsymbol{x} - \boldsymbol{x}^*, t - t^*) = \left(4\pi D_p(t - t^*)\right)^{-\frac{3}{2}} e^{-r_x^2/\left(4D_p(t-t^*)\right)} \tag{4.18}$$

$$G_{pij}^{tt} = \left(4\pi D_p \Delta t\right)^{-\frac{3}{2}} * \frac{3}{16} * a^{-3}\left[1 - 6a + (2a-1)e^{-4} + 4\pi^{\frac{1}{2}}a^{\frac{3}{2}}\,\mathrm{erf}\left(2a^{\frac{1}{2}}\right)\right] \tag{4.19}$$

$$G_{pij}^{tt} = \left(4\pi D_p \Delta t\right)^{-\frac{3}{2}} * \frac{3}{8} * a^{-2}x_0^{-1}\{(\pi a^{\frac{1}{2}}x_0\left(erfc\left[a^{\frac{1}{2}}(x_0 - 1)\right] - erfc\left[a^{\frac{1}{2}}(x_0 + 1)\right]\right) -$$

$$\exp[-a(x_0 - 1)^2] + exp[-a(x_0 + 1)^2]\} \tag{4.20}$$

$$G_p(\boldsymbol{x} - \boldsymbol{x}^*, t - t^*) = \left(4\pi D_p(t - t^*)\right)^{-\frac{3}{2}} e^{-r_{ij}^2/\left(4D_p(t-t^*)\right)} \tag{4.21}$$

$$a = \frac{r_t^2}{4\pi D_p \Delta t} \tag{4.22}$$

$$x_0 = \frac{r_{ij}}{r_t} \tag{4.23}$$

The third diffusive matrix $\bar{G}_{pij}^{tt}$ is calculated using Equations 4.24 through 4.27 below, where Equation 4.24 is Equation 4.15 at the end of the time interval Δt resulting from a constant unit point source at $\boldsymbol{x}^*$. $\bar{G}_{pij}^{tt}$ is computed as G_{pij}^{tt} was, though it is applied to Equation 4.24 rather than Equation 4.18. The same cutoffs of $x_0 = 0$ and $x_0 < 10$ are used to give Equations 4.25 and 4.26, while $x_0 \geq 10$ has Equation 4.24 use r_{ij} instead of r_x. The diffusive matrix $\bar{G}_{pij}^{vt}$ is calculated the same as G_{pij}^{vt} but over vessel segment i as opposed to the surface of segment i and during Δt, not the previous time step.

$$\bar{G}_p(\boldsymbol{x} - \boldsymbol{x}^*, \Delta t) = \left(4\pi D_p r_x\right)^{-1}\left\{1 - \mathrm{erf}\left[\frac{r_x}{\left(4D_p(\Delta t)\right)^{\frac{1}{2}}}\right]\right\} \tag{4.24}$$

$$\bar{G}_{pij}^{tt} = (4\pi D_p r_t)^{-1} * \frac{3}{40} * [10a^{-1} + (16 - 10a^{-1})erfc\left(2a^{\frac{1}{2}}\right) - (\pi a)^{-\frac{1}{2}}(-a^{-2} +$$

$$10a^{-1} + (a^{-2} + 6a^{-1} + 8)e^{-4a})] \quad (4.25)$$

$$\bar{G}_{pij}^{tt} = (4\pi D_p r_{ij})^{-1} * \frac{1}{4} * \{(\pi a)^{-\frac{1}{2}}[(x_0 - 2)(x_0 + 1) + a^{-1}] \exp[-a(x_0 + 1)^2] -$$

$$(\pi a)^{-\frac{1}{2}}[(x_0 + 2)(x_0 - 1) + a^{-1}] \exp[-a(x_0 - 1)^2] - \left[(x_0 - 2)(x_0 + 1)^2 + \frac{3}{2} *\right.$$

$$\left. x_0 a^{-1}\right] erfc\left[a^{\frac{1}{2}}(x_0 + 1)\right] + \left[(x_0 + 2)(x_0 - 1)^2 + \frac{3}{2} * x_0 a^{-1}\right] erfc\left[a^{\frac{1}{2}}(x_0 - 1)\right] -$$

$$K(x_0 + 2)(x_0 - 1)^2\} \quad (4.26)$$

$$K = 1 - sgn[x_0 - 1] \quad (4.27)$$

The fifth diffusive matrix $\bar{G}_{pij}^{tv}$ is the transpose of matrix $\bar{G}_{pij}^{vt}$, while the final matrix $\bar{G}_{pij}^{vv}$ is calculated using Equation 4.24 above and Equations 4.28 through 4.30 below. If i = j, Equation 4.24 is averaged over a cylinder of radius r_t and length L. The integral is over the curved surface with respect to $\boldsymbol{x}$ and over the interior volume with respect to $\boldsymbol{x}^*$. If i does not equal j, $\bar{G}_{pij}^{vv}$ is calculated as $\bar{G}_{pij}^{tt}$ but with a r_t for a sphere of volume equal to the larger segment volumes.

$$\bar{G}_{pij}^{vv} = \int_0^{\Delta t}\left(4\pi D_p \Delta t\right)^{-\frac{3}{2}} * \frac{1}{2} * b^{-1}[1 - e^{-2b} I_0(2b)] * c^{-1}[e^{-c} - 1 + (\pi c)^{\frac{1}{2}}\text{erf}\,(c^{1/2})]dt \quad (4.28)$$

$$b = \frac{r_v^2}{4D_p t} \quad (4.29)$$

$$c = \frac{L^2}{4D_p t} \quad (4.30)$$

With the diffusive matrices defined, the Green's function found in Equation 4.16 may alternatively be expressed in a discretised form as presented in Equations 4.31 and 4.32 for time step *k*. First, C_{pk}^t is approximated by piecewise values C_{pik}^t over each tissue element from the first integral in Equation 4.16. This approximation is then decomposed into a summation over all N_t tissue regions. For each source region *j* and receiving region *i*, the diffusive matrix G_{pij}^{tt} is applied

within the summation. The same procedure is performed for the temporally-related second integral over time span $[t_{k-1}, t_k]$. These summations together form the first half of Equation 4.31. The third summation in Equation 4.31 describes the total vascular source contributions to tissue concentrations, and G_{0pk} is the Green's function unknown constant. The same procedure is performed to produce Equation 4.32 but evaluates the concentration on the surface of vascular segments rather than within the tissue volumes.

$$C^t_{pik} = \sum_{j=1}^{N_t} V^t G^{tt}_{pij}\left(C^t_{pik-1} - G_{0pk-1}\right) + \sum_{j=1}^{N_t} \bar{G}^{tt}_{pij}\left(\phi_{pjk} - \frac{V^t\left(G_{0pk} - G_{0pk-1}\right)}{\Delta t}\right) + \sum_{j=1}^{N_v} \bar{G}^{tv}_{pij} q_{pjk} + G_{0pk} \quad for\ i = 1, \dots, N_t \tag{4.31}$$

$$C^e_{pik} = \sum_{j=1}^{N_t} V^t G^{vt}_{pij}\left(C^t_{pik-1} - G_{0pk-1}\right) + \sum_{j=1}^{N_t} \bar{G}^{vt}_{pij}\left(\phi_{pjk} - \frac{V^t\left(G_{0pk} - G_{0pk-1}\right)}{\Delta t}\right) + \sum_{j=1}^{N_v} \bar{G}^{vv}_{pij} q_{pjk} + G_{0pk} \quad for\ i = 1, \dots, N_v \tag{4.32}$$

In these expressions, C^e_{pik} denotes the average extravascular concentration of solute (cm^3 solute/cm^3) over the surface of segment *i*, while C^t_{pik} is the average concentration of solute (cm^3 solute/cm^3) over tissue region *i*. The variables q_{pjk} and ϕ_{pjk} represent unknown source strengths (cm^3 solute/cm^3/s) during time step *k* associated with the vessel segments and tissue regions respectively.

This discretisation of Equations 4.31 and 4.32 leads to a stable and well-behaved formulation regardless of time step or spatial step size. In Secomb *et al*., 2015 the time step was varied from 0.25 s to 100 s, with relative Δt/Δx ranging from 0.001 to 89.44: all simulations under these parameters showed convergence and only minor differences in the results when all other parameters were held constant. Time and spatial steps must be chosen based upon the physical systems under examination; it is recommended by Secomb *et al*., 2015 that the time step remain under 10 seconds for capillary microvasculature modelling.

The unknown source strengths ϕ_{pjk} are solved for using Equation 4.33, with variable $\bar{C}^t_{ijk}$ being defined by Equation 4.34. Equation 4.33 is a relationship between specified reaction rates of solute, the volume V^t, and the tissue source strengths.

$$\phi_{pjk} = V^t R_p\left(\bar{C}^t_{1jk}, \bar{C}^t_{2jk}, \dots, \bar{C}^t_{N_s jk-1}\right) \quad for\ j = 1, \dots, N_t \tag{4.33}$$

$$\bar{C}^t_{ijk} = \frac{C^t_{ijk-1} + C^t_{ijk}}{2} \tag{4.34}$$

Currently, the relationship presented in Equation 4.2 is nonlinear: for use in the Green's function method, it must be linearised. Equation 4.35 below is derived by integrating Equation 4.2 along each flow pathway within the vessel network to perform this necessary linearisation. Solute concentration in vessel segment *i* at time t_k is now expressed as a linear function of the corresponding concentrations at the preceding time point t_{k-1} and source strengths q_{pjk}. Within this equation, V_j is the volume of segment *j* (cm^3), γ_{ij} is a matrix giving the fraction of blood in segment *i* at time t_k that arrived from inflowing boundary node *j* during time step *k*, C^b_{pjk} is the prescribed concentration of solute *p* (cm^3 solute/cm^3) in the inflowing blood at node *j* during same time step *k*, and N_b is the number of boundary nodes. Additionally, the matrix β_{ij} gives the fraction of the blood contained in segment *i* at time t_k that arrived from segment *j* during time step *k* while the matrix α_{ij} gives the fraction of the time step Δt that the blood contained in segment *i* at time t_k spent in segment *j* weighted according to the fraction of flow on each flow pathway.

$$C^v_{pik} = \sum_{\substack{j=1 \\ inflow}}^{N_b} \gamma_{ij} C^b_{pjk} + \sum_{j=1}^{N_v} \beta_{ij} C^v_{pjk-1} - \sum_{j=1}^{N_v} \frac{\alpha_{ij} q_{pjk} \Delta t}{V_j} \quad for\ i = 1, \dots, N_v \tag{4.35}$$

Computation of solute concentration in outflowing blood is calculated with Equation 4.36. In this equation (compared to the previous equation), C^b_{pjk} represents the average concentration of solute in the outflowing blood at boundary node *i* during the time step *k*, while ξ_{ij} and ω_{ij} are both matrices that give the fractions of the outflowing blood that arrived from boundary node *j* and from

segment *j*, respectively. ζ_{ij} is an additional matrix that gives the fraction of the time step that the outflowing blood spent in segment *j* (s), weighted as for α_{ij} in Equation 4.35.

$$C_{pik}^{b} = \sum_{\substack{j=1 \\ inflow}}^{N_b} \xi_{ij} C_{pjk}^{b} + \sum_{j=1}^{N_v} \omega_{ij} C_{pjk-1}^{v} - \sum_{j=1}^{N_v} \frac{\zeta_{ij} q_{pjk} \Delta t}{V_j} \quad for\ i = 1, \ldots, N_b \tag{4.36}$$

Equation 4.36 differs from 4.35 in that 4.36 refers to the blood arriving at a boundary node during a time step, whereas the previous equation refers to the contents of a segment at the end of the time step. These equations are numerically time staggered to account for the transport of blood. Inflowing upstream blood solute concentration C_{pjk}^{b} at a current time step *k* forms a concentration gradient with C_{pik}^{v}; as time progresses, the gradient affects C_{pik}^{v}, so a new C_{pik}^{v} must be calculated from the C_{pik}^{v} at the previous time step *k*-1. This is similarly performed for C_{pik}^{b}, which is downstream of C_{pik}^{v}, with C_{pik}^{b} dependent on current C_{pjk}^{b} upstream (forming a concentration gradient at time step *k*) and the C_{pik}^{v} at the previous time step *k*-1.

Discretisation of Equation 4.2 produces Equation 4.37, where s_i denotes the length of segment *i* (cm) and P_{pi} represents a coefficient that depends on vessel wall permeability to the solute and on intravascular mass transport characteristics. For oxygen, the units of P_{pi} are cm^3 solute/cm/s/mmHg. Applying Equations 4.32 and 4.35 to Equation 4.37 returns Equation 4.38 below. In Equation 4.38, the left-hand side specifies the average tissue concentration adjacent to segment *i* based upon tissue transport, while the right-hand side specifies the same quantity based upon vessel transport.

$$q_{pik} = s_i P_{pi} \left[f_p^{-1}\left(C_{pik}^{v}\right) - \frac{C_{pik}^{e}}{\alpha_p^t} \right] \tag{4.37}$$

$$\sum_{j=1}^{N_t} V^t G_{pij}^{vt} \left(C_{pik-1}^{t} - G_{0pk-1}\right) + \sum_{j=1}^{N_t} \bar{G}_{pij}^{vt} \left(\phi_{pjk} - \frac{V^t\left(G_{0pk} - G_{0pk-1}\right)}{\Delta t}\right) + \sum_{j=1}^{N_v} \bar{G}_{pij}^{vv} q_{pjk} + G_{0pk} =$$

$$\alpha_p^t f_p^{-1} \left(\sum_{j=1}^{N_b} \gamma_{ij} C_{pjk}^{b} + \sum_{j=1}^{N_v} \beta_{ij} C_{pjk-1}^{v} - \sum_{j=1}^{N_v} \frac{\alpha_{ij} q_{pjk} \Delta t}{V_j} \right) - \frac{\alpha_p^t q_{pik}}{s_i P_{pi}} \quad for\ i = 1, \ldots, N_v \tag{4.38}$$

Applying Equations 4.4 and 4.5 to enforce zero net diffusive exchange at the region of interest boundaries produces Equation 4.39 below. Here, C_{pik}^{t} is calculated from Equation 4.31, and the source strengths during the interval are computed as the average of their initial and final values.

$$\sum_{j=1}^{N_t} \phi_{pjk} + \sum_{j=1}^{N_v} q_{pjk} = (V^t/\Delta t) \sum_{i=1}^{N_t} (C_{pik}^{t} - C_{pik-1}^{t}) \tag{4.39}$$

The solution procedure at time step k follows from the previous equations and is explained below. First, tissue source strengths are computed using Equation 4.33, then initial estimates of vessel sources strengths (q_{pik}) are selected. This step is normally performed by equating $q_{pik} = q_{pik-1}$. Next, the inverse function of Equation 4.38 (f_p^{-1}) is linearised about the current values of its inputs, which means that Equations 4.38 and 4.39 now comprise a linear system of $N_v + 1$ equations for variables q_{pjk} and G_{0pk}. This linear system is solved using the biconjugate gradient stabilised method. Finally, the updated values of C_{pik}^{t} are calculated using Equation 4.31 and iterated with updated values of q_{pjk} until convergence is achieved. For oxygen, values of C_{pik}^{t} are divided by a_p^t to return concentrations in terms of partial pressure (mmHg). A diagram illustrating this process is shown below in Figure 4.3.

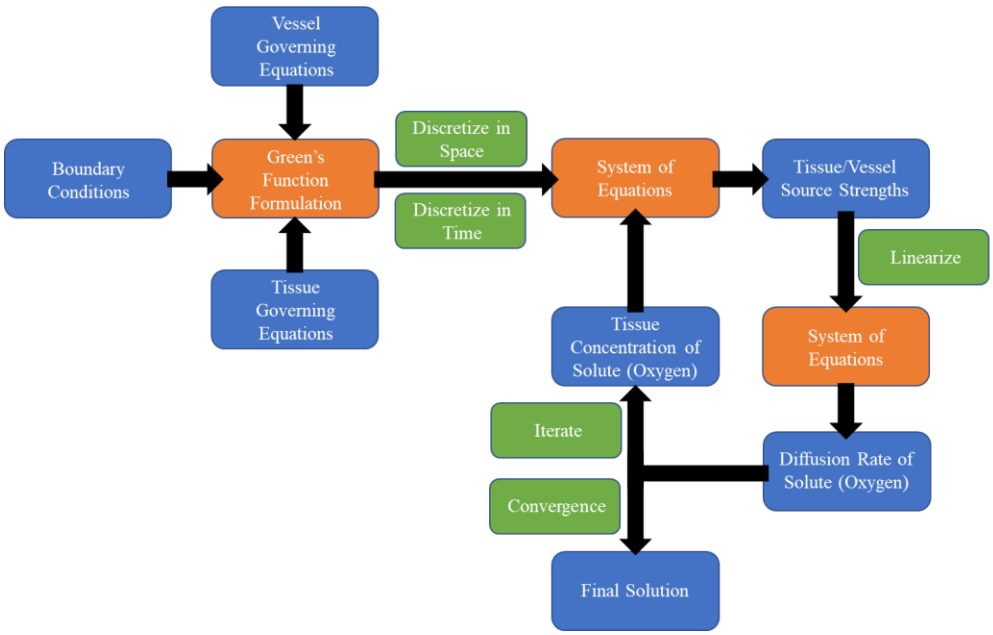

Figure 4.3: Flow chart illustrating iterative process for solving the time-dependent Green's function method application for solute transport in cerebral microvasculature. Blue boxes represent input and output data, orange boxes represent the governing equations, and the green boxes represent algorithms used to transform the data or equations.

4.2.3 Green's Function Model – Steady-State

The above algorithm was developed to handle the modelling of multiple solutes in the cerebral microvasculature. It was also of interest within this thesis to examine oxygen and AuNP under steady-state conditions. One method for performing these simulations is to simply run the time-dependent simulation until steady-state conditions are met and analyse the results at the final time point. This is potentially computationally expensive, as the amount of time it would take to reach steady state would depend on the simulation parameters and may take real-world hours or days. Instead, a streamlined model derived from the time-dependent model was created to simulate steady-state conditions.

The development of the steady-state model follows the same structure previously outlined: statement of assumptions, choice of boundary conditions, definition of governing equations,

formulation of the Green's function, and finally numerical implementations. Of these five steps, the assumptions and choice of boundary conditions are identical and may be referenced in the above sections.

The governing conservation of mass equations under steady-state conditions are derived from Equations 4.1 for the tissue space and 4.2 for the vessel space. They are shown below in Equations 4.40 and 4.41. The forms of the equations are still capable of handling multiple solutes: as oxygen is still being examined in this chapter, Equation 4.3 still applies.

$$D_p \nabla^2 C_p^t = R_p\left(C_1^t, C_2^t \ldots, C_{N_S}^t\right) \tag{4.40}$$

$$Q \frac{\partial C_p^v}{\partial s} = -q_p \tag{4.41}$$

Utilising potential theory, the Green's function for a steady-state domain may be represented as the potential (in this case concentration of solutes) at a point resulting from a nearby unit point source. This is ultimately defined below in Equation 4.42, where δ_3 is the three-dimensional delta function and reduces to Equation 4.43 under infinite domain boundary conditions.

$$D_p \nabla^2 G = -\delta_3(\boldsymbol{x} - \boldsymbol{x}^*) \tag{4.42}$$

$$G = G_1 = \frac{1}{4\pi D\alpha|\boldsymbol{x}-\boldsymbol{x}^*|} \tag{4.43}$$

The relation between the distribution of solute sources and sinks $\psi_p(\boldsymbol{x})$, the Green's function, and the solute concentration is given by Equation 4.44. This integral is the time independent form of Equation 4.12 and may also be derived as *t* approaches infinity.

$$C_p(\boldsymbol{x}) = \int_D^0 G_p(\boldsymbol{x} - \boldsymbol{x}^*)\psi_p(\boldsymbol{x}^*)d\boldsymbol{x}^* + G_0 \tag{4.44}$$

When implementing the spatial discretisation, the vessels and tissue region are again discretised into N_v short cylindrical segments and N_t small cuboid regions respectively. With the

removal of time dependency only two of the previous six diffusive interaction matrices remain: G_{pij}^{tt} (N_t x N_t) and G_{pij}^{vt} (N_v x N_t). Two new and necessary diffusive interaction matrices, G_{pij}^{vv} (N_v x N_v) (cm^3 solute/cm^3) and G_{pij}^{tv} (N_t x N_v) (cm^3 solute/cm^3) are created: matrix G_{pij}^{vv} gives the average solute concentration at the surface of vessel of segment *i* resulting from a unit source distributed on the surface of segment *j*, while G_{pij}^{tv} is the mirror of G_{pij}^{vt}.

Elements of G_{pij}^{vv} may be calculated by integrating the Green's function $G(\boldsymbol{x};\boldsymbol{x}^*)$ with respect to **x** and **x*** over the surfaces of appropriate vessel segments. Due to the nature of this system, integration is only needed for the diagonals of the matrix. For off-diagonal elements (which represent the solute concentration at one segment resulting from a unit source at a different segment), element G_{ij}^{vv} may be approximated by evaluating $G(\boldsymbol{x};\boldsymbol{x}^*)$ at the midpoints of two segments.

G_{ij}^{tt} no longer is calculated with Equations 4.18 through 4.30, as many of these formulas were time-dependent. Now G_{ij}^{tt} is simply calculated by taking the average tissue solute concentration in region *i* resulting from a unit source distributed over tissue region *j*. Its off-diagonal elements are approximated in the same manner as matrix G_{pij}^{vv}. G_{ij}^{vt} is now defined as the solute concentration within the tissue at the half-way point of vessel segment *i* from a unit source at the half-way point of tissue region *j*. With these definitions and Equation 4.44, Equations 4.45 and 4.46 are derived to describe the average solute concentration in vessel segments and tissue regions *i*, respectively.

$$C_{p,i}^{v} = \sum_{j=1}^{N_v} G_{ij}^{vv}\phi_j + \sum_{j=1}^{N_t} G_{ij}^{vt}\phi_j + G_0 \qquad for\ i = 1, \dots, N_v \tag{4.45}$$

$$C_{p,i}^{t} = \sum_{j=1}^{N_v} G_{ij}^{tv}\phi_j + \sum_{j=1}^{N_t} G_{ij}^{tt}\phi_j + G_0 \qquad for\ i = 1, \dots, N_t \tag{4.46}$$

Within these two equations, q_j represents the source strength of vessel segment *j* and φ_j represents the source strength of tissue region *j*. A negative value for either denotes a sink as opposed to a source. Constant G_0 is present to account for an arbitrary Green's function. An example of an arbitrary Green's function is the system under a no-flux boundary condition or no boundary conditions imposed. With the infinite domain boundary condition, G_0 is equal to 0.

As with the time-dependent numerical implementation, the concentration of solute in outflowing blood C_p^b must be calculated and related to C_p^v. This is performed using Equations 4.47 and 4.48 below. Equation 4.48 is obtained by integrating Equation 4.49, a variation of Equation 4.41 that focuses on conservation of mass between C_p^b and C_p^v.

$$C_{p,i}^v = C_{p,i}^b - K_i q_i \qquad for\ i = 1, \dots, N_v \tag{4.47}$$

$$C_{p,i}^b = C_{p,i}^{b,0} - \sum_{j=1}^{N_t} q_j \qquad for\ i = 1, \dots, N_t \tag{4.48}$$

$$\frac{dC_p^b}{ds} = -q_p(s) \tag{4.49}$$

Here, $C_{p,i}^{b,0}$ is the intravascular concentration of solute of segment *i* (cm^3 solute/cm^3) and is typically equal to the assumed concentration of solute of an upstream vessel before entering the tissue domain. K is a constant that depends on the solute being examined. Combining Equations 4.45, 4.47, 4.48 gives a set of N_v equations that produce Equation 4.50 below.

$$\sum_{j=1}^{N_v} G_{ij} q_j + G_0 - f^{-1}\left[C_{p,i}^b - \sum_{j=1}^{N_v} q_j\right] + K q_i = -\sum_{j=1}^{N_t} G'_{ij} \phi_j \qquad for\ i = 1, \dots, N_v \tag{4.50}$$

The procedure used to solve this system of equations involves a two-level iterative process. For this method, it is necessary to define the tissue solute levels and vessel sources with initial estimates and calculate preliminary tissue source strengths. The inner iteration scheme is used to compute the source strength of vessel segment *j* for each tissue source strength. The left-hand side of Equation 4.50 is then linearised about the current vessel source strengths, and the resultant linear

system is solved using the biconjugate gradients stabilised method. This gives updated values for the vessel source strengths.

As with the time-dependent algorithm, this procedure is repeated using the updated values until desired convergence is achieved. Outer iteration is utilised to update tissue solute levels from Equation 4.46, which in turn are used to update tissue source strengths. Inner iteration is then repeated, with outer iteration ending after convergence is reached (usually within several steps). Source strengths and solute levels of each vessel segment are solved for simultaneously and consider the dependence of intravascular solute concentration on the upstream source strengths.

4.2.4 Parameter Values

Secomb's work in 2004 had several defined parameters, displayed below in Table 4.1. Most of these parameters are specific to the subjects simulated in that study, particularly the constraints relevant to the network structure (such as domain size and vessel statistics), but the inflow partial pressure of oxygen and the oxygen consumption rate are used in this thesis. Table 4.2 presents a summary of the different boundary conditions examined by Secomb and their impact on hypoxic fraction in tissue. The infinite-domain solution was selected for this work for the reasons stated above. These parameters were used in both the steady-state and time-dependent simulations. For time-dependent simulations, it was assumed that oxygen was supplied to the network at a fixed rate within the time rate input file.

Table 4.1: Table of parameters used by Secomb *et al*., 2004 in his model.

Tissue	Tumour	Brain	Cremaster[a]
Domain Size (μm)	550 x 520 x 320	150 x 160 x 140	1100 x 1000 x 240
Number of Vessel Segments	104	50	295
Total Vessel Length (mm)	7.4	1.84	20.4
Number of Subsegments	517	237	1170
Total Blood Flow to Region (cm^3/s)	1.4×10^{-6}	1.8×10^{-7}	1.25×10^{-6}
Inflow PO_2 (mmHg)	40	50	50
Spacing of Tisse Points (μm)	30	10	30
Number of Tissue Points	2754	3360	10080
Oxygen Consumption Rate ($cm^3O_2(100\ cm^3)^{-1}min^{-1}$)	1.5	14	4, 10
Krogh Diffusion Coefficient for Oxygen ($cm^3O_2cm^{-1}s^{-1}mmHg^{-1}$)	4.2×10^{-10}	6×10^{-10}	9.5×10^{-10}

[a]The computational domain for the Cremaster simulation was reduced to a volume 25% of the surrounding cuboid. See Secomb *et al*., 2004 for further details.

Table 4.2: Boundary condition effect on hypoxic tissue fraction in Secomb *et al*., 2004.

		Pointwise No-Flux Solution	Net No-Flux Solution	Infinite-Domain Solution
Rat Tumour Network (Hypoxic Fraction)	≤ 3 mmHg	17.7%	11.5%	10.0%
	≤ 5 mmHg	25.0%	20.4%	20.3%
Rat Brain Network (Hypoxic Fraction)	≤ 1 mmHg	7.4%	2.2%	1.6%
	≤ 3 mmHg	13.9%	10.2%	10.1%
	≤ 5 mmHg	20.2%	17.9%	18.1%

4.2.5 Motivations for Studying Oxygen

While the assumptions and models presented previously may be generalized to handle any solute, this chapter has specifically concentrated on oxygen despite the fact the focus for this thesis is on gold nanoparticles. Oxygen was primarily studied as a reference with which to further explore solute delivery at these length and time scales while also functioning as a benchmark for computational model accuracy.

Oxygen serves as the ideal validation solute due to the large amount of literature and data publicly available. Over the span of decades precise cerebral oxygen distributions have been

measured through a variety of imaging techniques and over several length and time scales; additionally, the transport physics of oxygen are well-characterized. Critical parameters such as oxygen tissue diffusivity, blood diffusivity, solubility, and consumption rates are well-documented. Parameter sensitivity can thus be isolated from parameter uncertainty. Finally, the numerous studies available provide ample opportunity for model validation. The methods developed here will be compared against the Krogh Cylinder and against work performed by Secomb, though other studies are likely available for further validation.

With that said, there are a variety of differences between the two molecules. For example, oxygen is a much simpler molecule (two covalently bonded oxygen atoms) compared to gold nanoparticles and much smaller because of it. This chemical composition difference greatly affects the mechanics of transport: oxygen bonds to red blood cells during its time in the circulatory system while gold nanoparticles freely move in this system. With regards to the circulatory network, it is designed primarily for oxygen delivery (and other nutrients not as relevant to this thesis), though AuNPs are transported within the same system. This is represented most clearly in the difference in diffusion coefficients: typically in blood, the oxygen diffusion coefficient is on the order of magnitude $1x10^{-6}$ m^2/s (varies with solubility) while gold nanoparticles are 0.1 to $1x10^{-11}$ m^2/s. This difference is substantial, suggesting that the two will display different levels of transport; additionally, other effects such as oxygen-AuNP interactions or AuNP cellular transport may exacerbate this difference. Further analysis of the discrepancy in parameters is presented in Chapter 5.

Direct comparison between oxygen and AuNP distributions is not the goal of this thesis; their normalised concentrations will differ in magnitude and may exhibit different spatial patterns due to consumption versus accumulation. Instead, oxygen validates the methods implemented

within the steady-state and time-dependent models. AuNP simulations represent novel predictions requiring further experimental validation when data become available.

4.2.6 Statistical Synthetic Networks

In Chapter 2, a variety of methods for constructing or reconstructing a capillary bed for modelling purposes was discussed. This thesis utilises the statistical synthetic networks developed by El-Bouri *et al*., 2015 for use in the Green's function method model. In El-Bouri's work, these networks were employed with multi-scale homogenization methods to develop continuum models of blood flow in the human cortex.

The algorithm implemented by El-Bouri was proposed by Su *et al*., 2012. It used a modified spanning tree method (MSTM), where two spanning trees are generated from randomly seeded nodes on a given voxel which then merge to form a random capillary network (El-Bouri *et al*., 2015). The diameters of the capillaries are assumed to be normally distributed in accordance with experimental data taken from Cassot *et al*., 2006. Filters were then applied to remove or add vessels (depending on length) to fit the length distribution of the vessels found in Cassot *et al*., 2006.

The surfaces of the voxel were made symmetrical to impose spatial periodicity. This algorithm was performed for voxels ranging in size of 125-micron to 625-micron: this thesis focuses on two cubes sizes of 375- and 625-micron. Each cube contained inlet boundary nodes on the xy-, xz-, and yz- Cartesian planes; 9 for the 375 cube for a total number of 27 inlet nodes, 25 for the 625 cube for a total of 75 inlet nodes. Inlet node diameters ranged from 3.36 micron to 8.25 micron with average diameter of 6.12 micron for the 375-micron cube while the 625-micron cube displayed a range of 2.61 micron to 9.60 micron with average diameter of 6.29 micron. An example 375-micron cube from El-Bouri *et al*., 2015 is shown below in Figure 4.4.

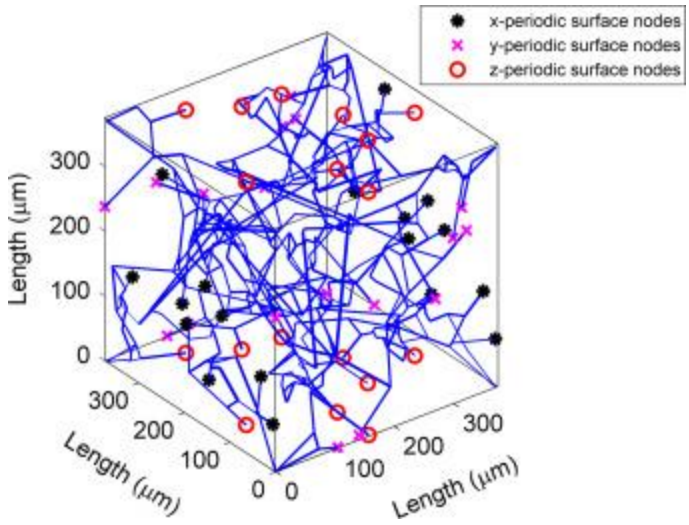

Figure 4.4: Representation of a typical cerebral capillary network, generated in a 375 μm cube. Reproduced with permission from El-Bouri *et al*., 2015.

4.2.7 Pre- and Post-processing

While the data provided by Secomb may be immediately used with his C++ code, the synthetic network data generated in-house had to be restructured to be utilised in the same manner. The data original format was a series of matrices containing values for conductivity (G), vessel radii, vessel connectivity, and vessel lengths that were run through MATLAB code to produce flow data amongst other quantities. With the flow data and vessel connectivity matrix, a text document was then created with MATLAB that held all necessary data and was formatted in the appropriate manner. Any post-processing was performed with MATLAB and Excel to generate the figures presented in Section 4.3.

4.2.8 Conclusions

In these sections, time-dependent and steady-state models were developed to simulate the flow of blood and oxygen delivery in the cerebral microvasculature. For the two Green's function method models, extensive simulation was performed to produce a variety of results for analysis.

The data collected from the two models and the verification of the code will both be presented and discussed in the next section.

4.3 RESULTS

4.3.1 Introduction

Using the methods described above, a variety of simulations were run to test the accuracy of the model when handling a variety of inputs and producing actionable results. First, the algorithm was initialized on a Krogh cylinder and on a rat brain network data set provided by Secomb alongside his C++ code. Then, the code was used to analyse 20 synthetic networks: two larger sets of cubes of size 375 micrometre and 625 micrometre, each with 10 variations. Next, solute parameters were varied and tested in the rat brain network and the synthetic networks. This process was repeated when considering the effects of time dependency on tissue solute levels. Finally, an analysis on the effects of algorithm parameters on tissue solute levels was performed under steady-state conditions.

4.3.2 Steady-State Results

4.3.2.1 Verification of Code

Initial verification of Secomb's code for custom networks was performed for a Krogh cylinder. The Krogh cylinder used here has a diameter of 11.534 micrometres, inlet pressure of 50 mmHg, tissue consumption rate of 0.0025 cm^3 O_2/cm^3 tissue/s, and haematocrit of 0.4. The total cube dimensions in micrometres for the tissue region of interest were 634.913 by 64.165 by 64.165 with spatial discretisation of 100, 20, and 20 tissue points in the x, y, and z directions respectively. The cylinder is centred on the y-z plane and extends into the x dimension. The vessel has 24 nodes, two of which are boundary, and 23 vessel segments. The inlet boundary node is at x = 0 and the outlet node is at x = 634.913. To better visualise the pressure gradients found within the Krogh cylinder, Figure 4.5(b) begins at x = 100 micrometres. The profile of the numerical Krogh cylinder analysis is represented below in Figures 4.5 below.

An analytic solution was also developed to compare against the numerical solution. The analytic solution was computed utilising MATLAB's symbolic solver and Microsoft Excel. A target 5% difference in solutions was desired as a test of the algorithm's validity and accuracy; the percent difference is widely known to depend on input data and discretisation strategy, meaning there is no standard acceptable error (Utku & Melosh, 1984). The selected percent difference was considered to be moderate and appropriate for this model. The analytic solution utilised the same input data as the numerical solution. It was found for each tissue point that the analytic solution was lower than the numerical solution by 4.95% on average. Figure 4.6 illustrates this difference for a selected y and z slice of the cylinder. Oxygen partial pressures were normalised to better display the different solution curves.

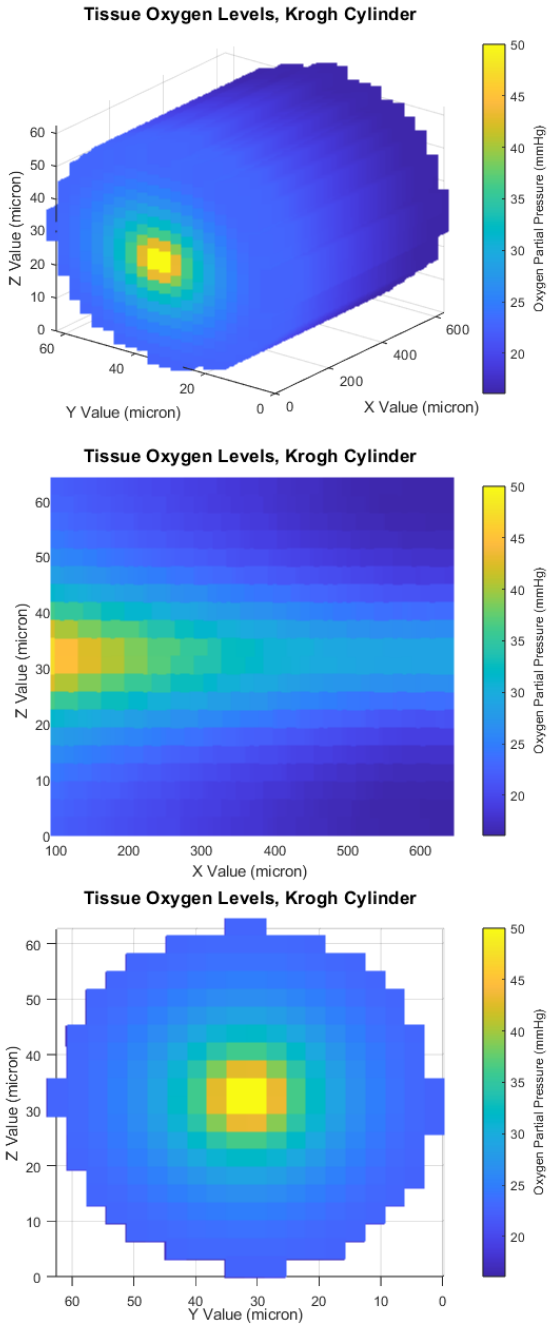

Figures 4.5: Krogh cylinder (a) full cylinder, (b) cross section along y-axis of cylinder centreline and (c) cross section along x-axis of cylinder inlet.

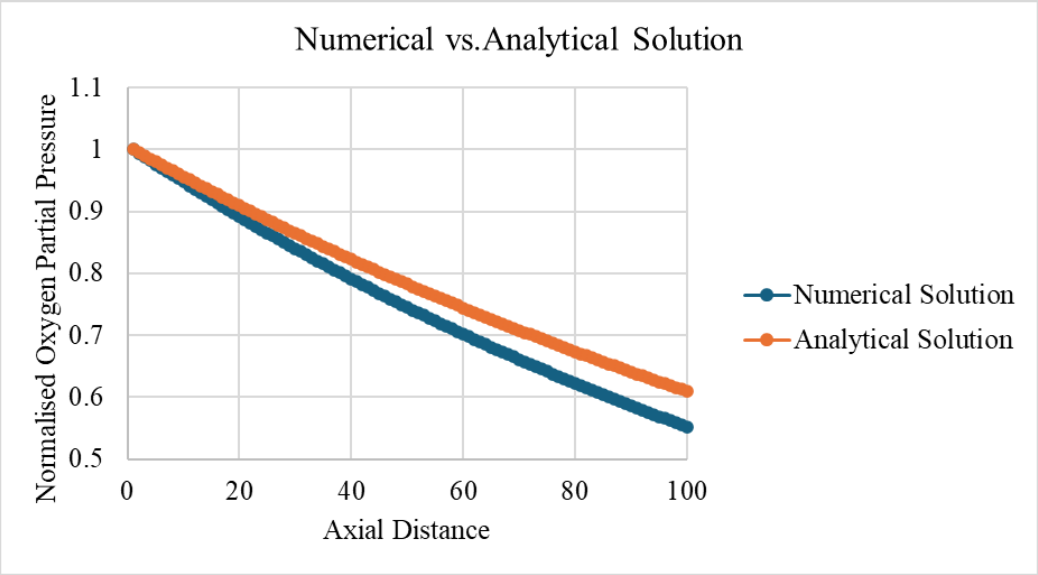

Figure 4.6: Comparison of different solutions for the Krogh cylinder model. Taken at tissue point y = 9 and z =12 across the range of axial tissue points.

4.3.2.2 Secomb Base Cases

Following the Krogh Cylinder, the code's capabilities were explored using an example case provided by Secomb. The example case is publicly available on GitHub and consisted of the parameters found in Table 4.1 and a reconstructed rat brain network. The results of the Secomb example case are products of this thesis and not obtained from his publications. Simulating the rat brain is intended as a benchmark of convergence and comparison to generated synthetic networks. The simulation was performed in five variations. Each run tested for a different tissue oxygen consumption rate, with the five values being 0.002, 0.0025, 0.003, 0.0035, and 0.004 cm^3 O_2/cm^3 tissue/s. These values were selected as 0.002 cm^3 O_2/cm^3 tissue/s is reasonable for a resting rat brain, while the higher values relate to either strenuous activity or disease.

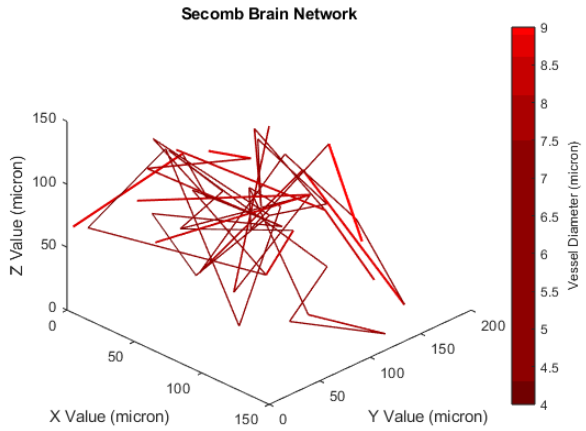

Figure 4.7: Secomb Rat Brain Network

It should be noted that the haematocrit used in this set of simulations was 0.4 not 0.45, as this was the value originally used in Secomb's work. A lower haematocrit value typically leads to an increase in hypoxic regions. Figure 4.8 below demonstrates how as oxygen consumption rate rises within the tissue, the greater the number of tissue nodes classified as hypoxic becomes. A node is defined as hypoxic if its value is under 10 mmHg (Xue *et al*., 2021). These hypoxic regions may be shown to be the furthest from any vessel, as shown in Figure 4.9 below. Figure 4.10 expresses the lowering of tissue oxygen concentration as oxygen consumption rates increases at a selected tissue slice. This particular slice is kept consistent when comparing consumption rates for better evaluation.

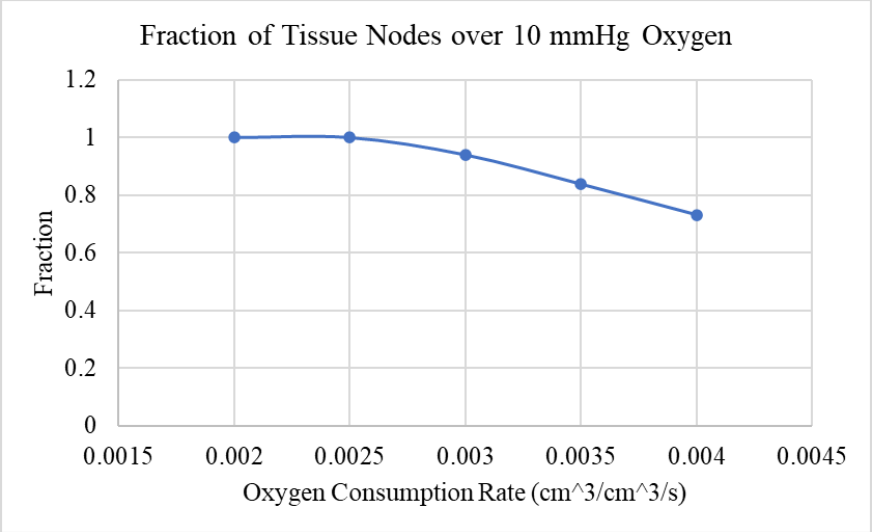

Figure 4.8: Fraction of non-hypoxic tissue for five separate oxygen consumption rates in rat brain tissue taken from Secomb *et al*., 2004.

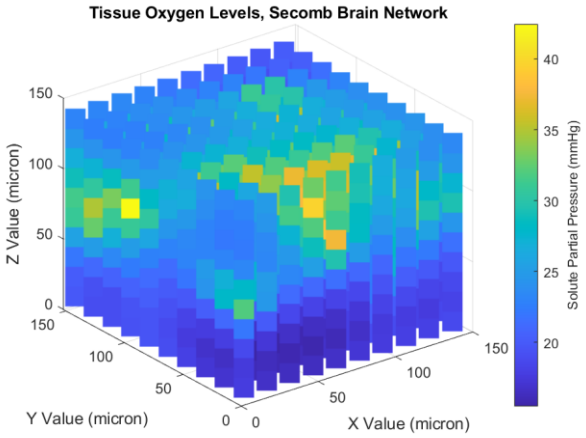

Figure 4.9: Rat brain network used by Secomb, Oxygen Consumption Rate 0.002 cm^3 O_2/cm^3 tissue/s.

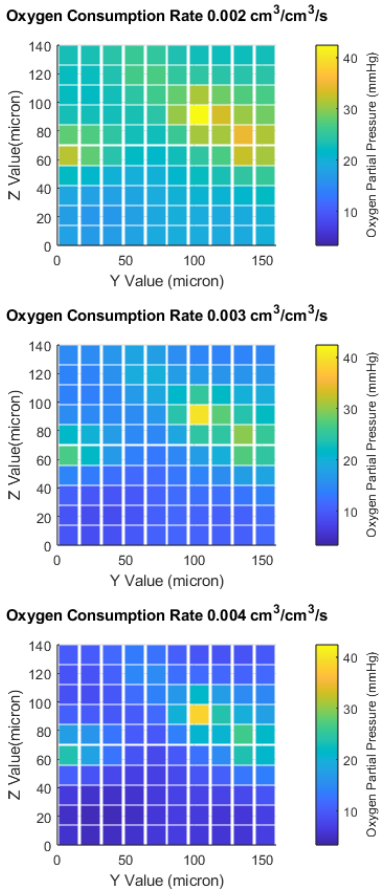

Figure 4.10: Secomb Brain, Selected Slice, Comparison of Oxygen Consumption Rates.

4.3.2.3 El-Bouri Synthetic Networks with Secomb Solute Parameters

The synthetic networks used in this project were originally developed by El-Bouri and utilised in his previous works, most notably in his 2015 work (El-Bouri *et al*., 2015). The networks are formatted as cubic sections of microvasculature tissue that come in two sizes: 375-micron and 625-micron. Example networks are presented below in Figure 4.11 for both sizes. These measurements refer specifically to the length of a cube edge. Within each category of size there are 10 variations of network structure to replicate capillary bed randomness. Tissue oxygen consumption rate for these simulations was chosen to be 0.0006 cm^3 O_2/cm^3 tissue/s as this is the

average for healthy young adults (Clarke & Sokoloff, 1999). This value produced no areas of hypoxia with the tissue cubes, so to better observe the effect of tissue consumption rate on hypoxic fraction extreme rate values of 0.002, 0.0025, 0.003, 0.0035, and 0.004 cm^3 O_2/cm^3 tissue/s were used for each tissue cube.

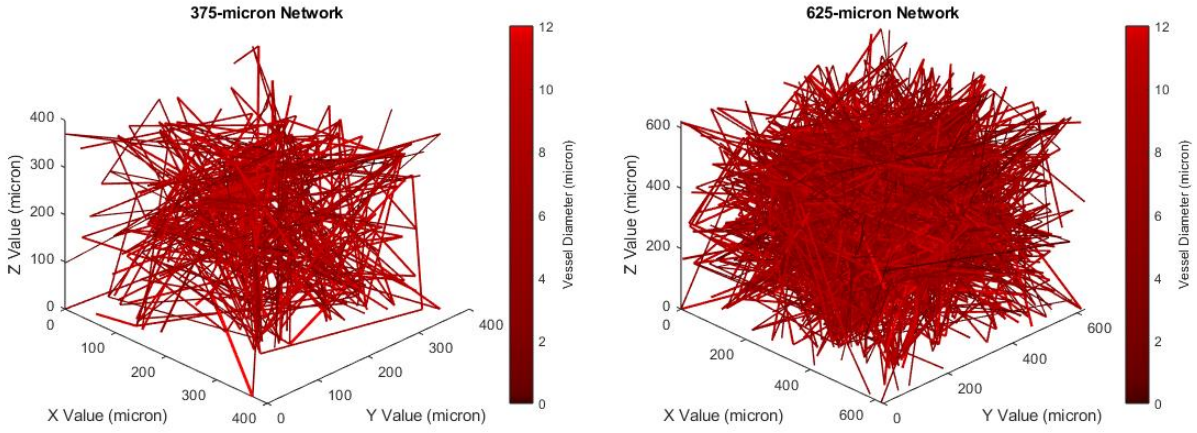

Figure 4.11: El-Bouri Synthetic Networks, 375-micron and 625-micron.

All runs in the synthetic network cases were run with inlet pressure of 27.35 mmHg for the 375 cases and 40.59 mmHg for the 625 cases unless otherwise noted. These values of inlet pressure are discussed later in the section. As previously mentioned, though the effect is negligible, it should be noted that Secomb used a haematocrit of 0.4, while the synthetic networks used a haematocrit of 0.45. Otherwise, the parameters are the same for both Secomb's work and the synthetic networks, shown below in Table 4.3. These parameter values are taken from Secomb *et al*., 2004.

Table 4.3: Model parameters used in the El-Bouri synthetic networks and Secomb networks

Parameter	Value	Units
Total Blood Flow	1.8E-07	cm^3/s
Inlet PO2	50	mmHg
Oxygen Binding Capacity	0.5	cm^3 O_2/cm^3 tissue/mmHg
Effective Solubility of Oyxgen in Blood	3.10E-05	cm^3 O_2/cm^3 tissue/mmHg
D*α	6.0E-10	cm^3 O_2/cm/s/mmHg

Typical visual representations of the tissue oxygen levels are presented below in Figures 4.12 and 4.13, with images of the full cube shown. Figure 4.12 shows the 375-micron network, while Figure 4.13 shows the 625-micron cube. Figures 4.14 and 4.15 present these data quantitatively, where Figure 4.14 plots the average tissue solute level (in mmHg) for all network variations taken at a single oxygen consumption rate and Figure 4.15 depicts the variation in standard deviation across the same parameters. Oxygen consumption rate is set to 0.0006 cm^3 O_2/cm^3 tissue/s, inlet pressure was set to 50 mmHg, and the tissue was discretised at 25 tissue points per xyz direction. The effect of identical inlet pressures on tissue spaces of different sizes is discussed in the results section.

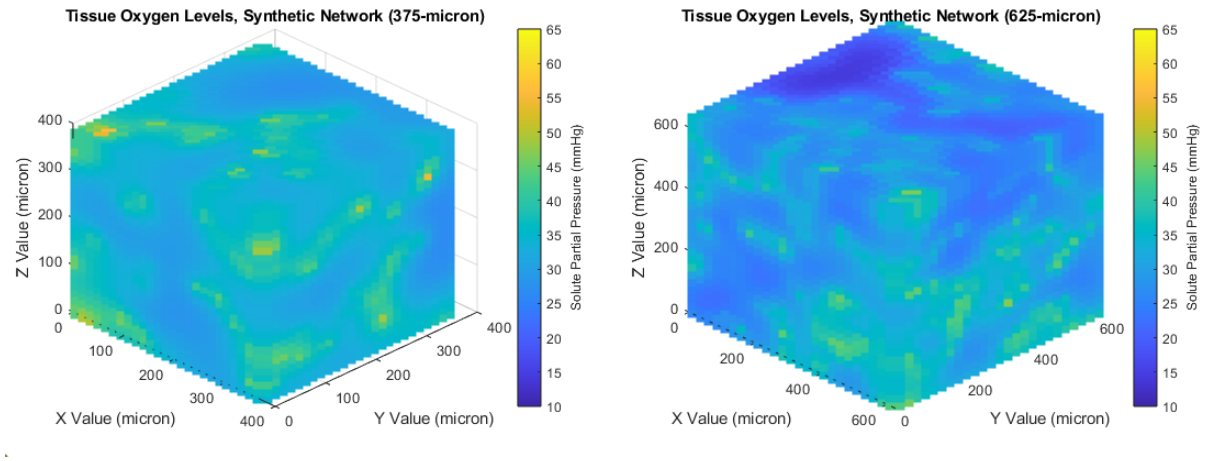

Figures 4.12 & 4.13: Visual representation of tissue oxygen levels in El-Bouri Synthetic Networks, 375-micron (Figure 4.12) and 625-micron (Figure 4.13).

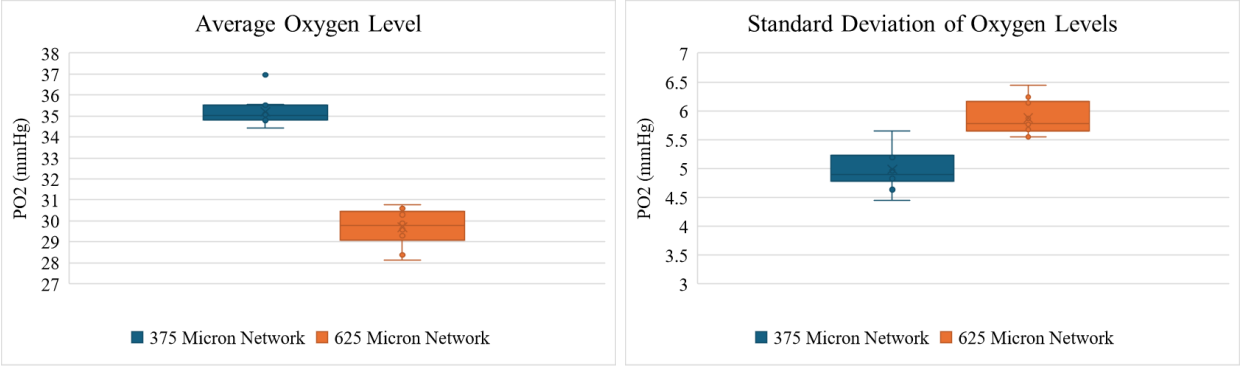

Figures 4.14 & 4.15: Average (Figure 4.14) and standard deviation (Figure 4.15) of tissue oxygen levels for each synthetic network. The variability here is the range of average tissue oxygen levels across all networks of a certain size.

The effect of different tissue oxygen consumption rate was also analysed. Figures 4.16 through 4.18 below show the impact of varying oxygen consumption rate on the level of oxygen in the tissue with Figure 4.17 quantifying these results in a line plot. This figure is taken at a selected tissue slice height that is kept constant for visual comparison. Additionally, the fraction of tissue that is hypoxic is calculated for the synthetic networks as a function of tissue oxygen

consumption rate as was done for Secomb's networks, shown below in Figure 4.18. These results will be discussed in greater detail below.

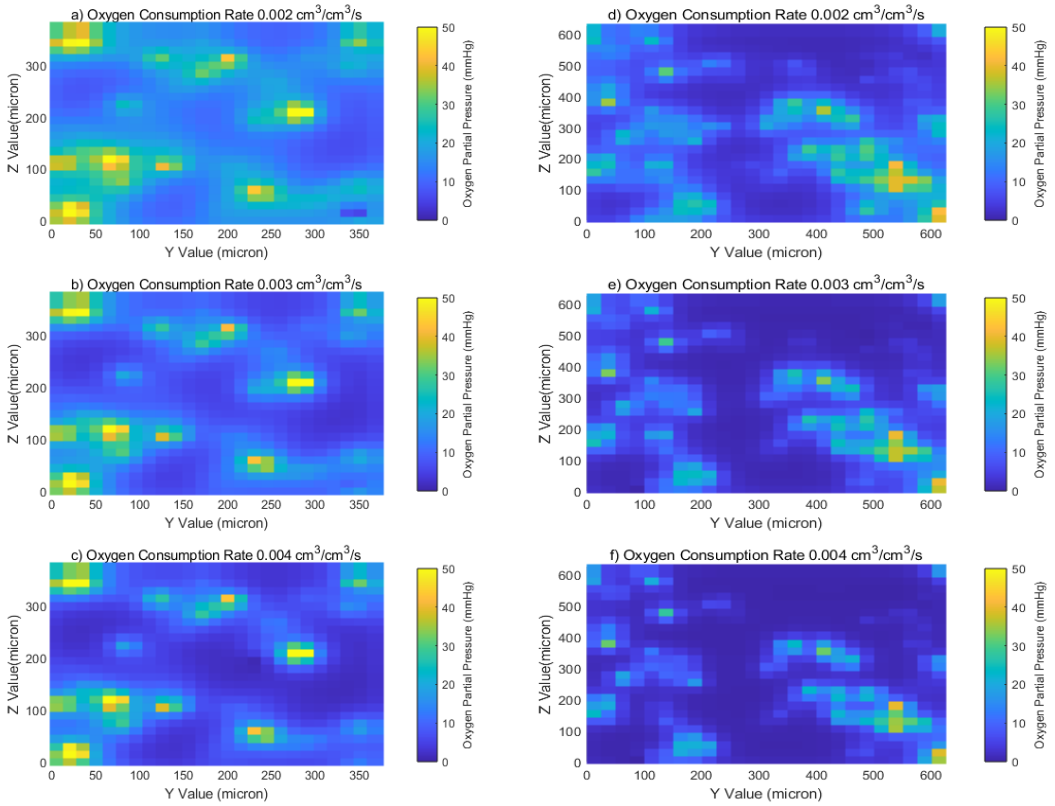

Figure 4.16: Comparisons of different oxygen consumptions at a selected slice for (a) 375 micron network, 0.002 cm^3 O_2/cm^3 tissue/s, (b) 375 micron network, 0.003 cm^3 O_2/cm^3 tissue/s, (c) 375 micron network, 0.004 cm^3 O_2/cm^3 tissue/s, (d) 625 micron network, 0.002 cm^3 O_2/cm^3 tissue/s, (e) 625 micron network, 0.003 cm^3 O_2/cm^3 tissue/s, and (f) 625 micron network, 0.004 cm^3 O_2/cm^3 tissue/s.

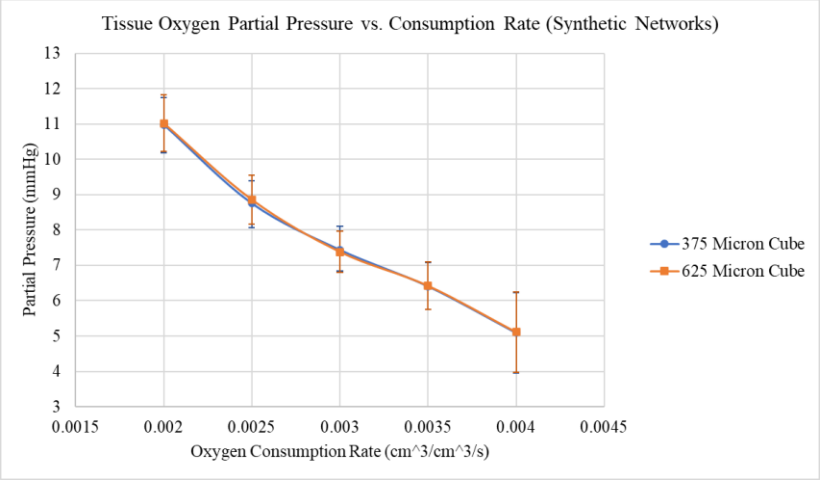

Figure 4.17: Average tissue oxygen partial pressure vs consumption rate. Calculated for the 375- and 625-micron capillary networks.

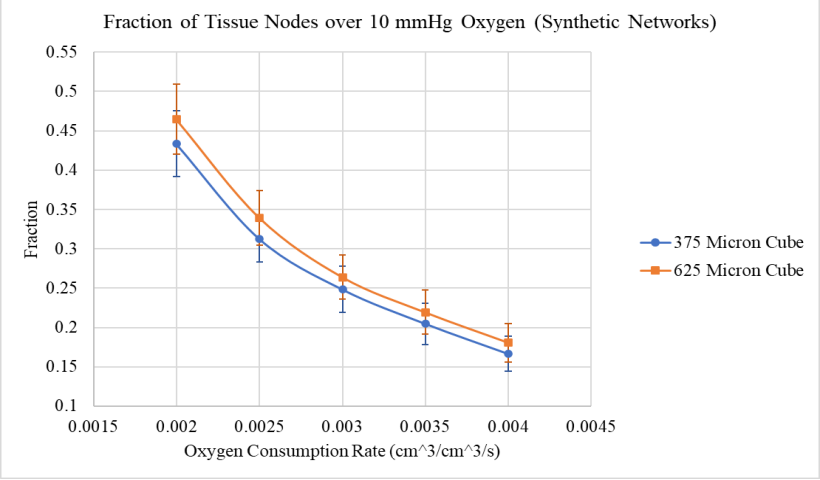

Figure 4.18: Fraction of tissue that is hypoxic for varying oxygen consumption rate. Calculated for the 375- and 625-micron capillary networks.

As previously discussed, the simulations were performed at an inlet pressure of approximately 27 mmHg for the 375-micron cube and 41 mmHg for the 625-micron cube. These pressures showed a significant fraction of hypoxic tissue (greater than 10%) that would normally cause lasting damage in a human brain, so several simulations were run on a 375-micron cube with

increasing inlet pressures in order to explore the impact of this variable. Figure 4.19 below displays the relationship between tissue oxygen pressure (and by extension non-hypoxic fraction) and inlet pressure.

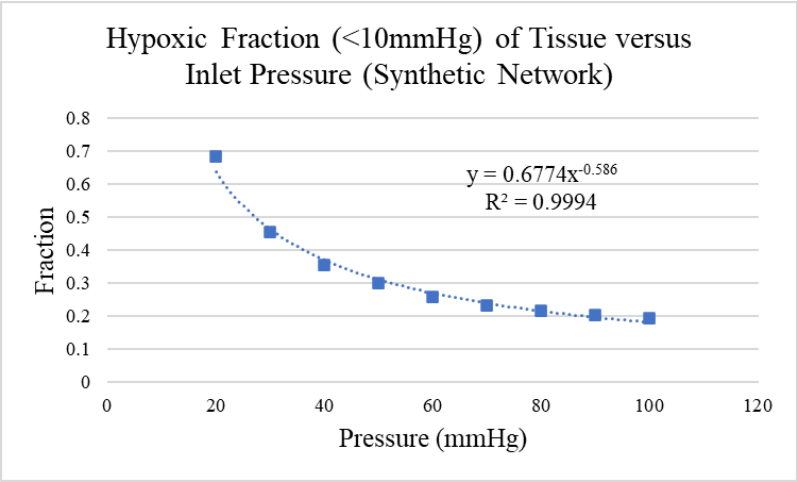

Figure 4.19: Fraction of non-hypoxic tissue versus network inlet pressure, taken at oxygen consumption rate of 0.002 cm^3 O_2/cm^3 tissue/s for the 375-micron synthetic network.

4.3.2.4 Analysis of Spatial Discretisation and Error Tolerance

This section examines the sensitivity of tissue oxygen partial pressure (and its spatial variability) to two computational parameters: error tolerance and spatial discretisation. The analysis was conducted on both the 375-micron and 625-micron tissue cubes. All simulations employed an oxygen consumption rate of 0.0006 cm^3 O_2/cm^3 tissue/s and an inlet partial pressure of 50 mmHg. Partial pressure variability is quantified as the standard deviation of partial pressure values throughout the synthetic network.

The error tolerance governs the convergence criterion for the iterative Green's function solution of tissue partial pressure. The iterative process terminates when the relative change in partial pressure between successive iterations falls below this threshold. Secomb's implementation recommends an error tolerance range of 1×10^{-5} to 1×10^{-4}. To validate this recommendation and

assess potential improvements or computational trade-offs, a broader range spanning 1×10^{-6} to 1×10^{-3} was also examined.

The tissue domain is discretised into a three-dimensional Cartesian grid for numerical solution via a Green's function method. The baseline simulations previously employed 25 tissue points in each spatial dimension (25×25×25 grid, including boundary tissue points). For the 375-micron cube, discretisations of 10, 20, 30, 40, and 50 points per dimension were employed. For the 625-micron cube, 15, 20, 30, 40, and 50 points per dimension were examined; the lower bound was set to 15 rather than 10 due to convergence failure at the coarser resolution.

Figures 4.20 and 4.21 below present the relationship between error tolerance and both mean tissue partial pressure and partial pressure variability for the 375-micron domain. The results demonstrate that both metrics remain remarkably stable across the range 1×10^{-6} to 1×10^{-4}; however, at the larger tolerance of 1×10^{-3}, a systematic deviation emerges in both mean pressure and variability, indicating insufficient convergence precision. Generally, as the error tolerance increases, both mean pressure and variability decrease. Figures 4.22 and 4.23 show analogous results for the 625-micron domain.

Figures 4.24 and 4.25 illustrate the influence of discretisation density on oxygen distributions within the 375-micron cubes. Mean tissue partial pressure exhibits a clear asymptotic behaviour, with values converging as grid density increases beyond approximately 30 points per dimension. Partial pressure variability similarly stabilises at higher discretisations, though the convergence pattern differs slightly, suggesting that higher-order spatial moments require finer resolution to achieve numerical stability. Figures 4.26 and 4.27 present corresponding results for the 625-micron cubes. The convergence characteristics mirror those observed in the smaller cube

size, with stabilisation occurring at similar grid densities. Unlike error tolerance, as the number of tissue points per dimension increases, mean pressure and variability also increase.

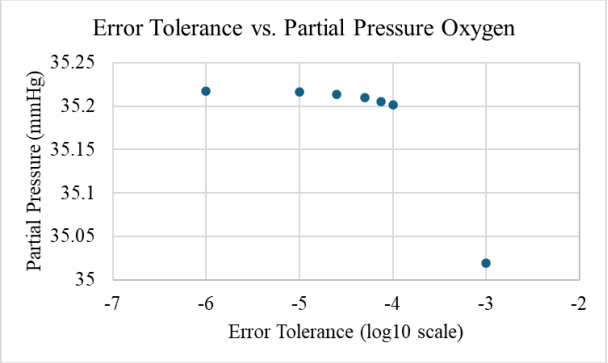

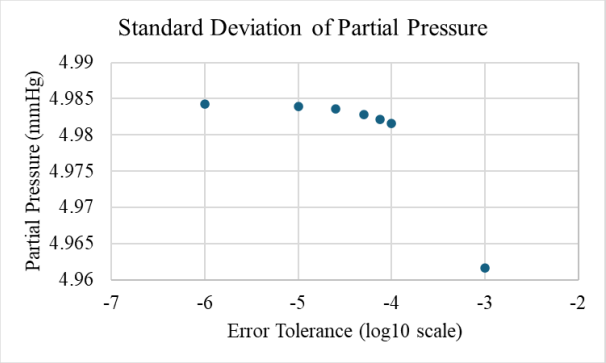

Figures 4.20 & 4.21: Average tissue patrial pressure of oxygen and average partial pressure variability vs. error tolerance. Performed on 375-micron cubes.

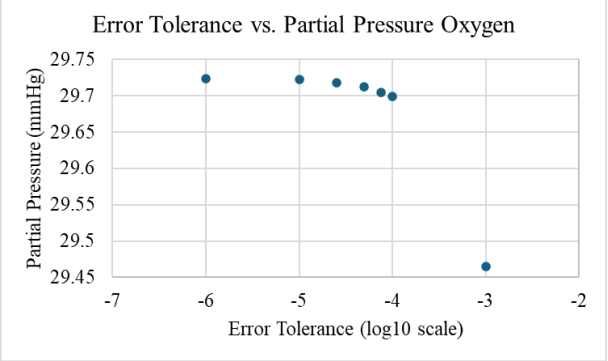

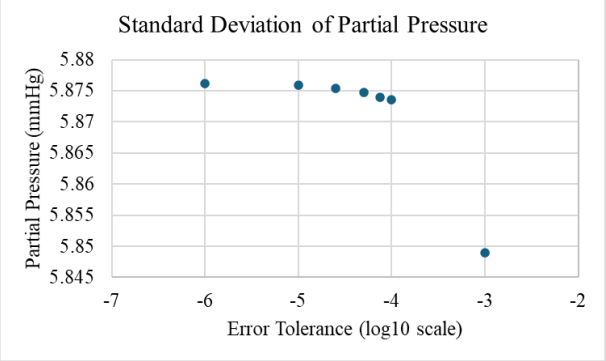

Figures 4.22 & 4.23: Average tissue patrial pressure of oxygen and average partial pressure variability vs. error tolerance. Performed on 625-micron cubes.

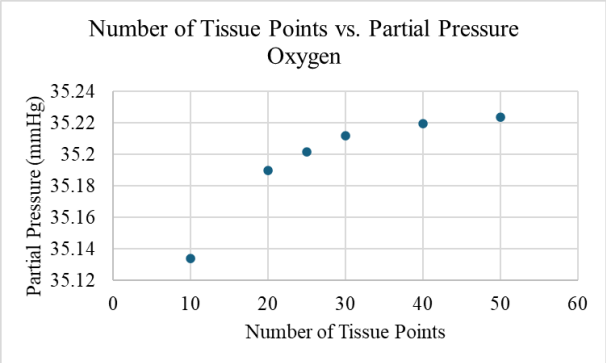

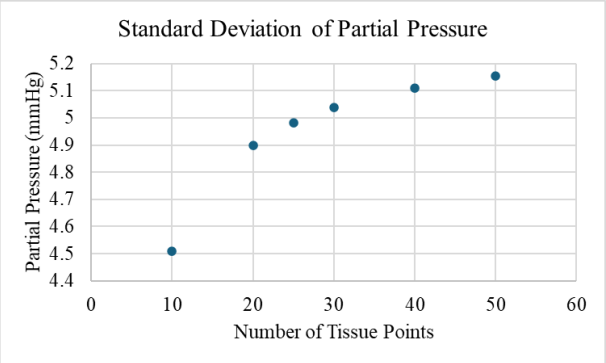

Figures 4.24 & 4.25: Average tissue patrial pressure of oxygen and average partial pressure variability vs. number of tissue points in discretisation. Performed on 375-micron cubes.

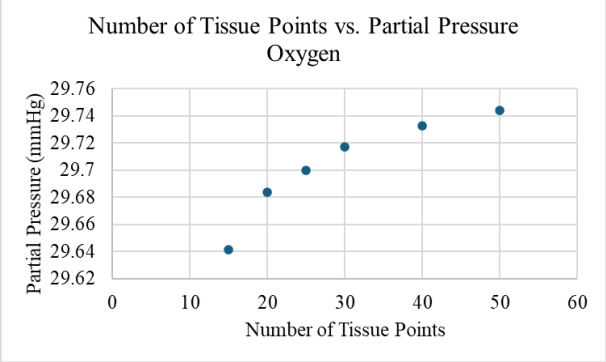

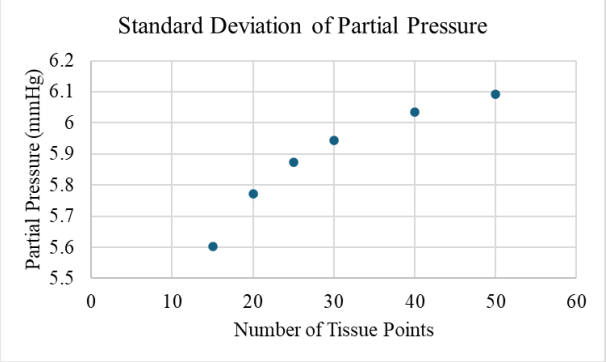

Figures 4.26 & 4.27: Average tissue patrial pressure of oxygen and average partial pressure variability vs. number of tissue points in discretisation. Performed on 625-micron cubes.

4.3.3 Time-Dependent Results

4.3.3.1 Secomb Base Cases

For the time-dependent case of oxygen delivery, the reconstructed rat brain network was again simulated using this model with Table 4.1 parameters. As with the steady-state model, the reconstructed rat brain simulation was performed as a benchmark of code convergence and comparison to generated synthetic networks.

The addition of time into the simulations does require new parameters to be set: the range of time, the time step within that range, and the input nature of the solute or solutes (in this instance

oxygen). The input nature described the influx of simulated solutes into capillary network and this influx behaviour over the range of time that was modelled. The input nature came in three options: zero, fixed, or variable. The zero-input option is a single dose of solute concentration at time (t) = 0 seconds. After t = 0 s, no more of that solute is added to the system. Fixed input is the opposite: within the specified time range, solute is added to the system at a constant value equal to the dose at time = 0 seconds. The final option, variable, allowed the user to specify solute concentration input as a function of time. As oxygen is ideally constantly supplied to the brain (at least in healthy, living individuals), the fixed input option was used for this section of the thesis.

The simulations below were performed for a time range of 1 to 400 seconds with two different time steps: for the range of 1 to 40, the time step was 1 second, and for the range of 40 to 400, the time step was 10 seconds. This time step discretisation scheme was selected so that the highly transient time following solute introduction into the system could be accurately modelled with small time steps and computational expense could be limited for later times once the simulation approached steady state. Simulations were performed for oxygen inlet pressure of 50 mmHg and oxygen consumption of 0.0025 cm^3 O_2/cm^3 tissue/s. Haematocrit was again set to 0.4 for the rat brain capillary network.

The results of this validation are shown in Figures 4.28 through 4.31 below. Figures 4.28 through 4.30 display the spatially averaged tissue partial pressure of oxygen within the tissue over time, with Figures 4.28 and 4.29 being line plots over the entire time range and Figure 4.30 visually comparing a slice of tissue at specific time steps. Figure 4.31 is the hypoxic fraction of the tissue as a function of time.

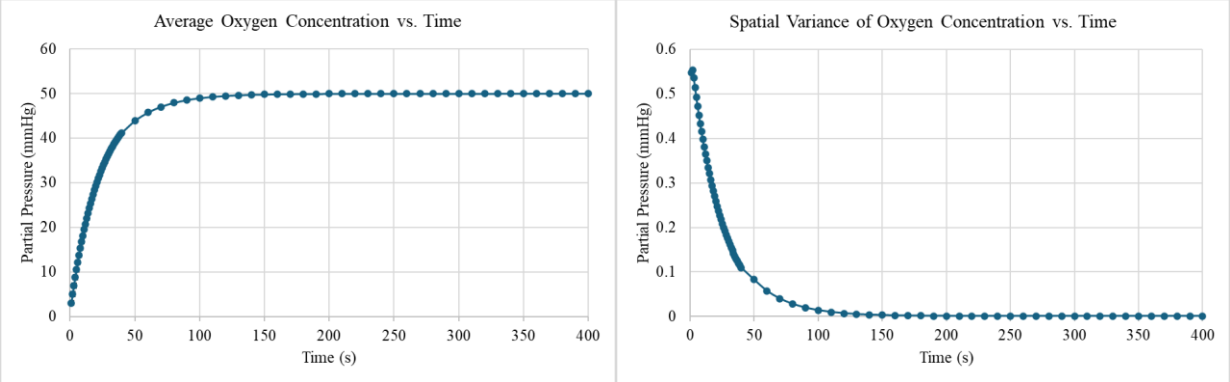

Figures 4.28 & 4.29: Line plots comparing oxygen concentrations (Figure 4.28) and spatial variance (Figure 4.29) in Secomb rat brain tissue for a time span of 1 to 400 seconds.

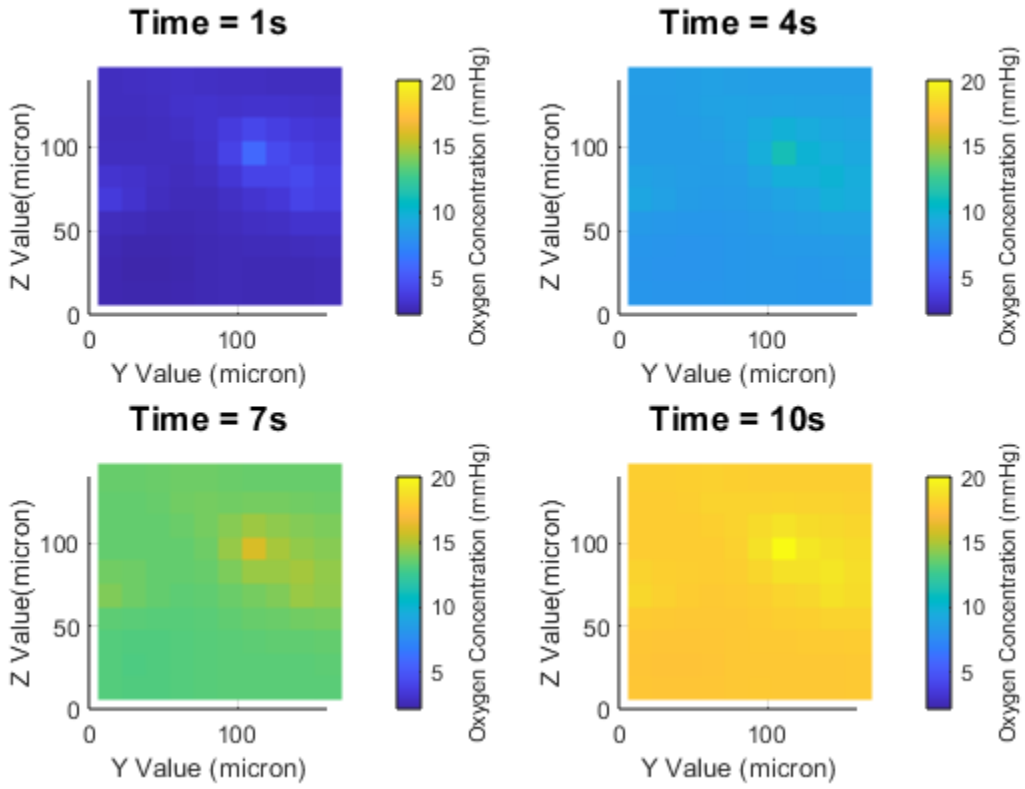

Figure 4.30: Selected slice of Secomb rat brain tissue for four separate times.

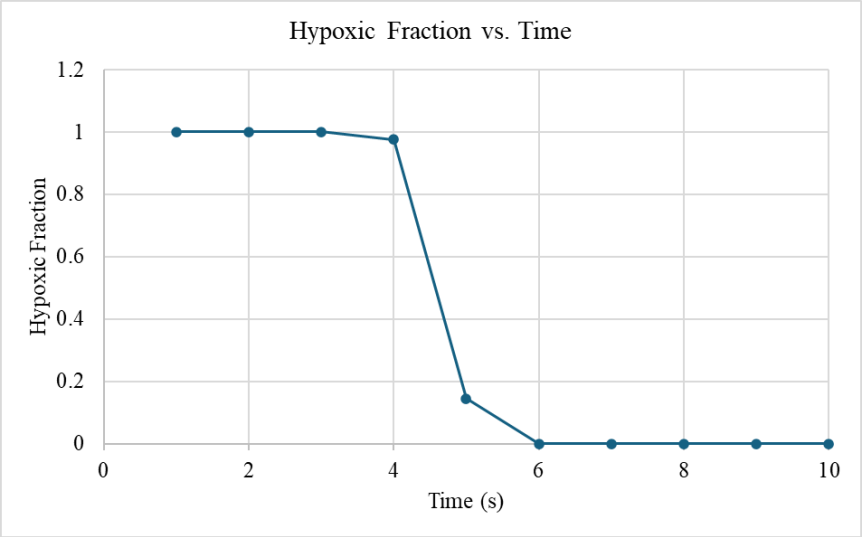

Figure 4.31: Fraction of hypoxic tissue in rat brain tissue taken from Secomb *et al.*, 2004.

4.3.3.2 El-Bouri Synthetic Networks with Secomb Solute Parameters

The synthetic networks used in this section are identical to the ones used previously in the steady-state model. The networks are formatted as cubic sections of microvasculature tissue that come in two sizes: 375-micron and 625-micron. Tissue oxygen consumption rate for these simulations was chosen to be 0.0006 cm^3 O_2/cm^3 tissue/s as this is the average for healthy young adults (Clarke and Sokoloff, 1999). As previously mentioned, this value produces no areas of hypoxia at steady-state; this value is still used, however, as hypoxic regions will appear as the system approaches steady state due to having no oxygen in the system. All runs in the synthetic network cases were simulated with an inlet pressure of 50 mmHg and haematocrit of 0.45. Otherwise, all other parameters remain the same and may be revisited in Table 4.3.

The results of these simulations are shown in Figures 4.32 through 4.35 below. Figure 4.32 is a visual representation of a 375-micron cube over several time steps for a selected tissue slice. Figures 4.33 and 4.34 display the spatially averaged tissue partial pressure and the partial pressure variance of oxygen within the tissue over time for 375- and 625-micron networks. Figure 4.35

displays the hypoxic fraction of the tissue as a function of time over the time range where changes occur.

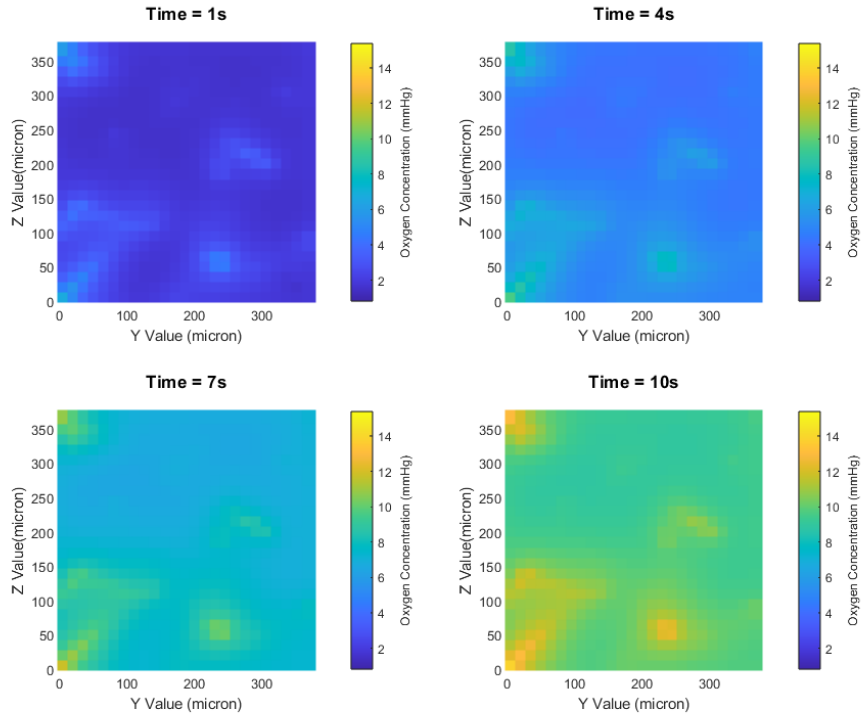

Figure 4.32: Visual comparison of oxygen concentrations in a 375-micron El-Bouri synthetic network for four different times.

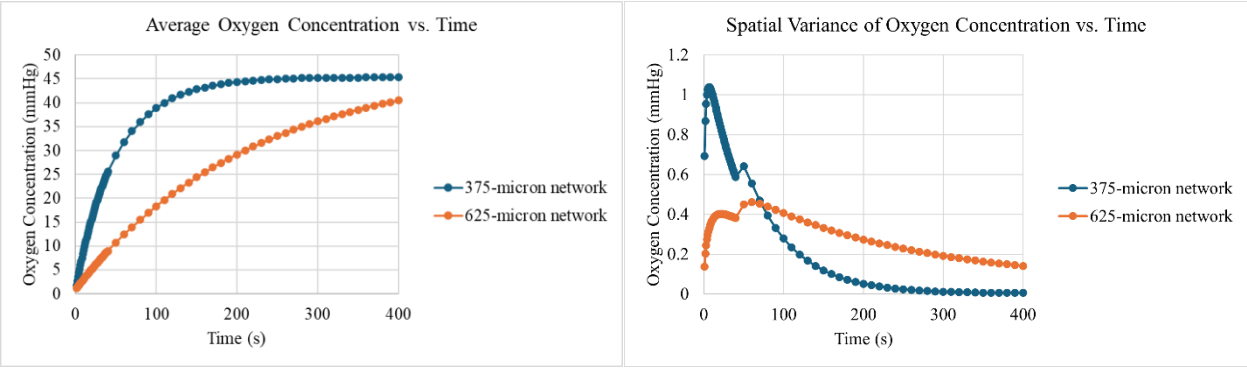

Figures 4.33 & 4.34: Line plots comparing oxygen concentrations (Figure 4.33) and spatial variance (Figure 4.34) in all El-Bouri synthetic networks for a time span of 1 to 400 seconds. Each network is spatially averaged, then all spatial averages of a certain size are averaged together.

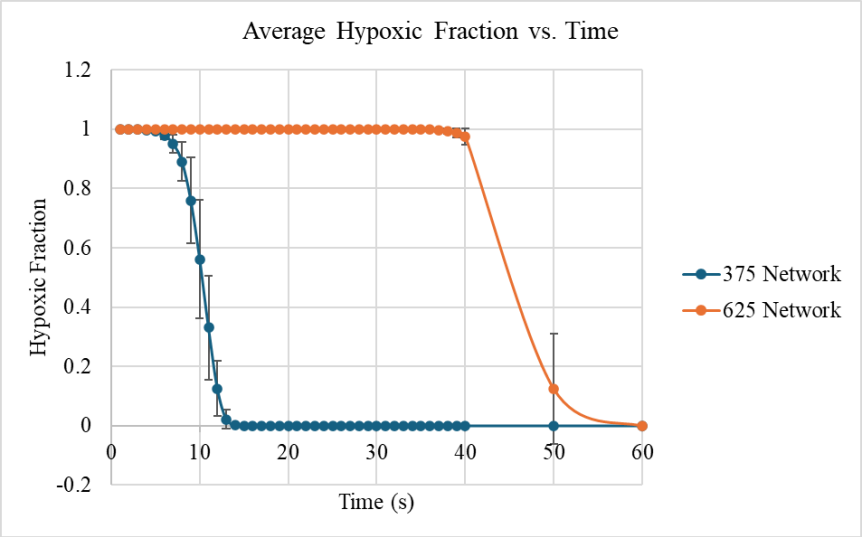

Figure 4.35: Fraction of tissue that is hypoxic for El-Bouri 375- and 625-micron capillary networks.

4.3.3.3 Analysis of Temporal Discretisation

Previously, the effects of error tolerance and spatial discretisation on the reported partial pressure of oxygen were examined. The spatial discretisation definitively influenced the numerical solution to the oxygen transport problem; it was thus assumed that time discretisation would also impact expected tissue partial pressures of oxygen. A series of time steps was conducted employing time steps of 1, 2.5, 5, 7.5, 10, and 40 seconds on 375-micron and 625-micron tissue domains. Oxygen consumption rate and inlet partial pressure were kept at continuous values of 0.0006 cm^3 O_2/cm^3 tissue/s 50 mmHg respectively. The temporal behaviour of tissue oxygenation under these varying discretisation schemes is presented in Figures 4.36 and 4.37 below.

Analysis of the results reveal that while each time step size simulation ultimately converges to a steady-state value of approximately 50 mmHg, the temporal trajectories tend to produce lower tissue concentrations during the transient approach to steady-state. Furthermore, simulations employing a coarser time discretisation demonstrate elevated spatial variability in oxygen

distribution throughout the tissue domain during transient phases. It is hypothesised that this discrepancy results from the inability to fully resolve the numerical solution with coarser time discretisation, amplifying errors within the Green's function method.

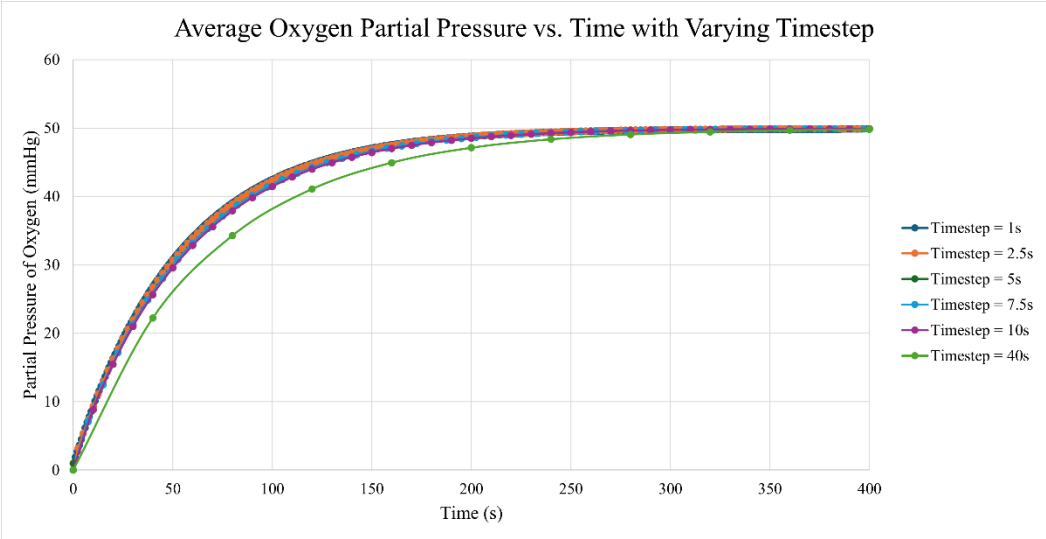

Figure 4.36: Average tissue partial pressure variability curves resulting from increasing time step size.

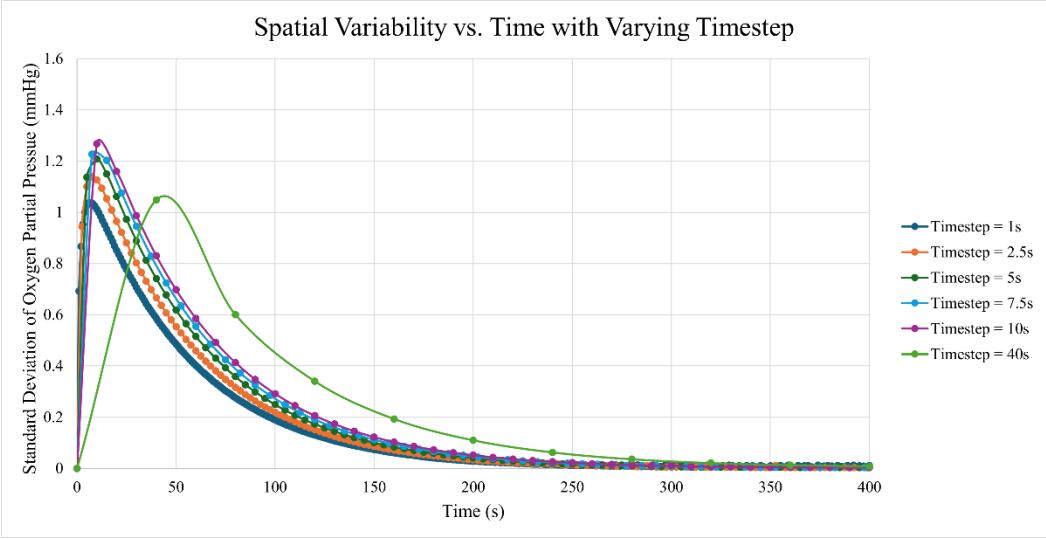

Figure 4.37: Average tissue partial pressure spatial variability of oxygen curves resulting from increasing time step size.

4.3.4 Conclusions

A Green's function model was successfully developed and simulated a variety of oxygen partial pressure data over several types of capillary networks. The results above are a valuable computational benchmark for accurately modelling nanoparticle delivery within the microvasculature and will tie in directly with the work presented in Chapter 5. The conclusions generated here have implications of their own and will be discussed in greater detail, as well as the validity of the underlying assumptions, in the following section.

4.4 DISCUSSION

4.4.1 Introduction

In the previous sections, a capillary blood flow model was presented that utilised a Green's function method and described solute delivery to brain tissue. Due to the complex nature of solute transport, a variety of simulations were conducted to develop a greater understanding of the impact of several quantities on the system. In this section, these simulations are analysed and compared in order to improve the model for future work with nanoparticle delivery

4.4.2 Code Verification

An important aspect of this chapter has been testing and verification of the Green's function method to determine how applicable this model will be for other networks. The two verification cases mentioned in this report are the Krogh cylinder and rat brain tissue provided by Secomb in conjunction with his open-source C++ code. The results of both were presented in the previous section.

For the Krogh cylinder, the important aspect of this verification was to determine the effectiveness of the Green's function method model on a simple, artificial network for validation purposes. The Krogh cylinder is a linear capillary vessel and is directly derived from Fick's laws of diffusion in their simplest form; Figure 2.5, shown previously, depicts a common analysis of

the Krogh cylinder. It is expected from simulations of a Krogh cylinder that similar results would be observed: it is found to be true in this case.

Figure 4.5 demonstrates that oxygen partial pressure exhibits a characteristic radial decay from the capillary wall and an axial decline from the inlet. This spatial distribution pattern is visually consistent with established findings in the literature. It should be noted that the selected input parameters precluded the formation of hypoxic regions within the tissue domain in the numerical solution.

To properly validate the numerical solution beyond qualitative visual comparison, an analytical solution of the Krogh cylinder model was computed. Comparative analysis revealed that the analytical solution consistently overestimated oxygen concentration, especially further along the capillary, with tissue points exhibiting an average percent difference of 4.95% above the numerical solution. This quantitative discrepancy suggests that the numerical predictions may underreport the true physiological values, though it should be noted that the analytical solution may not consider certain physiological phenomena (such as tissue receiving oxygen from multiple vessel segments) that the Green's function numerical solution does.

While a zero percent difference would represent an ideal outcome, such perfect agreement between numerical and analytical solutions is rarely achievable in practice. Consequently, an acceptable tolerance threshold of 5% was established prior to numerical solution analysis. The observed deviation of 4.95% falls just below this acceptable value, demonstrating that the numerical model achieves a high degree of accuracy and is fit for purpose.

It should be acknowledged that further refinement of the numerical model remains possible. Errors inherent to Green's function methods typically arise from multiple sources. Examples include the effects of discretisation (examined in greater detail in subsequent sections),

accumulation of rounding errors during computation, inaccuracies introduced through data manipulation procedures, and uncertainties in the input parameters themselves. Each of these error sources contributes to the total solution error (Utku & Melosh, 1984). A comprehensive investigation of these individual error components would be necessary to achieve further model improvement.

The second set of verification and benchmark simulations involved Secomb's reconstructed brain tissue samples and parameters. The focus of these solutions was on numerical artefact detection for a standardised publicly available dataset; direct error analysis was not performed as it was for the Krogh cylinder. These simulations ran on a series of parameters that differed slightly from the ones used for the synthetic networks and were run under steady-state and time-dependent conditions. A summary of these parameters may be found in Table 4.1. Compared to the Krogh cylinder, the steady-state simulations more accurately demonstrated capillary bed behaviour by having a full 3D vessel structure. The presence of multiple vessels allows for a single tissue point to potentially have more than one source of oxygen, which would increase oxygen tissue concentration as more oxygen diffuses towards that point.

Figures 4.9(a) and 4.9(b) show that the microvasculature and surrounding tissue at steady-state are heterogenous in nature and that tissue solute (in this case oxygen) is in its highest concentration around the vessels and decreases as distance from vessels increases. This was also the first instance in which tissue consumption rate of oxygen was first varied and observed. It was found that as consumption rate increased, the solute level within the tissue decreased. Considering that inlet pressure and other variables were kept constant, this is logical: the tissue is consuming solute at a rate quicker than may be supplied by the microvasculature. This may be directly seen in Figure 4.10 in a selected tissue slice, and the hypoxic fraction is shown to increase in Figure 4.8.

Figures 4.28 through 4.31 show the effect that time has on the microvasculature and surrounding tissue. Under time-dependent conditions, the oxygen concentration is heterogenous in nature just like in steady-state conditions. Oxygen concentration is at its highest around the vessels and decreases as distance from vessels increases; this effect persists regardless of the time step, though the concentration magnitudes increase as time increases. As the input of oxygen into the tissue is fixed, it is expected that the concentration will approach a steady-state value: in this case, 45 mmHg. Figure 4.28 additionally demonstrates that as time increases, the spatial variance of oxygen decreases as the molecule fully diffuses throughout the entire system.

Figure 4.31 plots the hypoxic fraction versus time. It is expected that the hypoxic fraction starts close to 1, as at time = 0 seconds there is no oxygen within the system. The hypoxic fraction does rapidly decrease within seconds, starting at around t = 3 seconds and reducing to almost 0 at t = 7 seconds. This physically makes sense: the rat brain tissue voxel was relatively small (150x160x140 micron) with high inlet pressure, allowing oxygen to diffuse quickly through brain tissue. The larger capillary networks (with inlet pressure held constant) will therefore produce less oxygen perfusion over time and subsequently a prolonged decrease in hypoxic fraction.

4.4.3 Steady-State Cases

The next set of experiments presented here utilise synthetic networks originally developed by El-Bouri. As previously discussed, synthetic networks are useful in a study such as this due to the fact they replicate real life networks on a statistical level, not requiring the lengthy process of acquiring and preparing biological samples for study. A total of 20 base simulations were performed: ten 375-micron networks, and ten 625-micron networks. The networks within each group used the same parameters but differed in vessel node locations and connectivity, statistically remaining similar but displaying different geometries when analysed for results.

Each of these twenty simulations was then repeated with an increased tissue consumption. It was found for these increased tissue consumption simulations that the hypoxic fractions within these simulations were much higher than that in the Secomb verification: 71.66% on average for the synthetic networks versus 9.82% for Secomb's. This was found to be associated with tissue inlet pressure and was thus also examined in another set of simulations.

Temporarily ignoring lower tissue oxygen levels, these simulations behaved in a manner like that of the verification cases: the tissue oxygen levels were heterogenous at this length scale, and increasing the tissue consumption rate saw the same decrease in tissue oxygen levels. With the addition of several more samples, the statistical nature of the synthetic networks could also be analysed. Across all samples, the tissue oxygen level average and standard deviation were plotted in box-and-whisker plots in Figures 4.14 and 4.15. It may be demonstrated from these figures that individual synthetic networks display heterogeneous behaviour.

Comparison of Figures 4.14 and 4.15 reveals that the 625-micrometre tissue cube demonstrated significantly lower average oxygen partial pressure and increased spatial variance compared to the 375-micrometre cube under identical simulated conditions. This phenomenon arises directly from the coupling of Poiseuille's law (Equation 3.15) with the mass balance equation (Equation 4.1), which together govern oxygen transport dynamics in microvascular networks. This coupling relates the dependence of oxygen delivery to volumetric blood flow rate (mass balance), which is itself proportional to the pressure gradient per unit length (Poiseuille's law). When a constant pressure differential is maintained across tissue cubes of differing dimensions, the larger tissue cube exhibits a reduced pressure gradient per unit length, resulting in diminished flow rates and consequently impaired oxygen perfusion to the tissue. This relationship imposes a critical

constraint on tissue and organ size: the ratio of driving pressure to characteristic length scale must exceed a minimum threshold to ensure adequate oxygenation and prevent hypoxic injury.

The inlet pressure of 50 mmHg employed in these simulations was determined from the pressure analysis presented in Figure 4.19. It is demonstrated that the relationship between inlet pressure and tissue oxygen level is a power law, with the fitted equation having an R^2 value of 0.9994 and displaying lower hypoxic fraction as the pressure increases. This value is taken from Table 4.1 and compared against Figure 4.18 as well as other literature sources (Secomb *et al*., 2004; Xue *et al*., 2021). It is normal for the inlet pressure to range from 36 mmHg to 66 mmHg. This analysis was performed solely for the 375-micron cube.

While the inlet pressure of 50 mmHg is appropriate for the 375-micron tissue cube size, the larger 625-μm tissue cubes would theoretically require higher inlet pressures to compensate for the increased diffusion distances and reduced pressure gradients inherent to their geometry and length scale. The observed reductions in both average solute concentration (whether oxygen or gold nanoparticles) and the increases in spatial variance for the larger cube are artefacts of maintaining equivalent inlet pressures.

Tissue consumption rate was also shown to impact the amount of oxygen within the tissue. The oxygen transport behaviour due to varying consumption within the synthetic networks demonstrated nearly identical behaviour to that found in the rat brain network. From a visual perspective, it is clear in Figures 4.16(a) through 4.16(f) that across the different synthetic networks tissue solute level decreases as the consumption rate increases, while Figures 4.17 and 4.18 show the same from a graphical perspective.

4.4.4 Variation of Algorithm Parameters

The error tolerance analysis reveals that Secomb's recommended range of 1×10^{-5} to 1×10^{-4} provides an optimal balance between computational efficiency and solution accuracy. Tightening the tolerance to 1×10^{-6} yields negligible improvement in predicted tissue oxygenation while substantially increasing computational cost due to additional iterations. Conversely, relaxing the tolerance to 1×10^{-3} compromises solution fidelity, as evidenced by shifts in both mean oxygen partial pressure and spatial heterogeneity. For practical applications, an error tolerance of 1×10^{-4} remains the optimal choice, providing reliable convergence without unnecessary computational cost.

The discretisation study demonstrates that tissue partial pressure of oxygen converges at all tested number of tissue points per dimension, though values of 25 and above tend to provide more accurate results. This finding has important implications for computational design. First, it establishes a minimum resolution requirement: coarser grids (particularly below 15-20 points per dimension) risk either convergence failure or significant numerical error. Second, it identifies a practical upper bound: while increasing the resolution beyond 40 points per dimension does provide better insight into the heterogenous nature of oxygen diffusion in cerebral tissue, there are diminishing returns. The higher resolutions additionally impose substantial computational penalties, as memory requirements scale with the cube of grid density and simulations take increasingly longer times to complete.

These results provide quantitative guidance for configuring computational parameters in microvascular oxygen transport simulations. The recommended configuration (error tolerance of 1×10^{-4} and discretisation of 30 points per dimension) achieves numerical convergence while maintaining moderate computational cost. This is particularly relevant for large-scale network

simulations or parametric studies requiring numerous model evaluations, though extrapolation to substantially larger domains or extreme physiological conditions (e.g., severe hypoxia or hyperoxia) should be approached with appropriate validation.

Two limitations warrant consideration. First, the analysis is confined to two specific cube sizes and a single combination of oxygen consumption rate and inlet pressure. While these conditions are physiologically representative, the parameter space of microvascular oxygen transport is vast. Future work should explore parameter sensitivity under varied metabolic demands, perfusion pressures, and network geometries to establish broader applicability. Second, the computational cost considerations, while qualitatively discussed, were not rigorously quantified in terms of execution time or memory usage. Formal computational profiling would enable more precise optimisation of the accuracy-efficiency trade-off.

4.4.5 Time-Dependent Cases

Figures 4.32 through 4.35 show the effect that time has on the microvasculature and surrounding tissue for the synthetic networks. The oxygen concentration is heterogenous in nature under time-dependent conditions just as it is under steady-state conditions. As seen with the Secomb rat brain network, oxygen concentration is at its highest around the vessels and decreases as distance from vessels increases; this effect persists regardless of the time step, though the concentration magnitudes do increase as time increases.

As the input of oxygen into the tissue is fixed, it is expected that the concentration will approach a steady-state value: in this case, an average of 45 mmHg for the 375-micron network. The 625-micron network did not reach steady-state for the given time range of 1:400s, so it is uncertain if this network size will also approach 45 mmHg. It is likely that the 625-micron network takes longer to reach steady-state because of its inlet pressure to length scale ration; the more tissue

space there is for a constant pressure drop, the longer it will take for oxygen to diffuse across it for a set oxygen diffusion coefficient.

Figures 4.33 and 4.34 are line plots that display the average tissue oxygen concentration and concentration variance respectively. These figures compare the 375- and 625-micron networks. Figure 4.34 displays interesting behaviour: the 375 micron-network, despite being smaller, has higher variance than the 625-micron network before t = 80 seconds then subsequently has less spatial variance after t = 80 seconds. This is likely due to the pressure drop/unit length ratio and the time it takes for full oxygen diffusion. The variance exponentially decays for both networks over the time range as the tissue becomes fully diffused with oxygen.

Another interesting phenomenon present in these figures is that as variance rises then exponentially decays, at t = 40 seconds there is a second spike before the spatial variance begins decaying again. One of the stipulations for the time-dependent Green's function method is that the time step must be small enough to properly resolve time-dependent limitations (Secomb *et al*., 2015). This assumption was further analysed in Figures 4.36 and 4.37, exploring the effects of varying time discretisations on tissue oxygen levels. It was found that the Green's function method was capable of convergence utilising large time steps, though the numerical solutions tend to increasingly differ with coarser time discretisation. As studies examining temporal responses to physiological conditions (such as stroke, or the application of therapeutics) typically require precise time data, it is advised that a time step no larger than 5 second be implemented; should the system under study take place over longer periods and are only concerned with steady-state behaviour, larger time steps can be employed with caution.

Returning to the anomaly in variance due to a mid-simulation change in time step, no such perturbation was observed in consistent temporal discretisation, even with a larger time step. This

suggests that the change in time step is the culprit. When designing numerical solutions to various transport problems a constant time step should be employed, even at the cost of computational efficiency. Further work is necessary to modify the algorithm to ensure proper handling of this feature, should it be desired in the future.

It is likely that a step size of 10 seconds is too large for proper resolution, and the jump from step size 1 to 10 causes computational errors. The large time step was chosen to reduce computational expense for a time range that had approached steady state: maintaining a smaller time step may resolve this abnormal behaviour in spatial variance. This will be explored in greater detail in Chapter 5. It should be noted that the computational cost considerations, as with the spatial discretisation, were not rigorously quantified with regards to computer memory usage or simulation run time.

Figure 4.35 plots the hypoxic fraction versus time for both network sizes. It is expected that the hypoxic fraction starts close to 1, as at t = 0 seconds there is no oxygen within the system. The hypoxic fraction starts decreasing at around 375 seconds for the 375-micron but only reduces to almost 0 at t = 14 seconds. This is slower that what was observed in the Secomb network. These numbers are higher for the 625-micron network, with hypoxic fraction beginning its decrease at t = 40 seconds and ending at around t = 60 seconds. A finer time discretisation will be required to obtain a more accurate tissue partial pressures of oxygen.

4.4.5 Significance of Results

The fundamental originality of this research exists in the strategic synthesis and adaptation of existing approaches to address a previously unexplored problem. Specifically, an established oxygen transport model utilising well-validated biological transport physics was analysed and repurposed into a predictive framework for gold nanoparticle (AuNP) delivery. Additionally, the

coupling of Secomb's solute transport algorithms with statistically generated synthetic capillary networks represents a methodological advancement. By utilising 20 synthetic network variations (10 each of 375μm and 625μm cubes), this thesis introduces statistical robustness to microvascular transport modelling. This addresses a limitation in cerebrovascular research: the dependency on limited biological samples. Conceptually, the use of oxygen as for benchmark validation of the computational models is useful but does not mean that the compound is a surrogate for predicting AuNP transport behaviour. Application of the above methods to AuNPs is novel and untested.

It was discovered that tissue oxygenation is highly variable within a synthetic network and moderately variable across synthetic networks of different sizes. This result demonstrates that individual synthetic networks display distinct heterogeneous behaviour, though the statistically accurate nature of the networks ultimately applies to tissue oxygenation as well. Previous studies (including Secomb's work) typically report results from single network realizations, while this work provides a novel probabilistic characterization of oxygen delivery heterogeneity at the microvascular scale.

An unexpected phenomenon was observed when the time step used in the time-dependent model was adjusted mid-simulation: the solution was perturbed around the time point of time step change, breaking convergence. While the Green's function methodology developed from Secomb *et al*., 2015 can handle a variety of time step sizes (limited only by the physical system constraints), the claimed ability to change time step mid-simulation is theoretical. This is either due to the discretisation methods and is inherent or due to improper code implementation. Further research into this phenomenon is required to determine the effects on overall simulations solutions and convergence.

4.5 CONCLUSIONS

The work thus far has been dedicated to creating a capillary blood flow model based upon the Green's function method and utilising synthetic networks. This would not have been possible without the groundwork laid down by Secomb, El-Bouri, Payne, Xue, and many other researchers. The current working model successfully generates data describing capillary blood flow and the transport of solute to tissue, validated against data for oxygen. It was determined that the developed model is capable of solute transport modelling within acceptable algorithm error. This model will serve as the main framework for the focus of Chapter 5: the modeling of pharmacokinetic behaviour of nanoparticles within the capillary bed.

CHAPTER 5: MODELLING OF NANOPARTICLE TRANSPORT

5.1 INTRODUCTION

With the work previously detailed, a model to simulate AuNP interactions within the cerebral microvasculature may be synthesised. The first section of this chapter will consider the assumptions and constraints that influence computational modelling of gold nanoparticle interactions. Next, the methodology behind the model is presented, which draws upon previous research performed by Secomb *et al*., 2004 and Foehrenbacher *et al*., 2013. Finally, results from this study are then presented and discussed with emphasis on how a variety of variables impact tissue AuNP levels. This chapter aims to lay the groundwork for subsequent investigations into the computational modelling of AuNP interactions, offering insights into the current understanding of this multifaceted research area and outlining future directions for advancing knowledge and capabilities in this field.

Understanding the temporal dynamics of AuNP transport is essential for optimizing therapeutic delivery protocols. Clinical drug administration occurs over finite periods (typically minutes to hours), after which plasma concentrations decline through clearance and metabolism. The transient accumulation phase determines therapeutic effectiveness, including time-to-peak tissue concentration, duration above minimum effective dose, and spatial homogeneity development. Furthermore, time-dependent modelling enables prediction of dosing interval requirements for repeated administration and may inform patient-specific treatment scheduling.

5.2 METHODS

5.2.1 General Overview

This chapter builds upon the work of Chapter 4, applying the work of Dr. Timothy Secomb and his open-source C++ code to gold nanoparticles in statistical synthetic networks. The code was developed to be self-contained, with four major input files determining the model parameters:

these files described the solute mass balance in the tissue, the vessel network and spatial discretisation, a directory of solute parameters (such as diffusion coefficients), and finally the time range and time discretisation (for the time-dependent model). These major input files were updated with AuNP parameters. The output data for gold nanoparticle concentrations are visualized using MATLAB and Excel. Figure 5.1 below is reproduced from Figure 4.1 with updated fields for AuNPs and illustrates the general overview of this process.

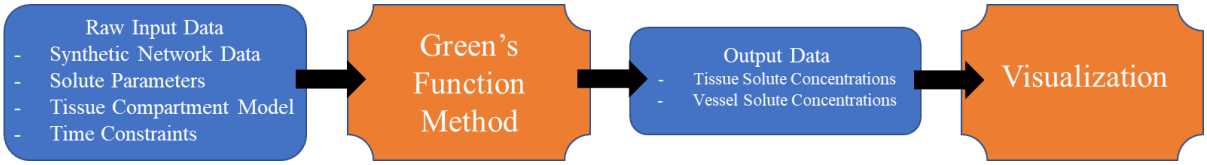

Figure 5.1: Schematic representing the major modules of the microvasculature modelling.

5.2.2 Assumptions

The transition from oxygen to AuNPs as the solute of interest necessitates a revised set of assumptions. These assumptions derive partly from a re-examination of those presented in Chapter 4 now applied to AuNPs and partly from considerations specific to AuNP behaviour. Many assumptions are specific to crossing the blood-brain barrier and the physiochemical properties of AuNPs that influence this phenomenon.

A total of five assumptions were employed for the Green's function model of oxygen under both steady-state and time-dependent conditions. The geometric assumptions (first and second) that regard the structure of the network are still applicable to nanoparticles as the capillary bed will not change between the two compounds. For reference, these are: one, the length and curvature of each vessel segment is much larger (minimum factor of 10) than the radius of the segment, and two, the distance from each segment to other segments and vessel boundaries are large compared to vessel radius.

Assumption three similarly holds when reformulated for nanoparticle flux, and the myoglobin transport component is inherently irrelevant for nanoparticles. The effects from these phenomena are second-order in nature and may be ignored.

Both oxygen formulations and AuNP formulations considered the vessel wall to be part of the tissue space. The endothelial layer of the vessel wall presents its own structure and therefore its own diffusion coefficient and flux with respect to AuNPs but treating the tissue and vessel wall as one homogenous space allows for improved simulation functionality and reduced computational complexity. With regards to the effective diffusion coefficient for AuNPs distributing through the brain tissue, this assumption means that the diffusion coefficient calculated for the BBB may also be used for the brain tissue. The validity of this assumption is discussed later in Chapter 6.4. Additionally, variations in nanoparticle flux and the concentration of gold nanoparticles in blood are too small to have a major impact on nanoparticle diffusion and are thus ignored. Should metabolism and decomposition be of interest, terms may be added to address this phenomenon.

The final oxygen assumption defines a linear relationship between oxygen partial pressure and concentration: as AuNPs are measured in units of molar (M), this assumption is not relevant. As with oxygen, provided that AuNP solubility remains fixed the associated diffusion equation within the tissue is linear and the Green's function method may be applied. In this application of the Green's function method, the solubility coefficient of AuNPs is assumed to be a constant value of 1. In reality, the solubility coefficient is unlikely to equal 1: the presence of functional groups affect solubility in a variety of media, and particle size may affect kinetic solubility (Sun *et al*., 2012). However, AuNP solubility coefficient data remain scarce, PEGylated or not. The computational framework is left flexible and able to simulate varying solubility coefficients should these data become readily available,

The remaining assumptions relate to the structure and pharmacokinetic interactions of gold nanoparticles. First, it should specifically be noted that the simulated AuNPs are considered to have had polyethylene glycol (PEG) strands affixed to the surface. This is a common practice, as PEGylation further prevents the human immune system from recognizing the nanoparticles as foreign objects and stopping them from being filtered out in the liver, spleen, or bone marrow, increasing half-life in the body (Reznickova *et al*., 2019). This will directly affect the diffusivity of the AuNP, as PEGylation significantly increases hydrodynamic diameter; Chen *et al*., 2022 recorded a 435% increase from the actual diameter of 8.8 nm to a hydrodynamic diameter of 38.3 nm (Chen *et al*., 2022). Schematics of PEG and PEGylated AuNPs are illustrated below in Figures 5.2 and 5.3.

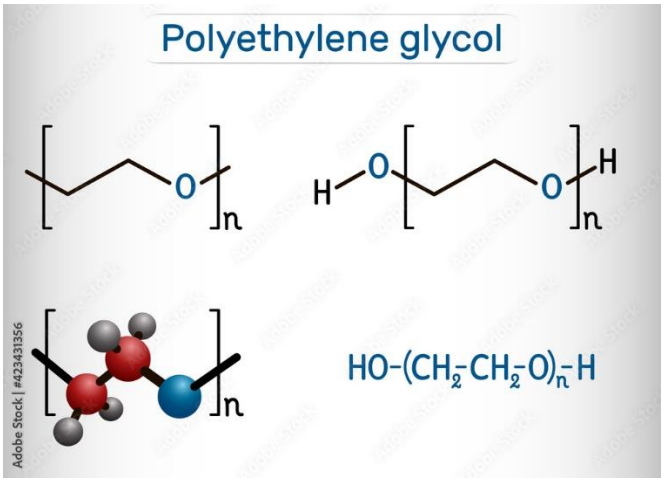

Figure 5.2: Schematic illustrating polyethylene glycol (PEG) in four different formats. Long chains of PEG may be formed by replacing one of the hydrogens on an end oxygen with another segment of PEG, creating a PEG polymer.

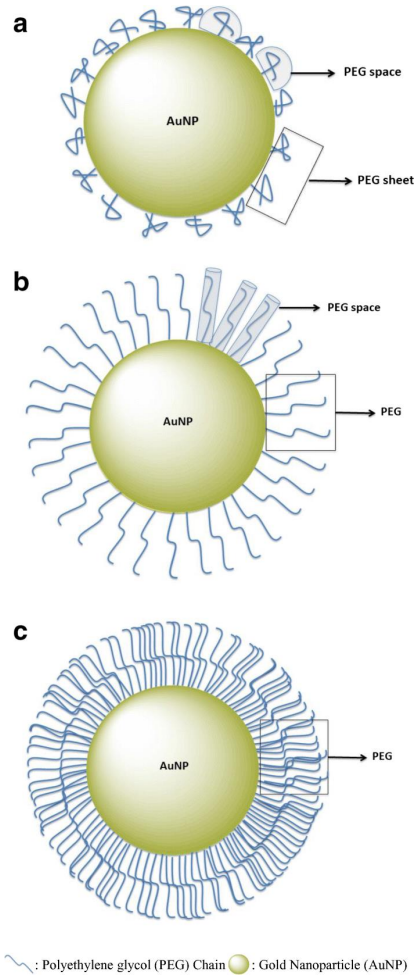

Figure 5.3: Schematic of PEGylated AuNPs in three different conformations: a) Mushroom, b) Brush, Cc Dense Brush. Conformation depends on the PEG density of the surface. Taken with permission from Verimli *et al*., 2019.

Second, as AuNPs are considered relatively inert (even more so with PEGylation) and cross the blood-brain barrier through passive transport, metabolism and decomposition of the compound are not considered here. As passive diffusion occurs in both directions across a membrane between two compartments, it is expected that the concentration of AuNPs in the tissue will approach the concentration of AuNPs in the blood stream under steady-state conditions and will not go beyond the blood stream concentration under time-dependent conditions. Metabolism and decomposition

would modify the AuNP tissue concentration but not by a significant amount worth investigating, as the focus of this thesis in on delivery and transport. As such, these terms are not included here, though they could be added within the intracellular compartment should that focus shift.

The final assumption concerns interactions between oxygen, AuNPs, and haemoglobin. This area has received limited investigation, yielding conflicting results. For instance, it has been found that hypoxic tissue regions tend to have reduced AuNP uptake, though it was unconfirmed whether this was due to a relationship to oxygen or the nature of cells under hypoxic conditions (Jain *et al.*, 2014). Additionally, some nanoparticles (including AuNPs) have been proven capable of binding with haemoglobin and red blood cell membranes, potentially altering suspected transport methods (Kanwal *et al*., 2023). Conversely, other studies have shown that AuNPs and red blood cells have negligible to no interactions with each other (Kumar *et al*., 2020). Given the example contradictory findings, AuNPs, oxygen, and haemoglobin are assumed to have no interactions with each other for computational simplicity.

5.2.3 Models and Parameters

Tissue gradients and gold nanoparticle transport were modelled using the three-dimensional synthetic microvasculature networks developed by El-Bouri. The model was implemented using a customized version of a Green's function method code published by Secomb and written in Visual C++.

The methodology developed in Chapter 4 was purposefully designed to remain general with respect to the solutes under analysis. Consequently, both the steady-state and time-dependent models developed therein are directly applicable to AuNPs. The only modifications necessary to fully encapsulate AuNP properties pertain to the four major input files of the C++ code: the network file, the tissue compartment model file, the solute parameter file, and the time

discretisation file. The network file remained largely unchanged, as the same synthetic capillary systems were examined; however, this file does specify inlet concentration and was therefore updated to include a desired AuNP starting concentration.

The tissue compartment model file contains the mass balance equations for the solutes being analysed. For oxygen, this included a source/sink term based upon Michaelis-Menten kinetics. The AuNPs tissue model is a two-compartment drug transport model derived from mass balance equations and adapted from Foehrenbacher *et al*., 2013. The original model was developed for PR-104, a cancer pro-drug used in the treatment of brain tumours. The modified equations describing the transport of AuNPs are given below in Equations 5.1 and 5.2. In these equations, φ denotes the volume fraction (dimensionless), C is the concentration of compound N (in this case AuNPs) (m^3 solute/m^3), t is time (s), ∇^2 is the Laplacian operator, $D_{N,eff}$ is the effective diffusivity (μM*m^5/m^3 solute/s), and k_{eiN} and k_{ieN} are the rate constants (1/s) for the transfer of AuNPs from the extracellular to the intracellular compartment and vice versa.

$$\varphi_e \frac{\partial C_{eN}}{\partial t} = D_{N,eff}\nabla^2 C_{eN} - \varphi_i(k_{eiN}C_{eN} - k_{ieN}C_{iN}) \tag{5.1}$$

$$\varphi_i \frac{\partial C_{iN}}{\partial t} = \varphi_i(k_{eiN}C_{eN} - k_{ieN}C_{iN}) \tag{5.2}$$

The effective diffusivity coefficient for AuNPs includes the effects of solubility following the formula $D_{N,eff} = \alpha_N D_N$, where α_N is the solute solubility (μM/m^3 solute/m^3) and D_N is the true diffusion coefficient (m^2/s). For this thesis, the solubility of AuNPs was set to 1, causing $D_{N,eff} = D_N$. Subscript i denotes the intracellular compartment while subscript e denotes the extracellular compartment, with φ_e being equal to 1 - φ_i.

While PEGylated AuNPs are considered stable within the human body and not easily metabolized, terms may be added to each compartment to account for these phenomena should a different type of nanoparticle be used. Additionally, the following model handles multiple types

of solutes, even those that undergo chemical conversion to new compounds within the human body provided a production term is included in Equation 5.2. A figure visualizing the model components is shown further below in Figure 5.4.

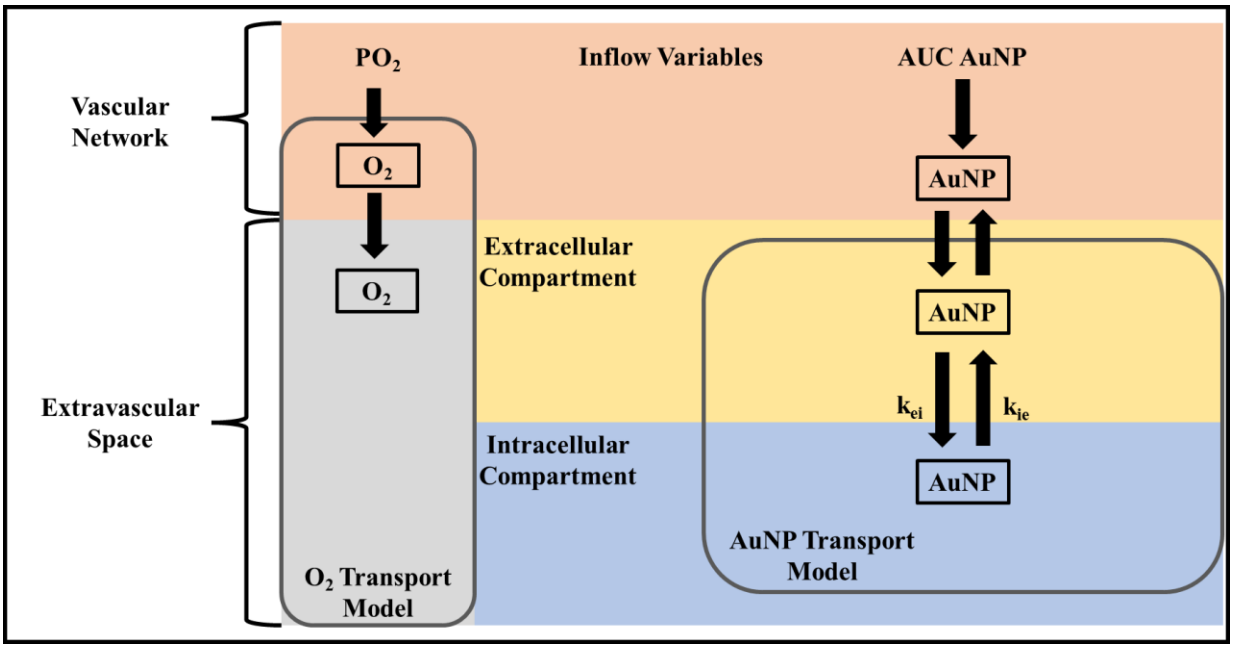

Figure 5.4: Schematic representation of the AuNP transport model. This model describes AuNP concentrations in the extracellular and intracellular compartments. Transfer between compartments is defined by rate constants k_{ei} and k_{ie}, where k_{ei} refers to the forward or extracellular-to intracellular rate constant and k_{ie} refers to the reverse or intracellular-to-extracellular rate constant. Diffusion within the extracellular compartment exists but is excluded from the diagram for clarity. The oxygen transport model does not differentiate between extracellular and intracellular compartments.

The solute parameter file contains input data and constants relevant to the molecular species under analysis. Therapeutic nanoparticle design involves numerous modifiable parameters, many of which are captured within this file. This study focuses on three such parameters for AuNPs:

the diffusion coefficient, the forward rate constant of transport of AuNPs from the extracellular tissue space to the intercellular space, and the intracellular volume fraction (ICVF or Greek letter phi). A final parameter of study, network inlet pressure, was investigated. This parameter affects the flow rates within each capillary, values for which are defined in the network file. Other design parameters are not included due to scope limitations of this thesis but warrant future investigation.

The diffusion coefficient was chosen for study due to its effect on tissue penetration and accumulation. Additionally, the diffusion coefficient can encompass other parameters such as particle size and functionalisation while being directly modifiable and optimised. For the diffusivity coefficient, example values were calculated for blood viscosity varying from $3x10^{-3}$ Pa*s to $4x10^{-3}$ Pa*s and for temperature of 37 °C. Using the diffusion equations presented previously in Chapter 2 and example AuNP diameters (ranging from 5 nm to 110 nm) from Zhou *et al*., 2018, the minimum tissue diffusivity D_N was found to be $0.0578x10^{-11}$ m^2/s while the maximum was $4.24\ x10^{-11}$ m^2/s. The initial set of simulations ran from $1x10^{-11}$ m^2/s to $10x10^{-11}$ m^2/s as a standard range with $1x10^{-11}$ m^2/s steps, with subsequent simulations in the low range varying from $0.1x10^{-11}$ m^2/s to $0.75x10^{-11}$ m^2/s and simulations in the high range at $100x10^{-11}$ m^2/s and $1000x10^{-11}$ m^2/s. The ICVF was held at 0.5, the forward rate constant was held at 0.1 1/s, and the inlet pressure was held at 50 mmHg.

The forward rate constant (or tissue-to-cell rate constant) was chosen as it governs cellular uptake efficiency. Even if AuNPs reach deep into the tissue, this holds no clinical significance if there is no intracellular retention. This parameter is also modifiable through choice of attached functional groups, such as receptor-targeting ligands or PEGylation as previously described. The forward rate constant experiments were run for values of 0.1, 0.25, 0.5, 0.75, and 1 1/s with the reverse (intracellular to extracellular) held at a constant of 0.1 1/s. The ICVF was held at 0.5 and

the diffusion coefficient was held at $4x10^{-11}$ m^2/s. All data regarding tissue solute levels produced from these experiments were then processed in Excel to produce the figures found in the results sections. When presenting the results of oxygen, oxygen tissue consumption was again chosen to be 0.0006 cm^3 O_2/cm^3 tissue/s, while tissue inlet pressure was 50 mmHg as per the results in Chapter 4.

While not a modifiable parameter in terms of AuNP therapeutic design, ICVF was chosen to be varied as abnormal values could indicate disease or other patient characteristics. The degree and direction of abnormality vary from disease to disease but is expected to be lower (a value of 0.31) in brain tumours for example (Foehrenbacher *et al*., 2013). ICVF additionally varies across the entire human brain irrespective of disease, with a maximum value of 0.84 and minimum of 0.39, the average settling at 0.63 (Burzynska *et al*., 2024). ICVF varies from person to person and within a person but does not vary on the time scale of drug delivery, thus ICVF is kept constant within a simulation. The range of values used in these simulations were 0.1, 0.25, 0.5, 0.75, and 0.99. Values of 0 and 1 were excluded as they are physiologically impossible and thus not of importance in this study. The diffusivity coefficient was held at $4x10^{-11}$ m^2/s while the forward rate constant was held at 0.1 1/s. These two parameters were held at these values based upon calculations below and Foehrenbacher *et al*., 2013, respectively. Inlet pressure was again held at 50 mmHg.

The final parameter, network inlet pressure, was selected to represent the influence of the larger arterial network on the capillary bed. It was observed in Chapter 4 that adjusting the inlet pressure into the capillary bed affected oxygen delivery to the tissue by affecting the flow of blood to the capillaries; it is assumed that the same phenomenon will be observed for AuNPs. The inlet pressure to the capillary bed is typically 45 mmHg but can vary by ±15 mmHg due to

autoregulation in the major arteries and patient-specific conditions (Payne, 2006). As with ICVF, this parameter is not modifiable in terms of AuNP therapeutic design. To capture the expected inlet pressure values and the behaviour under extreme conditions, a range of 20 to 100 mmHg with 10 mmHg steps was analysed. It is expected that even in a single patient the inlet pressure could vary with time; as the architecture is unable to change network files mid-simulation to reflect this change, this investigation was only performed under steady-state conditions. The diffusivity coefficient was held at $4x10^{-11}$ m^2/s, the forward rate constant was held at 0.1 1/s, and finally ICVF was held at 0.5. Table 5.1 below displays a summary of all the parameters used.

Table 5.1: Parameters and their units used in the simulations of gold nanoparticles.

Parameter	**Value**	**Units**
Diffusion Coefficient	0.1, 0.25, 0.5, 0.75, 1:1:10, 100, 1000	10^{-11} m^2/s
Intracellular Rate Constant	0.1, 0.25, 0.5,0.75, 1	1/s
ICVF	0.1, 0.25, 0.5,0.75, 0.99	Unitless
Network Inlet Pressure	20:10:100	mmHg

The time discretisation file defines temporal parameters necessary for simulating drug delivery scenarios. Three parameters were considered: the time range, the time step within that range, and the input nature of the solutes. The input nature described the influx of simulated solutes into capillary network and this influx behaviour over the range of time that was modelled. The input nature came in three options: zero, fixed, or variable. The zero-input option is a single dose of solute concentration at time = 0 seconds. After t = 0 s, no more of that solute is added to the system. Fixed input is the opposite: within the specified time range, solute is added to the system at a constant value equal to the dose at time = 0 seconds. The final option, variable, allows the user to specify solute concentration input as a function of time.

In realistic clinical scenarios, AuNP transport would require the variable input option: drugs that are added to biological systems often have a rapid uptake and accumulation followed by an exponential decay (Secomb *et al*., 2015). For this thesis, a fixed input scheme was used to observe AuNP concentration as it approaches steady state; due to the limits on the scope of this thesis, variable input was not explored. Simulating the transport of AuNPs with a fixed scheme provides a benchmark set of results and best-case-scenario with which to compare variable input schemes against.

The selected time frame of 1 to 400 seconds (6.67 minutes) captures the initial distribution and accumulation of AuNPs within the tissue. While typical drug therapies may extend into the hours, this time frame is sufficient for transport behaviour observation and approaches steady-state concentration in a well-perfused region. Extension to clinically relevant timescales represents important future work for accurate therapeutics design. The total time frame spanned 0 to 400 seconds with a time step of 5 seconds. Initial testing of the subdivided time frame procedure outlined in Chapter 4 displayed similar perturbations in solute variability around time step size change mid-simulation. The constant time step size of 5 seconds was chosen to balance temporal resolution and computational efficiency per the analysis found in Chapter 4.

5.2.4 Sensitivity Analysis

Four independent variables were selected to characterize the behaviour of gold nanoparticles within the simulation framework: the nanoparticle diffusion coefficient, the forward rate constant governing cellular uptake, the intracellular volume fraction (ICVF), and the network inlet pressure. To quantify the influence of these parameters on tissue AuNP concentration, a comprehensive sensitivity analysis was conducted using the 375-micron and 625-micron cubic computational domains generated from steady-state simulations.

Amongst the various sensitivity analysis techniques available, a one-at-a-time (OAT) approach was implemented for this investigation. While alternative methodologies were considered (such as global sensitivity analysis and variance-based methods), these shall be discussed in Chapter 6 as recommendations for future work. The OAT method was selected for two principal reasons: first, it is computationally simple and straightforward to interpret; and second, it is capable of leveraging existing simulation data without requiring additional computational expense.

The OAT procedure comprises two fundamental steps: parametric perturbation and iterative assessment. In step one, a single input parameter is varied over a specified range from its baseline value while all remaining parameters are maintained at their respective baseline values. The simulation is performed and results gathered. The second step returns the perturbed parameter to its baseline value, and the procedure is repeated systematically for each remaining input parameter. The sensitivity of the system to each parameter is subsequently quantified by evaluating the changes in output variables through either linear regression analysis or computation of partial derivatives.

The steady-state simulation data relating to the four input variables to tissue AuNP concentration were exported to Microsoft Excel for analysis. The sensitivity analysis was performed over five stages. First, for each simulation configuration the mean tissue AuNP concentration was calculated across all cubic domains for a given set of input variable values. Next, the averaged concentration values were stratified according to the independent variable under examination (diffusion coefficient, uptake rate constant, ICVF, or inlet pressure). Then, a single-variable nonlinear regression analysis was performed for each independent variable using Excel's Data Analysis Tool Pak add-in. This univariate analysis established the functional relationship

between each individual parameter and the tissue AuNP concentration while also generating necessary regression coefficients. In step four, the regression coefficients were subsequently incorporated into a comprehensive multivariate nonlinear regression model encompassing the entire parametric space. Finally, the linear regression applicability was assessed through regression summary statistics, analysis of variance (ANOVA), and examination of standardized regression coefficients. These statistical metrics provided the basis for determining parameter sensitivity and evaluating the implications for design optimisation and experimental planning.

5.3 RESULTS

5.3.1 Introduction

The methodological approaches outlined in Section 5.2 and Chapter 4 were applied to investigate AuNP transport within the capillary bed. Simulations were executed on El-Bouri 375- and 625-micron synthetic networks with varying AuNP parameters. Particular attention was devoted to the diffusion coefficient, as it was hypothesised to most significantly and directly influence AuNP delivery into the extracellular space; forward rate constant, intracellular volume fraction, and network inlet pressure were also systematically analysed. A sensitivity analysis was conducted to examine this hypothesis and provide context for AuNP considerations. Results are presented below, with discussion following in Section 5.4.

5.3.2 Steady-State Results

The starting concentration of AuNPs for all the experiments below was 25 μM. This value was chosen as higher concentrations generally have a higher risk of flocculation and crashing out of the system. Inlet pressure to the capillary network was 50 mmHg. Typical visual representations of the networks are presented below in Figures 5.5 and 5.6, with images of the full cube shown. Figure 5.5 shows the 375-micron network, while Figure 5.5 shows the 625-micron network.

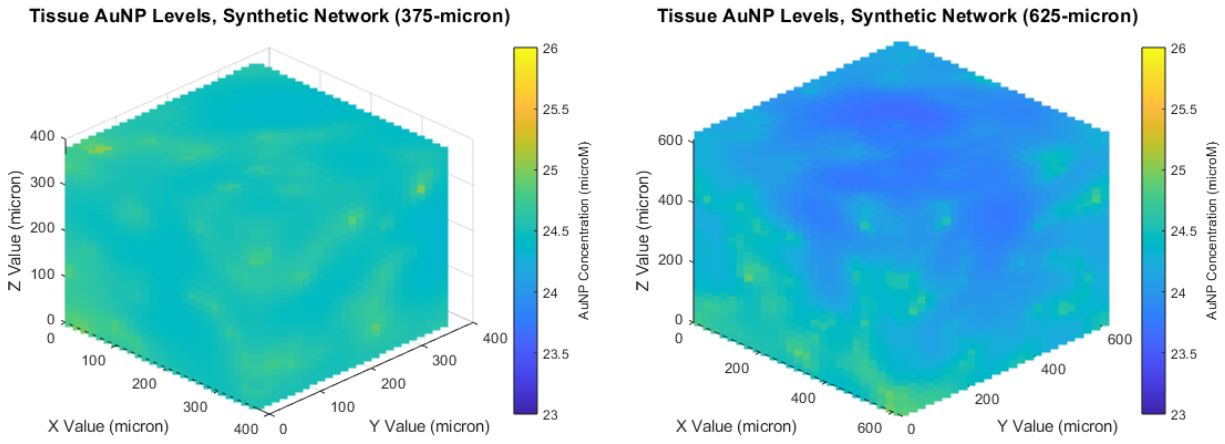

Figures 5.5 & 5.6: El-Bouri Synthetic Networks, 375-micron network (Figure 5.5) and 625-micron network (Figure 5.6), tissue diffusion coefficient of 4.0×10^{-11} m^2/s.

A visual presentation of the normalised distributions of AuNPs and oxygen in synthetic network tissue is given in Figures 5.7 and 5.8 below. These figures were taken at a selected tissue slice height that is kept constant for visual comparison. Figure 5.7 is for the 375-micron network while Figure 5.8 is for the 625-micron network. As previously mentioned, oxygen is not an analogue for AuNP due to the varying differences in physiochemical properties and transport mechanisms. The comparison given in these figures is intended to demonstrate this behaviour while also providing a surface-level assessment for glaring model artifacts. When color scale is adjusted for the different magnitudes, it is observed that both solutes present similar tissue distribution patterns, as expected of two compounds primarily undergoing passive diffusion.

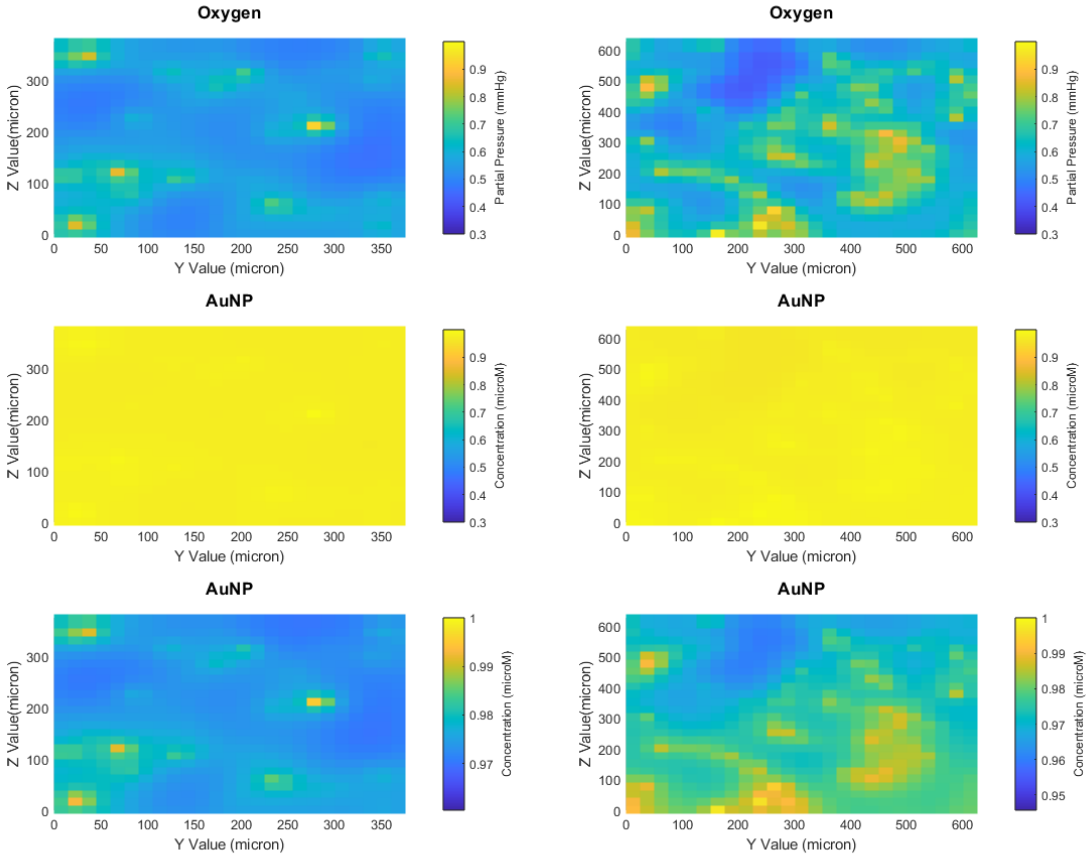

Figures 5.7 & 5.8: Comparison of AuNP and oxygen normalised tissue levels for the 375-micron network (Figure 5.7) and 625-micron network (Figure 5.8). Sub-figures (a) and (b) of each figure compare oxygen and AuNPs on the same colour scale, while sub-figure (c) of each figure displays normalised tissue levels of AuNPs on its own colour scale. A diffusion coefficient of 4.0×10^{-11} m^2/s was used for AuNPs. Oxygen concentration was originally measured as partial pressure (mmHg) and AuNP concentration was originally measured in μM.

Initial simulations varied AuNP tissue diffusivity in the synthetic networks and are displayed below in Figures 5.9 through Figure 5.14. The different tissue diffusivities were described previously and meant to encapsulate a wide range of different AuNP conditions. For better visualization, the results below may have solute concentrations (and potentially the tissue

diffusion coefficient) on a log10 scale. Concentration values of 0 μM were instead set to 0.0001 μM to allow for this transformation. In all box-and-whisker plots, a box represents the first and third quartiles and an error bar (whisker) represents the minimums and maximum concentration excluding outliers. Data points are defined as outliers if they fall outside 1.5 times the interquartile range beyond the first or third quartile. Outliers have been excluded from visualization but are still considered in calculations for mean, median, and standard deviation.

Figures 5.9 and 5.10 visually demonstrate the impact of varying diffusion coefficient on tissue AuNPs concentration. The tissue slice height of comparison is kept constant for visual comparison. Figure 5.9 is for the 375-micron network while Figure 5.10 is for the 625-micron network. Figures 5.11 and 5.12 quantify these respective results for all tested diffusion coefficients in both tissue domain cubes. Figure 5.13 compares the two via line plot. The variance of the AuNP concentration as a function of tissue diffusivity was also explored by examining the standard deviations in AuNP concentrations at each tissue diffusivity, depicted in Figure 5.14.

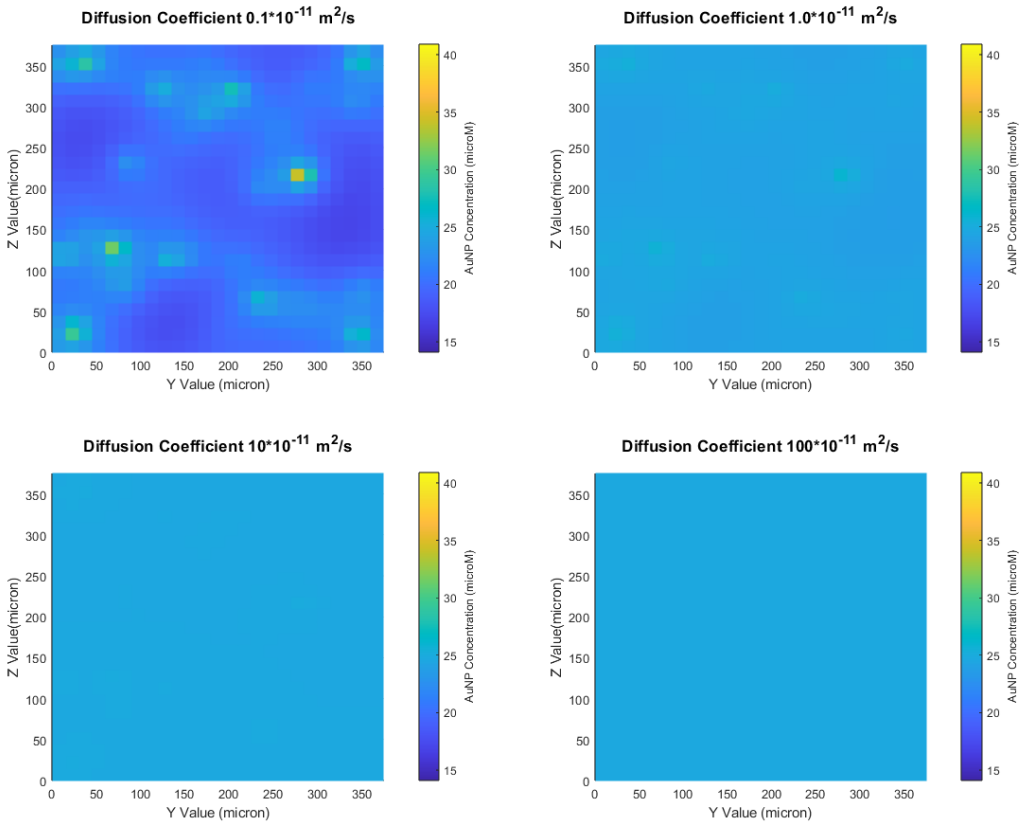

Figure 5.9: Comparisons of AuNP diffusion coefficients at a selected slice for the 375-micron network. Chosen diffusion coefficients were: (a) 0.1×10^{-11} m^2/s, (b) 1.0×10^{-11} m^2/s, (c) 10.0×10^{-11} m^2/s, and (d) 100.0×10^{-11} m^2/s.

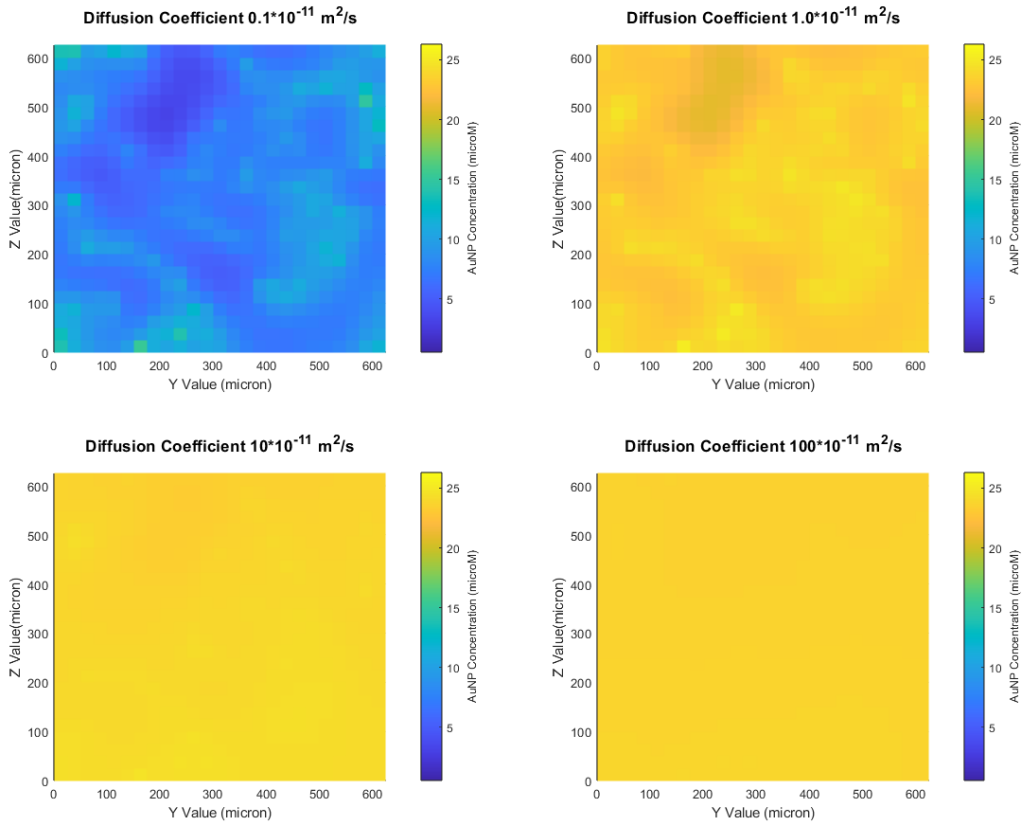

Figure 5.10: Comparisons of AuNP diffusion coefficients at a selected slice for the 625-micron network. Chosen diffusion coefficients were: (a) 0.1×10^{-11} m^2/s, (b) 1.0×10^{-11} m^2/s, (c) 10.0×10^{-11} m^2/s, and (d) 1000×10^{-11} m^2/s.

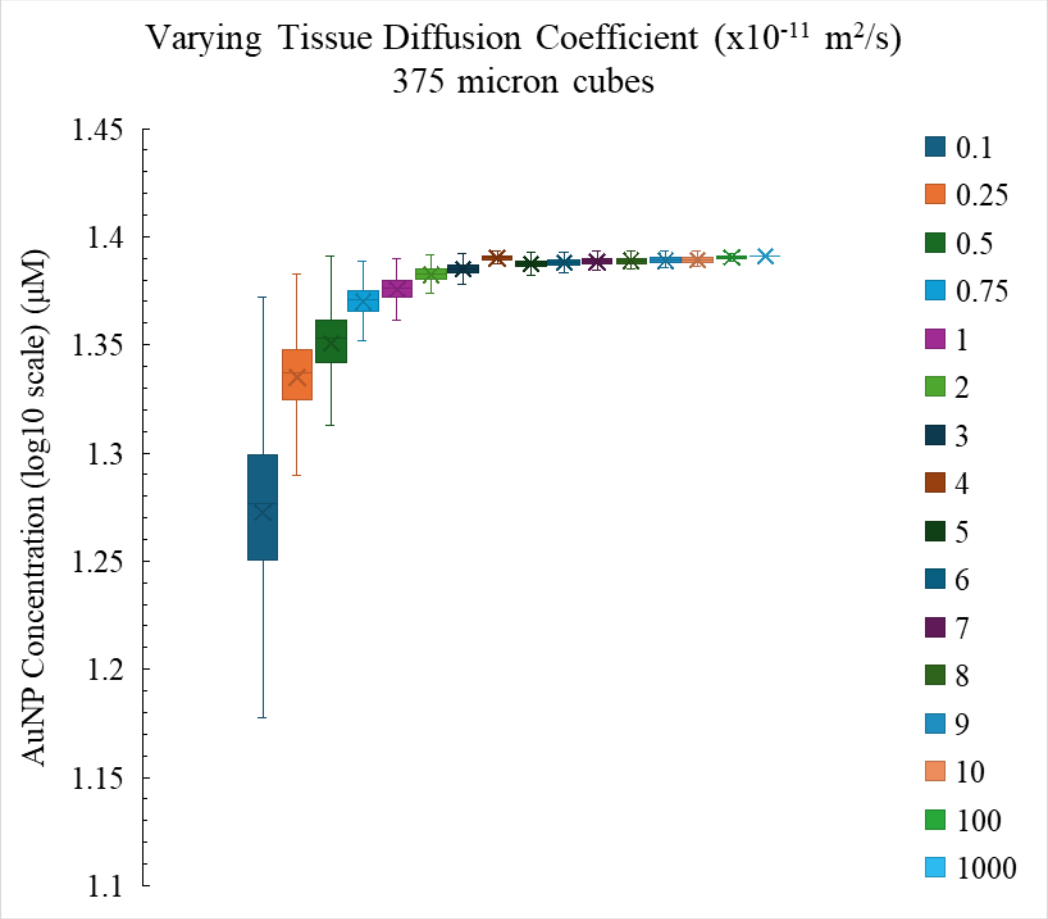

Figure 5.11: Tissue diffusion coefficients and their associated AuNP concentrations averaged over all 375-micron cubes.

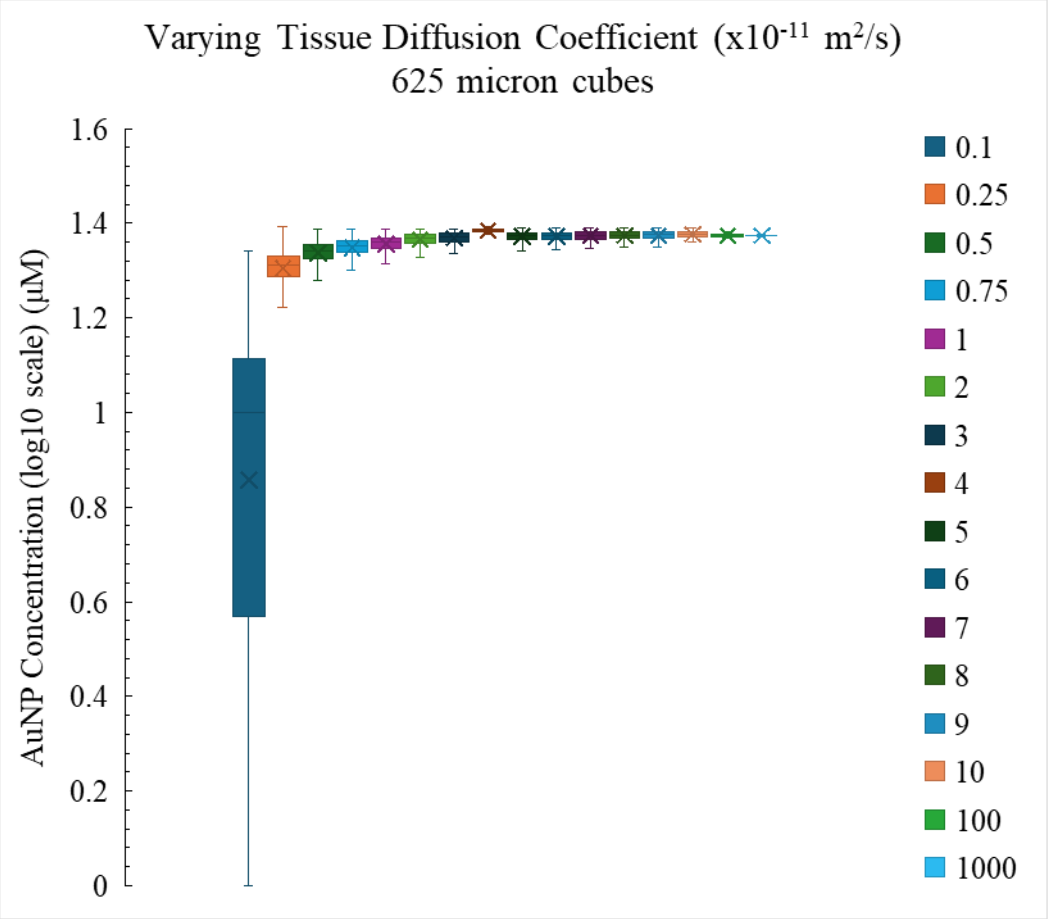

Figure 5.12: Tissue diffusion coefficients and their associated AuNP concentrations averaged over all 625-micron cubes.

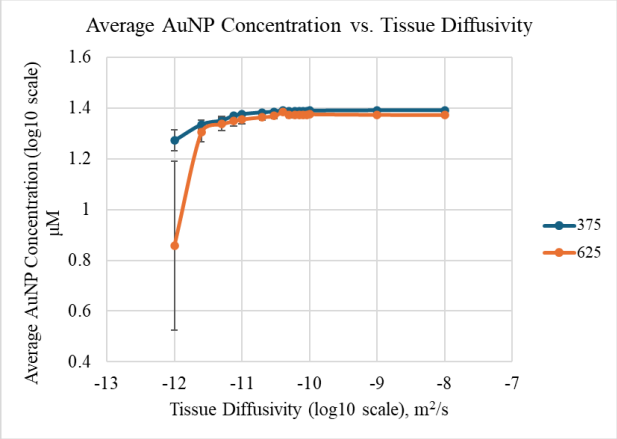

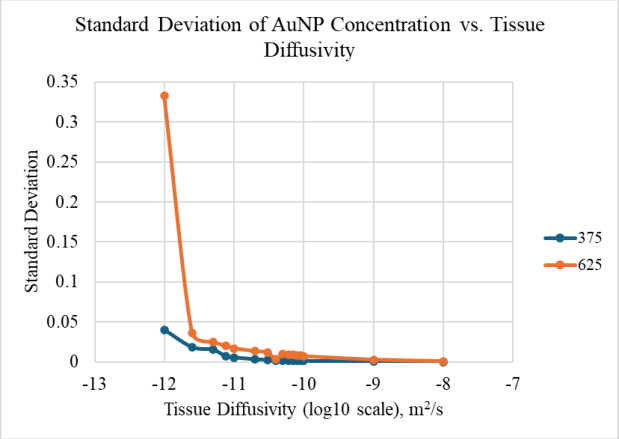

Figures 5.13 & 5.14: Comparison of 375-micron and 625-micron tissue cube AuNP statistics as a line charts. Figure 5.13 displays average AuNP tissue concentrations and is graphed on a log10 scale to better illustrate the diminishing returns as the diffusion coefficient increases. Points on the line are the average AuNP concentration, while the error bars designate other values within one standard deviation. Figure 5.14 displays standard deviations of spatial log10 AuNP concentrations averaged over each synthetic network, plotted against tissue diffusion coefficient.

The tissue-to-cell rate constant used in the two-compartment model, described earlier this chapter, was varied to simulate extra- to intracellular AuNP transport. Within the model, a reverse rate constant is also present, but only the forward rate constant is adjusted here. Figures 5.15 and 5.16 below illustrate AuNP concentration changes within the extracellular space as forward rate constant increases, while Figures 5.17 and 5.18 illustrate the same from the perspective of the intracellular space. It is observed that increasing the forward rate constant leads to a larger spread in AuNP tissue concentrations, as evidenced by larger data standard deviation (the boxes) and an increased difference between minimum and maximum tissue concentrations (the whiskers).

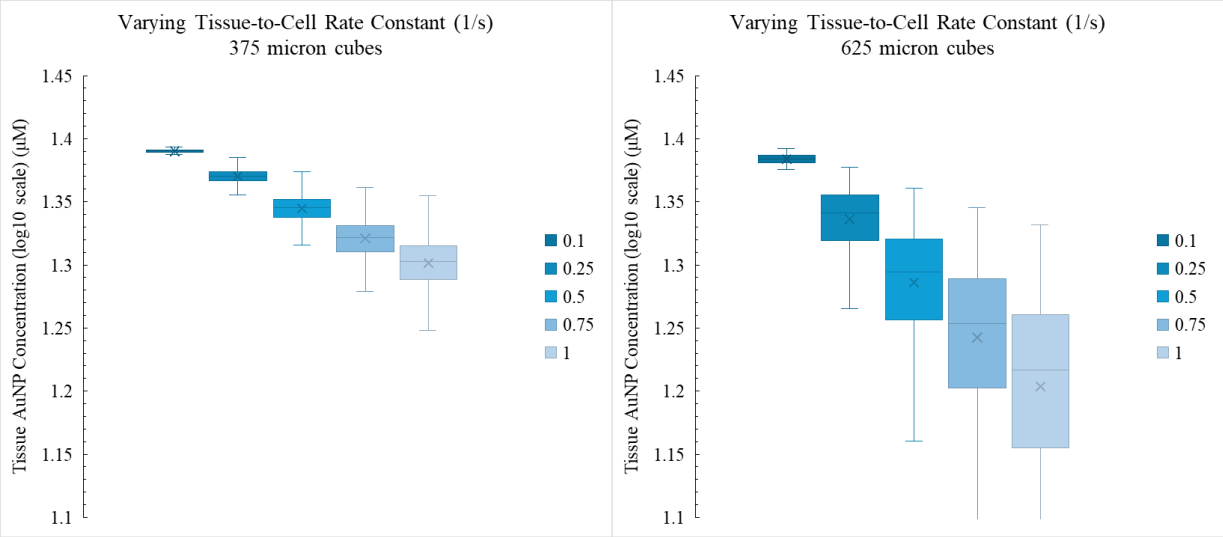

Figures 5.15 & 5.16: AuNP concentration for the 375-micron cubes and 625-micron cubes within the extracellular compartment as the forward rate constant (tissue-to-cell) increases.

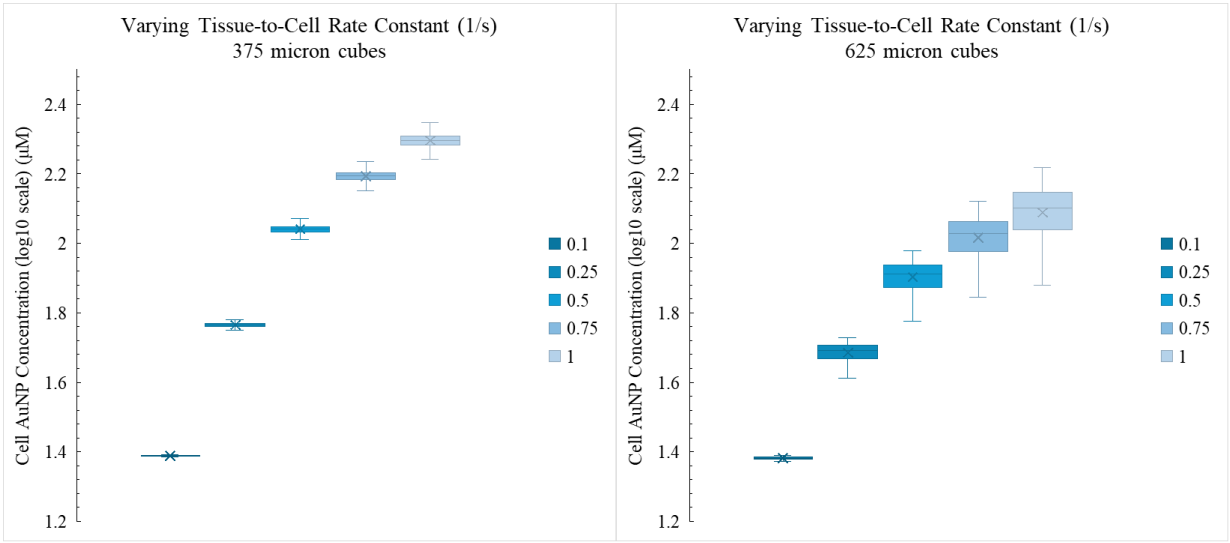

Figures 5.17 & 5.18: AuNP concentration for the 375-micron cubes and 625-micron cubes within the intracellular compartment as the forward rate constant (tissue-to-cell) increases.

The next series of simulations examined the effect of varying cellular density, represented as ICVF, on tissue AuNP concentration. As ICVF increases, the ratio of cells to extracellular space within the tissue increases, while a decrease in ICVF indicates decrease in cells and increase in extracellular space. Figures 5.19 and 5.20 below illustrate the change in extracellular tissue AuNP concentration as ICVF increases for both cube sizes.

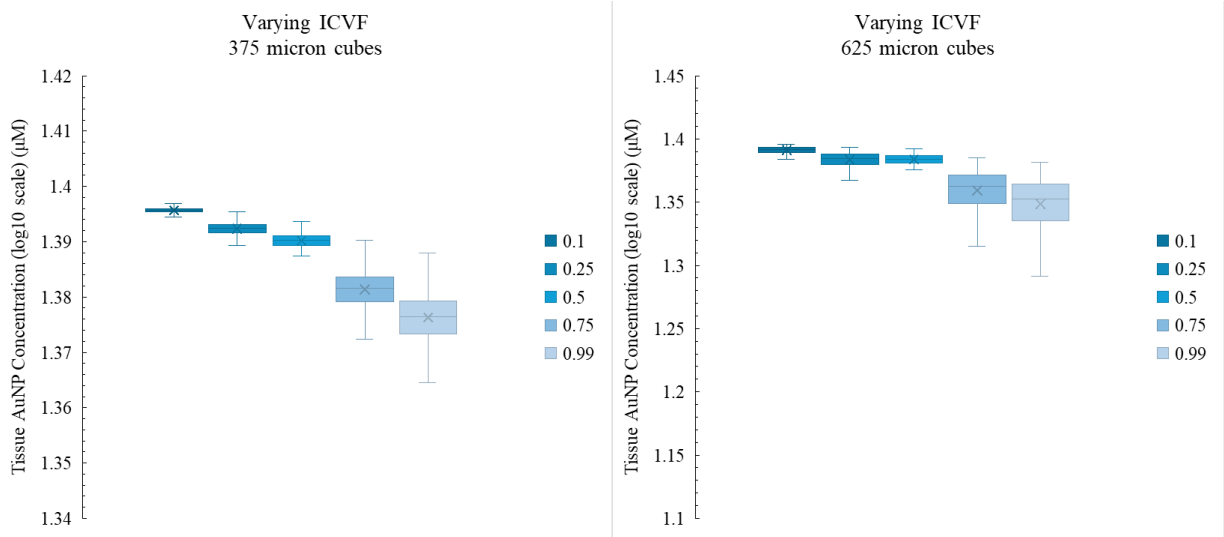

Figures 5.19 & 5.20: Tissue AuNP concentration for 375-micron and 625-micron cubes as intracellular volume fraction increases.

Finally, capillary network inlet pressure was varied to observe its impact on AuNP tissue concentration. An increased in inlet pressure equals an increase in blood flow rate as per Poiseuille's Equation (provided all other parameters remain constant). Figures 5.21 and 5.22 demonstrate the behaviour of AuNPs as a function of inlet pressure for both the 375- and 625-micron cube.

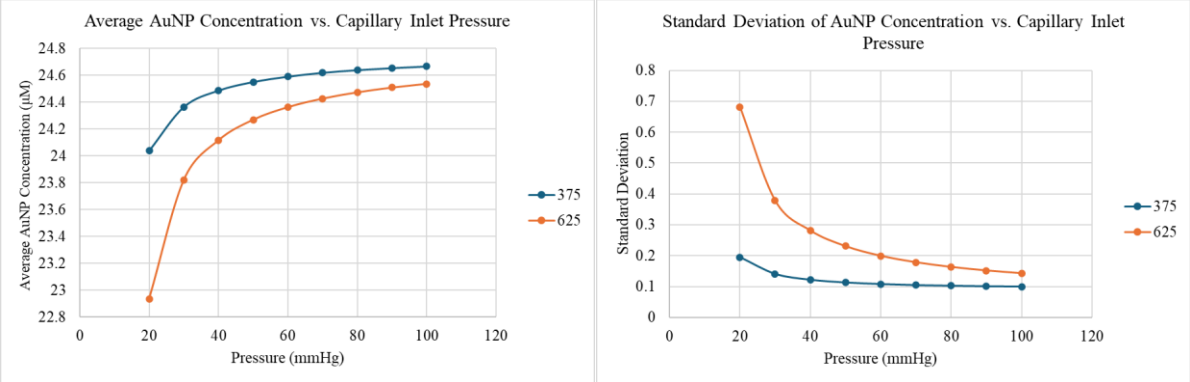

Figures 5.21 & 5.22: Tissue AuNP concentration for 375-micron and 625-micron cubes as capillary bed inlet pressure increases. Figure 5.21 displays average AuNP tissue concentrations while Figure 5.22 displays standard deviations of spatial AuNP concentrations.

5.3.3 Time-dependent Results

Time-dependent simulations were performed on El-Bouri synthetic networks using the methodology outlined in Chapter 4 and Section 5.2.2, with updated parameters defined in Section 5.2.3. The starting concentration of AuNPs and inlet pressure for all the experiments were identical to the steady-state simulations: 25 μM and 50 mmHg respectively. Variance of tissue solute is represented by the standard deviation of spatial solute concentration averaged over each synthetic network. A comparison of oxygen to AuNPs was performed over the time span of 0 to 400s with time step 5s and compared in Figures 5.23 and 5.24 below. The figures display line plots of the normalised distributions of AuNPs and oxygen; again, this analysis was performed as a qualitative, surface-level check for obvious numerical discrepancies in the AuNP model.

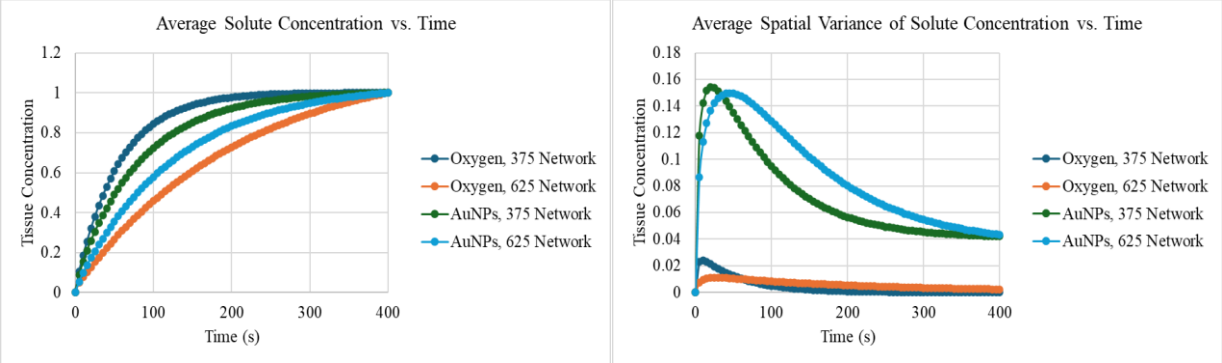

Figures 5.23 & 5.24: Normalised average concentrations (Figure 5.23) and average spatial variance (Figure 5.24) of AuNP and oxygen tissue for the 375-micron and 625-micron networks. The AuNP diffusion coefficient was 4.0×10^{-11} m^2/s.

Non-normalised AuNP tissue concentrations for the 375- and 625-micron networks were compared to observe if a larger tissue space impacted the rate of distribution. Figures 5.25 and 5.26 display these comparisons as line plots, with average AuNP concentration taken as the spatial average across all networks of a designated size.

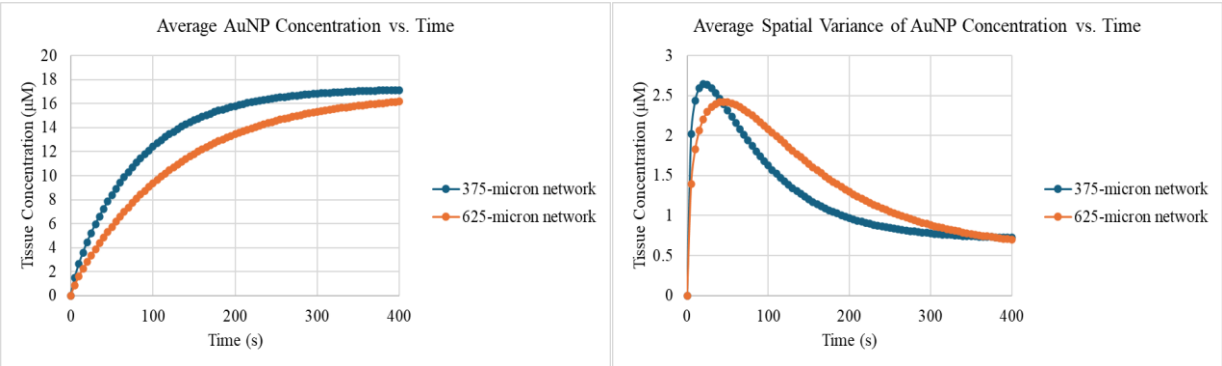

Figures 5.25 & 5.26: Average AuNP tissue concentration (Figure 5.25) and average AuNP spatial variance (Figure 5.26) for the for the 375-micron and 625-micron networks as a function of time. AuNP tissue diffusion coefficient was 4×10^{-11} m^2/s.

The next set of simulations varied tissue diffusivity within the 375- and 625- micron statistical synthetic networks and are displayed below in Figures 5.27 through 5.29. Selected diffusion coefficients of $1x10^{-11}$ m^2/s, $10x10^{-11}$ m^2/s, $100x10^{-11}$ m^2/s, and $1000x10^{-11}$ m^2/s were chosen to be displayed. Figure 5.25 displays a visual comparison of tissue slices at these diffusion coefficients while Figures 5.26 and 5.27 present these results as line plots over the time range of 0 to 400s with time step 5s.

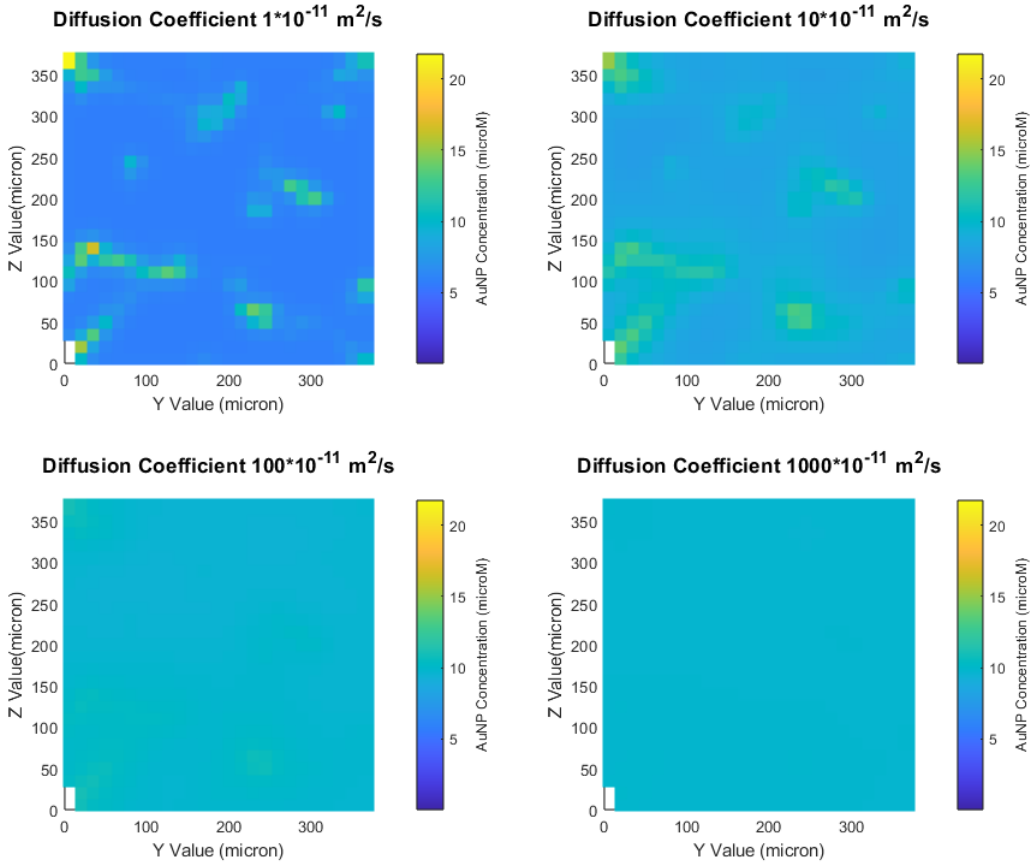

Figure 5.27: Visual comparison of AuNP diffusion coefficient impact on AuNP tissue concentration at a selected slice for the 375-micron network. Chosen diffusion coefficients were: (a) $1x10^{-11}$ m^2/s, (b) $10x10^{-11}$ m^2/s, (c) 100 $x10^{-11}$ m^2/s, and (d) $1000x10^{-11}$ m^2/s. Comparison is taken at a time step of 40 seconds.

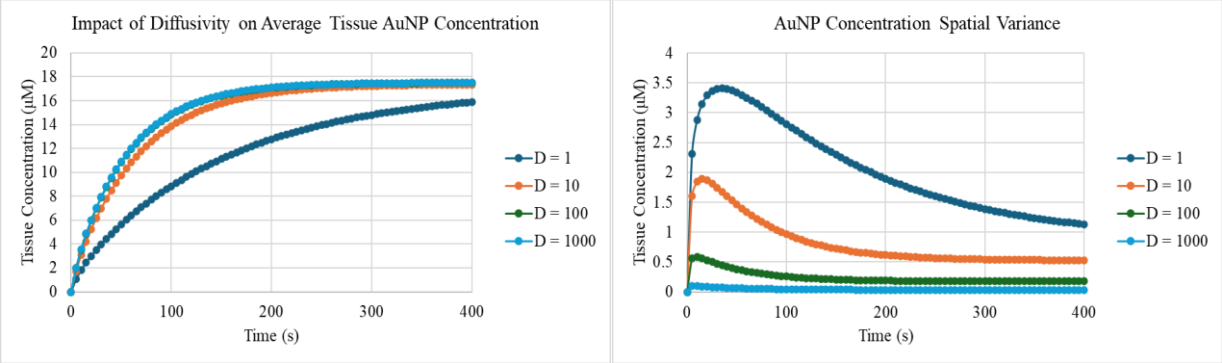

Figures 5.28 & 5.29: Line plots comparing the average AuNP tissue concentration (Figure 5.28) and spatial variance of AuNP tissue concentration (Figure 5.29) for select diffusion coefficients within the 375-micron network.

The next set of simulations observed the effects of varying the tissue-to-cell rate constant. Figures 5.30 through 5.32 below illustrate AuNP concentration changes within the extracellular space as forward rate constant increases for the time range of 0 to 40 seconds, while Figures 5.33 and 5.34 illustrate the same from the perspective of the intracellular space. It was found that as the rate constant increases the AuNP concentration decreases.

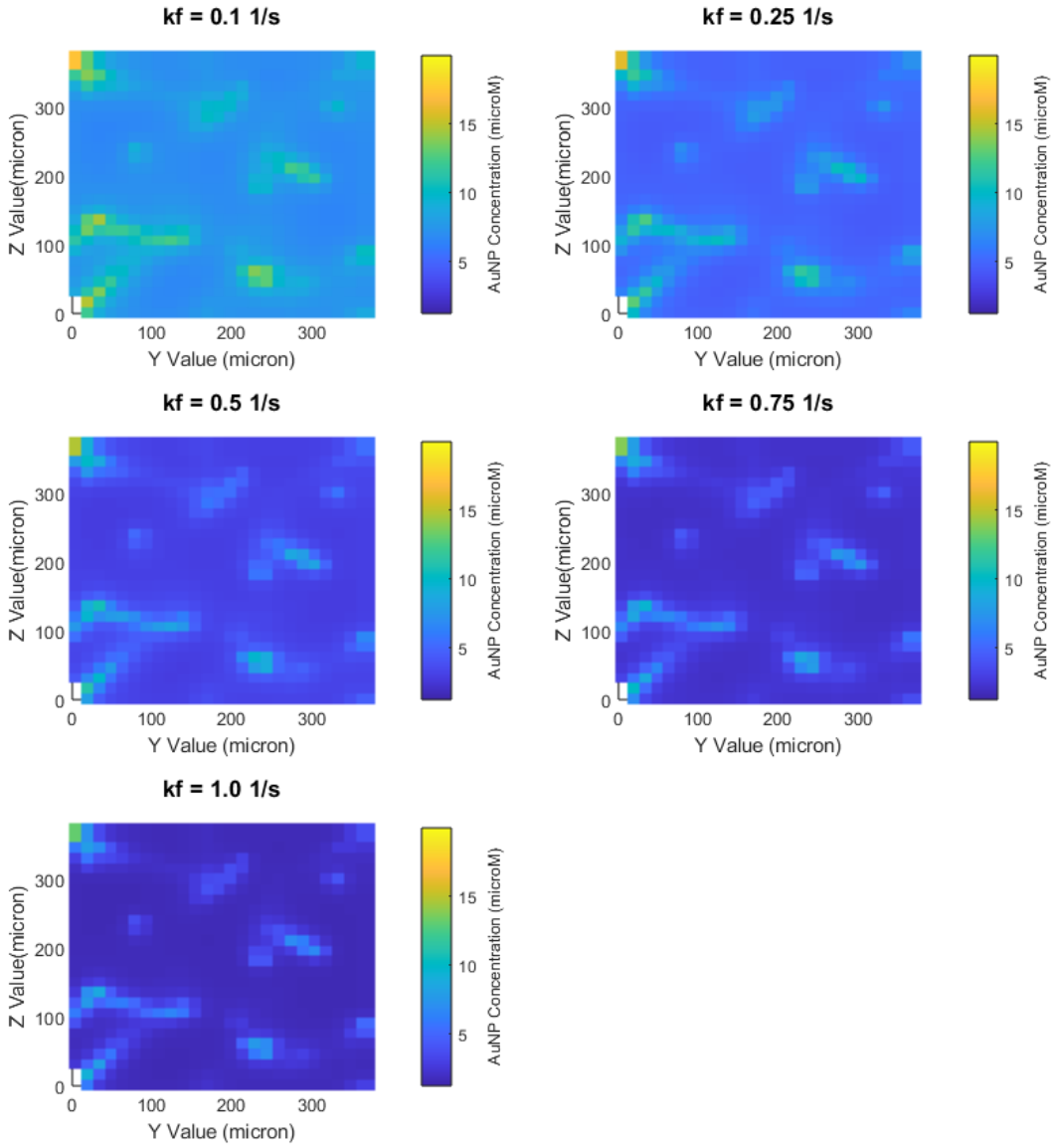

Figure 5.30: Comparison of AuNP forward rate constants at a selected slice for the 375-micron network. Chosen forward rate constants were: (a) 0.1 1/s, (b) 0.25 1/s, (c) 0.5 1/s, (d) 0.75 1/s, and (e) 1.0 1/s. Comparison is taken at a time step of 40 seconds and is for the tissue compartment.

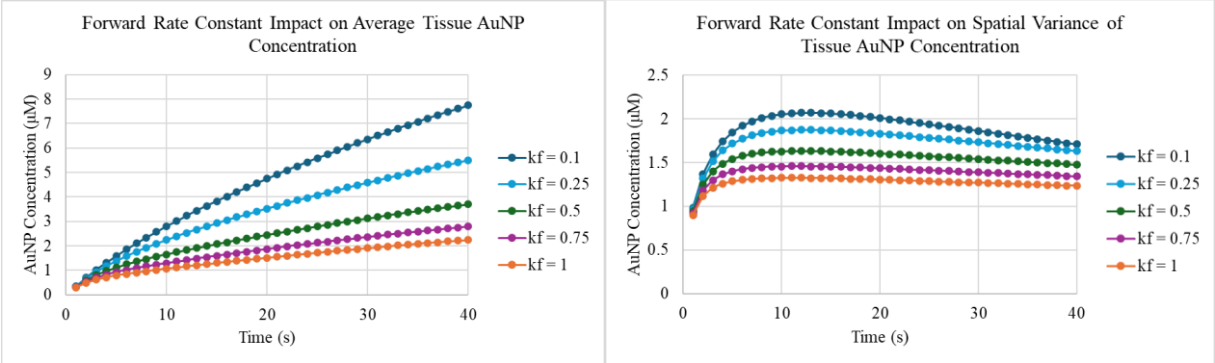

Figures 5.31 & 5.32: Average AuNP concentration (Figure 5.31) and spatial variance (Figure 5.32) for the 375-micron cubes within the extracellular compartment as a function of forward rate constant (tissue-to-cell).

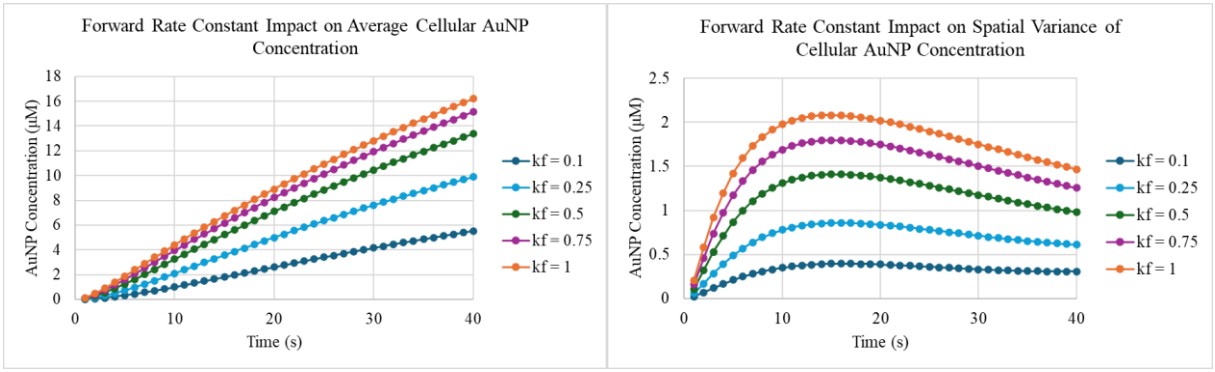

Figures 5.33 & 5.34: Average AuNP concentration (Figure 5.33) and spatial variance (Figure 5.34) for the 375-micron cubes within the intracellular compartment as a function of forward rate constant (tissue-to-cell).

A series of time-dependent simulations examined the effect of varying ICVF on AuNP transport. Figures 5.35 through 5.37 below illustrate the change in extracellular tissue AuNP concentration as ICVF increases for a cube size of 375-micron; Figure 5.35 presents a visual comparison while Figures 5.36 and 5.37 compare concentrations over 0 to 400 seconds (time step 5 seconds) with line plots.

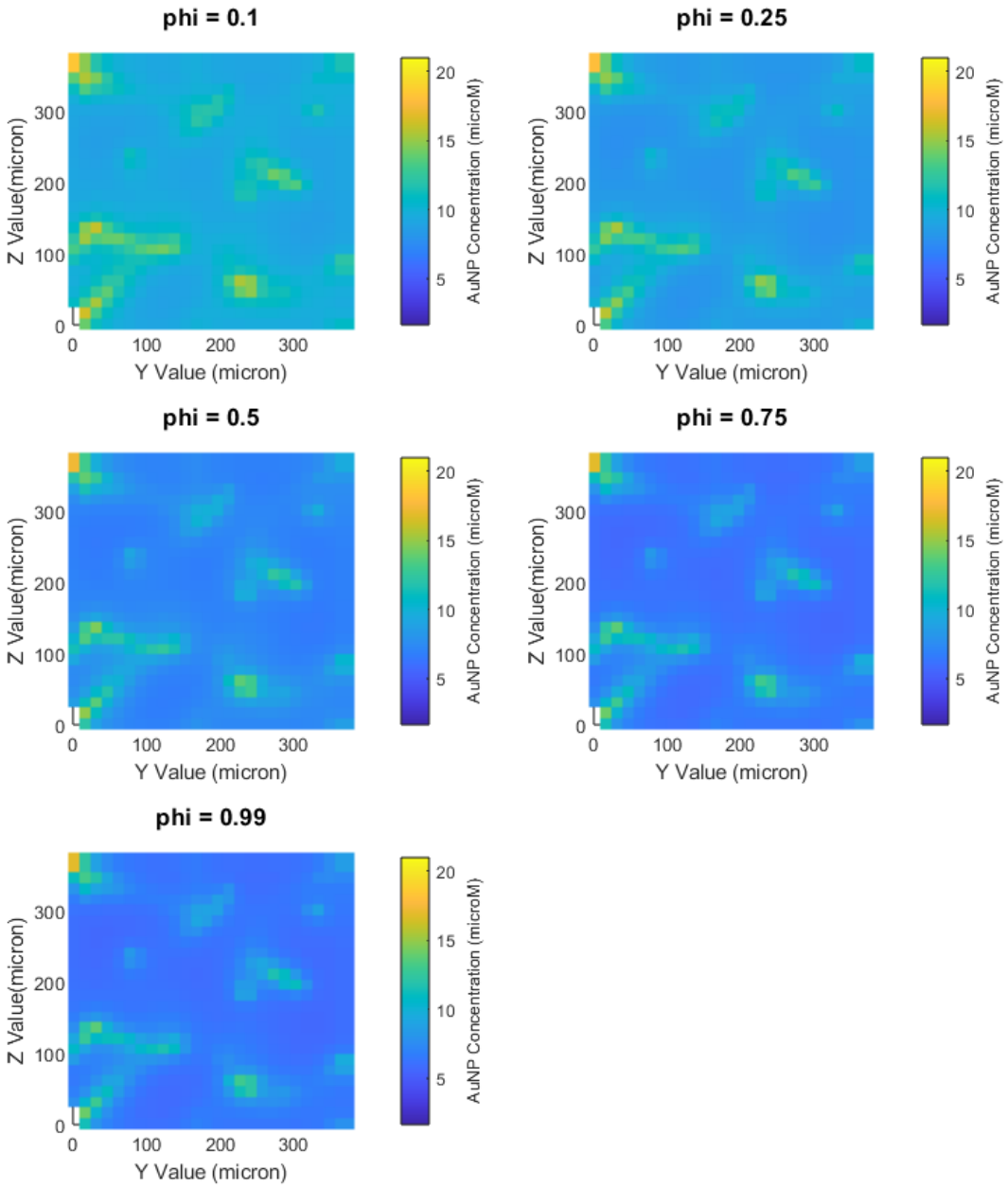

Figure 5.35: Visual comparison of ICVF impact on AuNP tissue concentration at a selected slice for the 375-micron network. ICVF fractions were: (a) 0.1, (b) 0.25, (c) 0.5, (d) 0.75, and (e) 0.99. Comparison is taken at a time step of 40 seconds.

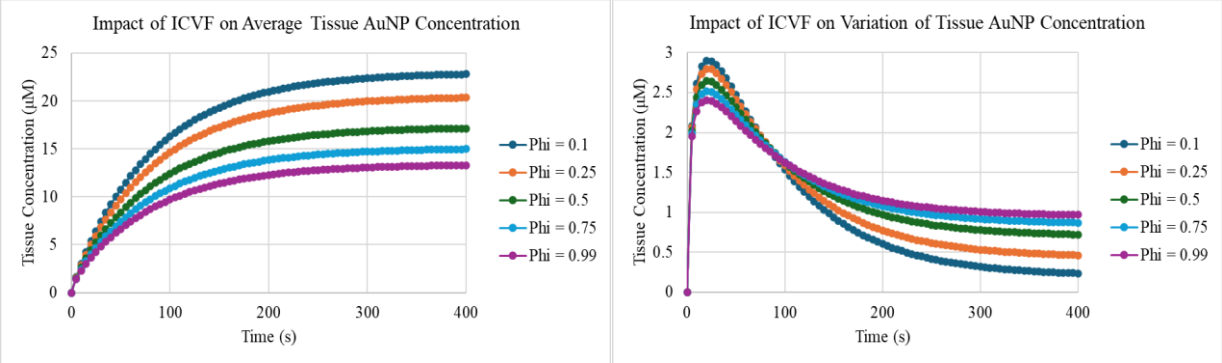

Figures 5.36 & 5.37: Average AuNP concentration (Figure 5.36) and AuNP spatial tissue variance (Figure 5.37) for 375-micron cubes as a function of ICVF.

5.3.4 Sensitivity Analysis

The simulations presented in Sections 5.3.2 and 5.3.3 demonstrate convergence under or toward steady-state conditions, providing a foundation for sensitivity analysis under equilibrium assumptions. By evaluating the system at steady-state, temporal dependencies are eliminated, thereby isolating the influence of four principal independent variables: the diffusion coefficient, the forward rate constant, the ICVF, and the capillary network inlet pressure. This approach permits a more focused examination of how these parameters govern AuNP accumulation in tissue.

Nonlinear regression analysis was performed in Excel using the Data Analysis Toolkit to quantify the individual relationships between each independent variable and the tissue-level AuNP concentration. Table 5.2 presents the nonlinear relationships, regression coefficients, and corresponding R^2 values for each parameter. These analyses are necessary to develop formulas describing the relationship between each input variable and tissue AuNP levels on an individual basis, with the R^2 value describing how well the data fit the regression model.

Table 5.2: Relationship between input parameters and tissue AuNP level with respective formula coefficients and R^2 values.

375-Micron Cube	Relationship to AuNP Tissue Level	Form	Coefficient Values	R Square
Diffusion Coefficient	Inverse	y = b/x + a	a = 24.449 b = -6.1e-12	0.992
Forward Rate Constant	Linear	y = bx + a	a = 24.820 b = -4.999	0.988
ICVF	2nd Order Polynomial	y = cx^2 + bx + a	a = 24.926 b = -0.640 c = -0.543	0.999
Inlet Pressure	Inverse	y = b/x + a	a = 25.017 b = -18.689	0.997
625-Micron Cube	**Relationship to AuNP Tissue Level**	**Form**	**Coefficient Values**	**R Square**
Diffusion Coefficient	Inverse	y = b/x + a	a = 24.183 b = -1.6e-11	0.985
Forward Rate Constant	Linear	y = bx + a	a = 24.336 b = -8.853	0.984
ICVF	2nd Order Polynomial	y = cx^2 + bx + a	a = 24.639 b = -0.575 c = -1.881	0.999
Inlet Pressure	Inverse	y = b/x + a	a = 25.566 b = -49.590	0.994

To capture potential interactions and combined effects among the three principal variables, a multivariate nonlinear regression analysis was conducted. The regression statistics, presented in Table 5.3, characterize the goodness-of-fit for the multivariate model. The multiple R value indicates the strength of the nonlinear relationship between the combined predictors and the response variable, while the R^2 value quantifies the proportion of variance in tissue AuNP levels explained by the three-parameter model. The adjusted R^2 accounts for the number of predictors, providing a more conservative estimate of model fit. Analysis of variance (ANOVA) was performed to assess the statistical significance of the regression model in Table 5.4.

Table 5.3: Regression statistics of combined linear regression analysis.

Regression Statistics	*375*	*625*
Multiple R	0.989010845	0.985022611
R Square	0.978142451	0.970269544
Adjusted R Square	0.969035139	0.957881855
Standard Error	0.253763277	0.680472696

Table 5.4: Analysis of Variance (ANOVA) of combined linear regression analysis.

325	*df*	*SS*	*MS*	*F*	*Significance F*
Regression	10	69.16230152	6.916230152	107.402	1.99475E-17
Residual	24	1.545499215	0.064395801		
Total	34	70.70780073			
625	*df*	*SS*	*MS*	*F*	*Significance F*
Regression	10	362.6798979	36.26798979	78.3253	7.76537E-16
Residual	24	11.11303417	0.463043091		
Total	34	373.7929321			

The ANOVA decomposition partitions the total variance into components attributable to the regression model and residual error. The F-statistic and associated p-value test (Significance of F) the null hypothesis that all regression coefficients are zero, thereby validating the model's explanatory power. The values df, SS, and MS are the degrees of freedom, Sum of Squares (variation in the dependent variable explainable by the model), and Mean Square respectively.

The sensitivity parameters derived from the multivariate regression are presented in Table 5.5, revealing the standardized coefficients, standard errors, t-statistics, upper and lower confidence intervals, and p-values for each dependent variable. Of these parameters, the t Stat and P-value are the biggest predictors of dependent variable impact and sensitivity.

Table 5.5: Sensitivity parameters of combined linear regression analysis.

375	*Coefficients*	*Standard Error*	*t Stat*	*P-value*	*Lower 95%*	*Upper 95%*
Intercept	25.34858487	0.580708582	43.6511	2.2E-24	24.15006127	26.54710848
Diffusion Coefficient	-6.14684E-12	2.5155E-13	-24.436	1.8E-18	-6.66602E-12	-5.62767E-12
Forward Rate Constant	-5.054244501	0.229292964	-22.043	1.9E-17	-5.52748192	-4.581007082
ICVF	0.142021814	0.932231009	0.15235	0.88019	-1.782008424	2.066052051
Inlet Pressure	-1.437482252	12.21150946	-0.1177	0.90727	-26.64079906	23.76583456
625	*Coefficients*	*Standard Error*	*t Stat*	*P-value*	*Lower 95%*	*Upper 95%*
Intercept	25.59945021	1.557184869	16.4396	1.5E-14	22.38557859	28.81332182
Diffusion Coefficient	-1.60121E-11	6.74537E-13	-23.738	3.5E-18	-1.74043E-11	-1.46199E-11
Forward Rate Constant	-9.460834994	0.614854929	-15.387	6.2E-14	-10.7298332	-8.19183679
ICVF	-1.752232438	2.499801217	-0.7009	0.49008	-6.911568575	3.407103698
Inlet Pressure	-12.40325583	32.74547396	-0.3788	0.70818	-79.98659242	55.18008077

5.3.5 Conclusions

Steady-state and time-dependent Green's function method models were developed for AuNPs with extra- to intracellular transport characterized through an integrated two-compartment model. These combined set of models were employed to simulate diverse datasets and parameters. A sensitivity analysis was then performed on the input variables of diffusion coefficient, ICVF, forward rate constant, and capillary network inlet pressure. The underlying assumptions and generated data of this chapter will be discussed in greater detail in the following section.

5.4 DISCUSSION

5.4.1 Introduction

In the previous sections, an AuNP model was presented that utilised a Green's function method and described solute delivery to brain tissue. Due to the complex nature of this computational model, a variety of simulations were conducted to develop a greater understanding of the impact of several quantities on the system. In this section, these simulations are analysed and compared in order to improve the model for future research.

5.4.2 Steady-State Cases

The first set of experiments for the steady-state cases investigated diffusion coefficient variation and its impact on AuNP concentration within the brain tissue. The diffusion coefficient values were selected based upon a previously described range of nanoparticle diameters and on blood viscosities ranging from $3x10^{-3}$ Pa*s to $4x10^{-3}$ Pa*s. Using the equations provided by Shamloo *et al*. and Chen *et al*., it was found that for a large nanoparticle diameter and a high blood viscosity the diffusion coefficient would be low (~$5x10^{-13}$ m^2/s). Conversely, a small nanoparticle diameter and low blood viscosity would give a diffusion coefficient of approximately $4x10^{-11}$ m^2/s. This behaviour is consistent with physical expectations, as large-diameter nanoparticles encounter difficulty traversing the smaller pores of the blood-brain barrier, whereas the small nanoparticles face no such impediment. Regarding blood viscosity, an elevated value relates to the increased resistance a nanoparticle encounters moving radially towards the vessel walls.

Concerning tissue AuNP concentration itself, it was observed that as the diffusion coefficient increases the tissue concentration also increases. This was tested from value of $1x10^{-12}$ m^2/s up to a value of $4x10^{-11}$ m^2/s. Values lower than $1x10^{-12}$ m^2/s approached an asymptote as concentrations reached nonphysical values. Values beyond $4x10^{-11}$ m^2/s were tested to observe the overall relationship in greater detail and determine the upper limit. Figures 5.11 through 5.13 above demonstrate these behaviours and show that the upper limit is the inlet concentration of AuNPs – in this case, 25 μM.

This physically aligns with expectations: as the diffusion coefficient increases, the barrier to AuNP transport decreases, and the tissue domain approaches homogeneity as AuNPs penetrate deeper into the tissue. This is further corroborated when observing variance changes resulting from increasing tissue diffusion coefficient. As the diffusivity approaches large values, the variance

drastically decreases and approaches 0. This may be observed in Figures 5.11 through 5.14. This effect displays diminishing returns, as physical limitation remains inlet concentration: there is little change between $10x10^{-10}$ m^2/s and $10x10^{-9}$ m^2/s in terms of tissue concentration or variability.

It was expected that AuNPs transport behaviour would differ from oxygen in transport behaviour due to the various differences in parameters and transport mechanism, despite both utilising the same vessel pathways. Figures 5.7 and 5.8 illustrate this difference while providing the opportunity to check for obvious numerical artefacts or unexplainable phenomena. One divergence in distribution pattern is AuNPs tended to accumulate in greater relative concentration in tissue spaces between vessels, likely due to the lack of a consumption term for AuNPs. This is further substantiated by the considerably higher normalised AuNP tissue concentrations compared to those of oxygen, a direct result: the lowest normalised values for AuNPs were 0.9604 for the 375-micron cube and 0.947 for the 625-micron cube, while the lowest normalised values for oxygen were 0.343 and 0.284 respectively. As was noted in Chapter 4, the larger 625-micron cube will typically display lower average solute tissue concentration and higher spatial variability due to the smaller pressure gradient per unit length ratio.

The subsequent simulations focused on the transport between the extracellular and intracellular compartments with the results presented in Figures 5.15 through 5.18. For preceding experiments and particularly this series, it was assumed that the supply of AuNPs is constant and that there is no consumption or degradation at any point in the transport process from blood to cell. These assumptions are critical in explaining the observed results, where increasing the forward rate constant (tissue-to-cell) yields elevated AuNP concentrations within the cellular compartment.

Increasing the rate from 0.1 1/s to 1 1/s resulted in a 726.12% increase in average intracellular AuNP concentration. This was accompanied by a decrease in AuNP extracellular

concentration, with average values declining by 17.396%. While the supply of AuNPs from the blood vessels remains constant, the cellular compartment must draw from available sources, and this increased uptake lowers the steady-state concentration of AuNPs within the extracellular space. The tissue (and by extension cells) closest to the blood vessels are the first to uptake AuNPs, and much like the observations on varying oxygen consumption in Chapter 4, the tissue further away receives less. This results in increased variability in both the average AuNP tissue concentration and the spatial variance of tissue concentration as the tissue-to-cell rate constant increases, as demonstrated by the increased size of boxes and whiskers within the plots.

The next set of experiments focused on cellular density within the tissue space. It was observed that increasing the ICVF decreased the AuNP concentration while also increasing concentration variability across the tissue space. An increase in ICVF dictates that there are more cells receiving AuNPs, thus reducing the amount available in the extracellular space in a manner similar to that found in rate constant experiments. Conversely, a lower ICVF implies a space populated with fewer cells receiving AuNPs and more open extracellular matrix. The magnitude of change is smaller here: there was only a 2.949% decrease in average AuNP tissue concentration between the relatively empty ICVF of 0.1 to an average value of 0.5 and a further decrease of 3.148% between an ICVF of 0.5 to the denser 0.99.

Finally, the influence of the capillary network inlet pressure on tissue AuNP concentration was examined. As the inlet pressure increased from a value of 20 mmHg to 100 mmHg, AuNP concentration also increased, though with diminishing returns. This is due to Poiseuille's Equation: for a capillary vessel (and provided all other parameters are held constant), an increase in the inlet pressure results in a linear increase in blood flow rate for that vessel. This increase in blood flow further results in an increase in AuNP delivery to deeper sections of the tissue as the delivery

transitions from diffusion dominated to flow dominated. However, like ICVF, the magnitude of change is small: average AuNP tissue concentration only increased by 2.090% from an inlet pressure of 20 mmHg to 50 mmHg and 0.468% for 50 mmHg to 100 mmHg.

5.4.3 Time-Dependent Cases

The investigation in the first set of simulations focused on tissue concentrations of oxygen and AuNPs over the time range of 0 to 400 seconds with a time step of 5 seconds. It was previously observed in Chapter 4 that the oxygen concentration curves were smooth with time, but the spatial variance curves were not smooth when utilising a variable time step scheme. At the point where the time step changed from 1 second to 10 seconds (t = 40 seconds), variance magnitude briefly spiked before resuming exponential decay. To avoid this phenomenon, a constant time step of 5 seconds was selected to balance sufficient temporal resolution with computational efficiency for most simulations (see Chapter 4). Figures 5.23 and 5.24 display the temporal behaviour of the two solutes and display smooth curves for both concentration and spatial variance, demonstrating the validity of this approach.

Figures 5.25 and 5.26 display the average tissue AuNP concentration and concentration variance respectively. These figures compare the 375- and 625-micron networks with tissue concentrations no longer normalised, as the comparison focuses on network impact on tissue concentration rather than oxygen versus AuNPs. It was observed that the 375-micron network achieved a steady-state value of 17.14 μM and the 625-micron network a value of 16.17 μM, though the 375-micron network achieved steady-state more rapidly than the 625-micron network. The spatial variation of the two networks also behaved in the manner previously discussed.

Next, tissue diffusivity was varied to observe its effect on AuNP tissue concentration over time. Results were presented in Figures 5.27 through 5.29. Consistent with steady-state simulations,

increasing the diffusion coefficient increased the average tissue concentration. This aligns with previous discussion on the topic: as the diffusion coefficient increases, the barrier to AuNP transport decreases, and the space approaches homogeneity as the AuNPs penetrate deeper into the tissue. Furthermore, as the diffusivity approaches large values, the variance drastically decreases and approaches 0. Increasing the diffusion coefficient also renders the exponential decay in variance shallower: the tissue concentration approaches homogeneity much more rapidly for larger diffusion coefficients. There are diminishing returns for this effect, as the physical limitation is inlet concentration: minimal change occurs between $10x10^{-10}$ m^2/s and $10x10^{-9}$ m^2/s with respect to tissue concentration or variability.

Figures 5.30 through 5.34 displayed the results of varying the forward rate constant between tissue and cellular compartments. In the steady-state simulation, increasing the rate from 0.1 1/s to 1 1/s resulted in a 726.12% increase in average cellular AuNP concentration coupled with a 17.396% decrease in AuNP extracellular concentration. The time range for these simulations was only 0 to 40 seconds, as there were convergence issues at longer times.

The movement of the AuNPs to the cellular compartment is analogous to oxygen consumption: the cellular compartment receives AuNPs from the tissue, lowering the average concentration of AuNPs within the extracellular space. The tissue (and by extension cells) closest to the blood vessels are the first to receive AuNPs from blood vessels which causes the tissue further away to receive less. This results in greater tissue AuNP variability as the tissue-to-cell rate constant increases, consistently observable as time increases from 0 to 40 seconds.

The final set of simulations focused on cellular density within the tissue space and were presented in Figures 5.35 through 5.37. It was noted that increasing the ICVF decreased the AuNP concentration while also increasing the variability of concentration values across the tissue space.

An increase in ICVF dictates that there are more cells receiving AuNPs, thus reducing the amount available in the extracellular space in a manner similar to that found in the rate constant simulations. Conversely, a lower ICVF implies a space populated with fewer cells receiving AuNPs and more open extracellular matrix. This phenomenon was observed consistently across the time range of 0 to 400 seconds.

5.4.4 Sensitivity Analysis

The sensitivity analysis from nonlinear regression presented in Section 5.3.4 provides insight into the mechanistic drivers of AuNP distribution within tissue compartments. From the nonlinear analysis, it was observed that each input variable (diffusion coefficient, forward rate constant, ICVF, and capillary network inlet pressure) has a different relationship to AuNP levels: the diffusion coefficient follows an inverse formula, the forward rate constant a linear formula, the ICVF a 2nd order polynomial, and finally the inlet pressure an inverse formula (with different parameters). Of the four, the ICVF formula displayed the best fit to available AuNP data with an R2 value of 0.999 for both tissue cube sizes. All R^2 values were above 0.95, suggesting that the data strongly fit each respective regression model.

The Multiple R and R^2 values in Table 5.3 characterize the collective explanatory power of the four-parameter model. A positive Multiple R approaching a value of 1 indicates that the diffusion coefficient, forward rate constant, ICVF, and capillary network inlet pressure, considered together, account for a substantial portion of the variability in tissue AuNP concentration. The R^2 value was previously explained, while the adjusted R^2 provides assurance that model fit is not artificially inflated by the inclusion of multiple input variables.

The ANOVA results (Table 5.4) test whether the regression model provides a significantly better fit than a null model (intercept only). A large F value (in this model 107.40 and 78.325 for

the 375 and 625 cube) and low p-value (typically below 0.05, in this model 1.99e-17 and 7.77e-16) associated with the Significance F-statistic confirms that at least one of the independent variables significantly influences the dependent variable, further validating the utility of the multivariate model.

Table 5.5 offers detailed insights into individual parameter contributions within the multivariate context. Of the available regression data, the t-statistics and associated p-values test are most significant for predicting which independent variable has a greater impact on the dependent variable after accounting for covariance. Typically, the further the t-statistic is away from zero and the lower the p-value is, the more impactful the associated input variable. From the regression model it is observed that diffusion coefficient, with t-statistic/p-value pairs -24.44/1.8e-18 for the 375 cube and -23.74/3.5e-18 for the 625 cube, is the largest predictor of tissue AuNP concentration, though the forward rate constant is a close second. The ICVF is reported to have little impact on tissue AuNP concentration, with a t-statistic/p-value pair of 0.152/0.880 for the 375 cube and -0.701/0.490 for the 625 cube. The inlet pressure displayed similar low impact, with a t-statistic/p-value pair of -0.118/0.907 for the 375 cube and -0.379/0.708 for the 625 cube. Considering the similar values of coefficients and similar regression statistics for both the 375-micron and 625-micron cubes, tissue domain size and flow rate have little impact on tissue AuNP concentration.

From this nonlinear regression, it is observed that tissue AuNP concentration is most sensitive to changes in the diffusion coefficient and forward rate constant. When designing nanoparticles, modifications that enhance or alter diffusive transport (such as size optimisation or surface functionalisation) will most improve therapeutic delivery to the tissue space. While only tissue concentrations were compared between the three parameters, the forward rate constant

displaying over a 700% increase in intracellular concentration for a ten-fold increase in rate constant value highlights its effectiveness for therapeutic delivery. This is done through choice of functional group, as this parameter can affect solubility and surface charge. Finally, it was observed that tissue concentration is less sensitive to ICVF and inlet pressure. This does not equate to zero relationship: despite being unoptimisable, both ICVF and the rate of blood flow to the capillary bed should be considered in therapeutic design as both directly relate to clinical cases.

The linear regression framework assumes additive, independent contributions from each parameter. While the OAT sensitivity analysis provides valuable insight into the design and transport of AuNPs, it may not fully capture higher-order interactions or the entire design space. Alternatives to the OAT method are discussed in Chapter 6 as future work to develop more rigourous sensitivity analyses.

5.4.5 Significance and Validity of Results

The primary innovation of Chapter 5 is the adaptation of a Green's function method to model gold nanoparticle transport across the blood-brain barrier. The work demonstrates originality in its statistical analysis spanning multiple synthetic networks and parameters. This approach is relatively unexplored: most experimental and numerical investigations focus on a single subject with univariate parameter analysis. The developed model not only addresses this gap in literature but also provides a framework for future studies expanding upon alternative nanotherapeutics and other design spaces with respect to these results.

Systematic variation of key parameters (tissue diffusivity, tissue-to-cell rate constant, and ICVF) established quantitative bounds on AuNP tissue concentrations. Increasing the diffusion coefficient produced diminishing returns of AuNP levels and spatial variance reduction; conversely, increasing the rate constant linearly decreased extracellular AuNP levels while greatly

increasing intracellular AuNP levels. The behaviours of these two parameters warrant particular interest given the modifiable nature of both parameters for therapeutic optimisation.

A set of unexpected results emerged from these investigations. It was observed that while both ICVF and capillary network inlet pressure do affect AuNP tissue concentration, a sensitivity analysis revealed that the solute concentrations are only mildly sensitive to variations in cellular density or flow rate. In contrast, both diffusion coefficient and forward rate constant displayed strong correlations (diffusion coefficient showing slightly more influence) The sensitivity analysis reinforces that the focus of therapeutic delivery schemes should focus on AuNP design, such as modifying surface ligands or molecular weight and density.

Several of the assumptions defined in Chapters 4 and 5 are formulated to enable computational model validation with respect to oxygen and subsequently simulate AuNPs. To enable these simulations, several AuNP transport mechanisms and parameters were simplified, not considered, or employed the same assumptions as oxygen. This will potentially cause discrepancies between simulated AuNP data and experimentally gathered data in future studies, when such data become available. The AuNP computational utilised two oxygen model assumptions that may not accurately reflect physiological phenomena: one, the vessel wall is characterised as tissue space rather than a barrier to AuNP transport, and two, both employed the same blood-phase transport mechanisms.

Oxygen freely diffuses across the BBB, but the BBB is meant to be a barrier to the diffusion of other solutes. While a vessel wall simplification facilitates AuNP transport modelling, it may not reflect physiological reality. Given that the BBB directly affects transport further study into this simplification is required. As for blood-phase modelling, the transport of oxygen and AuNPs in blood proceeds under different mechanisms. AuNPs are modelled as freely suspended in blood,

while oxygen is widely known to bind with haemoglobin in red blood cells. Consequently, the effective blood-phase diffusivity and vessel wall flux will differ substantially between the two solutes.

There are additional realistic conditions and features that, when included in the current model framework, may affect AuNP transport predictions: AuNP inlet concentration is temporally variable in therapeutic settings, AuNPs may interact with red blood cells and oxygen, pathological conditions typically affect the vessel network, and finally the AuNP solubility coefficient is variable and affects effective diffusivity. These design considerations, presented previously in Chapters 4 and 5, were not included for discussed reasons but may influence the validity and accuracy of the Green's function models. Several of these features are easily adjustable or capable of inclusion within the model architecture; the rest require further study or require data not presently available. Although all enumerated design considerations for AuNP transport simulation hold true and merit further study, constraints on the scope of this thesis necessitated selective examination of these features, discussed further in Chapter 6.

5.5 CONCLUSIONS

The work presented above has been dedicated to creating a gold nanoparticle pharmacokinetic model that utilises a two-compartment conservation of mass model paired with a Green's function method. The current working model successfully generates data predicting the transport of AuNPs to cerebral tissue under steady-state and time-dependent conditions. Three primary input parameters (diffusion coefficient, tissue-to-cell rate constant, and ICVF) were analysed to explore nanoparticle therapeutic design considerations. It was found through sensitivity analysis that AuNP properties have a significant effect on AuNP tissue concentrations. The findings here also highlight limitations of the current model with respect to advanced model features; these limitation present opportunities for prospective future research projects that will further improve model validity and applicability. These potential research topics will be discussed in Chapter 6.

CHAPTER 6: SUMMARY AND FUTURE WORK

6.1 SUMMARY

The purpose of this thesis was to develop a series of mathematical models that execute two tasks: one, recreate the blood flow environment within a variety of vascular networks; and two, model nanoparticle transport within this environment. This was performed through a variety of research, models, and data that were presented in the previous chapters. Chapter 1 of this thesis outlined the background of nanoparticle delivery in the human brain, the current challenges of this problem, and scope of this work.

Chapter 2 contained a comprehensive literature review detailing research into the four cerebral haemodynamic fields that have relevance to the thesis: cerebral arterial structure, microcirculation and perfusion, cerebral autoregulation, and nanoparticle pharmacokinetics. Within each topic, both qualitative and quantitative theory was presented with a focus on information pertinent to the models developed in this thesis. Research into each of these four haemodynamic fields yielded a variety of models: a select few were chosen to be further developed for this work. For the cerebral arterial structure and autoregulation, an algorithm was adapted from work by Badiani 2018 to determine flow data within patient networks presented by Wright *et al*., 2018.

A range of microcirculation models was presented: ultimately, a Green's function method model based upon work previously performed by Secomb was developed to analyse behaviour at this length scale. This model simulated both oxygen and gold nanoparticles and did so in a variety of capillary networks under both steady-state and time-dependent conditions. Simulations were performed on statistically generated synthetic capillary networks developed by El-Bouri. The Green's function method model was supplemented with parameters and pharmacokinetics drawn from Foehrenbacher *et al*., 2013, Zhou *et al*., 2018, and Chen *et al*., 2022.

Chapter 3 of this thesis presented the results of the large artery and autoregulation model. This model successfully implemented 3D arterial blood flow models based upon real world morphological patient-specific information. Data were generated describing cerebrovascular blood flow, such as volumetric flow rate and pressure, and compared against literature sources.

Chapter 4 was dedicated to creating a capillary blood flow model based upon the Green's function method and utilising synthetic networks. The work of Secomb, El-Bouri, Payne, and Xue was synthesised to develop this model. The current working model successfully generated data describing capillary blood flow and the transport of oxygen to cerebral tissue under both steady-state and time-dependent conditions. After discussing the experimental variations and the impact of different parameters upon the results, it was determined that the computational model is accurate and applicable to gold nanoparticles.

Chapter 5 adapted the model of Chapter 4 for the simulation of gold nanoparticle transport in human microvasculature. A AuNP pharmacokinetic model was developed that utilises a two-compartment conservation of mass model paired with the Green's function method. Again, this model was applied to synthetic networks developed by El-Bouri under steady-state and time-dependent conditions, with a sensitivity analysis performed at the end of the chapter analysing the impact of certain input parameters.

The various models presented in Chapters 3 through 5 successfully create a multi-model work that generates results describing cerebrovascular blood flow and solute levels (whether oxygen or gold nanoparticles). With that said, there is room for improvement within the models to more accurately simulate clinical settings for the design and optimisation of AuNPs. Such topics include the implementation of a variable input scheme for AuNP dosage, research and inclusion

of a AuNP solubility coefficient, effect of functionalisation and surface charge on tissue-to-cell rate constants, and many more.

The above topics represent future work specific to AuNPs; the research areas discussed and developed here represent more general modifications to improve overall model accuracy and applicability. These topics are: the performance of an alternate sensitivity analyses, including the vessel wall for modelling nanoparticle pharmacokinetics, modelling other nanoparticle types to develop the versatility of the models presented previously, and finally coupling of all the models presented throughout this thesis.

6.2 FUTURE WORK

6.2.1 Sensitivity Analysis

In Chapter 5, a sensitivity analysis was performed on the nanoparticle models under steady-state conditions with the purpose of determining which input variables have the largest effect when varied in addition to a variety of other benefits. Specifically, the diffusion coefficient, ICVF, and forward rate constant for cellular uptake were examined for this analysis.

Sensitivity analyses are a vital step in optimisation schemes, providing data that quantify the degree that changes in function parameters have on the optimal objective function value and the optimum itself (Castillo *et al*., 2008). For therapeutic design and delivery, the targets for optimisation are typically the accumulation amount of drug at a specific target site, clearance time of the drug, drug efficacy, and drug toxicity (Rana *et al*., 2023). These targets depend on a variety of factors but generally fall into the broad categories of biocompatibility, drug loading rate, and targeting efficiency (Jia *et al*., 2021). Should the model be developed further, these parameters will need to be examined as well.

Concerning this thesis, the most relevant targets for optimisation are nanoparticle accumulation and clearance time; these in turn depend on parameters such as particle diameter, surface charge, weight, shape, and chemical composition. Quantifying the effect that varying these parameters has on nanoparticle tissue accumulation may provide advice to those developing medical therapies, allowing for the design of a desired nanoparticle delivery system (Jia *et al*., 2021).

The sensitivity analyses performed in Chapter 5 were the simplest: the one-at-a-time (OAT) or one-way method. These analyses focused on the diffusion coefficient, ICVF, and rate constant as representative variables for the above parameters. The OAT method was chosen for its simplicity and straightforward comparison of results; however, the OAT method does not fully explore the input space as simultaneous variation of input variables is not considered. Four of the other common methods of sensitivity analysis are presented with a discussion of which is most appropriate for this model.

The first method, the derivative-based local methods, is a broad set (Qian & Mahdi, 2020). These methods involve taking the partial derivative of the output variable Y with respect to an input variable X. The sensitivity is determined through the size of the derivative, which itself is a measure of the perturbation caused by changes in variable X. These methods, like the one-at-a-time method, do not explore the entire input variable space, causing them to also not be as comprehensive as other global methods and may be more computationally intensive should a large number of input and output variables be present in the system. With the local methods, though, one may easily compare all the sensitivities through matrices, which may be beneficial for the case of many input and output variables (Qian & Mahdi, 2020).

Regression analysis is another method available for sensitivity analysis. As the name suggests, this method involves fitting linear regressions to the model responses and using the standardized regression coefficients as a measure of the sensitivity. This method may only be used if the model response is linear but boasts low computational cost and simplicity of analysis (Qian & Mahdi, 2020).

The third method is again a set of methods, the variance-based methods, often referred to as Sobol' method (Qian & Mahdi, 2020). These methods are probabilistic in nature, quantifying the input and output uncertainties as probability distributions. The output variance is then decomposed into parts associated with input variables and combinations of input variables. Sensitivity is measured by the amount of variance in the output caused by the input variable. These methods, unlike the previous methods, consider the entire input space rather than just points within, allowing them to handle interactions of variables and nonlinear responses. Due to the large number of simulations that need to be run for these methods to be utilised (Monte Carlo methods are often used for the calculations), variance-based methods are extremely expensive in terms of computation (Qian & Mahdi, 2020).

The final method presented here is the more recently developed variogram analysis of response surfaces method (VARS method for short) (Razavi & Gupta, 2016). The VARS method is capable of handling models with a spatially ordered response output (or response surface, hence the name) using variograms and covariograms. As the variability increases, the more heterogenous the response surface is along a particular direction or parameter for a specific perturbation scale; the variograms and covariograms are thus illustrations of the sensitivity themselves. The VARS method overcomes the scale limitations of the previous methods by considering the scale of the

analysis in its calculations. This is possible due to the sensitivity being scale dependent, which consequently produces low computational cost for the calculations.

For this research, with its variety of inputs and output variables across a large 3D space, the derivative-based local methods are not as applicable. Furthermore, due to computational restraints the variance-based methods are currently not ideal. Finally, considering the nonlinearity of the models used in this thesis, a regression analysis would not be feasible. Taking all these aspects into consideration, the currently used one-at-a-time or the VARS method would be viable for a sensitivity analysis regarding this research. The VARS method would be more comprehensive as it considers the entire input space and would have a low computational cost, making it the ideal choice; in the future, when more tuneable parameters are considered in the sensitivity analysis, the VARS method would be chosen rather than the OAT method.

6.2.2 Vessel Wall Modelling

One of the assumptions made for the nanoparticle microvasculature transport model is that the vessel wall offers little resistance and is considered to be part of the tissue. For oxygen, this is a natural assumption and is often implemented for many oxygen transport models; as oxygen is a vital resource for cerebral tissue, it is able to freely diffuse across the blood-brain barrier (Gawdi, 2023). This assumption does not necessarily hold true for nanoparticles, gold, PEGylated, or otherwise. A comparison of the endothelial diffusion coefficient (m^2/s) and the tissue diffusion coefficient (m^2/s) for AuNPs may be calculated using equations taken from Chen *et al*., 2022 discussed in Chapter 2 and reproduced below. For these equations, η is the membrane shear viscosity (Pa*s), k_B is the Boltzmann constant ($m^2*kg/s^2/K$), T is temperature (K), r_H is the particle hydrodynamic radius (nm), r is the particle actual radius (nm), and r_{pore} is the average radius of pores in the membrane, typically 10 nanometres (Chen *et al*., 2022).

$$D_{Tissue} = 0.56\frac{k_B T}{6\pi\eta r_H} \tag{6.1}$$

$$D_{endo} = D_B\left(1-\frac{r}{r_{pore}}\right)^2\left(1-2.1044\left(\frac{r}{r_{pore}}\right)+2.089\left(\frac{r}{r_{pore}}\right)^3-0.948\left(\frac{r}{r_{pore}}\right)^5\right) \tag{6.2}$$

Both equations are primarily dependent on particle radius: the upper and lower values chosen here are 1 to 101 nanometres (adapted from Table 2.2). For the purpose of calculating the endothelial diffusion coefficient, values for the actual particle radius are assumed to be the hydrodynamic radius divided by 4.35 (Chen *et al*., 2022). It was found that for AuNP diameters of 11 nm and below, the tissue diffusion coefficient was smaller than the endothelial diffusion coefficient. Past 11 nm, the tissue diffusion coefficient grew larger than the endothelial diffusion coefficient. Due to the nonlinear nature of Equation 6.2, the endothelial diffusion coefficient reached nonphysical values starting at AuNP diameters of 81 nm and above. Graphical comparisons of these diffusion coefficients are shown below in Figures 6.1 and 6.2 as loglog plots.

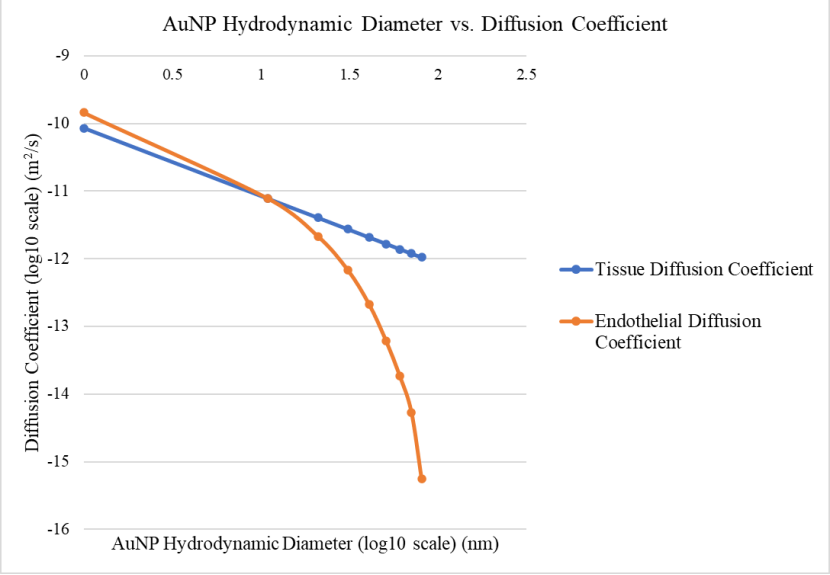

Figure 6.1: Comparison of the endothelial wall diffusion coefficient and the tissue coefficient as a function of AuNP hydrodynamic diameter. Both are calculated using a modified Equation 2.15 and Equation 2.18 taken from Chen *et al*., 2022.

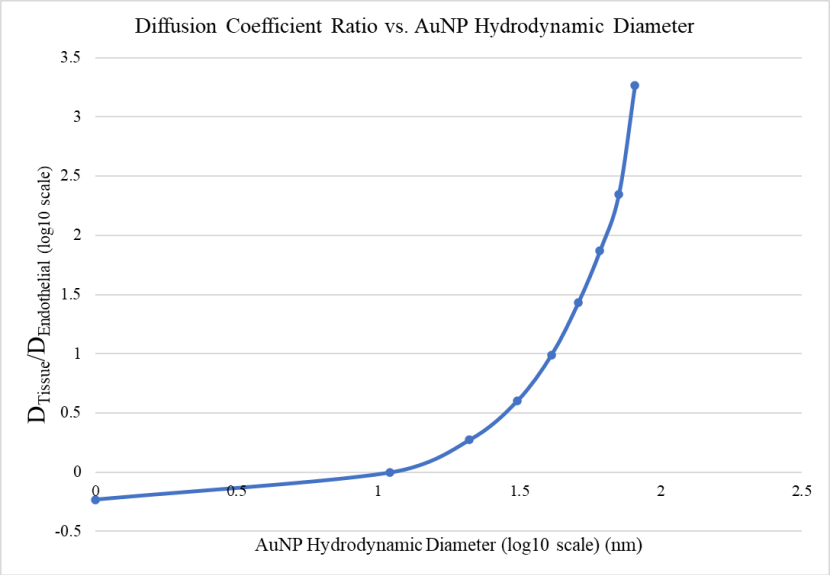

Figure 6.2: Ratio of tissue diffusion coefficient and endothelial wall diffusion coefficient as a function of AuNP hydrodynamic diameter. Both are calculated using a modified Equation 2.15 and Equation 2.18 taken from Chen *et al*., 2022.

Based upon the parameters discussed above, the diffusion coefficient for the tissue and the endothelial wall may vary to a significant degree. Conservatively, the assumption that these two regions may be considered as one for the sake of simplicity only holds true for particles up to 11 nm; more relaxed constraints could be a D_{Tissue}/D_{endo} ratio of 2 (found at particle size 22 nm) and 10 (particle size of 42 nm). Anything beyond an order of magnitude difference is unlikely to allow for a homogenous vessel/tissue space, thus requiring different or additional models to account for larger particle diffusion.

A variety of models may be considered to account for the effect of the blood-brain barrier on solute transport, but only a few may be properly utilised. The previous model utilised two compartments: one for the blood, and one for the tissue. The simplest solution is to add a third compartment to account for the endothelial wall effects on passive transport. The diffusion

coefficient for the endothelial wall compartment would be calculated using Equation 6.2 above. While this specific equation has been shown to have limited usage for larger-sized nanoparticles, the implementation of a three-compartment model would allow for quick modifications to the parameters within once diffusion coefficients are found for larger nanoparticles (either from other mathematical models or from experimental data).

A three-compartment model may also be considered for other nanoparticle types (see Section 5.2.3), even if they utilise active transport over passive transport. Active transport mechanisms include receptor- and adsorption mediated endocytosis and apply to nanoparticle structures such as liposomes and large polymers. This gives three ordinary differential equations based upon the mass transport equation that differ from the diffusion differential equations by not including a diffusive term. Equations 6.3 through 6.5 below show a typical set of three compartment model first order equations (Khan *et al*., 2018).

$$\frac{dC_{blood}}{dt} = -k_1 C_{blood} + k_{-1} C_{endo} \tag{6.3}$$

$$\frac{dC_{endo}}{dt} = k_1 C_{blood} - (k_{-1} + k_2) C_{endo} + k_{-2} C_{Tissue} \tag{6.4}$$

$$\frac{dC_{Tissue}}{dt} = -k_{-2} C_{Tissue} + k_2 C_{endo} \tag{6.5}$$

In these equations, *C* refers to the concentration of nanoparticle solute (μM) within a compartment and k refers to the rate constant (1/s). Subscripts are given as blood, endothelial cells, and tissue for the concentration, while for the rate constant 1 refers to transfer from the blood to the endothelial cell and 2 from the endothelial cell to the tissue. A negative subscript for the rate constant denotes a reverse rate constant. Rate constants are often determined experimentally and thus will vary depending on nanoparticle choice and testing conditions. These equations may be solved provided initial concentrations of nanoparticle and the rate constants are known (Khan *et al*., 2018).

6.2.3 Other Nanoparticles

The focus of this thesis has been on gold nanoparticles and their properties. Of the many available options for nanoparticles, AuNPs were chosen for their low cost, easy parameter tuning, low toxicity, and high stability (Zhou *et al*., 2018). While AuNPs are an excellent nanoparticle choice for medicinal therapies, the reality is that the other nanoparticle types are also commonly used. Liposomal and polymeric nanoparticles are other popular alternatives, while quantum dots see less use due to reports of toxicity (Hardman, 2006). Figure 6.3 below is Figure 2.20 previously shown in Chapter 2, reproduced here for convenience to display a few common nanoparticle types.

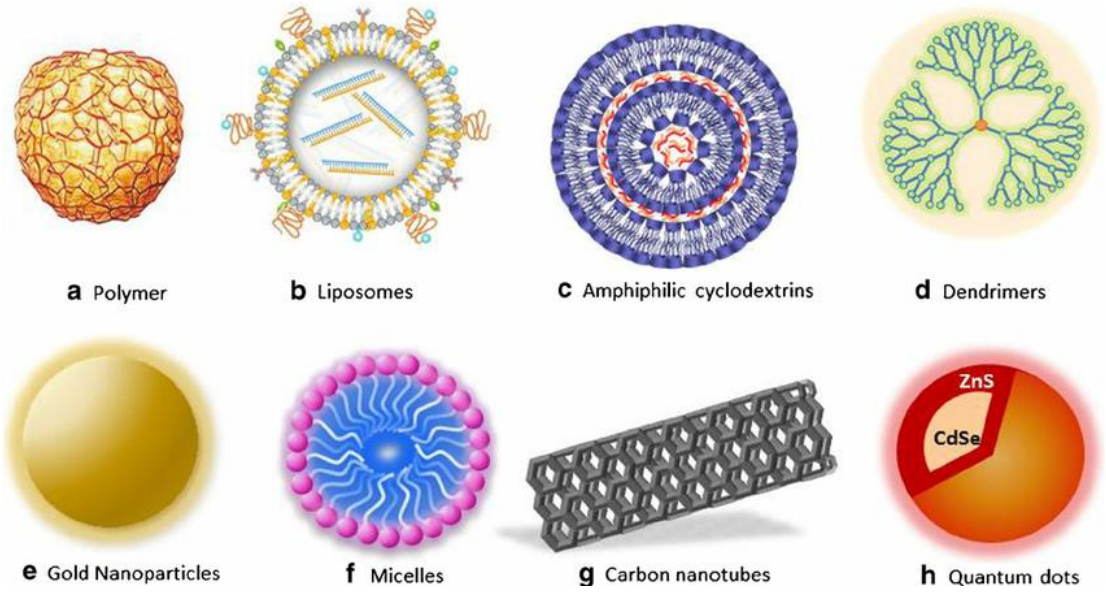

Figure 6.3: 8 most common types of nanoparticles used in therapeutic delivery. Reproduced with permission from McCarthy et. al 2014.

Different nanoparticles will display different pharmacokinetic behaviour due to different size, shape, surface chemistry, and weight. Perhaps the biggest impact on the current model is whether the nanoparticle in question is actively or passively transported. Active transport involves

the concentration of solute being transported against the concentration gradient with the assistance of cellular energy; there is still diffusion, just lower in magnitude compared to the active effects. This will affect many of the transport equations used at the very least and will potentially require an overhaul of how solute transport is implemented within the model.

Besides the transport method there is the question of stability. AuNPs are considered stable with low degradation in the blood stream or within the tissue without special activation conditions. This is not necessarily true for all nanoparticles. Biodegradable nanoparticles, such as protein and lipid nanoparticles are subjected to enzymatic and chemical degradation, with the degradation products usually excreted into urine and bile (Li *et al*., 2017). For liposomal nanoparticles, lack of surface alteration (such as PEGylation) or the presence of a high surface charge density may cause them to be rapidly cleared from cells, tissue, and the blood stream (Juhairiyah & de Lange, 2021). Part of this is due to aggregation, which in turn may further alter the degradation rate (Li *et al*., 2017).

The conditions of the blood and tissue also influence degradation: the *in vivo* acidic and oxidative conditions may change the physiochemical properties of nanoparticles, making the exact degradation process uncertain. This, in conjunction with varying enzyme activity in various tissues, may further complicate the degradation process, as there may be varying degradation rates for a nanoparticle of a single type within the blood and tissues where it accumulates (Li *et al*., 2017).

Some compounds have transitory states or higher degradation rates; they may also be released into the body with an activating co-compound (Li *et al*., 2017). This will complicate the mass balance equations used for determining the amount of solute transport that occurs, either in complexity, number, or both. Fortunately, the current model is capable of handling multiple

compounds undergoing transport, the challenge will be accurately determining and implementing the unique interactions for a compound of interest.

6.2.4 Coupling of the Large Artery, Capillary, and Transport Models

The large artery model, capillary model, and transport model developed within this thesis have been deliberately implemented as uncoupled systems, a decision grounded in both practical and theoretical considerations. The primary justification for maintaining independent model components relates to the necessity for validation against established experimental and clinical data. By decoupling the large artery haemodynamics from capillary-level diffusion and subsequent transport phenomena, each subsystem may be independently validated against its respective literature data without the confounding influence of propagated uncertainties from upstream model components. The influence of upstream model components is exacerbated due to the multi-scale nature of the entire system being simulated.

From a computational perspective, the uncoupled formulation confers substantial advantages in terms of parameter testing and sensitivity analyses. A fully coupled multi-scale model encompassing arterial haemodynamics, capillary perfusion, and advective-diffusive transport would necessitate solving systems with disparate spatial and temporal scales. The resulting computational burden would render analyses for a single parameter of interest difficult to perform. By contrast, the uncoupled approach permits targeted parameter studies within each subsystem, thereby reducing computational cost by several orders of magnitude while maintaining physical fidelity.

Despite the advantages of the uncoupled approach adopted in this thesis, developing a fully coupled multi-scale cardiovascular model is vital for creating a tool for patient-specific needs. Additionally, the impact of autoregulation may only be fully understood within the context of a

full multi-scale model. At all scales there are a large number of parameters that affect autoregulation; in turn, autoregulation affects these parameters, creating a feedback loop. The implementation of fully coupled models will require careful consideration of several challenges. Foremost among these is the treatment of spatial scale separation, wherein phenomena occurring at the millimetre scale of capillary networks must be appropriately homogenised or coarse-grained to interface with centimetre-scale arterial models without incurring prohibitive computational cost. There are techniques, such as the homogenized continuum approach, that offer avenues for bridging these scale disparities (Peyrounette *et al*., 2018).

Temporal multiscale coupling presents additional complexity, as the characteristic timescales of arteries, capillaries, and tissue-level transport phenomena differ drastically (Gopalan & Kirk, 2022). Methods utilised in other fields, such as partitioned time integration, offer a natural framework for addressing this challenge. Utilising a partitioned time integration scheme is a control system technique where different model components advance with time steps matched to their respective temporal scales (Abbiati *et al*., 2019). Alternatively, time-averaged boundary conditions may prove sufficient in terms of accuracy for transport phenomena; further testing will be required.

In conclusion, while the uncoupled modelling approach adopted in this thesis provides a computationally efficient framework for validating and investigating multi-scale cardiovascular phenomena, it is necessary to develop a fully coupled model to most accurately model the entire cerebral vasculature. The foundations established through the development and validation of uncoupled components provide the necessary groundwork upon which the more sophisticated coupled framework may be constructed, ensuring that future integrated models inherit the reliability demonstrated at the component level.

6.3 CONCLUSIONS

In this section various avenues of future research were discussed. Such endeavours range from taking a second look at assumptions to considering the intricacies of other nanoparticle pharmacokinetic models. The research areas presented here provide a strong road map for the expansion and improvement of the gold nanoparticle dynamics computational model.

ACKNOWLEDGEMENTS

I would like to thank Professors Stephen Payne and Eleanor Stride for their continued support and guidance in this endeavour. Their patience and insights are greatly appreciated. I would also like to thank fellow researchers Dr. Wahbi El-Bouri and Dr. Yidan Xue for their assistance with some of the more technological aspects of this thesis. Finally, I would like to thank Dr. Timothy Secomb for his availability in answering technical questions about his open-source Green's function method code.

REFERENCES

1) Abbiati G, Lagnese I, Cazzador E, Oreste SB, Pavese A. "A Computational Framework for Fast-Time Hybrid Simulation Based on Partitioned Time Integration and State-Space Modeling". *Structural Control and Health Monitoring*, **26**, (2019).
2) Acosta S, Penny DJ, Rusin CH. "An Effective Model of Blood Flow in Capillary Beds". *Microvascular Research*. **100**, 40-47 (2015).
3) Alastruey J, Parker KH, Peiró J, Byrd SM, Sherwin SJ. "Modelling the Circle of Willis to Assess the Effects of Anatomical Variations and Occlusions on Cerebral Flows". *Journal of Biomechanics*. **40**(8), 1794-1805 (2007).
4) Allen RJ, Rieger TR, Musante CJ. "Efficient Generation and Selection of Virtual Populations in Quantitative Systems Pharmacology Models". *CPT: Pharmacokinetics & Systems Pharmacology*. **5**(3), 140-146 (2016).
5) Attwell D, Mishra A, Hall CN, O'Farrell FM, Dalkara T. "What is a Pericyte?" *The Journal of Cerebral Blood Flow & Metabolism*. **36**(2), 451-455 (2016).
6) Bachler G, von Goetz N, Hungerbühler K. "A Physiologically Based Pharmacokinetic Model for Ionic Silver and Silver Nanoparticles". *International Journal of Nanomedicine.* **8**, 3365-3382 (2013).
7) Badiani RS. "Quantifying the Effects of Cerebrovascular Variability on Blood Flow and Perfusion in the Brain". *University of Oxford, Department of Engineering Science*. 1st Ed. (2018).
8) Balfourier A, Luciani N, Wang G, Lelong G, Ersen O, Khelfa A, Alloyeau D, Gazeau F, Carn F. "Unexpected Intracellular Biodegradation and Recrystallization of Gold Nanoparticles". *Proceedings of the National Academy of Sciences*. **117**(1), 103-113 (2019).

9) Barret MJP & Suresh V. “Extra Permeability is Required to Model Dynamic Oxygen Measurements: Evidence for Functional Recruitment?”. *Journal of Cerebral Blood Flow & Metabolism*. **33**(9), 1402-1411 (2013).

10) Bernier M, Cunnane SC, Whittingstall K. “The Morphology of the Human Cerebrovascular System”. *Human Brain Mapping*. **39**(12), 4962-4975 (2018).

11) Bryngelson SH, Gueniat F, Freund JB. “Irregular Dynamics of Cellular Blood Flow in a Model Microvessel”. *Physical Review E*. **100**(1), 012203 (2019).

12) Burzynska AZ, Anderson C, Arciniegas DB, Calhoun V, Choi I, Mendez Colmenares A, Kramer AF, Li K, Lee J, Lee P, Thomas ML. “Correlates of Axonal Content in Healthy Adult Span: Age, Sex, Myelin, and Metabolic Health”. *Cerebral Circulation – Cognition and Behavior*. **6**, 100203 (2024).

13) Carslaw HS, Jaeger JC. “Conduction of Heat in Solids” *Oxford University Press*. 2nd Ed. 1959.

14) Cassot F, Lauwers F, Fouard C, Prohaska S, Lauwers-Cances V. “A Novel Three-Dimensional Computer-Assisted Method for a Quantitative Study of Microvascular Networks of the Human Cerebral Cortex” *Microcirculation*. **13**, 1-18 (2006).

15) Castillo E, Mínguez R, Castillo C. “Sensitivity Analysis in Optimization and Reliability Problems”. *Reliability Engineering & System Safety*. **93**(12), 1788-1800 (2008).

16) Cebral JR, Castro MA, Soto O, Lohner R, Alperin N. “Blood Flow Models of the Circle of Willis from Magnetic Resonance Data”. *Journal of Engineering Mathematics*. **47**, 369-386 (2003).

17) Cebral JR, Putman CM, Alley MT, Hope T, Bammer R, Calamante F. “Hemodynamics in Normal Cerebrel Arteries: Qualitative Comparison of 4D Phase-Contrast Magnetic

Resonance and Image-Based Computational Fluid Dynamics". *Journal of Engineering Mathematics*. **64**(4), 367-378 (2009).

18) Charbel FT, Zhao MD, Amin-Hanjani S, Hoffman W, Du XJ, Clark ME. "A Patient Specific Computer Model to Predict the Outcomes of the Balloon Occlusion Test". *Journal of Neurosurgery*. **101**(6), 977-988 (2004).

19) Chen X, Buerk DG, Barbee KA, Jaron D. "A Model of NO/O_2 Transport in Capillary-perfused Tissue Containing an Arteriole and Venule Pair". *Annals of Biomedical Engineering*. **35**, 517-529 (2007).

20) Chen J, Yuan M, Madison CA, Eitan S, Wang Y. "Blood-Brain Barrier Crossing Using Magnetic Stimulated Nanoparticles". *Journal of Controlled Release*. **345**, 557-571 (2022).

21) Cho EC, Zhang Q, Xia Y. "The Effect of Sedimentation and Diffusion on Cellular Uptake of Gold Nanoparticles". *Nature Nanotechnology*. **6**(6), 385-391 (2011).

22) Cieslicki K & Ciesla D. "Investigations of Flow and Pressure Distributions in Physical Model of the Circle of Willis". *Journal of Biomechanics*. **38**(11), 2302-2310 (2005).

23) Cipolla MJ. "The Cerebral Circulation". *Morgan and Claypool Life Sciences*. 1st Ed. (2009).

24) Clarke DD & Sokoloff L. "Basic Neurochemistry: Molecular, Cellular and Medical Aspects". *Philadelphia: Lippincott-Raven*. 6th Ed. (1999).

25) DiLuca M & Oleson J. "The Cost of Brain Diseases: A Burden or a Challenge?" *Neuron*. **82**(6), 1205-1208 (2014).

26) Dotiwala AK, McCausland C, Samra NS. "Anatomy, Head and Neck: Blood Brain Barrier" *StatPearls Publishing (Internet)*. 1st Ed. (2023).

27) Dunås T, Wåhlin A, Ambarki K, Zarrinkoob L, Malm J, Eklund A. "A Stereotactic Probabilistic Atlas for the Major Cerebral Arteries". *Neuorinformatics*. **15**, 101-110 (2016).

28) Duvernoy HM, Delon S, Vannson JL. “Cortical Blood Vessels of the Human Brain” *Brain Research Bulletin*. **7**, 519-579 (1981).

29) El-Bouri WK & Payne SJ. “Multi-Scale Homogenization of Blood Flow in 3-Dimensional Human Cerebral Microvascular Networks”. *Journal of Theoretical Biology*. **380**, 40-47 (2015).

30) Ertürk A, Becker K, Jährling N, Mauch CP, Hojer CD, Egen JG, Hellal F, Bradke F, Sheng M, Dodt H. “Three-Dimensional Imaging of Solvent-Cleared Organs using 3DISCO”. *Nature Protocols*. **7**, 1983-1995 (2012).

31) Fan H, Cai Q, Qin Z. “Measurement and Modeling of Transport Across the Blood-Brain Barrier”. *Journal of Biomechanical Engineering*. **145**(8) (2023).

32) Fares J, Kanojia D, Rashidi A, Ulasov I, Lesniak MS. “Genes that Mediate Metastasis across the Blood-Brain Barrier”. *Trends in Cancer*. **6**(8), 660-676 (2020).

33) Foehrenbacher A, Secomb TW, Wilson WR, Hicks KO. “Design of Optimized Hypoxia-Activated Prodrugs using Pharmacokinetic/Pharmacodynamic Modelling”. *Frontiers in Oncology*. **3**:314 (2013).

34) Foehrenbacher, A., Patel, K., Abbattista, M., Guise, C.P., Secomb, T.W., Wilson, W.R., Hicks, K.O. “The Role of Bystander Effects in the Antitumor Activity of the Hypoxia-Activated Prodrug PR-104”. *Frontiers in Oncology*. **3**:263 (2013).

35) Gawdi R, Shumway KR, Emmady PD. “Physiology, Blood Brain Barrier”. *StatPearls Publishing (Internet)*. 1st Ed. (2023).

36) Gkontra P, El-Bouri W, Norton KA, Santos A, Popel AS, Payne SJ, Arroyo AG. “Dynamic Changes in Microvascular Flow Conductivity and Perfusion After Myocardial Infarction

Shown by Image-Based Modeling". *Journal of the American Heart Association*. **8**(7), (2019).

37) Goetz LH & Schork NJ. "Personalized Medicine: Motivation, Challenges, and Progress" *Fertility and Sterility*. **109**(6), 952-963 (2018).

38) Gopalan C & Kirk E. "Chapter 2 – The Blood Vessels" *Biology of Cardiovascular and Metabolic Diseases*. 35-51 (2022).

39) Grunewald WA, Sowa W. "Capillary Structures and O_2 Supply to Tissue. An Analysis with a Digital Diffusion Model as Applied to the Skeletal Muscle". *Rev Physiol Biochem Pharmacol.* **77**:149 (1977).

40) Hardman, R. "A Toxicologic Review of Quantum Dots: Toxicity Depends on Physiochemical and Environmental Factors". *Environmental Health Perspective*. **114**(2), 165-172 (2006).

41) Hillen B, Hoogstraten HW, Post L. "A Mathematical Model of the Flow in the Circle of Willis". *Biomechanics*. **19**(3), 187-194 (1986).

42) Hoover EE & Squier JA. "Advances in Multiphoton Microscopy Technology". *Nature Photonics*. **7**(2), 93-101 (2013).

43) Horton NG, Wang K, Kobat D, Clark CG, Wise FW, Schaffer CB, Xu C. "*In vivo* Three-Photon Microscopy of Subcortical Structures within an Intact Mouse Brain". *Nature Photonics*. **7**, 205-209 (2013).

44) Hsu R & Secomb TW. "A Green's Function Method for Analysis of Oxygen Delivery to Tissue by Microvascular Networks". *Mathematical Biosciences*. **96**: 61-78 (1989).

45) Ivanov KP, Kislyakov YY, Samoilov MO. "Microcirculation and Transport of Oxygen to Neurons of the Brain". *Microvascular Research.* **18**, 434 (1979).

46) Jain S, Coulter JA, Butterworth KT, Hounsell AR, McMahon SJ, Hyland WB, Muir MF, Dickson GR, Prise KM, Currell FJ, Hirst DG, O'Sullivan JM. "Gold Nanoparticle Cellular Uptake, Toxicity and Radiosensitisation in Hypoxic Conditions". *Radiotherapy and Oncology*. **110**(2), 342-347 (2014)

47) Jia L, Zhang P, Sun H, Dai Y, Liang S, Bai X, Feng L. "Optimization of Nanoparticles for Smart Drug Delivery: A Review". *Nanomaterials*. **11**(11), 2790 (2021).

48) Joseph TM, Mahapatra DK, Esmaeili A, Piszczyk L, Hasanin MS, Kattali M, Haponiuk J, Thomas S. "Nanoparticles: Taking a Unique Position in Medicine". *Nanomaterials*. **13**(3), 574 (2023).

49) Juhairiyah F & de Lange ECM. "Understanding Drug Delivery to the Brain Using Liposome-Based Strategies: Studies that Provide Mechanistic Insights Are Essential". *The AAPS Journal*. **23**(6), 114 (2021).

50) Kanwal A, Saif B, Muhammad A, Liu W, Liu J, Ren H, Yang P, Lei Z. "Hemoglobin-Promoted Growth of Polyhedral Gold Nanoparticles for the Detection of Glucose, H2O2, and Ascorbic Acid". *ACS Applied Nanomaterials*. **6**(6), 4734-4746 (2023).

51) Karch R, Neumann F, Neumann M, Schreiner W. "Staged Growth of Optimized Arterial Model Trees" *Annals of Biomedical Engineering*. **28**, 495-511 (2000).

52) Kety SS & Schmidt CF. "The Effects of Altered Arterial Tensions of Carbon Dioxide and Oxygen on Cerebral Blood Flow and Cerebral Oxygen Consumption of Normal Young Men". *Journal of Clinical Investigation*. **27**(4), 484-492 (1948).

53) Khan AI, Lu Q, Du D, Lin Y, Dutta P. "Quantification of Kinetic Rate Constants for Transcytosis of Polymeric Nanoparticle through Blood-Brain Barrier". *Biochimica et Biophysica Acta*. **1862**(12), 2779-2787 (2018).

54) Kim CSS, Kris C, Kwak D, David T. “Numerical Simulation of Local Blood Flow in the Carotid and Cerebral Arteries under Altered Gravity”. *Journal of Biomechanics*. **128**(2), 194-202 (2006).

55) Knisely MH, Reneau DD Jr, Bruley DF. “The Development and Use of Equations for Predicting the Limits on the Rates of Oxygen Supply to the Cells of Living Tissues and Organs. A Contribution to the Biophysics of Health and Disease”. *Angiology.* **20**(11), 1-56 (1969).

56) Kopylova V, Boronovskiy S, Nartsissov Y. “Approaches to Vascular Network, Blood Flow, and Metabolite Distribution Modeling in Brain Tissue”. *Biophysical Reviews.* **15**, 1335–1350 (2023).

57) Kotchey GP, Zhao Y, Kagan VE, Star A. “Peroxidase-Mediated Biodegradation of Carbon Nanotubes *in vitro* and *in vivo*”. *Advanced Drug Delivery Review.* **65**(15), 1921–1932 (2013).

58) Krogh, A. “The Number and the Distribution of Capillaries in Muscle with the Calculation of the Oxygen Pressure Necessary for Supplying the Tissue”. *The Journal of Physiology (London)*. **52**, 409–515 (1919).

59) Kumar S, Jha I, Mogha NK, Venkatesu P. “Biocompatibility of Surface-Modified Gold Nanoparticles towards Red Blood Cells and Haemoglobin”. *Applied Surface Science*. **512**, 145573 (2020).

60) Lassen, NA. “Cerebral Blood Flow and Oxygen Consumption in Man”. *Physiological Reviews*. **39**(2), 183-238 (1959).

61) Li M, Zou P, Tyner K. “Physiologically Based Pharmacokinetic (PBPK) Modeling of Pharmaceutical Nanoparticles”. *The AAPS Journal*. **19**, 26-52 (2017).

62) Lin E & Alessio A. “What are the Basic Concepts of Temporal, Contrast, and Spatial Resolution in Cardiac CT?” *Journal of Cardiovascular Computed Tomography*. **3**(6), 403-408 (2009).

63) Linninger AA, Gould IG, Marinnan T, Hsu CY, Chojecki M, Alaraj A. “Cerebral Microcirculation and Oxygen Tension in the Human Secondary Cortex”. *Annals of Biomedical Engineering*. **41**, 2264-284 (2013).

64) Liu G, Luo Q, Wang H, Zhuang W, Wang Y. “*In Situ* Synthesis of Multidentate PEGylated Chitosan Modified Gold Nanoparticles with Good Stability and Biocompatibility”. *RCS Advances*. **5**, 70109-70116 (2015).

65) Marchand PJ, Lu X, Zhang C, Lesage F. “Validation of Red Blood Cell Flux and Velocity Estimations Based upon Optical Coherence Tomography Intensity Fluctuations”. *Scientific Reports*. **10**, (2020).

66) McCarthy D, Malhotra M, O'Mahony AM, Cryan JF, O'Driscoll CM. “Nanoparticles and the Blood-Brain Barrier: Advancing from *In Vitro* Models Towards Therapeutic Significance”. *Pharmaceutical Research*. **32**(4), 1161-1185 (2014).

67) McConnell FK & Payne SJ. “The Dual Role of Cerebral Autoregulation and Collateral Flow in the Circle of Willis after Major Vessel Occlusion”. *Transactions on Biomedical Engineering*. **64**(8), 1793-1802 (2017).

68) Meneses LDM, Brito PF, Rocha BM, Santos RW, Queiroz RAB. “Construction of Arterial Networks Considering a Power Law with Exponent Dependent on Bifurcation Level”. *VII Latin American Congress on Biomedical Engineering CLAIB 2016, Bucaramanga, Santander, Colombia*. **60**, 545-548 (2017).

69) Metzger H. “The Influence of Space-Distributed Parameters on the Calculation of Substrate and Gas Exchange in Microvascular Units”. *Mathematical Biosciences.* 30:31 (1976).

70) Milanovic S, Shaw K, Hall C, Payne SJ. “Investigating the Role of Pericytes in Cerebral Autoregulation: a Modeling Study” *Physiological Measurement*. **42**(5) (2021).

71) Moss DM & Siccardi M. “Optimizing Nanomedicine Pharmacokinetics Using Physiologically Based Pharmacokinetics Modelling”. *British Journal of Pharmacology*. **171**(17), 3963-3979 (2014).

72) Mouches P & Foukert ND. “A Statistical Atlas of Cerebral Arteries Generated Using Multi-Center MRA Datasets from Healthy Subjects”. *Scientific Data*. **6**(29), (2019).

73) Nader E, Skinner S, Romana M, Fort R, Lemonne N, Guillot N, Gauthier A, Antoine-Jonville S, Renoux C, Hardy-Dessources MD, Stauffer E, Joly P, Bertrand Y, Connes P. “Blood Rheology: Key Parameters, Impact on Blood Flow, Role in Sickle Cell Disease and Effects of Exercise”. *Frontiers in Physiology*. **10**, 1329 (2019).

74) Nagata K, Yamazaki T, Takano D, Maeda T, Fujimaki Y, Nakase T, Sato Y. “Cerebral Circulation in Aging”. *Ageing Research Reviews*. **30**, 49-60 (2016).

75) Nicholson C, Chen KC, Hrabetova S, Tao L. “Diffusion of Molecules in Brain Extracellular Space: Theory and Experiment”. *Progress in Brain Research*. **125**, 129-154 (2000).

76) Papantchev V, Stoinova V, Aleksandrov A, Todorova-Papantcheva D, Hristov S, Petkov D, Nachev G, Ovtscharoff W. “The Role of Willis Circle Variations During Unilateral Selective Cerebral Perfusion: A Study of 500 Circles”. *European Journal of Cardio-thoracic Surgery*. **44**(4), 743-753 (2013).

77) Payne SJ. “A Model of the Interaction between Autoregulation and Neural Activation in the Brain”. *Mathematical Biosciences*. **204**(2), 260-281, (2006).

78) Payne SJ. “Cerebral Blood Flow and Metabolism: A Quantitative Approach”. *World Scientific Publishing Co. Pte. Ltd*. 1st Ed. (2017).

79) Payne SJ. “Mathematical Models of the Cerebral Microcirculation in Health and Pathophysiology”. In: Linninger A, Mardal KA, Zunino P (eds). Quantitative Approaches to Microcirculation. *SEMA SIMAI Springer Series*, vol 36. Springer, Cham. (2024).

80) Payne SJ, Józsa TI, El-Bouri, WK. “Review of *in silico* Models of Cerebral Blood Flow in Health and Pathology”. *Progress in Biomedical Engineering.* **52**(2), (2023).

81) Pelaz B, del Pino P, Maffre P, Hartmann R, Gallego M, Rivera-Fernández S, de la Fuente JM, Nienhaus GU, Parak WJ. “Surface Functionalization of Nanoparticles with Polyethylene Glycol: Effects on Protein Adsorption and Cellular Uptake” *ACS Nano*. **9**(7), 6996-7008 (2015).

82) Peyrounette M, Davit Y, Quintard M, Lorthois S. “Multiscale modelling of blood flow in cerebral microcirculation: Details at capillary scale control accuracy at the level of the cortex”. *PLOS ONE*. **13**(1), 1-35 (2018).

83) Popel AS. “Theory of Oxygen Transport to Tissue”. *Critical Reviews in Biomedical Engineerings*. **17**, 257–321 (1989).

84) Pries AR, Neuhaus D, Gaehtgens P. “Blood Viscosity in Tube Flow: Dependence on Diameter and Hematocrit”. *American Journal of Physiology*. **263**, 1770-1778 (1992).

85) Pries AR, Reglin B, Secomb, TW. “Remodeling of Blood Vessels: Responses of Diameter and Wall Thickness to Hemodynamic and Metabolic Stimuli”. *Hypertension*. **46**(4), 725-731 (2005).

86) Qian S & Mahdi A. “Sensitivity Analysis Methods in the Biomedical Sciences”. *Mathematical Biosciences*. **323** (2020).

87) Rana A, Adhikary M, Singh PK, Das BC, Bhatnagar S. “‘Smart’ Drug Delivery: A Window to Future of Translational Medicine”. *Frontiers in Chemistry*. **10** (2023).

88) Razavi S & Gupta HV. “A New Framework for Comprehensive, Robust, and Efficient Global Sensitivity Analysis: 1. Theory” *Water Resources Research*. **52**(1), 423-439 (2015).

89) Reichold J, Stampanoni M, Keller AL, Buck A, Jenny P, Weber B. “Vascular Graph Model to Simulate the Cerebral Blood Flow in Realistic Vascular Networks”. *Journal of Cerebral Blood Flow and Metabolism*. **29**(8), 1429-1443 (2009).

90) Reinhart WH, Piety NZ, Shevkoplyas SS. “Influence of Feeding Hematocrit and Perfusion Pressure on Hematocrit Reduction (Fåhraeus Effect) in an Artificial Microvascular Network. *Microcirculation.* **24**(8), (2017).

91) Reznickova A, Slavikova N, Kolska Z, Kolarova K, Belinova T, Kalbacova MH, Cieslar M, Svorcik V. “PEGylated Gold Nanoparticles: Stability, Cytotoxicity and Antibacterial Activity”. *Colloids and Surfaces A: Physiochemical and Engineering Aspects*. **560**, 26-34 (2019).

92) Rhee CJ, da Costa CS, Austin T, Brady KM, Czosnyka M, Lee JL. “Neonatal Cerebrovascular Autoregulation”. *Pediatric Research*. **84**, 602-610 (2018).

93) Safaeian N, Sellier M, David T. “A Computational Model of Hemodynamic Parameters in Cortical Capillary Networks”. *Journal of Theoretical Biology*. **1**(21), 145-156 (2011).

94) Schleyer G, Patterson EA, Curran JM. “Label Free Tracking to Quantify Nanoparticle Diffusion through Biological Media”. *Scientific Reports*. 18822 (2024).

95) Schmid F, Barret MJP, Jenny P, Weber B. “Vascular Density and Distribution in Neocortex”. *NeuorImage*. **197**, 792-805 (2019).

96) Schreiner W. “Computer Generation of Complex Arterial Tree Models”. *Journal of Biomedical Engineering*. **15**(2), 148-150 (1993).

97) Secomb TW “A Green’s Function Method for Simulation of Time-Dependent Solute Transport and Reaction in Realistic Microvascular Geometries”. *Mathematical Medicine and Biology*. **33**(4), 475-494 (2015).

98) Secomb TW, Hsu R, Park EYH, Dewhirst MW. “Green's Function Methods for Analysis of Oxygen Delivery to Tissue by Microvascular Networks”. *Annals of Biomedical Engineering*, **32**, 1519-1529 (2004)

99) Secomb TW, Hsu R, Dewhirst MW. “Synergistic Effects of Hyperoxic gas Breathing and Reduced Oxygen Consumption on Tumor Oxygenation: A Theoretical Model”. *International Journal of Radiation Oncology, Biology, Physics*, **59**, 572-578 (2004).

100) Sela H, Cohen H, Elia P, Zach R, Karpas Z, Zeiri Y. “Spontaneous Penetration of Gold Nanoparticles through the Blood Brain Barrier (BBB)”. *Journal of Nanobiotechnology*. **13**(71), 1-9 (2015).

101) Sethuraman M. “Chapter 4 - Neurophysiology”. In: Essentials of Neuroanesthesia. *Academic Press*. 1st Ed. (2017).

102) Shamloo A, Pedram MZ, Heidari H, Alasty A. “Computing the Blood Brain Barrier (BBB) Diffusion Coefficient: A Molecular Dynamics Approach” *Journal of Magnetism and Magnetic Materials*. **410**, 187-197 (2016).

103) Sherwin SJ, Franke V, Peiró J, Parker K. “One-Dimensional Modelling of a Vascular Network in Space-Time Variables”. *Journal of Engineering Mathematics*. **47**, 217-250 (2003).

104) Shipley RJ, Smith AF, Sweeney PW, Pries AR, Secomb TW. “A Hybrid Discrete-Continuum Approach for Modelling Micorcirculatory Blood Flow”. *Mathematical Medicine and Biology*. **37**(1), 40-57 (2020).

105) Siepmann J & Siepmann F “Mathematical Modeling of Drug Delivery” *International Journal of Pharmaceutics*. **364**(2), 328-343 (2008).

106) Siepmann J & Siepmann F “Modeling of Diffusion Controlled Drug Delivery” *Journal of Controlled Release*. **161**(2), 351-362 (2012).

107) Smith AF, Doyeux V, Berg M, Peyrounette M, Haft-Javaherian M, Laure A, Slater JH, Lauwers F, Blinder P, Tsai P, Kleinfeld D, Schaffer CB, Nishimura N, Davit Y, Lorthois S. “Brain Capillary Networks Across Species: a Few Simple Organizational Requirements are Sufficient to Reproduce Both Structure and Function”. *Frontiers in Physiology*. **10**, 233 (2019).

108) Strandgaard S & Paulson OB. “Cerebral Autoregulation”. *Stroke- A Journal of Cerebral Circulation*. **15**(3), 413-416 (1984).

109) Su SW, Catherall M, Payne SJ. “The Influence of Network Structure on the Transport of Blood in the Human Cerebral Microvasculature”. *Microcirculation*. **19**, 175-187 (2012).

110) Sun J, Wang F, Sui Y, She Z, Zhai W, Wang C, Deng Y. “Effect of Particle Size on Solubility, Dissolution Rate, and Oral Bioavailability: Evaluation using Coenzyme Q_{10} as Naked Nanocrystals”. *Internation Journal of Nanomedicine*. **7**, 5733-5744 (2012).

111) Teleanu DM, Chircov C, Grumezescu AM, Volceanov A, Teleanu AI. “Impact of Nanoparticles on Brain Health: An Up to Date Overview”. *Journal of Clinical Medicine*. **7**(12), 490 (2018).

112) Terman D, Chen L, Hannawi Y. “Mathematical Modeling of Cerebral Capillary Blood Flow Heterogeneity and its Effect on Brain Tissue Oxygen Levels”. *Journal of Theoretical Biology*. **527**, (2021).

113) Tsai PS, Kaufhold JP, Blinder P, Friedman B, Drew PJ, Karten HJ, Lyden PJ, Kleinfeld D. “Correlations of Neuronal and Microvascular Densities in Murine Cortex Revealed by Direct Counting and Colocalization of Nuclei and Vessels”. *Journal of Neuroscience*. **29**(46), 14553-14570 (2009).

114) Ursino M. “A Mathematical Study of Human Intracranial Hydrodynamics. Part 2 -- Simulation of Clinical Tests”. *Annals of Biomedical Engineering*. **16**(4), 403-416 (1988).

115) Ursino M. “Mechanisms of Cerebral Blood Flow Regulation”. *Critical Reviews in Biomedical Engineering*. **18**(4), 255-288 (1991).

116) Ursino M & Lodi CA. “Interaction among Autoregulation, CO_2 Reactivity, and Intracranial Pressure: A Mathematical Model”. *American Journal of Physiology - Heart and Circulatory Physiology*. **274**(5), 1715-1728 (1998).

117) Ursino M, Ter Minassian A, Lodi CA, Beydon L. “Cerebral Hemodynamics during Arterial and CO_2 Pressure Changes: *in vivo* Prediction by a Mathematical Model”. *American Journal of Physiology- Heart and Circulatory Physiology*. **279**(5), 2439-2455 (2000).

118) Ursino M & Giannessi M. “A Model of Cerebrovascular Reactivity Including the Circle of Willis and Cortical Anastomoses”. *Biomedical Engineering*. **30**(3), 265-272 (2010).

119) Utku S & Melosh RJ. “Solution Errors in Finite Element Analysis”. *Computer & Structures.* **18**(3), 379-393 (1984).

120) Verimli N, Demiral A, Yılmaz H, Çulha M, Erdem SS. “Design of Dense Brush Conformation Bearing Gold Nanoparticles as Theranostic Agent for Cancer”. *Applied Biochemistry and Biotechnology*. **189**, 709-728 (2019).

121) Viedma, A, Jiminez-Ortiz C, & Marco V. “Extended Willis Circle Model to Explain Clinical Observations in Periorbital Arterial Flow”. *Journal of Biomechanics*. **30**(3), 265-272 (1997).

122) Weber B, Keller AL, Reichold J, Logothetis NK. “The Microvascular System of the Striate and Extrastriate Visual Cortex of the Macaque”. *Cerebral Cortex*. **18**(10), 2318-2330 (2008).

123) Williams LR & Leggett RW. “Reference Values for Resting Blood Flow to Organs of Man”. *Clinical Physics and Physiological Measurement*. **10**(3), 187-217 (1989).

124) Williford CW, Bruley DF, Artigue RS. “Probabilistic Modeling of Oxygen Transport in Brain Tissue”. *Neurological Research.* **2**, 153-170 (1980).

125) Wilson B. “Drug Targeting Strategies into the Brain for Treating Neurological Diseases”. *Journal of Neuroscience Methods*. **311**, 133-146 (2019).

126) Windberger U, Bartholovitsch A, Plazenzotti R, Korak KJ, Heinze G. “Whole Blood Viscosity, Plasma Viscosity and Erythrocyte Aggregation in Nine Mammalian Species: Reference Values and Comparison of Data”. *Experimental Physiology*. **88**(3), 431-440 (2003).

127) Wright SN, Kochunov P, Mut F, Bergamino M, Brown KM, Mazziotta JC, Toga AW, Cebral JR, Ascoli GA. “Digital Reconstruction and Morphometric Analysis of Human

Brain Arterial Vasculature from Magnetic Resonance Angiography". *Neuroimage*. **82**, 150-181 (2013).

128) Xue S, Gong H, Jiang T, Luo W, Meng Y, Liu Q, Chen S, Li A. "Indian-Ink Perfusion Based Method for Reconstructing Continuous Vascular Networks in Whole Mouse Brain". *PLOS One*. **9**(1), (2014).

129) Xue Y, El-Bouri WK, Józsa TI, Payne SJ. "Modelling the Effects of Cerebral Microthrombi on Tissue Oxygenation and Cell Death". *Journal of Biomechanics*. **127** 110705 (2021).

130) Zagzoule M & Marc-Vergnes JP. "A Global Mathematical Model of the Cerebral Circulation in Man." *Biomechanics*. **19**(12), 1015-1022 (1986).

131) Zhou Y, Peng Z, Seven ES, Leblanc RM. "Crossing the Blood-Brain Barrier with Nanoparticles" *Journal of Controlled Release*. **270**, 290-303 (2018).